UNIVERSITY OF COPENHAGEN

UCPH NANOSCIENCE

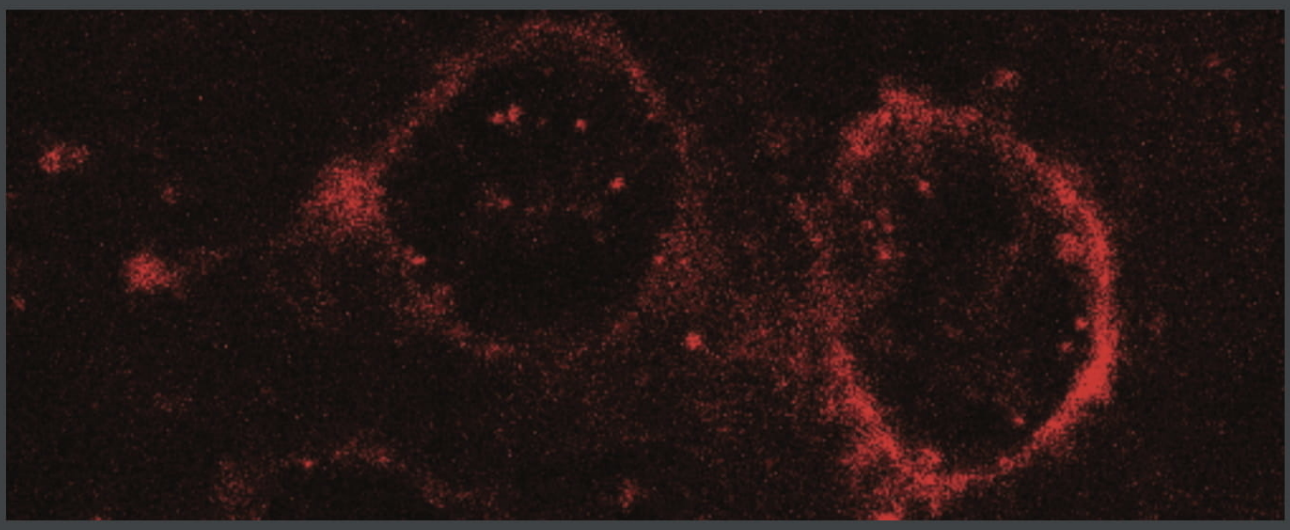

UCPH Nanoscience

Student Journal

Vol. 1 2018

UCPH Nanoscience

a student research journal

Udgivet af Nano-Science Center, Københavns Universitet, Danmark
E-versionen findes på tidsskrift.dk/index.php/NanoVidenskabKU
Printet af www.lulu.com
Denne udgivelse kan købes på markedspladsen på www.lulu.com

ISSN: 2446-1873

About the journal

UCPH Nanoscience is not a peer reviewed journal, it is a journal that published opinion pieces and news from the Nano-Science Center and serves as a repository for student research performed as part of the nanoscience degree programme at the University of Copenhagen.

Editorial

All beginnings are difficult. For the nanoscience students it has been difficult to perceive our ambition with this journal without tangible evidence of what the nanoscience student journal is. For the publishers it has been a nightmare of administrative procedures and a Gordian Knot of copyright rules and protective supervisors. But now we are ready to publish the first nanoscience bachelor thesis, and hopefully the next issue of UCPH Nanoscience will arrive with fewer difficulties.

UCPH Nanoscience is to be considered an online archive of bachelor thesis and other reports from the nanoscience students at the University of Copenhagen. Thus, there are no infringements on publication of results elsewhere. We are lucky that there are many examples of similar archives (ArXiv.org, ChemRxiv.org, BioRxiv.org etc.) where manuscripts are deposited prior to publication without any impact on the scientific publication process. So please let your bachelor thesis become part of the UCPH Nanoscience expressed in this journal.

The editors of UCPH Nanoscience are always looking for new people to help in the publication of the student journal. We would like to expand the News and Views section with reports from students, to have students write the thesis summaries, and to publish short reports from student studying abroad, and from all nanoscience events. To find and convince the people that has been studying abroad to contribute, and to write the various short stories and reports we need you. So please contribute, not only with your thesis but in all the ways you can imagine.

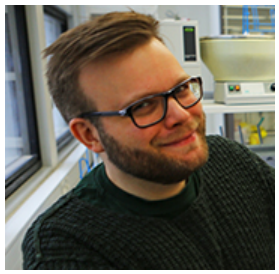

Thomas Just Sørensen
Editor-in-chief

Competition

UCPH NanoScience
NanoVidenskab KU
University of Copenhagen
student research papers

UCPH Nanoscience need a logo

Can you do better? The journal needs a logo to replace the temporary logo designed by the editor in chief. All suggestions are welcome, but you are encouraged to design a logo that reflects spirit of the Copenhagen flavour of nanoscience and the nanoscience student body. The prize is two vintage bottles of Verdi sparkling vine.

Suggestions should be sent to the editor-in-chief by December 1st 2016 at tjs@chem.ku.dk.

People Wanted!

UCPH Nanoscience is looking for staff

We are looking for 4 junior editors/reporters determined to shape the future of the student journal. The junior editors will be responsible for running the journal and provide student relevant content for the News & Views section.

Table of contents

Mission Statement

The scope of UCPH Nanoscience – a student research journal is to document the breadths of research performed by students at the Nano-Science Center at the University of Copenhagen. This is accomplished by publishing all bachelor theses submitted to obtain a bachelor degree in nanoscience. Each volume of the journal will contain up to four issues, and will be published online at:
tidsskrift.dk/index.php/NanoVidenskabKU
The journal is not indexed in any abstracts services, and the papers may only be cited as opinion pieces, bachelor theses, and reports.

Target audience

Current, past and prospective students of nanoscience and the related disciplines, and the faculty of the Nano-Science Center, University of Copenhagen.

Contributors

The main contribution will come through the mandatory submission of all bachelor theses as articles in this journal. 'Forskningspraktik' research trainee reports must also be submitted in order to qualify for examination. All theses and reports must be written in the supplied templates (Word/LaTeX) and adheres to a strict page limit, supporting information may be included. For each report, a short summary is written by the editorial staff. The summary will feature a photo of the student.
Students are encouraged to submit research articles written as part of their course work to the journal. Shorter letters, full papers, and reviews will be included in the journal as papers
Submitting of opinion pieces and relevant News & Views items are encouraged from students and faculty at the Nano-Science Center.

Content

Each issue will contain:

- Masthead
- Editorial
- Table of content
- News & Views
- Papers
- Theses
- Reports

The Papers and Reports sections will only be included if contributions have been received.

Editorial line & Peer review

The editors consider the quality of the submitted papers and the tone of the opinion pieces. Reports and thesis are submitted for examination and is published as is. There is no peer review on the theses and reports.

Thomas Just Sørensen
Editor-in-chief

Professor Bo W Laursen
Director of the Nano-Science Center

Professor Per Hedegård
Head of studies, Nanoscience

Picture Per Hedegård is the Head of studies for the nanoscience degree programme and Professor of Physics at the University of Copenhagen.

Picture Bo W. Laursen is the Director of the Nano-Science Center and Professor of Chemistry at the University of Copenhagen.

Thesis in this issue

The following students have graduated with a BA in nanoscience in 2017. Their theses have been included in this issue of UCPH Nanoscience.

Thesis marked by an asterix (*) are under embargo and will be published in a later issue of UCPH Nanoscience.

UCPH NanoScience, 2018, 1, 201801 10p

Optimization of experimental procedure for assessing transition metal FRET in LeuT by Alma Winther Sørensen

Alma Winther Sørensen worked in the Neuropharm and Genetics lab that with, amongst other things, Neurotransmitter Sodium Symporters in relation to drug addiction and treatment.

Almna graduated Nanoscience B.Sc. June 2017, where she focused on primarily biology and neuroscience.

Supervisor: Lektor Claus Juul Løland

Thesis abstract: Neurotransmitter sodium symporters (NSSs) are important for the regulation of neurotransmitters, such as dopamine and serotonin, which are involved in addiction and depression, along with several other diseases. The bacterial NSS, LeuT, has been proven to be a good model protein for the mammalian NSSs. Conformational changes of LeuT can be examined using transition metal ion F¨orster Energy Resonance Transfer (tmFRET), where the energy transfer between a fluorescein dye and a di-histidine bound Ni^{2+} is measured. When utilizing tmFRET, free Ni^{2+} is added to the solution, which also adds to the unspecific quenching signal detected. It is therefore necessary to remove the signal from the unbound Ni^{2+},in order to properly investigate the impact of specific bound Ni^{2+}. Here we investigate whether the effect of Zn^{2+} can be used to inhibit FRET contribution from specifically bound Ni^{2+} and thereby isolate the non-specific signal. We found that Zn^{2+} can competitively inhibit the binding of Ni^{2+} to the di-histidine motif of LeuT, thereby representing an easier, and perhaps more consistent, method for removing the signal from unbound Ni^{2+} during tmFRET measurements.

UCPH NanoScience, 2018, 1, 201802 12p

Weyl semimetals in models for ultracold atoms by Andreas Hansen

Andreas Hansen

Supervisor: Dr. Michele Burrello

Thesis abstract: I study the effect of a non-Abelian gauge potential on a Weyl semimetal phase appearing in a particular 3D tight-bindingmodel of fermions. The lattice I consider is characterized by a C_3 rotational symmetry and by staggered $\pi/2$ magnetic fluxes on the triangular plaquettes in its horizontal planes. The energy spectrum is characterized by both singleWeyl points with linear energy dispersions in all three momenta directions, and double Weyl points with quadratic energy dispersions in two directions and linear dispersion along the axis of the rotational symmetry.

UCPH NanoScience, 2018, 1, 201803 10p

Platinum nanoparticles in photothermal therapy of cancer cells by Bunya Sarmad Aswad and Iliriana Qoqaj *

Dunya Sarmad Aswad worked in the Optical Tweezers Group at the Niels Bohr Institute that work at the cross roads of physics, optics, biophotonics, chemistry molecular biology, and medicine.

Dunya has a B.A. in Nanoscience from the University of Copenhagen (U CPH), with a focus on nanobiophysics and nanomedicine. Dunya is currently studying my Master degree in Nanoscience and Technology in Beijing, China at Sino-Danish Center (SDC).

Iliriana Qoqaj worked in the Optical Tweezers Group at the Niels Bohr Institute that work at the cross roads of physics, optics, biophotonics, chemistry molecular biology, and medicine. Iliriana has a B.A. in

Nanoscience from the University of Copenhagen (UCPH) focused on nanobiophysics/nanomedicine.
Iliriana is currently studying my Master degree in Nanoscience and Technology in Beijing, China at Sino-Danish Center (SDC).
Supervisor: Postdoc Henrik Klingberg
Thesis abstract: Noble nanoparticles are potential photothermal therapy agents, due to their properties, such as ability to modify particle surface chemistry, and efficient light-to-heat conversion. In this work, we study the possible application of platinum nanoparticles as agents in photothermal therapy, their uptake, and toxicological response in the human ovarian cancer cell line (SK-OV-3) by flow cytometry. No oxidative stress, or toxicological response of the platinum nanoparticles was observed in the cells. Laser irradiation revealed photothermal destruction of SK-OV-3 cells exposed to 70 nm platinum nanoparticles at power density 45 W/cm2 after 5 minutes using an 808 near infrared laser.

UCPH NanoScience, 2018, 1, 201804 8p

Synthesis and characterization of $CuCrO_2$ delafossite nanoplatelets through Rietveld refinement and Pair distribution function analysis by Emil Thyge Skaaning Kjær

Emil Thyge Skaaning Kjær work with structure determination of crystallographic challenged materials using advanced x-ray and neutron techniques.
Emil is an enthusiastic supporter of the "Putte for president" campaign. I like not walking at the beach and when seeing people drinking Fernet Brance.
Supervisor: Adjunkt Kirsten M.Ø. Jensen
Thesis abstract: Delafossite (ABO_2) nanostructures such as $CuCrO_2$ nanoparticles have shown promising properties indye-sensitized solar cells (DSSCs). Previous studies have shown that changing the metal on either the A or B site in the structure, influences both the conditions required to synthesize delafossite compounds, their properties, and their tendency of forming nanocrystals or bulk particles. The crystallites can further be doped changing the conductivity further. Here, we present a series of syntheses with varying parameters, illustrating how the conditions must be optimized to obtain the pure delafossite $CuCrO_2$ phase. Structure characterization was done through Powder X-ray Diffraction (PXRD) showing change in crystallite size with increasing synthesis time and temperature. By varying both temperature and time, the amount of secondary phase (CuO) in the final product can be minimized. It was only possible to synthesize pure delafossite when certain criteria regarding pH, temperature and time were met. Rietveld refinement of the PXRD data showed anisotropic nanocrystallites with approximate sizes of 130x130x40Å with the trigonal delafossite unit cell. However, the crystallites are too small and anisotropic to give a satisfying fit using conventional Rietveld refinement, and the sizes were obtained through anisotropic "no rules" model. Pair Distribution Function (PDF) analysis of X-ray total scattering data were used to obtain further understanding of structural disorder in the crystallites.

UCPH NanoScience, 2018, 1, 201805 6p

Heterogeneous Nucleation of Calcium Carbonate: Effects of Substrate Chemistry by Lasse V. Nikolajsen

Lasse V. Nikolajsen work in the nanogeo group, researching surface physical chemistry. Particularly calcium and iron based minerals.
Lasse is a nanoscience bachelor student, and has followed mostly nanochemical courses. Lasse is interested in studying surface physical chemistry and the intermolecular interactions occurring in near surface environments.
Supervisor: Adjunkt Karina K. Sand
Thesis abstract: Investigating heterogeneous calcium carbonate nucleation is essential in the pursuit to the barriers of nucleation. However, heterogeneous calcium carbonate systems are difficult to characterize due to the influence of homogeneous nucleation. Homogeneous nucleation must be removed in order to reliably report the saturation indices used in the experiments. In this paper, homogeneous nucleation and heterogeneous nucleation are experimentally examined with atomic absorption spectroscopy, optical microscopy and ultraviolet-visible spectroscopy. The impact of homogeneous nucleation on concentration and the correlation between concentration and induction time are investigated. We document a significant impact on concentration suggesting data from current literature is compromised. Based on data,

we propose a concentration range of 0.7 mM – 0.9 mM for obtaining barriers to nucleation using optical microscopy. Learning how surfaces influence the barriers and kinetics of CaCO nucleation can increase our understanding of biomineralization and improve carbon sequestration.

UCPH NanoScience, 2018, 1, 201806 7p

Local Current Through Helical Orbitals by Louise Oxen Høgh Hyllested

Louise Oxen Høgh Hyllested worked in the molecular electronics theory group, researching molecules ability to transport electrons through chemistry and physics. Louise is a student interested in chemistry and physics and have mainly followed courses relating to the theory.

Supervisor: Lektor Gemma C. Solomon

Thesis abstract: Traditional chemical research has given great information about the physical properties of molecules. This research provides understanding of how molecules work in the classical ways, but the limit is reached when molecules are used in a non-traditional way. Now molecules can be inserted in molecular junctions, which makes it possible to examine molecules in new ways. Recent theoretical work has shown that some linear molecules can have helical orbitals. Here the question of interest is whether the current density around these particular molecules are affected by the helical orbitals and the coupling of the electrodes. We show that the helical orbitals in combination with the coupling of the electrodes, indeed has an impact on the current and that the orbitals contribute to a circular current around these linear molecules. As the understanding of the currents behavior around the molecules expand, it paves the way for new chemical questions about how we can control the current. For example, how helical current may induce magnetic properties in non-magnetic molecules, and how chemical substituent can be used to impact these effects.

UCPH NanoScience, 2018, 1, 201807 10p

Predicting insertion: external force application onto cells allow nanowire arrays to insert into cytosol by Nicolai Vanggaard Bærentsen*

Nicolai Vanggaard Bærentsen explore innovative interfaces of newly developed nano-tools with biological samples for the development of novel biosensors to be used for pharmacological investigation and diagnostics. Such new methods are developed in the perspective of personalized medicine, providing well-suited therapies (better efficiency and limited side effects).

Emphasis is put on the exploitation of novel nanotechnologies and biophysical techniques for the investigation of G protein coupled receptors (GPCRs) representing major drug targets.

Nicolai holds a bachelor degree in nanoscience from University of Copenhagen and currently studying a semester in China at the SDC programme at University of Chinese Academy of Sciences. Enrolled as nanoscience masters student at KU. Made my bachelor project in the Nanobio Group at KU, and had several courses taught by members of the group.

Supervisor: Karen Martinez

Thesis abstract: The use of vertical nanowires in biosensing application is limited by the extend of how efficient nanowires can reach the intracellular domains. Studies have found nanowire insertion to be successful through single nanowire experiments with high force pr. nanowire, using AFM. This is inadequate for producing high throughput analysis of several cells with multiple nanowires inserting in each cell. Here, we present a model for prediction of the nanowire insertion rates, when centrifugating cell samples down onto arrays of vertical indium arsenide nanowires, with a diameter of 100 nm, height of 3 mm and spacing of 3-5 mm. The model utilizes sedimentation rate of cells in conjunction with the centrifugal force field applied to objects subjected to centrifugation. Various conditions tested with the model, including lowering the temperature of the experiment from room temperature to 4 °C, show that cell viability is not negatively affected by any of the conditions. The insertion rate has been shown to be largely affected by the density of the nanowire array substrate, with a

lower density resulting in a higher NW insertion rate, as the model predicts. The percentage of cells with at least one successful nanowire insertion is, however, oppositely affected by density, as a higher density results in larger percentage of cells with successful insertions.

UCPH NanoScience, 2018, 1, 201808 8p

Speciation and structure of dipicolinate complexes and Eu(III) ions in solution by Patrick Nawrocki

Patrick R. Nawrocki work with tanthanide Coordination Chemistry. Patrick likes the movie "The Road to El Dorado"

Supervisor: Lektor Thomas Just Sørensen

Thesis abstract: Complexation between Eu(III) ions and dipicolinate tridentate ligands (DPA) have been studied to expand on our current understanding of structural and photophysical properties of lanthanides in solution. The dynamic ligand-exchange of labile lanthanide ions, has made it difficult to properly identify the bis ligated Eu(III) complex, as optical spectroscopy only reveals a weighted average of the present species. In this article, evidence for the bis ligated Eu(III) complex will be presented, which is a necessary component in accurately determining the binding constants and to gain further insight in the structureproperty relationship of the systems. Additionally, NMR, luminescence spectroscopy and X-ray scattering were used as structural corroboration to further establish the relationship between the solution structure and the intensities of Laporte parity forbidden *f-f* transitions, characteristic of the lanthanides.

UCPH NanoScience, 2018, 1, 201809 9p

Population size matters: The cause & effect of heterogeneous B1AR expression and its influence on receptor internalization by Sylvester Houstrup Langvad*

Sylvester Houstrup Langvad worked in the group of Karen Martinez that strives to explore the field of novel biosensors for pharmacological investigation and diagnostic.

When Sylvester is not studying nanoscience for the greater good, he is pondering philosophical trolley dilemmas and helping small kittens get down from trees. Study hard, play harder.

Supervisor: Karen Martinez

Thesis abstract: In cellular physiology, the impact of heterogeneous receptor expression is a topic that has recently started to receive much attention from the scientific community. However, much is still not understood about the specifics on the origin of this heterogeneity nor how it affects bulk measurements of heterogeneous population. While the literature often acknowledges this heterogeneity, it falls short of offering an explanation of what practical implications this variability may have. In this paper, we examine two methods for evoking protein expression of G Protein-Coupled Receptors, transient transfection and inducible cell lines, and show that these methods have markedly different expression variabilities. While the inducible cell lines have relatively homogeneous expression profiles, the transient transfected cells showed large variability to an extent that bulk measurements of transfected cells may yield misleading data. We hope that the results presented in this paper may inspire future research in the field to fully consider the effects of heterogeneous expression profiles.

New Nanoscience Bachelors

The following students have graduated with a BA in nanoscience in 2017. Their theses will not be published in UCPH Nanoscience.

Nicolai Ree conducted his bachelor's project in the group of Prof. PhD, Dr.Scient. Kurt V. Mikkelsen at the Center for Exploitation of Solar Energy, Department of Chemistry. Here we apply different electronic structure methods to calculate quantum chemical properties of molecules. Current projects involve the design and optimization of molecular energy storage and dye-sensitized solar cells. As well as, theoretical calculations of electrochemical properties.

During the bachelor in nanoscience, Nicolai worked on my first article and got it published just before obtaining my bachelor's degree:

N. Ree *et al.*, J. Phys. Chem. A, 2017, 121 (46), pp 8856–8865

Supervisor: Prof. PhD, Dr.Scient. Kurt V. Mikkelsen

Thesis title: A Methodology for Calculating Redox Potentials of Azulene Derivatives

---

Tahreem Aejaz Bukhari is interested in nanobio and organic chemistry particularly with focus on medical applications. Tahremm's hobbies include reading lots of books, baking cookies and playing Pokémon. She also enjoys taking naps.

Chastine Fleischer Munk worked on structure determination of LeuT using tmFRET to investigate the hellical unwinding mechanism of TM5 and TM7.

Chastine spend 6 months on exchange in Australia petting koalas and taking selfies with kangaroos. Chastine's favorite ice cream is raspberry sorbet, and Chastine is a professional when it comes to faceplanting when she wakeboards (that's why Chastine looks lost sometimes).

Supervisors: Lektor Nikos Hatzakis & Lektor Claus Juul Loland,

Thesis title: Investigating LeuT TM5 and TM7 Hellical Unwinding Dynamics Using tmFRET.

Emil Vogt performs research in the field of physical chemistry. The groups research is aimed at understanding atmospheric radical reactions. They are able to determine the reactivity of molecules and radicals in a range of different reactions by determining reaction rate constants. Their research is also aimed at determining properties of atmospheric molecules and hydrogen-bonded complexes to achieve a better understanding of the mechanisms of aerosol formation.

Emil has chosen to specialize in the field of quantum- and computational chemistry. His main interest lies in the theory of properties concerning vibrational spectroscopy. In my bachelor project he developed a model for obtaining parameters for the Deng-Fan potential. Furthermore, Emil compared XH-stretching transition frequencies and oscillator strengths using a numeric potential, the Deng-Fan potential and the Morse potential.

Supervisor: Professor Henrik Grum Kjærgaard

From students to students

A summer research project in Barcelona by Henrik Pinholt, Stud. Scient. Nanoscience 2016

For a long time, I have tried to find out how stem cells coordinate their collective behavior in the earlier developmental stages of fetal development. This work culminated the summer of 2016 in the form of three weeks of research at ”Centro de Régulación Genómica” (CRG) in Barcelona. The research was done in James Sharpe’s’ group: ”Multicellular Systems Biology” with aid from technician Heura Cardona under the observation of Sharpe. Our goal was to get more insight into the spatial regulation of the bone-inducing gene *SOX9* in the fingers of mouse fetuses. More specifically, we sought to investigate how cell environment affects *SOX9* expression due to effects of pressure from neighboring cells. We investigated this based on a model system: We grew mesenchymal EGFP-SOX9 stem cells from developing mice in micro cultures. The cultures were grown in homemade champers with the opportunity for pressure application with pistons. The pressure was meant to simulate cell condensations in chondrogenesis. In micro culture, these cells express a spatially periodic pattern of SOX9. This provides a model system to study the mechanism in charge of spatially positioning bone formation in digital regions and apoptosis in interdigital regions. We took CLSM pictures of the cultures, and studied the pattern changes due to pressure from the pistons. This probably sounds simple in theory, but it turned out to be quite troublesome to apply pressure to these cells without ruining the culture, and still being able to image the pattern. This heavily reduced the amount of usable data available. We did, however, manage to find indication towards a pressure-induced pattern change. Due to the lack of large amounts of proof, this study stands as an inspiration. My hope with this work is that it will add new perspectives to a field, which has mainly focused on spatial regulation through diffusing signals. This might not be the case in general, and new evidence suggest, that pressure might have influence not just on gene regulation locally, but also spatially. The problem is that this issue is rather difficult to address experimentally, and this is why this study is important. Because it provides a first attempt to investigate spatial gene regulation from compression in development.

Other news

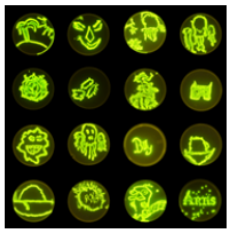

ARTiS: Art in Science

Art in Science or ARTiS is the outreach programme of Nano-Sceince center meant to use art to communicate science to a broad audience.
This includes an original approach to educate and engage children in scientific disciplines. It is furthermore a unique opportunity for scientists to talk about their work in an original context.
ARTiS 2017 was composed of the yearly picture contest, children boot camps and the yearly picture exhibition. About 100 pictures were part of the picture contest 2017 attracting 3,500 people to the ARTiS 2017 exhibition in the ceremonial hall of University of Copenhagen during Culture Night.
This programme is headed by Karen L. Martinez, associate professor and head of the BioMeP group. It has been sponsored by Lundbeckfonden and University of Copenhagen.

ARTiS 2017 Winners

1st prize 2017
“Beauty in seawater” by Jannicke Wiik-Nielsen, Norwegian Veterinary Institute.

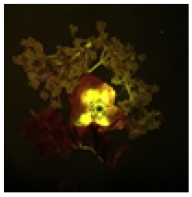

Young Art-scientist Prize 2017
”Flower” by Andrii Lapytskyi

COMMUNICATIONS & FULL PAPERS

UCPH NanoScience
NanoVidenskab KU

tidsskrift.dk/index.php/NanoVidenskabKU

Thesis Paper

Optimization of experimental procedure for assessing transition metal ion FRET in LeuT †

Alma Louise Winther Sørensen,[a]

Received June 2017, Accepted April 2018

Neurotransmitter sodium symporters (NSSs) are important for the regulation of neurotransmitters, such as dopamine and serotonin, which are involved in addiction and depression, along with several other diseases. The bacterial NSS, LeuT, has been proven to be a good model protein for the mammalian NSSs. Conformational changes of LeuT can be examined using transition metal ion Förster Energy Resonance Transfer (tmFRET), where the energy transfer between a fluorescien dye and a di-histidine bound Ni^{2+} is measured. When utilizing tmFRET, free Ni^{2+} is added to the solution, which also adds to the unspecific quenching signal detected. It is therefore necessary to remove the signal from the unbound Ni^{2+}, in order to properly investigate the impact of specific bound Ni^{2+}. Here we investigate whether the effect of Zn^{2+} can be used to inhibit FRET contribution from specifically bound Ni^{2+} and thereby isolate the non-specific signal. We found that Zn^{2+} can competitively inhibit the binding of Ni^{2+} to the di-histidine motif of LeuT, thereby representing an easier, and perhaps more consistent, method for removing the signal from unbound Ni^{2+} during tmFRET measurements.

1 Introduction

Transport proteins are essential building blocks of life. They are among other things involved in transporting ions and small molecules, such as neurotransmitters or amino acids across biological membranes. The majority of known neurotransmitter transporters belong to the neurotransmitter sodium symporter (NSS) family [1]. NSSs transport their solute by utilizing the energy gained from the sodium gradient, which is created by the Na^+/K^+ ATPase. Furthermore, all mammalian NSS co-transport Cl^-. [1] Important members of this family include transporters of dopamine (DAT), noradrenaline (NET) and serotonin (SERT). [2] NSSs are involved in the removal of transmitters from the synapse, thereby terminating transmission from neurotransmitters. This involvement in the control of synaptic signaling has made NSSs key targets for therapeutics and illicit drugs, such as cocaine or amphetamines [3]. The regulation of neurotransmitters such as dopamine and serotonin are thereby involved in addiction, as well as depression and other diseases such as ADHD or schizophrenia [4]. This makes NSSs very interesting to examine. However, the mammalian transporters have proven exceptionally challenging to purify sufficiently, as satisfactory stability, yield and purity has been difficult to obtain in order to properly investigate their structure. The bacterial NSS, LeuT, from the Aquifex aeolicus has, however, proven to be much easier to purify. Furthermore, LeuT has been shown to be a suitable model protein, as a high degree of structural conservation has been observed between LeuT and the mammalian NSSs [5]. Crystal structures of the mammalian SERT and dDAT, show great similarity to the LeuT structure [6 7]. Like most NSSs LeuT has 12 transmembrane domains, as well as a substrate binding site adjacent to two Na^+-binding sites located roughly halfway though the membrane bilayer. [8] LeuT is an amino acid transporter. LeuT undergoes structural conformations in order to transport its solute. Recent studies, based on tmFRET experiments, suggest that LeuT has an outward-open conformation when Na+ is bound, but adapts an outward-closed conformation in the presence of K+, when examining the extracellular side. [2 9]

Förster Resonance Energy Transfer (FRET) is useful for investigating molecular distances. Conventional FRET utilizes the energy transfered from a donor fluorophore, which has been excited by energy from a light source, to an acceptor fluorophore (Figure S1). The FRET efficiency, E, decreases inversely to the sixth power of the distance, R, between the donor and acceptor fluorophore. This is given by the equation $E = R_0^6/(R_0^6 + R^6)$, where R_0 is the critical transfer distance, also known as the Förster distance, and represents the donor-acceptor distance where the efficiency of the energy transfer is 50 %. [10] While FRET is very useful for intermolecular investigations, it is not always suitable for the investigations of intramolecular conformational movements, due to the limited window around

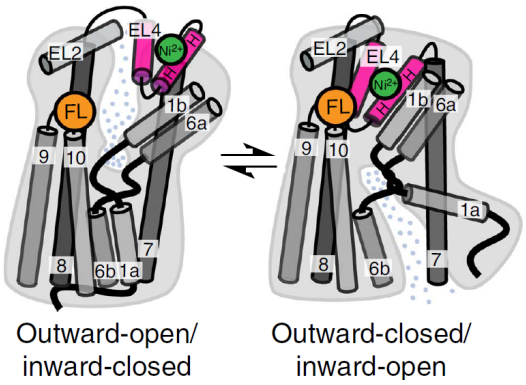

Fig. 1 Cartoon of LeuT with EL4:TM10 tmFRET pair shown in outward open and outward closed states depicting the principle behind changes in tmFRET as a result of conformational changes. The tmFRET pair reports distance-dependent quenching of fluorescence from fluorescien conjugated to an inserted cysteine at the top of TM10 (orange sphere, K398C) by Ni^{2+} coordinated by a His-X3-His motif in EL4 (green sphere, A313H-A317H). Figure adapted from Billesbolle et al [2016][2]

R_0. This is primarily due to the high R_0 values of typical FRET pairs (30-60 Å), as well as the large size of most fluorescent dyes and the dependence upon the orientation of the fluorophores, which all can influence the FRET efficiency.[11]

Transition metal ion FRET (tmFRET), however, has proven to be very useful for investigating intramolecular conformational movements of proteins[12] (Supporting information S1. Theory). Using tmFRET, R_0 values are reduced to about 10 Å.[13] Using tmFRET it is possible to measure the FRET between fluorescien, bound to an inserted cysteine, and a Ni^{2+} ion, which have a R_0 of about 12 Å.[13] The Ni^{2+} ion is bound by a di-histidine motif, which has been introduced into the protein by adding two histidines, spaced one turn apart in an alpha helix[14]. The fluorescien binds to the the cystein by its malamide group, which reacts with the cystein's thiol group. The ability to bind fluorophores to inserted cysteins, is another reason to use LeuT for investigating NSSs. LeuT doesn't naturally have any cysteins, in contrast to many mammalian NSSs, which allows us to insert a cystein strategically, enabling us to utilize it for tmFRET.

To investigate tmFRET in LeuT, we inserted a cystein in K398 at the top of TM10 and a di-histidine site in the helical part of EL4 (Figure 1). The construct K398C-A313H-A317H will from here on be named $LeuT^{tmFRET}$. In order to measure specific binding for FRET it is necessary to remove the signal from the unbound Ni^{2+} ions in the solution. This problem has previously been addressed by also conducting the same measurements on a protein without the di-histidine motif, LeuT mutant K398C ($LeuT^{K398C}$). Thus being able to remove the contribution from the unbound Ni^{2+} by subtracting the $LeuT^{K398C}$ signal from the $LeuT^{tmFRET}$ signal. One study showed that it is possible to entirely remove the effect of Ni^{2+} by adding Zn^{2+} to the solution.[2] As Zn^{2+} is colorless, it should not be able to absorb energy from the relaxation of fluorescien to its ground state. At high enough concentrations the Zn^{2+} ions will competitively inhibit the binding of Ni^{2+} at the di-histidine motif. This should make it possible to use the Zn^{2+} saturated $LeuT^{tmFRET}$ mutant to remove the signal from the unbound nickel, rather than using $LeuT^{K398C}$. In this way it would be possible to completely forgo the $LeuT^{K398C}$ mutant, thereby optimizing the process. The purpose of this paper is to investigate the effect of Zn^{2+} ions binding to the di-histidine motif, aiming to find an alternative to the $LeuT^{K398C}$ mutant for removal of the contribution from the unbound Ni^{2+}.

2 Results and Discussion

2.1 Purification of LeuT

The LeuT mutants were purified twice on two separate occasions. The protein concentration was first examined by absorption at 280 nm. Fractions of 1 mL from the protein elution were examined, and the fractions with the highest protein concentrations were then mixed and aliqouted. The total average protein concentrations for each purification are summarized in table 1. (Further information in Figures S4 and S5)

Table 1 Total protein concentrations from purifications

	1st purification	2nd purification
LeuT(K398C)	0,429 mg/L culture	0,577 mg/L culture
LeuT(tmFRET)	0,105 mg/L culture	0,0496 mg/L culture

The degree of labeling was calcuated to be 64.7 % for $LeuT^{K398C}$ and 74.19% for $LeuT^{tmFRET}$ (Experimental section 3.2) for the first purification.

Protein purity was determined using SDS PAGE (Figure 2). Fraction 1 shows the wash after LeuT was bound the Ni^{2+} resin, where other membrane proteins not bound to the resin can be observed. Fractions A-H show protein elution. Here, the gel shows a clear band at 37 kD, however, we know that LeuT has a molecular weight of about 58 kD[15]. This difference could be due to the common observation of "gel-shifting", when working with membrane proteins. Gel-shifting is a result of the larger amount of hydrophobic domains binding more SDS, therefore making the protein run faster on the gel.[16] A small band at 75 kD can also be observed for $LeuT^{K398C}$. This could perhaps indicate the presence of a LeuT dimer.

Scintillation proximity assay (SPA) was performed in order to investigate amino acid binding of the LeuT mu-

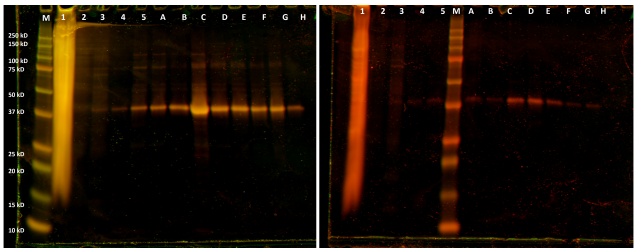

Fig. 2 Determination of LeuT molecular weight using SDS-PAGE from second LeuT purification. Fraction 1 shows the wash after LeuT was bound to the Ni^{2+} resin, fractions 2-5 are from the wash with increasing amounts of imidazole diluted in NSWB (0, 60, 90, 100 mM, respectively), fractions A-H show protein elution with 300 mM imidazole. M indicates the kaleidoscope marker Left) $LeuT^{K398C}$ right) $LeuT^{tmFRET}$

tants compared to wild type LeuT $LeuT^{WT}$ (Supporting information S2. Methods). The histidine tail binds to the YSi-Cu^{2+} HisTag beads. The scintillation liquid in the YSi-Cu^{2+} HisTag beads will then emit photons, when exposed to β-radiation. Radiotracer ^{3}H-leucine was used. The competitive binding between ^{3}H-leucine and amino acids, leucine and alanine, was investigated (Figure 3a and 3b). It was observed that both $LeuT^{K398C}$ and $LeuT^{tmFRET}$ had leucine and alanine binding affinity comparable to $LeuT^{WT}$. Comparing the two, it appears that the binding affinity for leucine is better than for alanine, despite the fact that some studies show that alanine is actually transported more easily by LeuT. This could be due to leucine's binding affinity, being so high that it actually could slow transport [15].

From the SPA data it was possible to determine Half maximal effective concentration EC50 (Table 2). The EC50 values for the LeuT mutants correlate well with $LeuT^{WT}$.

Table 2 EC50 values for LeuT mutants

EC50	$LeuT^{WT}$	$LeuT^{K398C}$	$LeuT^{tmFRET}$
Ala	8.5 μM	15 μM	14 μM
Leu	28 nM	0.1 nM	33 nM

The leucine saturation of the mutants does not diverge much from $LeuT^{WT}$ either (Figure 3c). K_d was determined from the saturation of leucine to be 13 +/- 3 for $LeuT^{WT}$, 7.6 +/- 1.7 for $LeuT^{K398C}$ and for $LeuT^{tmFRET}$ it was determined to 10 +/- 2. Thus, confirming that the mutation of the protein does not appear to have an influence on its affinity for leucine. The sodium dependency on leucine binding was also investigated (Figure 3d). It can be observed that this dependency has been retained in the $LeuT^{K398C}$ and $LeuT^{tmFRET}$ mutants, compared to $LeuT^{WT}$.

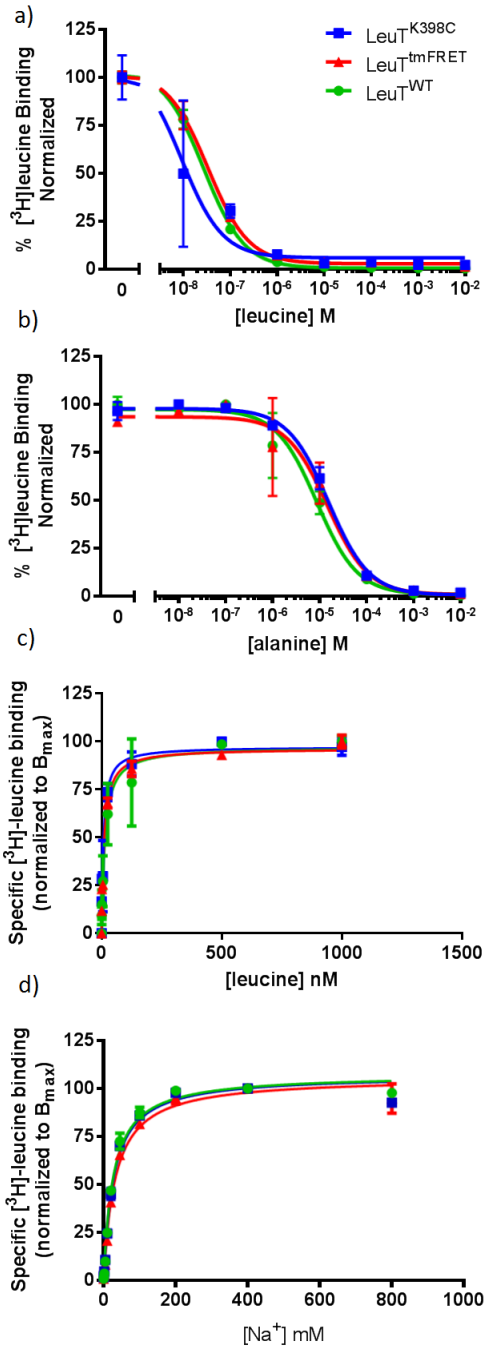

Fig. 3 SPA data shows, LeuT mutants show same saturation and affinity for leucine as wild type LeuT a) $LeuT^{K398C}$ and $LeuT^{tmFRET}$ affinity for leucine correlates with $LeuT^{WT}$ b) $LeuT^{K398C}$ and $LeuT^{tmFRET}$ affinity for alanine correlates with $LeuT^{WT}$ c) Leucine saturation d) Leucine sodium dependency. n=1, performed in duplicates

2.2 tmFRET investigation of LeuT

tmFRET was conducted on $LeuT^{K398C}$ and $LeuT^{tmFRET}$ in 20 mM Tris-HCl pH 8.0, 200 mM ChCl, 100 uM TCEP

and 0.05 % DDM buffer. At increasing concentrations of Ni^{2+}, a saturation of tmFRET signal can be observed (Figure 4). At 10 mM Ni^{2+} there will almost constantly be a Ni^{2+} ion coordinated to the di-histidine site, which will give off the maximum possible tmFRET signal for the protein.

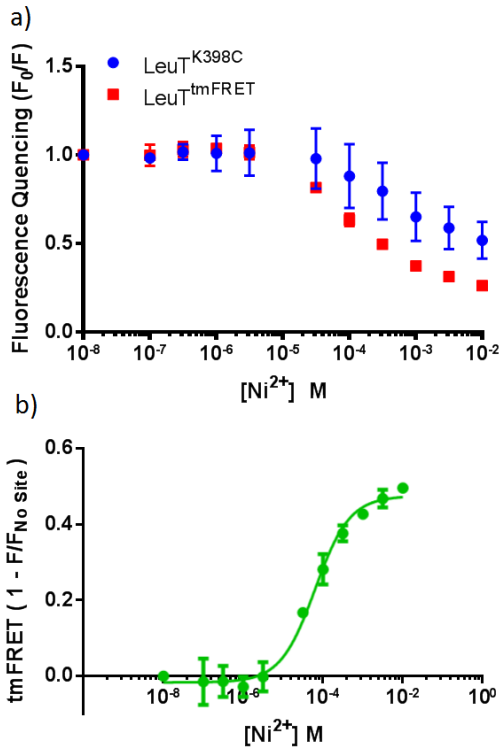

Fig. 4 tmFRET measurements of LeuT a) Fluorescent quenching of $LeuT^{K398C}$ and $LeuT^{tmFRET}$ b) tmFRET of LeuT, where signal from unspecific Ni^{2+} has been removed by subtraction of $LeuT^{K398C}$ signal. n=1, performed in triplicates

2.3 Screening for optimal Zn^{2+} conditions

The buffer used previously for tmFRET on LeuT was a 20 mM Tris-HCl pH 8.0, 200 mM ChCl, 100 uM TCEP and 0.05 % DDM buffer.[2] However, this buffer quickly proved to be unsuitable for solubilizing Zn^{2+} as it precipitated (Figure 5). It was therefor necessary to find a different buffer both suitable for the protein and for solubilizing the Zn^{2+}. As the histidine side chain of LeuT has a pKa of 6.04, the buffer was constricted to pH above about 6.5 in order to keep the histidines from protonating.

In order to determine which component of the buffer was causing the precipitate, 10 mM $ZnCl_2$ was added to four solutions, each missing one component of the original buffer. Each solution was incubated at room temperature for 10 minutes and precipitate investigated. It was found

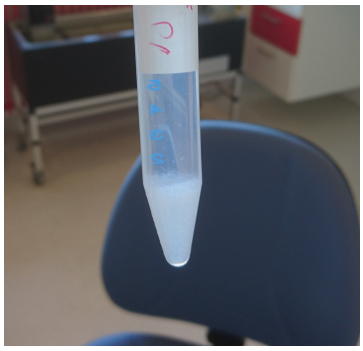

Fig. 5 Zn^{2+} precipitate, 10 mM $ZnCl_2$ in Tris-based fluorescence buffer at pH 8.0

that only the solution without Tris-HCl did not form precipitate. Indeed, it has previously been shown that Zn^{2+} forms complexes with Tris[17]. Other buffer components were investigated to replace Tris. However, the solubility of Zn^{2+} is also highly dependent on pH, therefore the Tris based buffer was also tested at pH 7.5. For all buffers tested, $ZnCl_2$ was added and centrifuged. Surprisingly, the Tris buffer showed no pellets at 10 mM $ZnCl_2$. However, when this buffer was used for tmFRET on the protein with Zn^{2+}, it showed higher FRET signal than other buffers tested (Figure 6c compared to 6a). This indicates that Tris may still be forming invisible complexes with the Zn^{2+} ions, which might prevent Zn^{2+} from binding to the di-histidine motif.

Several other buffers were tested. All buffers were centrifuged with varying concentrations of $ZnCl_2$ for 5 min at 1000 g in order to view pellets from Zn^{2+}. Previous studies suggested buffers from the morpholinic or piperazinic families for the best suitability with Zn^{2+} ions.[18] The results of buffer tests executed are summarized in Table 3. Coincidentally, some of these buffers had buffer ranges at slightly lower pH than the Tris family. It was found that pH was a determining factor in preventing Zn^{2+} precipitation. Additionally, it was found that Tris is an unsuitable buffer component when using Zn^{2+}, as it appears that Zn^{2+} isn't capable of competitively inhibiting Ni^{2+} in the Tris buffer as well as in other buffers, such as MOPS (Figure 6). This is most likely due to complexes formed between Zn^{2+} and Tris. Comparing experiments conducted in the MOPS pH 7.0 and MOPS pH 7.5 buffer, the MOPS pH 7.0 buffer showed slightly lower FRET signals in the presence of Zn^{2+} (Figure 6). This indicates that the MOPS 7.5 buffer could have been continuing to interact with the Zn^{2+} ions, in a manner which disturbed the FRET signal. Therefore, all further experiments were conducted with MOPS pH 7.0 buffer.

Additionally, it was attempted to stabilize Zn^{2+} through the addition of other substrates. Citric acid and ammonium

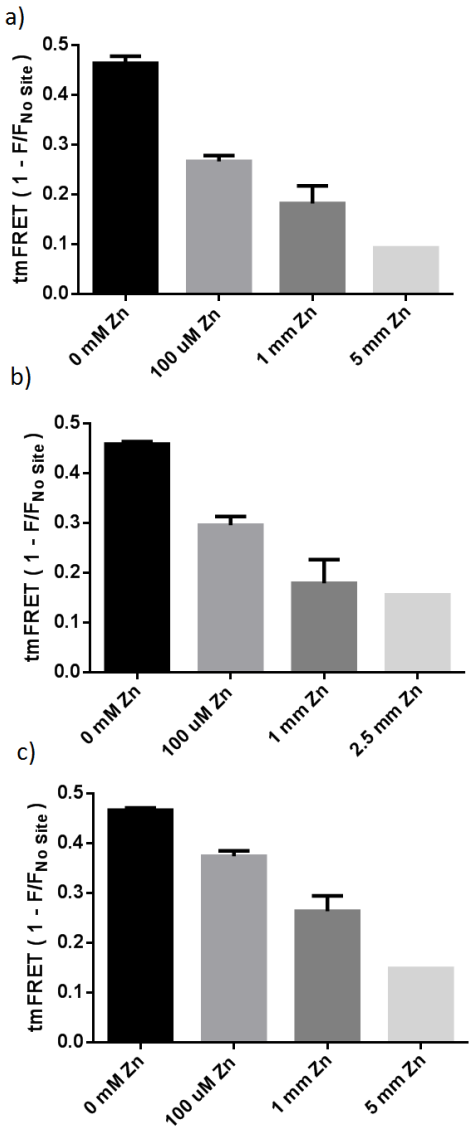

Fig. 6 tmFRET results from LeuT in different buffers at varying Zn^{2+} concentrations with 10 mM Ni^{2+} a) MOPS buffer pH 7.0 b) MOPS buffer pH 7.5 c) Tris buffer pH 7.5, show higher signals in Tris buffer and MOPS pH 7.5 buffer compared to MOPS pH 7.0 buffer. n=1, performed in triplicates

chloride were tested, as these have been found to form complexes with Zn^{2+} [19], which might stabilize the Zn^{2+}, but still allow it to bind the the di-histidine motif. 10 mM of the substrates were added to the chosen buffer and centrifuged with 10 mM Zn^{2+}, in order to view Zn^{2+} pellets. When citric acid was added and the pH was adjusted to 8.0 using KOH, there was no significant difference in pellet size. There was no difference in pellet size observed at the addition of ammonium chloride either, indicating that neither citric acid or ammonium chloride was capable of keeping Zn^{2+} from precipitating.

Table 3 Summary of Zn^{2+} precipitation in different buffers at varying pH

	10 mM Zn^{2+}	2.5 mM Zn^{2+}
Hepes pH 8.0	Pellet	
EPPS pH 8.0	Pellet	
MOPSO pH 7.5	Small pellet	No pellet
MOPS pH 7.5	Small pellet	No pellet
MOPS pH 7.0	Small pellet	No pellet
MOBS pH 8.0	Pellet	Pellet
Tris pH 8.0	Pellet	Pellet
Tris pH 7.5	No pellet	No pellet

2.4 The impact of Zn^{2+} on FRET signal

In order to confirm that the protein still behaved as previously in the MOPS buffer, FRET values for the protein were measured in buffers with different salts; ChCl, NaCl and KCl (Figure 7). In general, the tmFRET values were consistent with values observed in the lab on previous occasions (unpublished).

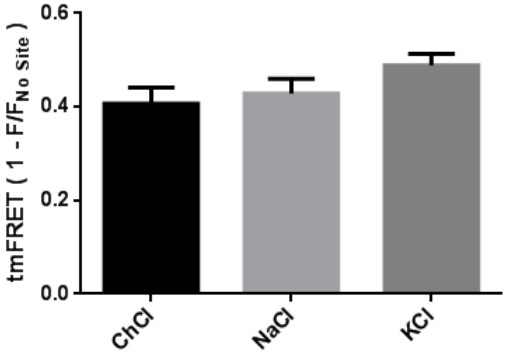

Fig. 7 Effect of different salts on tmFRET signal at 10 mM Ni^{2+}. From the left: ChCl, NaCl and KCl. Slightly heightened tmFRET signal at KCl indicate effect of K^+ on protein conformation. n=1, performed in triplicates

In the KCl buffer we observe a slightly higher FRET value than for the ChCl and NaCl (Figure 7). This could indicate the K^+-effect of conformational change from outward open to inward open conformation, as described in previous studies. [2]

The effect of addition of Zn^{2+} was investigated (Figure 8a). Here it is shown that Zn^{2+} inhibition of Ni^{2+} binding is concentration dependent. At increasing concentrations of Zn^{2+} the saturation point is likewise pushed towards the right, as the Ni^{2+} and Zn^{2+} compete for the di-histidine binding site, also indicating the competitive binding. At 5 mM Zn^{2+} an almost complete inhibition of Ni^{2+} binding was observed. Observing this, it can be deduced that it is possible to use the signal from $LeuT^{tmFRET}$ with 5 mM

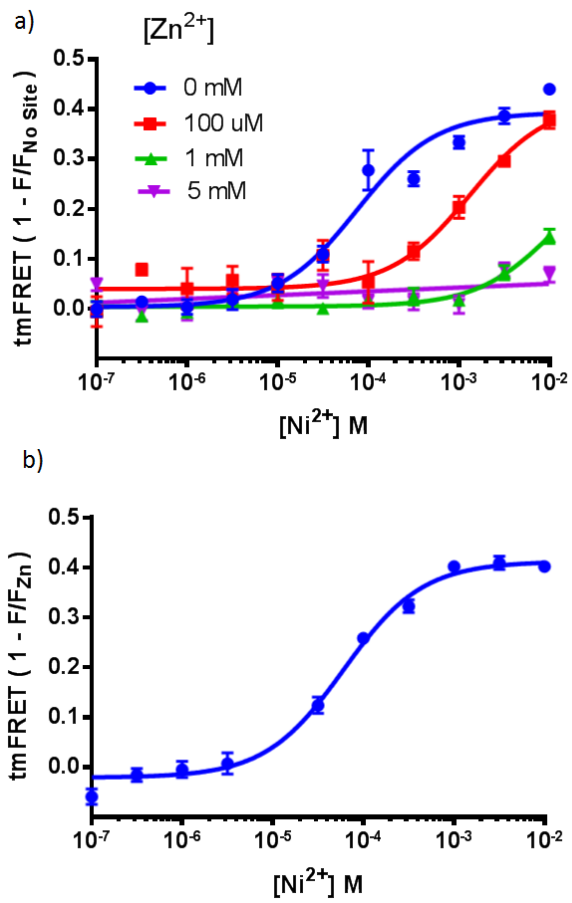

Fig. 8 tmFRET saturation curves at different Zn^{2+} concentrations a) using $LeuT^{K398C}$ to remove contribution from the unbound Ni^{2+} b) using $LeuT^{tmFRET}$ with 5 mM Zn^{2+} to remove contribution from the unbound Ni^{2+}. Data indicates 5 mM of Zn^{2+} can almost completely out-compete Ni^{2+} at the di-histidine motif. n=2, in triplicates

$ZnCl_2$ to remove the contribution from the unbound Ni^{2+} (Figure 8b). This finding should make subtraction of the contribution from $LeuT^{K398C}$ mutant unnecessary, hereby making purification faster and easier, as well as possibly making measurements more consistent as they would be made on the same LeuT mutant.

The concentration dependent inhibition of Ni^{2+} binding to the di-histidine motif can be illustrated as on Figure 9. Here it can be observed how the Zn^{2+} ions increase the fluorescent quenching, by competitively inhibiting Ni^{2+} binding at the di-histidine motif. At 5 mM an almost complete blocking of the signal from the Ni^{2+} bound to the di-histidine motif is observed, hereby rendering the $LeuT^{K398C}$ and $LeuT^{tmFRET}$ essentially identical (Figure 9d).

The effect of Zn^{2+} ions on the intensity was investigted. Despite the fluorescence quenching signals of $LeuT^{K398C}$

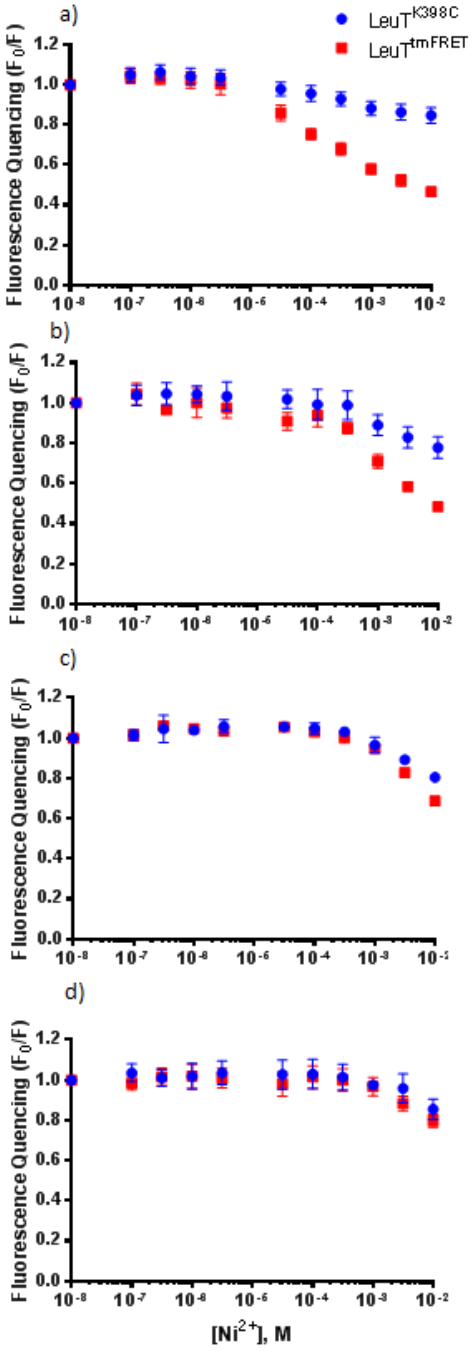

Fig. 9 Fluorescent quenching at increasing concentrations of Zn^{2+} a) 0 mM Zn^{2+} b) 100 uM Zn^{2+} c) 1 mM Zn^{2+} d) 5 mM Zn^{2+} shows increasing quenching of the $LeuT^{tmFRET}$ mutant. n=2, in triplicates

and $LeuT^{tmFRET}$ appearing identical (Figure 9), an effect of Zn^{2+} on the protein was observed (Figure 10). The intensity was measured on the $LeuT^{K398C}$ mutant with increasing concentrations of Zn^{2+} (Figure 10a). Here, the presence of Zn^{2+} surprisingly increases the intensity. This

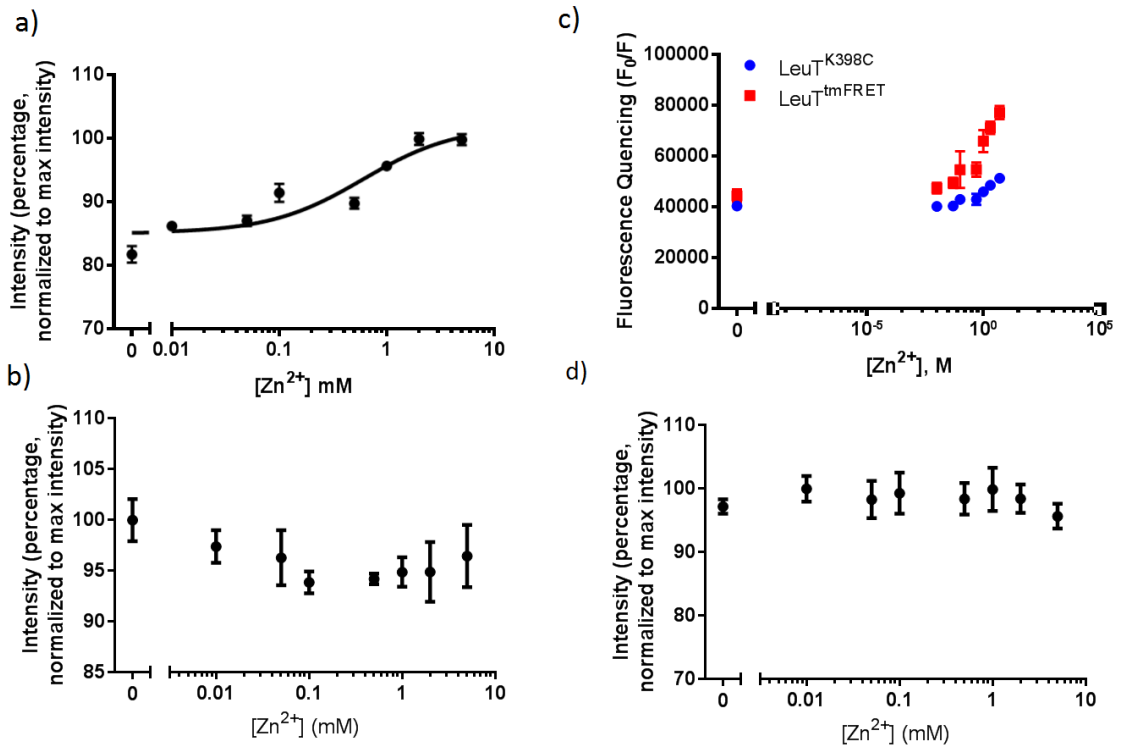

Fig. 10 Zn^{2+} titration curves a) $LeuT^{K398C}$ shows increasing intensity at increasing concentrations of Zn^{2+}, when incubated for one hour before measurements b) $LeuT^{K398C}$ shows no difference in intensity at increasing concentrations of Zn^{2+}, when measured immediately after addition of Zn^{2+} c) Both $LeuT^{K398C}$ and $LeuT^{tmFRET}$ with 10 mM Ni^{2+} show increasing intensity at increasing concentrations of Zn^{2+} d) Zn^{2+} titration curve with fluorescien, but without protein shows no significant difference at increasing concentrations of Zn^{2+}. a and c n=2, in triplicates. b and d n=1, in triplicates

increase in intensity is not observed if measured immediately after addition of Zn^{2+} (Figure 10b), indicating that the sample may need time to potentially form complexes or react with LeuT.

The titration of Zn^{2+} in both the $LeuT^{K398C}$ and $LeuT^{tmFRET}$ mutant in the presence of 10 mM Ni^{2+} was investigated (Figure 10c). Here we also see an increase of intensity in both the $LeuT^{K398C}$ and $LeuT^{tmFRET}$ mutant in the presence of Zn^{2+}. In order to investigate if this property was a function of Zn^{2+} and the protein itself or of Zn^{2+} and the fluorescien directly, Zn^{2+} was titrated into buffer containing free fluorescien, not coupled to LeuT (Figure 10d). This indicates that the Zn^{2+} concentration does not have an influence on the signal, when the protein is not present. This indicates that the increased intensity must be due to an effect Zn^{2+} has on LeuT, which in turn, influences the fluorescien intensity.

If this increase in intensity from Zn^{2+} comes from complexes or an effect on the protein, it poses a problem in using a Zn^{2+} inhibited $LeuT^{tmFRET}$ to subtract the signal from the unbound Ni^{2+}, as it won't be completely accurate at high concentrations. No great difference in intensity as a function of Zn^{2+} concentration is observed on the $LeuT^{K398C}$ signal till about 2 mM (Figure 10c). This could allow the usage of Zn^{2+} inhibited $LeuT^{tmFRET}$ to subtract the signal from the unbound Ni^{2+}, only using a lower concentration of Zn^{2+}. It appears that a concentration of 1 mM Zn^{2+}, does not change the intensity and thus could be used (Figure 10c). This would not allow as high a concentration of Ni^{2+}, as the lower Zn^{2+} concentration would not be able to competitively inhibit it, thus removing the signal. It can be deduced that a concentration of 1 mM Ni^{2+}, should be able to be competitively inhibited by 1 mM Zn^{2+} (Figure 8a). While not being able to do a full saturation curve with only 1 mM Ni^{2+}, it still allows for a relatively good indication of comparative FRET and conformation of the LeuT protein. Even with these limitations, this method has the advantage of being able to do measurements on the same protein.

This allows measurements to be more consistent, as they will no longer be a comparison between two different mutants of LeuT. This will make it possible to forgo the purification of $LeuT^{K398C}$, thereby optimizing the purification process. However, this increased intensity could also be due to the inner filter effect. The inner filter effect has previously been observed in the lab from Ni^{2+}. If this is

the case, using Zn^{2+} inhibited $LeuT^{tmFRET}$ may actually offer a better solution, as it would not only only allow us to conduct the measurements on the same protein, but it would also allow for the subtraction of the inner filter effect. To determine if these findings are significant, further experiments would have to be conducted and statistical tests would have to be done.

3 Experimental section

3.1 Purification of LeuT

Unless otherwise stated, all chemicals used were purchased from Sigma-Aldrich. Two mutants of LeuT were purified; A313H-A317H-K398C ($LeuT^{tmFRET}$) and K398C ($LeuT^{K398C}$) - one with and without the di-histidine motif.

For the purification the following buffers were used: Lysis buffer (LYB), Sucrose buffer (SUB), Solubilization buffer (SOB) and No Sodium Wash Buffer (NSWB).

Lysis buffer: 100 mM KCl, 50 mM Tris-Hcl (pH 8.0)

Sucrose buffer: 100 mM KCl, 50 mM Tris-HCl (pH 8.0), 1mM EDTA, 0.5 M sucrose

Solubilization buffer: 50 mM Tris-HCl (pH 8.0), 30 % glycerol, 300 mM KCl, 5 mM MgCl2, 1 mM TCEP

No Sodium Wash Buffer: 20 mM Tris-HCl (pH 7.5), 200 mM KCl, 100 uM TCEP, 20 % glycerol, 0.05 % n-dodecyl-β-D-maltosepyranoside (DDM) (Anatrace)

One aliquot freestock of the E. Coli Stock strain C41, transformed with the desired LeuT construct was added to Lysogeny Broth containing 75 ug/ml ampicilin and grown overnight at 37C with 180 rpm shaking.

50 ml inoculation culture was added to 1000 mL LB containing ug/ml ampicilin and grown for 2.5 hours at 37C. Protein expression was induced at OD600 0.5-0.6 by the addition of isopropyl β-D-1-thiogalactopyranoside (IPTG). The culture was then incubated at 20C with 180 rpm shaking overnight.

The cells were pelletzied for 10 min at 6000 rpm 4 C in Sorvall LYNX 6000 Superspeed centrifuge (Thermo Fisher Scientic Inc.). The pellets were then resuspended in lysis buffer and 10 ml sucrose buffer, 200 uL of 0.2 M phenylmethylsolfonyl fluoride (PMSF) , 200 uL protease inhibitor (PI) was added to each pellet. The cells were ruptured through double passage through high-pressure cell disrupter (Constant Systems Ltd) at 2.30 bar and flushed with supplemented solubilization buffer (SOB). The solution was centrifuged for 15 min at 1000 g at 4C in Sigma 6K15 centrifuge (SciQuip Ltd) and subsequently the supernatant was ultracentrifuged in OptimaTM L-80 XP Ultracentrifuge (Beckman Coulter, Fullerton) for 2 hours at 125171 g at 4C. Hereafter, the pellet was resuspended in supplemented Solubilization buffer. Membrane fractions were then stored at -80C.

n-dodecyl-β-D-maltosepyranoside (DDM) from Anatrace was then added to a final concentration of 1 percent in order to solubilize LeuT, and then incubated for 1 hour at 4C under slow rotation. LeuT was bound to ProBond Ni-IDA resin (Life Technologies), afterwards it was incubated in No Sodium Wash Buffer (NSWB). The membrane fraction was pelletized by centrifugation at 38.000g for 30 min at 4C by Sorvall LYNX 6000 Superspeed centrifuge (Thermo Fisher Scientic Inc.). Fluorescein-5-maleimide (FL) was added dropwise to a final concentration of 200 uM for fluorescent conjugation.The protein-bound resin was then incubated for 16 hours under slow rotation at 4C, away from light.

Protein bound resin was centrifuged by Sorvall LYNX 6000 Superspeed centrifuge (Thermo Fisher Scientic Inc.) at 1.000 rpm for 3 min at 4C with NSWB and the pellets were then washed with NSWB containing imidazole in order to remove unconjugated fluorescien. Protein elution was done with 300 mM imidazole. SDS PAGE analysis was run in order to quantify protein amount in obtained fractions. Furthermore, protein content was determined at absorbance at 280 nm with NanoDrop 2000 UV-Vis Spectrophotometer (Thermo Fisher Scientic Inc.), correcting for the protein being fluorescently labeled. Aliquotes of 100 uL were then made and stored at -80C.

3.2 Calculation of protein concentration and degree of labeling

The total protein concentration of the collected fractions was determined using Lambert-Beers law: $C = \frac{A}{\varepsilon * l}$, where A is the absorbance, ε is the molar absorptions coefficient and l is the length of the light path. Using ε for LeuT 113300 $\frac{L}{mol*cm}$ and ε for fluorescien 80000 $\frac{L}{mol*cm}$. Protein concentration for $LeuT^{K398C}$ was determined to 6.8 uM (1st purification) and 9.9 uM (2nd purification). For $LeuT^{tmFRET}$ the protein concentration was determined to 3.1 uM (1st purification) and 1.5 uM (2nd purification). For fluorescein the concentration was determined to 4.4 uM (1st) and 5.3 uM (2nd) for the $LeuT^{K398C}$ mutant. For $LeuT^{tmFRET}$ the concentration was determined to 2.3 uM (1st) and 1.6 uM (2nd), for fluorescien. The absorbance was determined by absorption at 480 nm for fluorescien. From these protein concentrations the degree of labeling was calculated as $[LeuT^{K398C}{}_{FL}]/[LeuT^{K398C}]$ and $[LeuT^{tmFRET}{}_{FL}]/[LeuT^{tmFRET}]$

3.3 tmFRET

Samples were prepared for tmFRET by the addition of 0.0005 mg/mL protein to the fluorescence buffer (20 mM MOPS-KOH buffer pH 7.0 , 200 mM ChCl, 100 uM TCEP and 0.05 % DDM).

For the saturation curves, $ZnCl_2$ was added to each sample at 100uM, 1 mM and 5 mM, respectively. The sample was mixed well and 330 uL was transferred to each eppendorf tube. Samples were then incubated for one hour at room temperature, shielded from light. After incubation, 3.3 uL from the following dilution series was was added to each tube: $1*10^{-5}$, $3.16*10^{-5}$, $1*10^{-4}$ M, $3.16*10^{-4}$ M, $1*10^{-3}$ M, $3.16*10^{-3}$ M, $1*10^{-2}$ M, $3.16*10^{-2}$ M, $1*10^{-1}$ M, $3.16*10^{-1}$ M, 1 M. The samples were immediately measured on the FluoroMax 4 spectrofluorometer (Horiba Scientic Ltd.).

For the Zn^{2+} titration curves a similar approach was used. Zn^{2+} was added to the sample in increasing concentrations, 0 M, 0.01 mM, 0.05 mM, 0.1 mM, 0.5 mM, 1 mM, 2 mM and 5 mM, respectively. The sample was mixed well and 330 uL of the mixture was transfered to each eppendorf tube. The samples were then incubated at room temperature, shielded from light for one hour. For the experiment shown on Figure 10c, 10 mM Ni^{2+} was then added to each sample. All samples were then immediately measured on the FluoroMax 4 spectrofluorometer (Horiba Scientic Ltd.).

Settings for the FluoroMax 4 spectoflurometer: Excitation slit width: 3.5, emission slit width: 3.5, wavelength excitation: 496 nm, wavelength emission 519 nm. All measurements were conducted in triplicates.

4 Conclusions

In this study, tmFRET was used for investigating the competitive binding of Zn^{2+} and Ni^{2+} at the di-histidine site of LeuT mutant A313H-A317H-K398C ($LeuT^{tmFRET}$). Suitable buffers were investigated, and it was found that Tris based buffers were unsuitable, while MOPS based buffers showed great promise. It was furthermore found that the pH of the buffer needed to be below 7.5 in order for the setup to function. It was found that Zn^{2+} was capable of inhibiting Ni^{2+} binding, indicating that a Zn^{2+} saturated $LeuT^{tmFRET}$ could be used to remove the signal from unbound Ni^{2+}. However, indications that Zn^{2+} in concentrations above 1 mM increased the fluorescence intensity was also found. The described technique, however, can still be utilized at Zn^{2+} concentrations below 1 mM. Doing so limits the concentration of Ni^{2+} as well, but it does allow for investigation of the conformational changes of the protein. The increase in fluorescence intensity could, however, also be due to inner filter effect. This finding will allow tmFRET measurements to be more consistent as they can be performed on the same LeuT mutant $LeuT^{tmFRET}$, as well as optimize the purification process as the $LeuT^{K398C}$ mutant would be rendered obsolete.

5 Acknowledgements

I would like to express my gratitude towards my supervisor Claus Juul Løland, associate professor, Institute for Neuroscience and pharmacology at Copenhagen University for great guidance and constructive feedback throughout the last few months.

I would like to thank my internal supervisor Nikos Hatzakis, associate professor, Department of Chemisty at Copenhagen University for making it possible for me to write my thesis at Center for Neuroscience.

I would like to thank Jonas S. Mortensen, PhD at Center for Neuroscience at Copenhagen University, for the great help he has provided, introducing me to the lab and guiding me throughout the entire project.

I would also like to thank Solveig G. Schmidt for always being helpful and available for both discussions and help in the laboratory.

I would also like to thank lab technician Lone Rosenquist, as well as the entire Neuropharm and Genetics Lab for help during the day to day lab experiments.

References

1 C. J. Loland, *Biochimica et Biophysica Acta*, 2014, 500–510.
2 C. B. Billesbolle, J. S. Mortensen, A. Sohail, S. G. Schmidt, L. Shi, H. H. Sitte, U. Gether and C. J. Loland, *Nature Communications*, 2016.
3 A. Kristensen, J. Andersen, T. Jorgensen, L. Sorensen, J. Eriksen, C. Loland, K. Stromgaard and U. Gether, *Pharmacol. Rev.*, 2011, **63**, 585–640.
4 Z. Lin, J. J. Canales, T. Bjrgvinsson, M. Thomsen, H. Qu, Q. R. Liu, G. E. Torres and S. B. Caine, *Prog Mol Biol Transl Sci.*, 2011, **98**, 1–46.
5 A. Yamashita, S. K. Singh, T. Kawate, Y. Jin and E. Gouaux, *Nature*, 2005, **437**, 215–223.
6 J. A. Coleman, E. M. Green and E. Gouaux, *Nature*, 2016, **532**, 334–339.
7 K. H. Wang, A. Penmatsa and E. Gouaux, *Nature*, 2015, **521**, 322–327.
8 A. Penmatsa and E. Gouaux, *J Physiol.*, 2013, **592**, 863–869.
9 H. Krishnamurthy and E. Gouaux, *Nature*, 2012, **481**, 469–474.
10 *Principles and Applications of Photochemistry*, ed. B. Wardle, Wiley, 1st edn, 2009.
11 R. B. Best, K. A. Merchant, I. V. Gopich, B. Schuler, A. Bax and W. A. Eaton, *Proc Natl Acad Sci U S A.*, 2007, **104**, 18964–18969.
12 J. W. Taraska, M. C. Puljung and W. N. Zagotta, *PNAS*, 2009, **106**, 16227–16232.
13 J. W. Taraska, M. C. Puljung, N. B. Olivier, G. E. Flynn and W. N. Zagotta, *Nature Methods*, 2009, **6**, 532–537.
14 S. S. Suh, B. L. Haymore and F. H. Arnold, *Protein Eng.*, 1991, **4**, 301–305.
15 S. Singh, C. Piscitelli, A. Yamashita and E. Gouaux, *Science*, 2008, **322**, 1655–1661.
16 A. Rath, M. Glibowicka, V. G. Nadeau, G. Chen and C. M. Deber, *PNAS*, 2009, **106**, 1760–1765.
17 L. Cheng, Y.-Y. Sun, Y.-W. Zhang, and G. Xub, *X*, 2008, **114**, 30989–31003.
18 C. M. H. Ferreira, I. S. S. Pinto, E. V. Soares and H. M. V. M. Soares, *Royal Society of Chemistry*, 2015, **114**, 30989–31003.

19 *Chemistry Principles and Reactions*, ed. L. Lockwood, Brooks/Cole, 20 Davis Drive, Belmont, CA, USA, 7th edn, 2012.

UCPH NanoScience
NanoVidenskab KU

tidsskrift.dk/index.php/NanoVidenskabKU

Thesis Paper

Weyl semimetals in models for ultracold atoms

Andreas Hansen

Received June 2017, Accepted April 2018

I study the effect of a non-Abelian gauge potential on a Weyl semimetal phase appearing in a particular 3D tight-binding model of fermions. The lattice I consider is characterized by a C_3 rotational symmetry and by staggered $\pi/2$ magnetic fluxes on the triangular plaquettes in its horizontal planes. The energy spectrum is characterized by both single Weyl points with linear energy dispersions in all three momenta directions, and double Weyl points with quadratic energy dispersions in two directions and linear dispersion along the axis of the rotational symmetry.

1 Introduction

The study of topological phases of matter are at the focus of both theoretical and experimental studies. Most of the efforts have been devoted to the study of topological insulators and superconductors, which are gapped energy systems that can display non-local, topological features, which are robust against local noise and perturbations. The main robust features are usually related to the existence of gapless boundary states protected by the symmetries of the system [1]. These protections were believed to be based on the presence of an energy gap in the band structure but in the most recent years, it was proven that also gapless systems can display similar features. The simplest and first examples were Weyl semimetals [2], which are based on the massless fermions called Weyl fermions, that Hermann Weyl derived from the Dirac equation in 1929 [3].
The 3D Weyl semimetal contains zero-energy bulk modes with linear dispersion in all three momenta directions, called Weyl nodes, and their stability against perturbations gives rise to protected gapless surface modes called Fermi arcs [4]. The Weyl nodes also carry topological features corresponding to monopoles of the Berry flux.
Weyl semimetals are not the only possible semimetallic phase of matter with topological features as there are several proposals to create more exotic topological materials. Some of the proposals suggests topological materials characterized by multiple Weyl points, which have quadratic or even higher dispersion relations with multiple monopoles of the Berry flux [5].
The Weyl nodes were obtained in solid states systems by breaking the spatial inversion symmetry in several compounds such as tantalum arsenide [6–8] and niobium arsenide [9]. The appearance of gapless Fermi arcs have also been observed in tantalum arsenide through photoemission measurements [8]. Experimental realizations of Weyl nodes have also been found in photonic crystals with gyriod geomtry, where the inversion symmetry was broken by drilling holes with an additional element [10]. The breaking of time-reversal symmetry to obtain Weyl nodes has not been done experimentally but several proposals have been made [11,12].
The study of topological phases of matter is not only limited to solid state systems as the example of the photonic crystals showed. One of the other platforms to implement systems with topological features is with ultracold gases trapped in optical lattices and it gives an environment practically free from disorder, where the interactions among particles can be controlled with good accuracy. Recent experiments in the ultra cold atom platform demonstrated the possibility of engineering large magnetic fluxes, for example through laser-assisted tunneling [13,14] and spin-orbit couplings [15–17] .
In this paper I will make a proposal to obtain Weyl nodes with linear dispersions, called single Weyl points, and quadratic dispersions, called double Weyl points, in a 3D triangular lattice with $\pi/2$-flux and non-Abelian gauge potential. I will study a tight-binding model of two-component fermions with nearest-neighbor hoppings. In Section 2 I discuss the properties of a system with $\pi/2$-fluxes implemented by an Abelian gauge potential. In Section 3 I add a non-Abelian gauge potential, which resembles a spin-orbit coupling, to the system. In Section 4 I study and discuss the band structure and Weyl points (Section 4.1) and the symmetries of the system (Section 4.2). Finally, Section 5 is an overview of the possible future developments of the models, which include the analysis of its Fermi arcs and the experimental techniques to observe its band structures.

2 Triangular Lattice with staggered $\pi/2$-fluxes

Experiments have shown that it is possible to tune staggered magnetic fluxes in a triangular lattice with artificial gauge fields[18]. It is therefore reasonable to consider the theoretical analysis of a lattice model of fermions in a 3D stack of overlapping horizontal triangular lattices to get Weyl semimetals.
The x-y plane of the triangular lattice is shown in Figure 1. The lattice vectors $\vec{a}$ are given by:
$\vec{a}_1 = a\hat{x}$, $\vec{a}_2 = a\left(\frac{1}{2}\hat{x}+\frac{\sqrt{3}}{2}\hat{y}\right)$, $\vec{a}_3 = a\left(\frac{1}{2}\hat{x}-\frac{\sqrt{3}}{2}\hat{y}\right)$, $\vec{a}_4 = a\hat{z}$
where a is the lattice constant and $a = 1$ for simplicity.
The first Brillouin zone of the triangular lattice is defined by the reciprocal lattice vectors: $\vec{b}_1 = 2\pi\left(\hat{k}_x - \frac{1}{\sqrt{3}}\hat{k}_y\right)$, $\vec{b}_2 = \frac{4}{3}\sqrt{3}\,\hat{k}_y$, $\vec{b}_3 = 2\pi\left(\hat{k}_x + \frac{1}{\sqrt{3}}\hat{k}_y\right)$ and $\vec{b}_4 = 2\pi\hat{k}_z$.

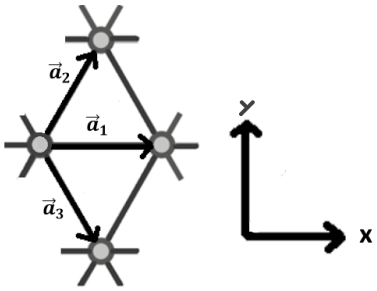

Fig. 1 The 2D x-y plane of the triangular lattice with hopping amplitudes t and lattice vectors a_1, a_2 and a_3 . The extension in the third direction, $\vec{a}_4$, is just an unitary vectors like $\vec{a}_1$.

I introduce an Abelian gauge potential $\vec{A}_{AB}$, which leads to induced fluxes with opposite sign for upwards and downwards pointing plaquettes in the triangular lattice[18] as shown in Figure 2. The flux in each plaquette is obtained through Stoke's theorem, which is the sum of the three hopping phases $\theta_j(\vec{r}) = \int_{\vec{r}}^{\vec{r}+\vec{a}_j} \vec{A}_{AB}(\vec{r}\,') \cdot d\vec{r}\,'$ equal to $\pm\pi/2$. The gauge choice does not have any physical consequences for the system, but the flux configuration shown in Figure 2 is gauge invariant property and defines the model.
The general tight-binding Hamiltonian for a system with phases is given as:

$$H = -t\sum_{\vec{r},\,j} e^{i\theta_j(\vec{r})}\, c^{\dagger}_{\vec{r}+\vec{a}_j} c_{\vec{r}} + h.c. \tag{2.1}$$

where $c^{\dagger}$ and c are creation and annihilation operators for fermions on the lattice, t is the hopping amplitude, $\theta_j(\vec{r})$ are the fluxes and $\vec{a}_j$ are the lattice vectors $\vec{a}_1$, $\vec{a}_2$, $\vec{a}_3$ and $\vec{a}_4$.

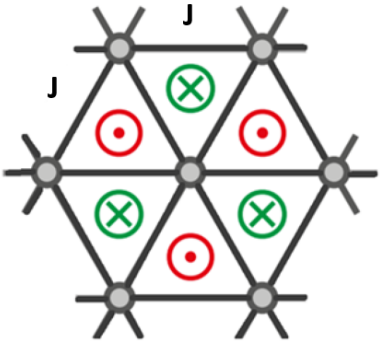

Fig. 2 Illustration inspired by J. Struck et al[18], which shows the gauge field applied to the triangular lattice system. The crosses correspond to inwards pointing gauge fluxes and dots correspond to outwards. The hopping amplitudes J are imaginary and the triangular lattice has the same lattice vectors $\vec{a}_j$ as in Figure 1.

I choose the specific configuration of $\pi/2$-fluxes for this model, so the triangular lattice gets imaginary hopping amplitude $J = i\,t$ and hopping vectors a_j as in Figure 1. The gauge choice gives the system $\pi/2$ phases in the x-y plane and z-direction and none of the vertical plaquettes have fluxes. The system has C_3 rotational symmetry around the z-axis, which will be discussed in Section 4.2.

3 Non-Abelian gauge potential as spin-orbit coupling

In the previous section I introduced staggered $\pi/2$ fluxes in the system, which only has a single band, and therefore not sufficient to give Weyl points. I expand the model with spin degree of freedom. In ultracold atom experiments the two spin species are usually given by hyperfine atomic species in current experiments[19,20]. Therefore to study the Weyl cones I introduce a spin 1/2 degree of freedom, whose dynamics is dictated by a non-Abelian gauge potential $\vec{A}_{NAB}$:

$$\vec{A}_{NAB} = q(\sigma_x, \sigma_y, \sigma_z) \tag{3.1}$$

where σ are Pauli matrices and the parameter q determines the intensity of the non-Abelian term $\vec{A}_{NAB}$[20]. The non-Abelian gauge potential couple, in general, the spin and the dynamics of the particles, like a spin-orbit coupling, which is different from the usual spin-orbit coupling like Rashba or Dresselhaus. The realization of this "3D Weyl spin-orbit coupling" has been proposed through suitable laser schemes in ultra-cold atoms[21,22] .
With the new gauge potential $\vec{A}$ consisting of $\vec{A}_{NAB}$ and $\vec{A}_{AB}$ the Hamiltonian can be written as:

$$H = -t\sum_{\vec{r},j,s,s'} U^{j}_{s,s'}\, c^{\dagger}_{\vec{r}+\vec{a}_j,s} c_{\vec{r},s'} + h.c. \tag{3.2}$$

where s and s' label the spin states. The unitary operators U are determined by the Abelian phases $e^{\,i\theta_j(\vec{r})}$, which match the ones in Section 2, and the non-Abelian component $\vec{A}_{NAB}$:

$$U^{\,j}_{s,\,s'} = e^{\,i\theta_j(\vec{r})} e^{i\int_{\vec{r}}^{\vec{r}+\vec{a}_j} \vec{A}_{NAB}(\vec{r}\,')\cdot d\vec{r}\,'} \tag{3.3}$$

I consider the unitary operators in Equation 3.3, which are the tunneling operators in the system, consisting of the staggered Abelian $\pi/2$ fluxes from Section 2 and the non-Abelian "Weyl" spin-orbit coupling given by Equation 3.1. The tunneling operators are:

$$\begin{aligned} U_1 = i\,e^{iq\sigma_x}\ ,\ U_2 = i\,e^{iq\left(\frac{1}{2}\sigma_x+\frac{\sqrt{3}}{2}\sigma_y\right)}\ , \\ U_3 = i\,e^{iq\left(\frac{1}{2}\sigma_x-\frac{\sqrt{3}}{2}\sigma_y\right)}\ ,\ U_4 = i\,e^{iq\sigma_z} \end{aligned} \tag{3.4}$$

With the tunneling operators in Equation 3.4 the Hamiltonian for the system in momentum space $H(\vec{k})$ is written in the Weyl Hamiltonian form:

$$H(\vec{k}) = \alpha_0(\vec{k})\sigma_0 + \alpha_x(\vec{k})\sigma_x + \alpha_y(\vec{k})\sigma_y + \alpha_z(\vec{k})\sigma_z \tag{3.5}$$

where σ_0 is the 2x2 identity matrix and the momentum coefficients are given as :

$$\alpha_0 = 2t\cos(q)\left(\sin(k_x) + 2\sin\left(\frac{k_x}{2}\right)\cos\left(\frac{\sqrt{3}k_y}{2}\right) + \sin(k_z)\right) \tag{3.6}$$

$$\alpha_x = 2t\sin(q)\left(\cos(k_x) + \cos\left(\frac{k_x}{2}\right)\cos\left(\frac{\sqrt{3}k_y}{2}\right)\right) \tag{3.7}$$

$$\alpha_y = -2\sqrt{3}\,t\ \sin(q)\left(\sin\left(\frac{k_x}{2}\right)\sin\left(\frac{\sqrt{3}k_y}{2}\right)\right) \tag{3.8}$$

$$\alpha_z = 2t\sin(q)\cos(k_z) \tag{3.9}$$

When the Hamiltonian in Equation 3.5 is diagonalized the energy is given by:

$$E(\vec{k}) = \alpha_0(\vec{k}) \pm \sqrt{\left(\alpha_x(\vec{k})\right)^2 + \left(\alpha_y(\vec{k})\right)^2 + \left(\alpha_z(\vec{k})\right)^2} \tag{3.10}$$

When the $q = 0$ the energy E in Equation 3.10 reduces to α_0 which is equivalent to Equation 3.6, and it matches the spectrum of the $\pi/2$-flux model from Section 2, and the Hamiltonian H in Equation 3.5 also reduces to this model. The parameter q is limited to $0 \leq q < \pi$ because of the relation $H(q) = -H(q+\pi)$.
The spectrum of the Hamiltonian in Equation 3.5 is characterized by both Weyl points and double Weyl points, and the the properties of the points and symmetries of the Hamiltonian will be discussed in Section 4 based on the works of Reference 5.

4 Weyl points of the system

4.1 Band structure and Weyl points

The single Weyl points have a linear energy dispersions along the three momenta directions and have a topological charge, which is associated with Berry flux of $2\pi\kappa$ where $\kappa = \pm 1$ is the chirality[23]. The double Weyl points are quadratic along two directions and linear in the third and carry a double monopole of the Berry flux, which is behaving topologically as two Weyl points with the same charge.
In order to identify and describe the Weyl points properly we first look at the band touching points of the first Brillouin zone. The energy spectrum of Equation 3.10 gives band touching points for any value of $q \neq 0$ at $\pi\left(0, \frac{2}{\sqrt{3}}, \pm\frac{1}{2}\right)$, $\pi\left(\pm\frac{2}{3}, 0, \pm\frac{1}{2}\right)$, $\pi\left(\pm\frac{2}{3}, \frac{4}{\sqrt{3}}, \pm\frac{1}{2}\right)$, $\pi\left(\pm\frac{4}{3}, \pm\frac{2}{\sqrt{3}}, \pm\frac{1}{2}\right)$, which corresponds to four inequivalent Weyl points and two double Weyl points in the first Brillouin zone. The band touching points can be studied if one consider the gap between the valence (lowest) and conduction (highest) band, given by $\Delta E = 2\sqrt{\alpha_x^2 + \alpha_y^2 + \alpha_z^2}$, in the first Brillioun zone for one of the momenta planes (k_x-$\tilde{k}_y$ plane). The shifted momentum $\tilde{k}_y$ is a gauge transformation, $\tilde{k}_y = k_y - \frac{2\pi}{\sqrt{3}}$, and the k_x-$\tilde{k}_y$ plane is shown in Figure 3.

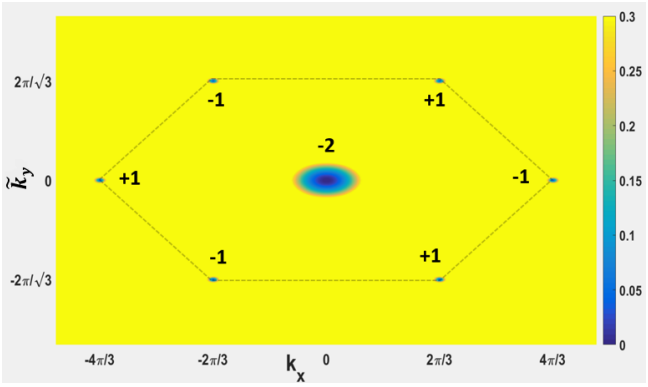

Fig. 3 Energy gap between the valence and conduction band in one of the k_x-$\tilde{k}_y$ planes ($k_z = +\pi/2$) where the band touching points are shown with their corresponding topological charge. The momenta direction k_y is shifted as $\tilde{k}_y = k_y - \frac{2\pi}{\sqrt{3}}$. There are two inequivalent Weyl points with ± 1 charge at the corners of the first Brillouin zone (shown as black dotted hexagon) and one double Weyl point with -2 charge at the middle of the 2D projection of the Brillouin zone.

The band touching points corresponds, as mentioned earlier, to two inequivalent Weyl points with topological charges ± 1 and one double Weyl point with topological charge $+2$ in the plane shown in Figure 3 and opposite topological charges for the k_x-$\tilde{k}_y$ plane with $k_z = -\pi/2$.

In this 2D Brillioun Zone all the single Weyl points are on the corners of the first Brillioun zone, and the double Weyl point is in the center. An important requirement to satisfy in regards to the topological charge is the Nielsen-Ninomiya theorem[24] which states that the sum of the topological charge for all the Weyl points (single and double) must be 0. This is also true for this system since all the Weyl points comes in pair in the first Brillouin zone.

The filling of the bands, and how the parameter q, in the spin-orbit term, changes the energy of the bands, will be discussed in the following. I will first consider $q = \pi/2$, resulting in $\alpha_0 = 0$, and then how the system evolves for q different from $q = \pi/2$.
I plot the energy in the k_x-$\tilde{k}_z$ plane ($k_y = 0$) with $q = \pi/2$, where the shifted momentum is $\tilde{k}_z = k_z - \frac{\pi}{2}$, in Figure 4, which shows three Weyl points. Two of the Weyl points are single Weyl points in which the energy dispersions are linear in all momenta directions, and for the double Weyl point the energy dispersion is quadratic in the k_x-k_y plane and linear in k_z.

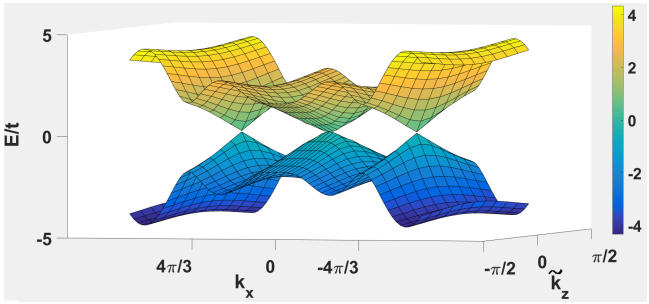

Fig. 4 The energy dispersion with $q = \frac{\pi}{2}$ for the k_x-$\tilde{k}_z$ plane is shown for $k_y = 0$. The momentum is shifted as $\tilde{k}_z = k_z - \frac{\pi}{2}$. Two inequivalent Weyl points with different charges ± 1 with linear dispersions in the k_x-$\tilde{k}_z$ plane are shown. The double Weyl point has quadratic dispersion in k_x-direction and in k_z-direction it has linear dispersion.

The Weyl points all have zero energy at $q = \pi/2$, which means the Fermi surface at half filling includes only discrete points, and therefore both the bands are partially filled.
In the case of $q \neq \pi/2$ the bands start to overlap in energy as shown in Figure 5, where $q = 2\pi/5$. In the Brillouin zone two single Weyl points with different charges have the highest energy and two Weyl points with opposite charges at the lowest energy.
The energy value of the double Weyl points is still 0 as in the case for $q = \pi/2$ thus it does not depend on the parameter q and the filling of the double Weyl with fermions can be expressed as $N_E = L^3$, where L is length of one of the dimensions of the system.

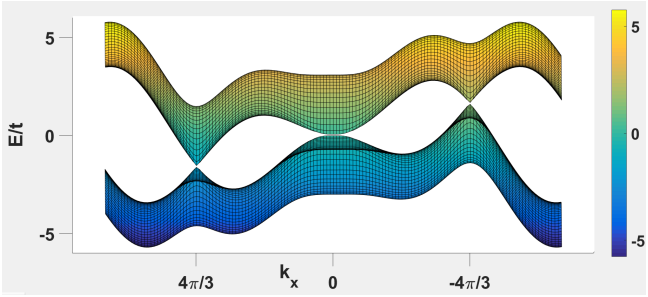

Fig. 5 An example of one the k_x-$\tilde{k}_z$ planes ($k_y = 0$). The energy dispersion with $q = \frac{2\pi}{5}$ for the k_x-$\tilde{k}_z$ plane is shown for $k_y = 0$. Only the k_x direction is shown in this Figure for better clarity of the energy values. In this plane the single Weyl point with negative topological charge has negative energy and positive charge has positive energy.

4.2 Symmetries of the system

The single Weyl points are protected by their topological charge and they can only be destroyed by coupling a pair of Weyl points with opposite charges. This means that, if they lie in different positions in momentum space, it is not possible to open a gap with weak perturbations, unless these perturbations break translational invariance. The single Weyl points are protected by translational invariance and local and uniform perturbations can not destroy the single Weyl points.
I will consider the effect of local and uniform perturbations on the double Weyl points and consider what symmetries are protecting them. A double Weyl points can be split in general into two equal Weyl points by local perturbations. I consider the generic effect of a local, translational invariant perturbation P on the Hamiltonian:

$$H = H_0 + P \tag{4.1}$$

where H_0 is the non-perturbed Hamiltonian. The perturbation P is a local and position independent operator and I will only consider the perturbations which do not break the single Weyl points, since that double Weyl points are more fragile than the single Weyl points. The perturbation consists of Zeeman terms $(\sigma_x, \sigma_y, \sigma_z)$, where σ_z does not break the rotational symmetry of the system, since it is along the z-axis, and will shift the double Weyl points along the z-axis. The other Zeeman terms, σ_x and σ_y, do break the rotational symmetry and destroy the double Weyl points, which is consistent with the results of Reference 5. A study has shown C_6-symmetry can protect the double Weyl point[5] and another study shows C_3 with time-reversal symmetry also protects the double Weyl[25].
The system described by Section 4 has C_3-symmetry (shown in Appendix D) and particle-hole symmetry (shown in Appendix E), which is reminiscent of the C_3 with time-reversal symmetry.

To analyze the band touching points in this model, I expand the Hamiltonian close to a double Weyl and translate the momenta k_y and k_z and consider the Taylor expansions on an effective low-energy level and get the effective Hamiltonian H_{eff}. The band structure of the model close to the double Weyl points, with the shifted momenta $\tilde{k}_y$ and $\tilde{k}_z$ can be described by:

$$H_{eff}(\vec{k}) = \left(-\frac{3}{4}\, t\ sin(q)\ k_x^2 + \frac{3}{4}\, t\ sin(q)\ \widetilde{k}_y^{\,2}\right)\sigma_x + \left(\frac{3}{2}\, t\ sin(q)\ k_x\, \widetilde{k}_y\right)\sigma_y - 2\, t\ sin(q)\ \widetilde{k}_z\ \sigma_z \tag{4.2}$$

The effective Hamiltonian H_{eff} is invariant under C_6-symmetry and therefore the energy bands of H_{eff} are eigenvalues of C_6. I label u_c and u_v the eigenvalues of the conductance and valence bands under a $\pi/3$ rotation. When u_c and u_v are different from each other $\langle\psi_1|P|\psi_2\rangle = 0$ unless the perturbation P is not invariant under C_6-symmetry .
If P does not depend momentum or position the gap cannot open unless it violates the C_6-symmetry and so it must be that the double Weyl points are protected from any perturbation which does not violate the rotational symmetry.

5 Further developments of the model

As seen in Figure 3 the band touching points with the same k_x and k_z coordinates have the same topological charge. This suggests than when they are projected in the k_y directions opposite topological charges do not overlap. Therefore Fermi arcs appear on surfaces at fixed y. It could be possible to explore the Fermi arcs if a hard-wall potential is confining the potential and gives the system a finite size in the y-direction ($y = 0, ..., L$) [4]. The detailed analysis of the wavefunctions and properties of the Fermi arcs of the confined system are beyond the scope of this work and may be subject of further investigations.
A proposal for the detection of the band touching points experimentally is the Landau Zener experiments[26,27], which looks at the transitions of some of the fermions from the lower band to the upper band. It may be possible to detect how many fermions are in the upper band by time of flight measurements and ideally distinguish between the single and double Weyl points . If the Landau Zener experiments becomes able to detect band touching points and Weyl points, it could be an interesting way to study the model presented in this paper experimentally.

6 Conclusions

I analyzed a tight-binding model of fermions hopping in a 3D lattice and subjected it to a gauge potential and I introduced staggered $\pi/2$ fluxes on the triangular plaquettes with an Abelian gauge potential. To study Weyl points I expanded the model with spin degree of freedom and introduced a spin 1/2 degree of freedom, whose dynamics was dictated by a non-Abelian gauge potential. The non-Abelian gauge coupled the spin and the dynamics of the particles like a spin-orbit coupling.
The band structure was characterized by four single Weyl points at the corners of the first Brillouin zone and two double Weyl points in the center of the k_x-k_y planes, which had topological charges. The energy of the single Weyl points were depend on the spin-orbit intensity but the double Weyl points were at 0 energy at any intensity.
The symmetries protecting the double Weyl points were explored as the system contained C_3 rotational symmetry and particle hole symmetry. At a low-energy level the system had C_6 symmetry, which can protect the double Weyl points from any pertubation, which does not violate the rotational symmetry. I finally suggested possible further developments of the model, which included the study of Fermi arcs of the system and the detection of Weyl points through Landau Zener experiments.

7 Acknowledgements

I would like to thank my supervisor Michele Burrello for the inspiration to this project, and for helping whenever a problem occurred. It has been a good introduction into the realm of condensed matter theory, ultracold atoms and Weyl semimetals.

References

1 M. Z. Hasan and C. L. Kane, *Rev. Mod. Phys.*, 2010, **82**, 3045–3067.
2 F. C. Yan, B., *Annual Review of Condensed Matter Physics*, 2017, **8**, 337–354.
3 H. Weyl, *Zeitschrift fur Physik*, 1929, **56**, 330–352.
4 X. Wan, A. M. Turner, A. Vishwanath and S. Y. Savrasov, *Phys. Rev. B*, 2011, **83**, 205101.
5 C. Fang, M. J. Gilbert, X. Dai and B. A. Bernevig, *Phys. Rev. Lett.*, 2012, **108**, 266802.
6 B. Q. Lv and et al., *Nature Physics*, 2015, **11**, 724–727.
7 B. Q. Lv and et al., *Phys. Rev. X*, 2015, **5**, 031013.
8 M. Z. Hasan, S.-Y. Xu and et al., *Science*, 2015, **349**, 613–617.
9 M. Z. Hasan, S.-Y. Xu and et al., *Nat Phys*, 2015, **11**, 748–754.
10 L. Lu, Z. Wang, D. Ye, L. Ran, L. Fu, J. D. Joannopoulos and M. Soljačić, *Science*, 2015, **349**, 622–624.
11 A. A. Burkov and L. Balents, *Phys. Rev. Lett.*, 2011, **107**, 127205.
12 S. Ganeshan and S. D. Sarma, *Physical Review B*, 2015, **91**, 125438.
13 M. Aidelsburger, M. Atala, M. Lohse, J. T. Barreiro, B. Paredes and I. Bloch, *Physical Review Letters*, 2013, **111**, 185301.
14 H. Miyake, G. A. Siviloglou, C. J. Kennedy, W. C. Burton and W. Ketterle, *Physical Review Letters*, 2013, **111**, 185302.
15 B. M. Anderson, G. Juzeliūnas, V. M. Galitski and I. B. Spielman, *Physical Review Letters*, 2012, **108**, 235301.
16 B. Yadin and V. Vedral, *Phys. Rev. A*, 2016, **93**, 022122.
17 J. Armaitis, J. Ruseckas and G. Juzeliūnas, *Phys. Rev. A*, 2017, **95**, 033635.

18 J. Struck, M. Weinberg, C. Ölschläger, P. Windpassinger, J. Simonet, K. Sengstock, R. Höppner, P. Hauke, A. Eckardt, M. Lewenstein and L. Mathey, *Nature Physics*, 2013, **9**, 738–743.
19 J. Dalibard, F. Gerbier, G. Juzeliūnas and P. Öhberg, *Reviews of Modern Physics*, 2011, **83**, 1523–1543.
20 N. Goldman, G. Juzeliūnas, P. Öhberg and I. B. Spielman, *Reports on Progress in Physics*, 2014, **77**, 126401.
21 J. Armaitis, J. Ruseckas and G. Juzeliūnas, *Phys. Rev. A*, 2017, **95**, 033635.
22 J. P. Vyasanakere, S. Zhang and V. B. Shenoy, *Phys. Rev. B*, 2011, **84**, 014512.
23 A. M. Turner and A. Vishwanath, *ArXiv e-prints*, 2013.
24 H. B. Nielsen and M. Ninomiya, *Phys. Lett.*, 1981, **B105**, 219–223.
25 W.-J. Chen, M. Xiao and C. T. Chan, *Nature Communications*, 2016, **7**, 13038.
26 L. Tarruell, D. Greif, T. Uehlinger, G. Jotzu and T. Esslinger, *Nature*, 2012, **483**, 302–305.
27 W.-Y. He, S. Zhang and K. T. Law, *Phys. Rev. A*, 2016, **94**, 013606.
28 N. Goldman, G. Juzeliūnas, P. Öhberg and I. B. Spielman, *Reports on Progress in Physics*, 2014, **77**, 126401.
29 E. Matsuoka, K. Hayashi, A. Ikeda, K. Tanaka, T. Takabatake and M. Matsumura, *Journal of the Physical Society of Japan*, 2005, **74**, 1382–1385.

A Appendix: Second Quantization

Second quantization is the standard formulation of quantum many-particle theory. I will consider a free non-relativistic in a box with indistinguishable particles, which are translation invariant. This means the single particle wavefunctions are plane waves and for fermions we need to also consider the spin, so the single particle wavefunctions are given by:

$$\psi_{\vec{k},s} = \frac{1}{\sqrt{V}} e^{i\,\vec{k}\cdot\vec{r}}\sigma_s \tag{A.1}$$

where s is a spin index of either spin up or spin down. We would like to label the basis states in Fock space with occupation numbers $\{n_k\} = \{n_1, n_2, ...\}$ We now introduce the creation operator $c^\dagger_{\vec{k}}$ acting on some state in our Fock space, which adds a particle to the system. The Hermitian conjugate of the creation operator is the annihilation operator $c_{\vec{k}}$, which removes (or annihilates) a particle from the system. By definition the annihilation operator acting on a vacuum state $|0\rangle$ with no particles is given as:

$$c_{\vec{k}}\,|0\rangle = 0 \tag{A.2}$$

In the case of fermions the creation $c^\dagger_{\vec{k}}$ and annihilation operators $c_{\vec{k}}$ have anti-commutation relations since the wavefunction is antisymmetric:

$$\{c_{\vec{k}}, c^\dagger_{\vec{k}'}\} = \delta_{k,k'} \tag{A.3}$$

$$\{c_{\vec{k}}, c_{\vec{k}'}\} = \{c^\dagger_{\vec{k}}, c^\dagger_{\vec{k}'}\} = 0 \tag{A.4}$$

The single particle momentum state $|k\rangle$ can be expressed as:

$$c^\dagger_{\vec{k}}\,|0\rangle = |\vec{k}\rangle \tag{A.5}$$

which is the creation operator $c^\dagger_{\vec{k}}$ acting on the vaccum state $|0\rangle$.
The single particle in a box has a wavefunction, which can be expressed at the integral over the box:

$$|\vec{k}\rangle = \frac{1}{\sqrt{V}} \int d^3\vec{r}\; e^{i\,\vec{k}\cdot\vec{r}}\,|\vec{r}\rangle \tag{A.6}$$

and the inverse relation with real space wavefunction:

$$|\vec{r}\rangle = \frac{1}{\sqrt{V}} \sum_{\vec{k}} e^{-i\,\vec{k}\cdot\vec{r}}\,|k\rangle \tag{A.7}$$

It is required that the real space creation operator $|\vec{r}\rangle$ satisfies:

$$c^\dagger_{\vec{r}}\,|0\rangle = |\vec{r}\rangle \tag{A.8}$$

The relations between the creation annihilation and creation creation operators in momentum space and real space can be defined by the use of Equations A.5, A.6 and A.8. given as:

$$c_{\vec{k}} = \frac{1}{\sqrt{V}} \sum_{\vec{r}} e^{i\,\vec{k}\cdot\vec{r}} c_{\vec{r}} \tag{A.9}$$

and the inverse Fourier transform:

$$c_{\vec{r}} = \frac{1}{\sqrt{V}} \sum_{\vec{k}} e^{-i\,\vec{k}\cdot\vec{r}} c_{\vec{k}} \tag{A.10}$$

We can proof the transformation and inverse transformation:

$$c_{\vec{r}} = \frac{1}{\sqrt{V}} \sum_{\vec{k}} e^{-i\,\vec{k}\cdot\vec{r}} c_{\vec{k}} = \frac{1}{\sqrt{V}} \sum_{\vec{k}} e^{-i\,\vec{k}\cdot\vec{r}} \sum_{\vec{r}\,'} e^{i\,\vec{k}\cdot\vec{r}\,'}\, c_{\vec{r}\,'} = \sum_{\vec{r}\,'} c_{\vec{r}\,'} \frac{1}{\sqrt{V}} \sum_{\vec{k}} e^{-i\,\vec{k}(\vec{r}-\vec{r}\,')} = \sum_{\vec{r}\,'} c_{\vec{r}\,'}\,\delta_{\vec{r}\,\vec{r}\,'} = c_{\vec{r}} \tag{A.11}$$

An example of how to Fourier transform the sums from real space to momentum space is shown for a 1D chain given the sum $\sum_r c^\dagger_{r+1}\, c_r$:

$$\sum_r c^\dagger_{r+1}\, c_r = \sum_r \frac{1}{\sqrt{L}} \sum_k e^{i\,k(r+1)} c^\dagger_k \frac{1}{\sqrt{L}} \sum_{k'} e^{-i\,k'r} c_{k'} = \frac{1}{L} \sum_r \sum_{k,k'} e^{i\,k(r+1)} e^{-i\,k'r} c^\dagger_k c_{k'} \tag{A.12}$$

and using $e^{i\,k(r+1)} e^{-i\,k'r} = e^{i(k-k')\,r+i\,k}$ and seperating them:

$$\frac{1}{L} \sum_r \sum_{k,k'} e^{i\,k(r+1)} e^{-i\,k'r} c^\dagger_k c_{k'} = \sum_{k,k'} c^\dagger_k c_{k'}\; e^{i\,k} \frac{1}{L} \sum_r e^{i\,(k-k')\,r} = \sum_{k,k'} c^\dagger_k c_{k'}\; e^{i\,k}\; \delta_{k\,k'} = \sum_k c^\dagger_k c_k\; e^{i\,k} \tag{A.13}$$

The transformation is for the 1D case:

$$\sum_r c^\dagger_{r+1}\, c_r = \sum_k c^\dagger_k c_k\; e^{i\,k} \tag{A.14}$$

and for the Hermitian conjugated:

$$\sum_r c^\dagger_r\, c_{r+1} = \sum_k c^\dagger_k c_k\; e^{-i\,k} \tag{A.15}$$

B Appendix: Gauge Transformations

I will review some basic concept about gauge transformations in quantum systems and for simplicity consider the case of a wavefunction in free space. However the following definitions can be generalized to the lattice case relevant for ultracold atoms trapped in optical lattices. [28].

B.1 Abelian gauge transformation

The Abelian gauge transformation is a local transformation and, if we describe a dynamical system, depended on the space-time coordinates , with a complex function $\psi(x)$, we can express the Abelian gauge transformation as:

$$\psi(x) \rightarrow \psi'(x) = U(x)\psi(x) \tag{B.1}$$

where $U(x) = e^{i\theta(x)}$ is a unitary operator and belongs in the unitary group $U(1)$ and it depends on the position in $\theta(x)$. When a particle follows a path from a reference point j to a point k. It acquires a "magnetic phase factor" [28]:

$$\psi(\vec{r}_k) = exp\left(\frac{i}{\hbar}\int_j^k A(x)\cdot d\vec{l}\right)\psi_0(\vec{r}_k) = U_{jk}\psi_0(\vec{r}_k) \tag{B.2}$$

where $\psi_0(\vec{r}_k)$ is the wavefunction in the absence of the gauge potential and $U_{jk} = e^{i\phi_{jk}}$ is the tunneling operator.
In the case of an Abelian gauge transformation a particle subjected to a local gauge potential $A(x)$ and the non-relativistic single-particle Hamiltonian reads:

$$H = \frac{(p+A(x))^2}{2m} \tag{B.3}$$

where $p = -i\partial x$ and with the phase difference term $U(x)$ we can calculate that:

$$H = \frac{U^\dagger(p+A(x))^2U}{2m} \rightarrow \frac{(-i\partial x + \partial x\theta(x) + A(x))^2}{2m} \tag{B.4}$$

where the gauge potential $A(x)$ for the Abelian gauge transformation is transformed as:

$$A(x) \rightarrow A'(x) + \partial x\theta(x) = A(x) + U^\dagger(-i\,\partial x\,U) \tag{B.5}$$

The tunneling operators transforms as:

$$U_{jk} \rightarrow U'_{jk} = U_{jk}\,exp\left(i\,\frac{\theta(\vec{r}_k) - \theta(\vec{r}_j)}{\hbar}\right) \tag{B.6}$$

The following is a inclusion of lattice models. We will consider a square lattice in the explanation of plaquettes. The plaquettes, a closed region in space delimited by a set of points, are connected by links as shown in Figure B.1:

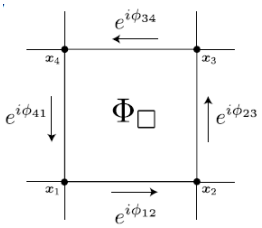

Fig. B.1 Figure from Ref. 28 showing the plaquette, tunneling operators and magnetic flux.

When the particle performs a loop $\square$ around the plaquette it gains an Aharonov-Bohm phase:

$$\psi(\vec{r}_1) \rightarrow \frac{i}{\hbar}\oint_\square A(x)\cdot d\vec{l}\,\psi(\vec{r}_1) = e^{2\pi i\Phi_\square}\psi(\vec{r}_1) \tag{B.7}$$

where $\Phi_\square$ is the number of magnetic flux quanta Φ_0 penetrating the plaquette $\square$ and it is expressed with the "loop product"t of tunneling operators U_{jk}:

$$e^{2\pi i\Phi_\square} = U_{12}\,U_{23}\,U_{34}...U_{L-1}\,U_{L1} = \prod_\square U_{jk} = exp\left(i\sum_\square \phi_{jk}\right) \tag{B.8}$$

In order to describe a lattice of a quantum system subject to a gauge potential the gauge potential A the lattice description should include:

1. A set of lattice sites $\vec{r}_j$
2. A set of links, j to k, connecting the sites and defining plaquettes
3. A set of tunneling operators U_{jk} associated with the links

B.2 Non-Abelian gauge transformation

If the tunneling operators U_{jk} couple to internal degrees of freedom, like the spin, gauge potentials act differently on the different spin states, and they are now matrix-valued objects. Tunneling operators now belong to the $SU(2)$ group and the potential $\vec{A}$ is a vector of matrices $\vec{A} = q(\sigma_x, \sigma_y, \sigma_z)$
The tunneling operator U_{jk} is given now dependent on the link j to k and the different spin states s and s' :

$$U_{jk,s,s'} = P \exp\left(\frac{i}{\hbar}\int_j^k \vec{A}_{s,s'} \cdot d\vec{l}\right) \tag{B.9}$$

where P is a path ordered integral and is required because at at different points of the path the matrices $\hat{A}_{z,y}$ do not necessarily commute.
In the case of the non-Abelian gauge transformations we must distinguish between global and local gauge transformations.

Global non-Abelian gauge transformation:
The global non-Abelian gauge transformation is given by

$$\psi \to \psi' = U\psi \tag{B.10}$$

where the unitary operator $U = e^{i\vec{\alpha}\vec{\sigma}}$ is not position dependent and it belongs to the $SU(2)$ unitary group.
The Hamiltonian for a system subjected to a global non-Abelian gauge transformation is

$$H = \frac{(\vec{p}\,\sigma_0 + \vec{A})^2}{2m} \to \frac{U^\dagger(\vec{p}\,\sigma_0 + \vec{A})^2 U}{2m} \tag{B.11}$$

and through calculations the global non-Abelian gauge potential can be described as

$$\vec{A} \to \vec{A}' = U^\dagger \vec{A}\, U \tag{B.12}$$

Local non-Abelian gauge transformation:
The local non-Abelian gauge transformation is given by:

$$\psi(x) \to \psi'(x) = U(x)\psi(x) \tag{B.13}$$

where the unitary operator $U = e^{i\vec{\alpha}(x)\vec{\sigma}}$ is position depend and it belongs to the $SU(2)$ unitary group.
The Hamiltonian for a system subjected to a local non-Abelian gauge transformation is:

$$H = \frac{(\vec{p}\,\sigma_0 + \vec{A}(x))^2}{2m} \to \frac{U^\dagger(x)(\vec{p}\,\sigma_0 + \vec{A}(x))^2 U(x)}{2m} \tag{B.14}$$

and through calculations the local non-Abelian gauge potential can be described as:

$$\vec{A}(x) \to \vec{A}(x)' = U^\dagger \vec{A}(x) U + \partial x \vec{\alpha}(x) \cdot \vec{\sigma} \tag{B.15}$$

C Appendix: Calculation of Berry Monopoles

I will briefly review how to calculate the Chern number of a touching point, which corresponds to the topological charge of a Berry monopole.
Given the Hamiltonian $H(\vec{k}) = -\vec{k}\cdot\vec{\sigma}$, where $\vec{\sigma}$ is the Pauli matrix, we consider the states $|\uparrow\rangle$ and $|\downarrow\rangle$ and label the states α and β.
If we consider the Bloch sphere in Figure C.1 we can describe the wave function of a band by spherical coordinates.

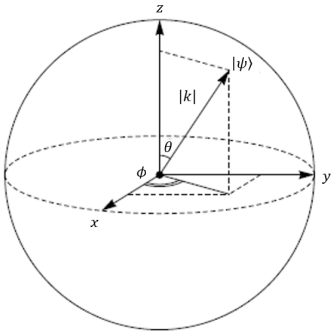

Fig. C.1 The Bloch sphere with the spherical coordinates ϕ, θ and k.

I consider the example with the state $|\psi\rangle$ given by Equation C.1

$$|\psi\rangle = \begin{pmatrix} \alpha = \cos(\frac{\theta}{2}) \\ \beta = e^{i\,\phi}\sin(\frac{\theta}{2}) \end{pmatrix} \tag{C.1}$$

Then we calculate the Berry connection $A(\vec{k})$, which is similar to a vector potential in momentum space and is given by Equation C.2

$$A(\vec{k}) = i\,\langle\psi(\vec{k})|\vec{\nabla}_k\psi(\vec{k})\rangle \tag{C.2}$$

If $\vec{\nabla}_k$ is written in spherical coordinates, as shown in Equation C.3, we can calculate the Berry connection in Equation C.2.

$$\vec{\nabla}_k = \left(\partial k, \frac{1}{k}\partial\theta, \frac{1}{k\,\sin(\theta)}\partial\phi\right) \tag{C.3}$$

The three spherical components of the Berry connection is calculated in Equation C.4-C.6

$$A_k(\vec{k}) = 0 \tag{C.4}$$

$$A_\theta(\vec{k}) = \frac{1}{k}\left(-\frac{1}{2}\cos\left(\frac{\theta}{2}\right)\sin\left(\frac{\theta}{2}\right) + \frac{1}{2}\cos\left(\frac{\theta}{2}\right)\sin\left(\frac{\theta}{2}\right)\right) = 0 \tag{C.5}$$

$$A_\phi(\vec{k}) = -\frac{1}{k\sin(\theta)}\left(\sin^2\left(\frac{\theta}{2}\right)\right) \neq 0 \tag{C.6}$$

The Berry connection in the ϕ direction (Equation C.6) is the only term not equal to 0.
We can use the Berry connection as a vector potential in regards to calculate the magnetic field given as C.7

$$\vec{F} = \vec{\nabla}\times\vec{A} \tag{C.7}$$

where the curl $\vec{\nabla}\times\vec{A}$ in spherical coordinates is given as C.8

$$\vec{F} = \vec{\nabla}\times\vec{A} = \frac{1}{k\sin(\theta)}\left(\frac{\partial}{\partial\theta}(A_\phi sin(\theta)) - \frac{\partial A_\theta}{\partial\phi}\right)\hat{k} + \frac{1}{k}\left(\frac{1}{sin(\theta)}\frac{\partial A_k}{\partial\phi} - \frac{\partial}{\partial k}(kA_\phi)\right)\hat{\theta} + \frac{1}{k}\left(\frac{\partial}{\partial k}(kA_\theta) - \frac{\partial A_k}{\partial\theta}\right)\hat{\phi} \tag{C.8}$$

We can reduce Equation C.7 by using the results of the Berry connections in Equations C.4-C.6 as shown in Equation C.9-C.11

$$F_k = \frac{1}{k\sin(\theta)}\left(\frac{\partial}{\partial\theta}(A_\phi sin(\theta))\right) = -\frac{1}{2k^2} \tag{C.9}$$

$$F_\theta = \frac{1}{k}\left(-\frac{\partial}{\partial k}(kA_\phi)\right) = \frac{1}{k}\frac{\partial}{\partial k}\left(\frac{1}{\sin(\theta)}\,\sin^2\left(\frac{\theta}{2}\right)\right) = 0 \tag{C.10}$$

$$F_\phi = \frac{1}{k}\left(\frac{\partial}{\partial k}(kA_\theta) - \frac{\partial A_k}{\partial\theta}\right) = 0 \tag{C.11}$$

Since we have fluxes from a sphere the only direction we consider is the k direction, which goes outward of the sphere, so the surface I consider is a oriented surface. The Chern number c_n can be calculated as the surface integral of magnetic fluxes given in Equation C.12 [29]

$$c_n = \frac{1}{2\pi}\int d^2k\;\hat{k}\cdot\vec{F} = \frac{1}{2\pi}\int d^2k\;F_k \tag{C.12}$$

The integral is the area of the Bloch sphere and the Chern number becomes:

$$c_n = \frac{1}{2k^2}(4\pi k^2)\left(-\frac{1}{k^2}\right) = -1 \tag{C.13}$$

The Chern number -1 corresponds to a Berry monopole with topological charge of -1.
If one considers different wave functions of a band $|\psi\rangle$ the topological charges may change to be ± 1.

D Calculation of the C_3 rotation symmetry

To show the C_3 rotation symmetry we need to satisfy the following:

$$\tilde{H}_0(R\vec{k}) = C_3^{\dagger}\tilde{H}_0 C_3 \tag{D.1}$$

where R is the rotation operator which shifts the momenta in the k_x and k_y as $2\pi/3$:

$$e^{i\,\frac{2\pi}{3}L_z}\,\vec{k}\,e^{-i\,\frac{2\pi}{3}L_z} = R\vec{k} \;\rightarrow\; e^{i\,\frac{2\pi}{3}L_z}\tilde{H}_0(\vec{k})e^{-i\,\frac{2\pi}{3}L_z} = \tilde{H}_0(R\vec{k}) \tag{D.2}$$

We must rewrite the Weyl Hamiltonian $H(k_x,k_y,k_z)$, given in Equation 3.5, with $H(k_x,\tilde{k}_y,k_z)$, where $\tilde{k}_y = k_y - \frac{2\pi}{\sqrt{3}}$. The k_z terms will not be considered because they are invariant under any rotation along the $\hat{z}$ axis:

$$\begin{aligned}\tilde{H}_0(k_x,\tilde{k}_y) = {} & 2t\cos(q)\left(\sin(k_x) - 2\sin\left(\frac{k_x}{2}\right)\cos\left(\frac{\sqrt{3}}{2}\tilde{k}_y\right)\right)\sigma_0 \\ & +2t\sin(q)\left(\cos(k_x) - \cos\left(\frac{1}{2}k_x\right)\cos\left(\frac{\sqrt{3}}{2}\tilde{k}_y\right)\right)\sigma_x \\ & +2t\sin(q)\left(\sin\left(\frac{1}{2}k_x\right)\sin\left(\frac{\sqrt{3}}{2}\tilde{k}_y\right)\right)\sigma_y\end{aligned} \tag{D.3}$$

The tunneling operators given in Equation 3.4 are:

$$U_1 = i\,e^{iq\sigma_x} \tag{D.4}$$

$$U_2 = i\,e^{iq\left(\frac{1}{2}\sigma_x + \frac{\sqrt{3}}{2}\sigma_y\right)} \tag{D.5}$$

$$U_3 = i\,e^{iq\left(\frac{1}{2}\sigma_x - \frac{\sqrt{3}}{2}\sigma_y\right)} \tag{D.6}$$

$$U_4 = i\,e^{iq\sigma_z} \tag{D.7}$$

If we look at Figure 3 the system has a $\frac{2\pi}{\sqrt{3}}$ translation in the k_y direction and it corresponds to sign change of U_2 and U_3:

$$\tilde{H}_0(k_x,\tilde{k}_y) = -t\,U_1 e^{i\,k_x} + t\,U_2 e^{i\,\frac{1}{2}k_x + \frac{\sqrt{3}}{2}\tilde{k}_y} + t\,U_3 e^{i\,\frac{1}{2}k_x - \frac{\sqrt{3}}{2}\tilde{k}_y} + h.c. \tag{D.8}$$

With the counterclockwise $2\pi/3$ rotation of the momenta:

$$\tilde{H}_0(R\vec{k}) = -t\,U_1 e^{-\frac{1}{2}\,i\,k_x + \frac{\sqrt{3}}{2}\,i\,\tilde{k}_y} + t\,U_2 e^{-i\,k_x} + t\,U_3 e^{i\,\frac{1}{2}k_x + \frac{\sqrt{3}}{2}\tilde{k}_y} + h.c. \tag{D.9}$$

The C_3 rotation operator is defined as:

$$C_3 = e^{i\,\frac{\pi}{3}\sigma_z} = \frac{1}{2}\sigma_0 + \frac{\sqrt{3}}{2}\,i\,\sigma_z \tag{D.10}$$

If the following equalities are fulfilled the system has C_3 rotational symmetry:

$$C_3^{\dagger}U_1C_3 = -U_3^{\dagger} \tag{D.11}$$

$$C_3^{\dagger}U_2C_3 = -U_1^{\dagger} \tag{D.12}$$

$$C_3^{\dagger}U_3C_3 = U_2 \tag{D.13}$$

I calculate the equalities:

$$C_3^{\dagger}U_1C_3 = i\,cos(q)\sigma_0 + sin(q)\left(\frac{1}{2}\sigma_x - \frac{\sqrt{3}}{2}\sigma_y\right) = -U_3^{\dagger} \tag{D.14}$$

$$C_3^{\dagger}U_2C_3 = i\,cos(q)\sigma_0 + sin(q)\sigma_x = -U_1^{\dagger} \tag{D.15}$$

$$C_3^{\dagger}U_3C_3 = i\,cos(q)\sigma_0 + sin(q)\left(-\frac{1}{2}\sigma_x - \frac{\sqrt{3}}{2}\sigma_y\right) = i\,e^{iq\left(\frac{1}{2}\sigma_x + \frac{\sqrt{3}}{2}\sigma_y\right)} = U_2 \tag{D.16}$$

E Calculation of the particle-hole symmetry

The canonical way of defining particle hole symmetry is

$$CH^*(-\vec{k})C^\dagger = -H(\vec{k}) \tag{E.1}$$

where $H(\vec{k})$ is the Weyl Hamiltonian shown in Equation 3.5 and C is a suitable matrix that we have to find.
The Weyl Hamiltonian in Equation 3.5 (with a negative sign) is given as:

$$\begin{aligned} -H(\vec{k}) = &-2\,t\,\cos(q)\left(\sin(k_x)+2\,\sin\left(\frac{1}{2}k_x\right)\cos\left(\frac{\sqrt{3}}{2}k_y\right)+\sin(k_z)\right)\sigma_0 - 2\,t\,\sin(q)\left(\cos(k_x)+\cos\left(\frac{1}{2}k_x\right)\cos\left(\frac{\sqrt{3}}{2}k_y\right)\right)\sigma_x \\ &+2\,t\,\sin(q)\left(\sin\left(\frac{1}{2}k_x\right)\sin\left(\frac{\sqrt{3}}{2}k_y\right)\right)\sigma_y - 2\,t\,\sin(q)\,\cos(k_z)\sigma_z \end{aligned} \tag{E.2}$$

The complex conjugated Weyl Hamiltonian with negative $\vec{k}$ is given as:

$$\begin{aligned} H^*(-\vec{k}) = &-2\,t\,\cos(q)\left(\sin(k_x)+2\,\sin\left(\frac{1}{2}k_x\right)\cos\left(\frac{\sqrt{3}}{2}k_y\right)+\sin(k_z)\right)\sigma_0 + 2\,t\,\sin(q)\left(\cos(k_x)+\cos\left(\frac{1}{2}k_x\right)\cos\left(\frac{\sqrt{3}}{2}k_y\right)\right)\sigma_x \\ &+2\,t\,\sin(q)\left(\sin\left(\frac{1}{2}k_x\right)\sin\left(\frac{\sqrt{3}}{2}k_y\right)\right)\sigma_y + 2\,t\,\sin(q)\,\cos(k_z)\sigma_z \end{aligned} \tag{E.3}$$

The unitary operators C must be defined so Equation E.1 is fulfilled and therefore the operators must show following properties:

$$\sigma_0 \to \sigma_0 \tag{E.4}$$

$$\sigma_x \to -\sigma_x \tag{E.5}$$

$$\sigma_y \to \sigma_y \tag{E.6}$$

$$\sigma_z \to -\sigma_z \tag{E.7}$$

Therefore the operator C, which has the properties shown in Equation E.4-E.7, is the Pauli matrix σ_y given as:

$$C = \begin{bmatrix} 0 & -i \\ i & 0 \end{bmatrix} = \sigma_y \tag{E.8}$$

With the Pauli matrix σ_y Equation E.1 is reduced to:

$$\sigma_y H^*(-\overrightarrow{k})\sigma_y = -H(\overrightarrow{k}) \tag{E.9}$$

UCPH NanoScience
NanoVidenskab KU

tidsskrift.dk/index.php/NanoVidenskabKU

Thesis Paper

Platinum nanoparticles in photothermal therapy of cancer cells

Dunya Sarmad Aswad and Iliriana Qoqaj

Received June 2017, Accepted April 2018

Noble nanoparticles are potential photothermal therapy agents, due to their properties, such as ability to modify particle surface chemistry, and efficient light-to-heat conversion. In this work, we study the possible application of platinum nanoparticles as agents in photothermal therapy, their uptake, and toxicological response in the human ovarian cancer cell line (SK-OV-3) by flow cytometry. No oxidative stress, or toxicological response of the platinum nanoparticles was observed in the cells. Laser irradiation revealed photothermal destruction of SK-OV-3 cells exposed to 70 nm platinum nanoparticles at power density 45 W/cm^2 after 5 minutes using an 808 near infrared laser.

Introduction

Nanotechnology has offered a revolutionary breakthrough throughout the past years in the fight against cancer[1,2]. It has created new methods for cancer diagnostics, drug delivery and therapeutics[3]. Currently, different approaches are used to treat cancer, the most common being chemotherapy and radiation therapy, but these are not the most optimal methods, as they also attack healthy cells in the body in addition to the cancerous ones. By scaling down materials to nanometer scale we find nanoparticles (NPs) with extraordinary properties, including optical, magnetic, electronic and structural properties, which makes these nano-scaled particles promising for different approaches in the biomedical field[3,4]. Gold nanoshells (Au NSs), consisting of a silica core surrounded by a gold shell, have received much attention because of their excellent properties, such as their surface modification, biocompatibility, and efficient light-to-heat conversion[4–6]. Previous studies have shown that Au NSs could be the most promising NPs so far[5,7]. The potential difference that could separate treatment with NPs from chemotherapy and radiation therapy could be that the amount of healthy cells being attacked would potentially be reduced as well as the amount of cancer cells that die would be increased[1,3]. Plasmonic noble metal NPs have long been researched, due to their remarkable surface plasmon resonance (SPR)[4,8]. When metal particles are exposed to light, it induces an oscillation of the free electrons of the metal[4]. The SPR happens when the amplitude of the oscillation reaches its maximum at a specific frequency[4]. The SPR produces a strong absorption of the light and that absorption can be measured using a UV-Vis-NIR spectrometer[4]. The wavelength where the absorption peaks, is where the particles gets heated up most efficiently. This resonance peak also acts as a marker of the most effective laser wavelength to use for treatment[4]. A spectrometer is an instrument in which the reflection and absorption characteristics of a sample is measured, termed absorbance[9]. The radiation wavelength for the ultraviolet (UV), visible (vis), and near infrared (NIR) regions can be defined from 300 nm to 400 nm, 400 to 765 nm, and 765 nm to 3200 nm, respectively[10]. The absorbance can be used to characterize the optical properties of NPs. To determine some of the properties of NPs (or other macromolecules), including their size and shape, the common technique, dynamic light scattering (DLS) can be used[11–13]. The first outcome from a DLS experiment is an intensity distribution of the particle sizes[13]. Particles experience Brownian motions when suspended in liquid, and random collisions with solvent molecules causes particles to diffuse throughout the liquid[13]. The particles are irradiated with a laser, and the light is scattered. The observed intensities of the scattered light are the result of the interference of light scattered by each particle, which depends on the position of each element, this is known as the diffusion coefficient[13].

In recent years, scientists have been curious about the general properties of Pt NPs[14,15]. Our interest for Pt NPs are their possible application in the particle enhanced photothermal treatment (PTT) of cancer tumours. PTT relies on NPs with high light absorbing properties that are taken up by cancer cells. NPs get irradiated by a laser with wavelength in the NIR region and transform the light into localized heat energy, that penetrates the tissue, melts the lipids and kill targeted cell, hopefully, without damaging non-targeted cells[3,16,17]. The advantage of the NIR wavelength region is due to the biological window or therapeutic window, which is a range of wavelengths where light has maximum depth of penetration in tissue and low absorption[5,7]. Heating of the NPs leads them to oscillate, possibly causing the cancer cells to die either from active self-destruction (apoptosis) or from swelling until they burst (necrosis), tumour growth is stopped and the cancer cells are destroyed[18]. PTT is a well-researched topic as it could possibly replace methods being used at the present[3,7,18,19].

Cell death can occur in different situations, for example by apoptosis or necrosis. Apoptosis are recognized as the most common type of “programmed” death that occurs, especially during embryonic development[20,21]. Apoptosis can also occur as defence mechanism when cells are damaged by several causes.

Phosphatidylserine (PS) is a phospholipid, preferably located on the cytosolic portion of the plasma membrane, in normal viable cells (normal conditions)[21]. While, during apoptotic conditions a systematic change occurs in the plasma membrane as a result from the apoptotic signal. PSs are translocated from the cytosolic portion (inner leaflet) to the outer section (outer leaflet) of the plasma membrane, which exposes the PSs to the outside cellular environment[22–24]. The human vascular anticoagulant, Annexin V, is a protein that is commonly used as a bait to examine cells that are apoptotic, as Annexin V is a Ca^{2+}- dependent phospholipid- binding protein that binds to PS[21,24]. Annexin V tends to attach to phospholipids (phospholipids are the integral part of the cell membranes)[21]. In the early stage of apoptosis, once the cell is transferred to the apoptotic condition, Annexin V will bind to the PSs in the presence of Ca^{2+} and this can be detected by adding a fluorescence tag to Annexin V. Annexin V can therefore act as an apoptotic assay[24]. Necrosis is an accidental and inactive kind of cell death induced from environmental changes and is normally considered to be an uncontrolled kind of cell death[22,25,26]. Necrosis is often referred to as a kind of damage that happens spontaneously, although it can be classified as programmed cell death in some situations[27]. Necrosis occurs mostly when the cell swells up and the membrane then collapses leaving the cell destroyed[27]. The LIVE/DEAD stain can be used to examine the viability of cells by flow cytometry[28]. Necrotic cells have permeable cell membranes which can results in intense fluorescent staining as the dye will stain the whole cell due to the reaction of the amines in the cell[28]. Whilst, living cells will show a weak fluorescent staining as the dye only react with the amines on the cell surface. This approach can be used to investigate whether the cells die when exposed to NPs[28,29]. Oxidative stress, refers to the "raised intracellular levels of reactive oxygen species (ROS)"[30] that can cause damage to DNA, protein and lipids. ROS are chemically reactive molecules containing oxygen. If oxygen gains one or two electrons, it can lead to the formation of molecules such as superoxides or peroxides that can potentially be dangerous to the cells. These and other dangerous oxygen derivatives are called ROS[30]. If these ROS produces are not actually controlled, they can react with cell components and cause oxidative damage, among other things, cancer[30]. These ROS has two faces – redox biology, which occurs in the body all the time, where a small increase in ROS concentration activates biological processes[30]. Whilst, oxidative stress designates high concentrations of ROS which leads to damage of DNA, proteins and lipids[30]. Meaning that large changes are usually an indication of oxidative stress causing toxicity[30]. NPs can be toxic to the cells and sometimes the cells undergo oxidative stress because of the NPs toxicology and produce these ROS, which is a form of stress marker[31,32]. CellROX Oxidative Stress Reagents (Deep Red) are fluorescent probes that have the feature to detect and measure reactive oxygen species (ROS) in living cells. The fluorescence resulting from CellROX Oxidative Stress Reagents can be measured by using flow cytometry[31]. Cell analysis can be performed by a flow cytometer where thousands of cells pass through a laser beam per second and capture the light signal from each cell as it passes through[33,34]. The data gathered can be analysed statistically by a flow cytometry software to report cellular characteristics such as size, complexity, phenotype and health[33–35]. The interrogation point is the center of the system. This is where the laser and the sample criss-cross and the optics collect the resulting scatter and fluorescence[34,35]. Laser light is used to detect individual cells in the stream, as a cell passes though the laser it will refract or scatter light at all angles[33,34]. Fluorescence gives information about structure and function of cells, the fluorescent signal is emitted and detected[33,34]. Forward scatter (FSC) is when light is refracted by a cell in the flow channel and continues in the direction of the light travelling path (light scattered in the forward direction). The refracted light is detected by a detector. The magnitude of FSC is roughly proportional to the relative size of the cell. Therefore, generally smaller cells will produce smaller amount of forward scattered light and larger cells will produces larger FSC[34]. Side scatter (SSC), on the contrary, to forward scattered light, the light is scattered in a direction outside the light travelling path. This scattered light is focused through a lens system and is collected by a separate detector usually located perpendicular from the lasers path, these detectors usually gives information about the cell granularity and complexity, and in some cases how many NPs are present in the cell[33,34]. Therefore, cells with large complexity and high granularity produce more scattered light, than a cell with low complexity and low granularity[34]. Increase in SSC signal in cells have been associated with increasing NP uptake[8].

The aim of this study is the possible application of Pt NPs in PTT of a cancer cell model. We investigated if Pt NPs with diameters of 30 nm (Pt30), 50 nm (Pt50) and 70 nm (Pt70) were taken up by cells (by SSC detection using flow cytometry). In this study we used a human ovarian cancer cell line (SK-OV-3), that overexpresses the HER-2 (Neu/ErbB-2) gene[29], which is a tyrosine-protein receptor that is highly expressed in some cancerous cells[29,36]. To characterize the optical properties, we want to perform UV-Vis analysis, and to investigate if different medium conditions change the hydrodynamic size, we will perform DLS analysis. Furthermore, we will examine if the Pt NP uptake leads to a toxicological response in the SK-OV-3 cells by them self (with no laser treatment), as some noble metals have revealed being toxic[37–39]. Moreover, we will examine the stress level (if any) the Pt NPs induce in SK-OV-3 cells, with the use of CellROX.

Methods

Particle characteristics by manufacturer

The Pt NPs were declared to be spherical and citrate stabilised by manufacturer. The characteristics of the Pt NPs declared by the manufacturer (nanoComposix) are listed below.

Table 1 *Characteristics of the different sized platinum nano-particles (Pt NPs) declared by the manufacturer.*

Pt NPs	Diameter (TEM)	Coefficient of Variation	Hydrodynamic Diameter
Pt30	30 ± 3 nm	11.2 %	39 nm
Pt50	51 ± 7 nm	13.2 %	61 nm
Pt70	71 ± 4 nm	5.1 %	71 nm

Cell culture

Human ovarian cancer (SK-OV-3) were grown in cell culture flask using McCoy's 5A medium (GE Healthcare Life Sciences, HyClone Laboratories) under normal cell growth conditions at 37℃, 5% CO_2 and 95% humidity.

Cells for experiments were seeded in 24-well cell culture plates (Nunclon Delta, Nunc, Thermo Fischer Scientific) or 35 mm petri dish with, 20 mm microwell (Part No# P35G-1,5-20-C, MatTek Corporation) in McCoy's 5A growth medium with a seeding density of 2.5 x 10^4 cells per cm^2 under normal cell growth conditions at 37℃, 5% CO_2 and 95% humidity. The cells were count by using a cell counter (Countess II FL, life technologies).

Nanoparticle preparation and cellular exposure

The nanoparticles were prepared by centrifugation (Eppendorf, Centrifuge 5417C) and removing of supernatant and then sonicated for 5 minutes (2510 Brandson). Then the particles were re-suspended in the relevant solution. For cell exposure, UV-Vis and DLS, McCoy's 5A medium (with no phenol red) with 10% foetal bovine serum (FBS) was used, Milli-Q water (18.2 MΩ at 25℃, Ultrapure (Type 1) Water, Direct-Q*3 UV) were used for UV-Vis and DLS experiments.

For cell exposure experiments, normal McCoy's 5A medium was removed and replaced with NP containing McCoy's 5A medium one day after seeding, and was added at the described concentrations. The cells were incubated for 24 hours under normal cell growth conditions.

Nanoparticle characterisation

The optical properties of the NPs were examined by UV-Vis *(See Appendix, Figure 1-4)* (Agilent Technologies, Cary 5000 UV-Vis-NIR Spectrophotometer), and the hydrodynamic sizes were examined by DLS (Malvern Instruments Nordic) done by placing a small sample of the solution we want to investigate in the machine using a cuvette.

The experiments were performed for particles in the following conditions: in Milli-Q water, McCoy's 5A medium after 0 hour of incubation, McCoy's 5A medium after 24 hours incubations (37℃), and McCoy's 5A medium after 24 hours incubation together with cells (under normal cell growth conditions).

Flow cytometry and sample preparations

For flow cytometry experiments cells were seeded in 24-wells and exposed to Pt NPs as previously explained.

CellROX medium was prepared by adding CellROX® Deep Red (#cat C10422, Molecular Probes) in McCoy's 5A medium for each sample and it was protected from light.

The 24-well containing cells was placed on a cooling block. The cells were transferred to Falcon FACS tubes (Falcon®), and the well was washed with ice-cold Annexin V binding buffer (aVbb) and placed on a pre-cooled cooling rack. The cells were centrifuged for 5 min at 400 x G, and the supernatant were removed and the cells were re-suspended in aVbb with LIVE/DEAD® Fixable Near-IR Dead Cell Stain (LD) (cat# L34975, Molecular Probes) diluted 1:1000 from stock solution. Annexin V alexa488 V Alexa Fluor® 488 (cat# A13201, Molecular Probes) diluted 1:100 from stock solution (concentration was not mentioned) were added to each sample, and were incubated for 30 minutes protected from light. Ice-cold aVbb was added to each sample, and the cells were centrifuged for 5 minutes at 400 x G, the supernatant was then removed. Finally, ice-cold aVbb was added and the samples were kept on ice until analysis on the Flow cytometer.

Control samples with no Pt NPs and staining was also prepared, as well as single staining controls for each probe (CellROX, Annexin V, and LD). These controls were used to perform digital signal compensation to remove overlapping fluorescent signals (spectral mixing) between the different fluorophores.

Cell damage were examined by flow cytometry. Cell death assay were performed using Flowing Software (version 2.5.1). This assay gives an idea of the state the cells are in and if they react to the particles. We placed a quadrant on the dot plot and thus the cells can be divided into living cells (lower left) with a low Annexin V and LD signal, early apoptotic cells (upper left) with a high Annexin V and low LD signal, late apoptotic (upper right) with a high Annexin V and high LD signal, and necrotic cells (lower right) with a low Annexin V high LD signal. *(See Appendix for illustration, figure 5 and 6)*

Flow cytometry was performed on a BD FACS canto II (Becton, Dickinson and Company). FSC and SSC were detected using blue laser (488 nm) and detection at the same wavelength. The levels of Annexin V, Alexa Fluor® 488 conjugate was detected using blue excitation laser (488 nm) and a 530/30 nm emission filter. CellROX® Deep Red Reagent and LIVE/DEAD® Fixable Near-IR Dead Cell Stain was detected using red excitation laser (633 nm) and a 660/20 nm emission filter and a 780/60 nm emission filter, respectively.

Laser exposure and imaging

Cells were seeded on 35 mm petri dish with, 20 mm microwell. 24 hours after exposure to Pt NPs (or 24 hours after cells seeding for laser treatment only) the Pt NP exposure medium was removed and cells were washed 3 times with PBS, and replaced by McCoy's 5A medium (without phenol red). Laser treatment was performed by a Modulight ML6600 laser system (Modulight) using a custom 5 mm spot illumination kit.

24 hours after the laser treatment the cell medium was removed and replaced with cell medium containing 5 µM calcein-acetoxymethyl (AM) (Molecular Probes), "a membrane-permeable live-cell labeling dye" a probe that only fluoresces in live cells, and cells were incubated for 15 min. Cells were imaged using cell medium without phenol red.

Cells were imaged using the Nikon wide-field fluorescent microscope (Eclipse T*i*) using the FITC excitation/emission cube set. *(See Appendix for detailed protocols, page 4-6).*

Statistics

All statistical test was performed using IBM SPPS statistics (version 24). ANOVA was performed, and to test for homogeneity of variance Levene's test was performed. For data passing Levene's test of similar variance between groups, a Tukey post-hoc test was performed, for samples failing Levene's test a Gemes-Howell post-hoc test was used. In all cases a significant level of $P < 0.05$ was used. *(See Appendix for further details, page 7-16).*

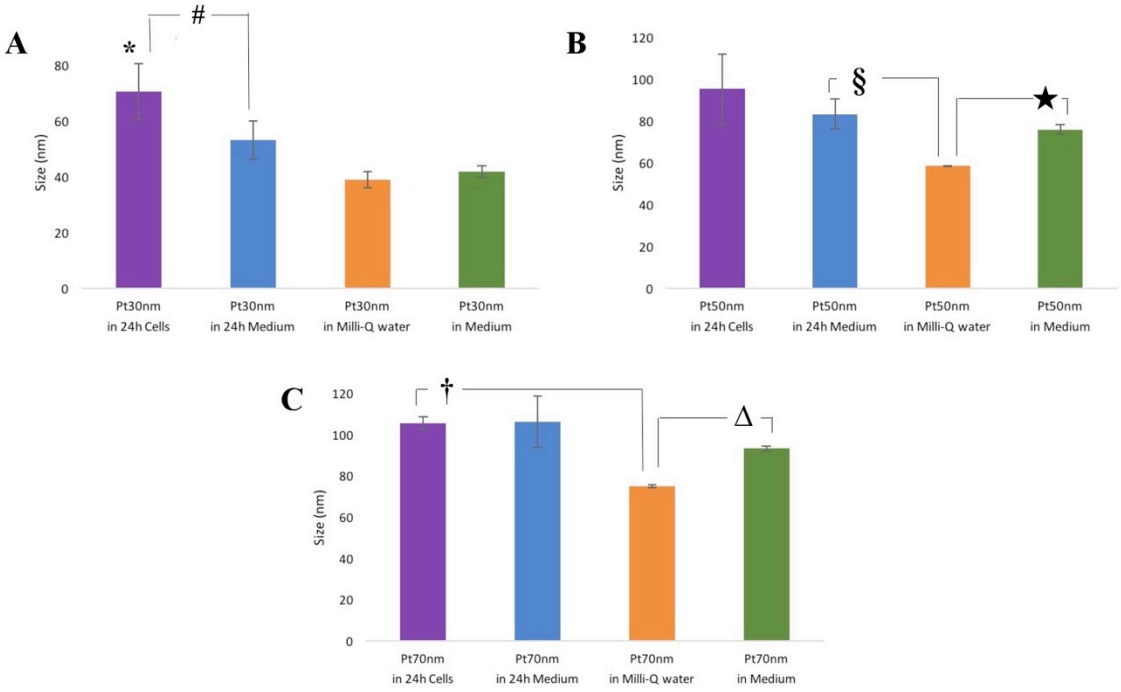

Figure 1 *Dynamic light scatter (DLS) analysis of platinum nanoparticles (Pt NPs) with a diameter of 30 nm, 50 nm, and 70 nm, respectively. Panel **A** shows the mean hydrodynamic size of Pt30 in different conditions, with cells for 24 hours (purple), in medium for 24 hours (blue), in MilliQ water (orange), and in medium (green). # P = 0.094 and * P < 0.005. In the same conditions is also shown for Pt50 (Panel **B**) § P = 0.096 and ★ P = 0.023, and for Pt70 (Panel **C**) † P = 0.009 and Δ P = 0.000.*

Results

Nanoparticle characterisation

We determined the hydrodynamic sizes of the different Pt NPs by DLS *(Figure 1)*. In Milli-Q water the Pt30 showed a small increase in size with an average of 38.9 nm and a standard deviation of 2.89. The Pt50 showed a small increase as well with an average of 58.5 nm and a standard deviation of 0.22. Finally, the Pt70 also showed the same increase with an average of 74.8 nm and a standard deviation of 0.74.

In medium the Pt NPs showed a consistent increase of the diameter between 10-30 nm *(Figure 1)* compared to Milli-Q water.

The Pt NPs were also investigated after a 24-hour period in medium which showed a 20-40 nm increase of the diameter *(Figure 1)*. Furthermore, the PtNPs were investigated over a 24-hour period incubated with SK-OV-3 cells. Characterization showed that they all increased approximately 40 nm in average diameter *(Figure 1),*

In *Figure 1, Panel **A*** we observed a significant increase of Pt30 in 24 hours cells. It is significantly different from Milli-Q water (P = 0.005) and medium (P = 0.008). The interest is whether there is a difference between the diameter of the NPs when in 24 hours cells, and 24 hours medium. It appears that they are slightly larger, when in 24 hours cells, but it is not significant, however close, due to the low P-value (P = 0.094).

From the statistics, in *Panel **B** (Figure 1)* Pt50 showed a significant difference in medium (P = 0.023) compared to Milli-Q water. The Pt50 in 24 hours medium, showed being close to significant (P = 0.096) also compared to Milli-Q water.

Finally, in *Panel **C** (Figure 1)*, Pt70 in 24 hours cells showed to be significantly different from Milli-Q water (P = 0.009) and medium is significantly different from Milli-Q water as well (P = 0.000).

The Poly Dispersity Index (PDI) is a width parameter that gives information about the dispersity of the sizes *(Table 2)*.

From the statistical interpretation, we observed that Pt30 in Milli-Q water was significantly different to all conditions with a P value of 0.000. Pt50 in Milli-Q water showed a significant difference from medium (P = 0.000), and 24 hours medium (P = 0.029). Pt70 in Milli-Q water showed a significant difference from medium (P = 000.0) and also 24 hours medium (P = 0.001).

Table 2 *Dynamic light scattering (DLS) analysis of the different sized platinum nanoparticles (Pt NPs). The mean values of the Poly Dispersity Index (PDI) indicates the spread in the distribution of the Pt NP sizes in the different conditions.*

Pt NPs	**Solutions**			
	24h Cells (PDI)	**24h Medium (PDI)**	**Milli-Q water (PDI)**	**Medium (PDI)**
Pt30	0.52±0.02	0.51±0.01	0.23±0.04	0.5±0.002
Pt50	0.35±0.08	0.29±0.02	0.14±0.002	0.27±0.004
Pt70	0.32±0.11	0.23±0.01	0.08±0.008	0.21±0.007

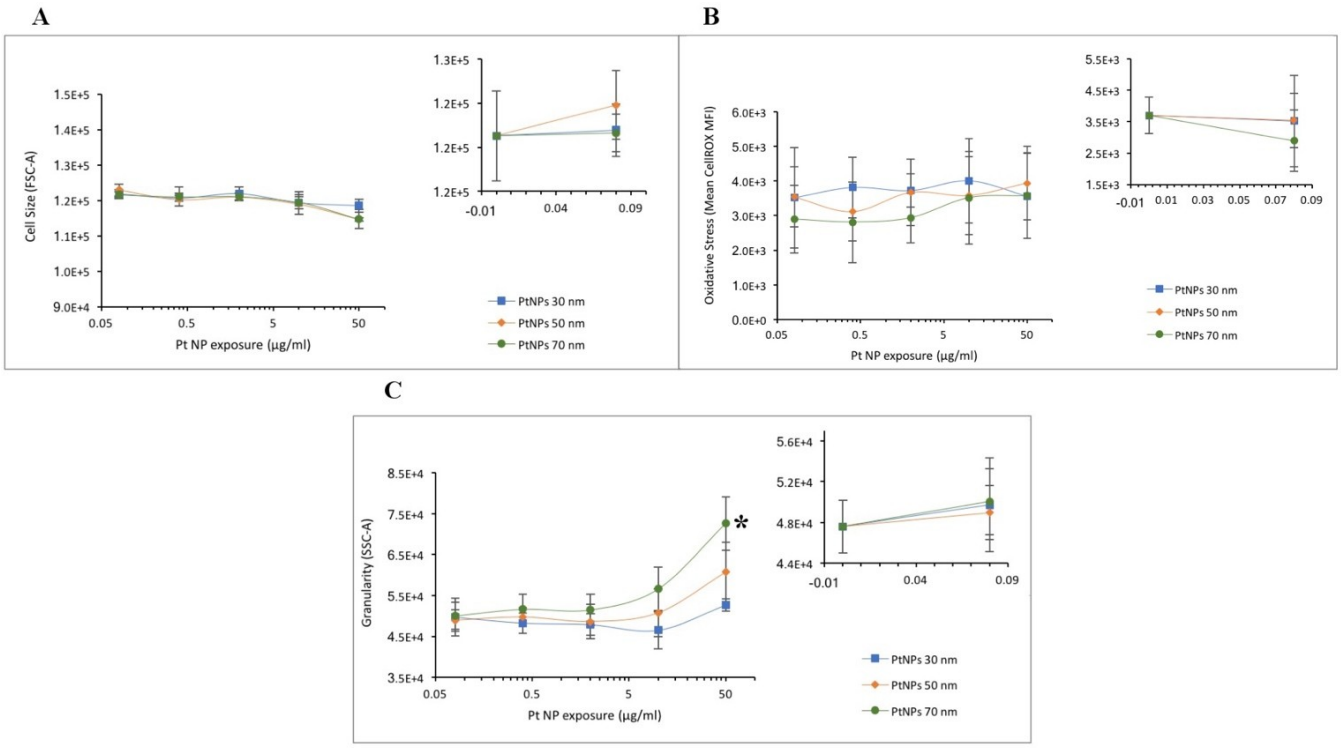

Figure 2 *Flow cytometric analysis of SK-OV-3 cells in different concentrations of platinum nanoparticles (Pt NPs). Panel* ***A*** *shows the size (FSC-A) of cells exposed to particles at different concentrations, 0.08, 0.4, 2, 10, 50 µg/ml. The window illustrates the SK-OV-3 cells with no particles and with 0.08 µg/ml. Panel* ***B*** *shows oxidative stress (CellROX) of cells exposed to particles at different concentrations, 0.08, 0.4, 2, 10, 50 µg/ml. The window illustrates the SK-OV-3 cells with no particles and with 0.08 µg/ml. Panel* ***C*** *shows the granularity (SSC-A) of cells exposed to particles at different concentrations, 0.08, 0.4, 2, 10, 50 µg/ml. The window illustrates the SK-OV-3 cells with no particles and with 0.08 µg/ml. * P < 0.000.*

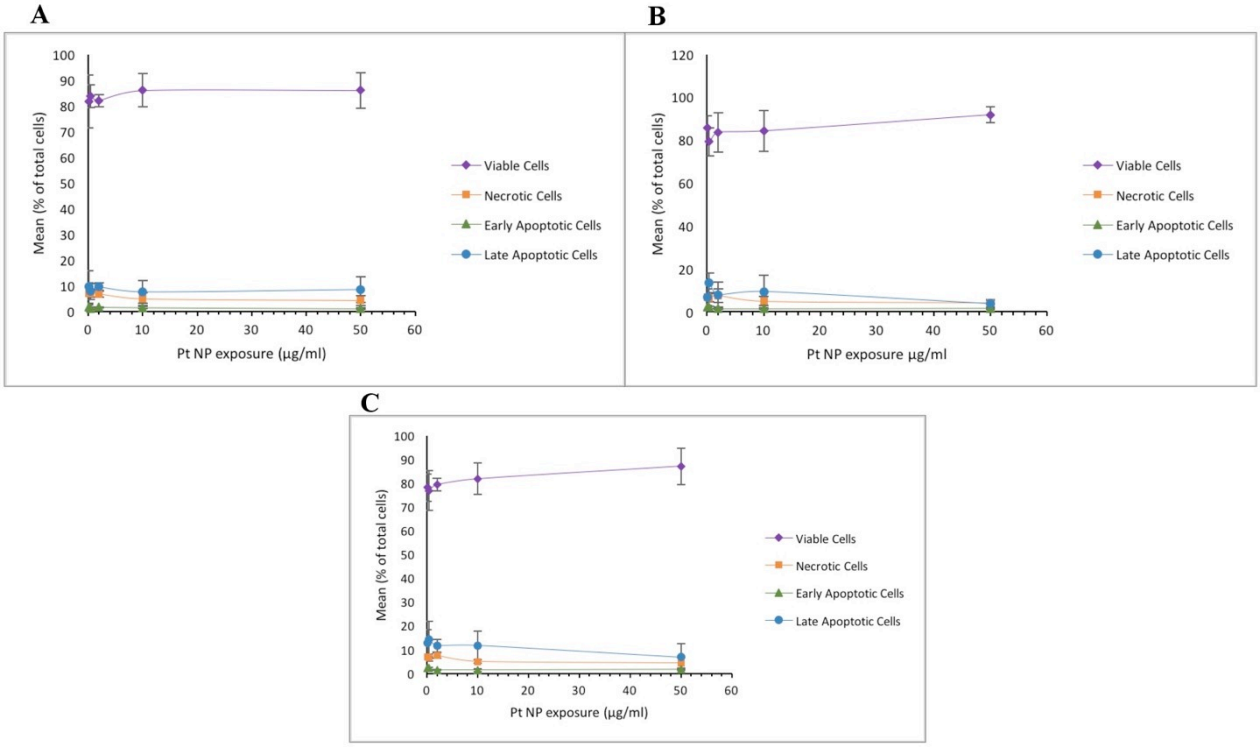

Figure 3 *Flow cytometric analysis of SK-OV-3 cells treated with Annexin V (Alexa Fluor 488®) and LIVE/DEAD™ stain. Cell death assay show the living and dead cells, respectively. The dead cells are divided into early apoptotic, late apoptotic, and necrotic. This applied when the cells were exposed to Pt30 (Panel* ***A****), Pt50 (Panel* ***B****), and finally Pt70 (Panel* ***C****).*

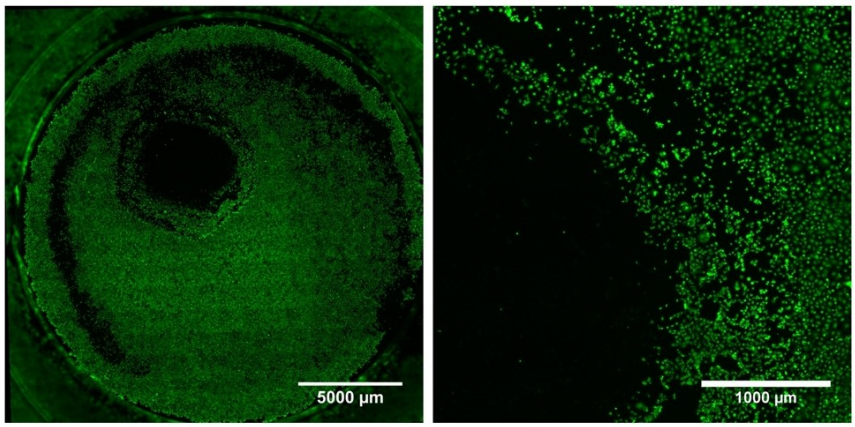

Figure 4 *Microscope images after laser treatment (808 nm, 45 W/cm^2, 5 min) of SK-OV-3 cells with Pt70 NPs.*

Measurement of PtNP-uptake, oxidative stress and cell death by flow cytometry

The SK-OV-3 cells were exposed to a concentration of 0-50 µg/ml of Pt30, Pt50, Pt70 for 24 hours *(Figure 2, panel **C**)*. We did not observe any significant increase of the cell granularity (SSC-A) before 10 µg/ml, for all Pt NP size. Only at 50 µg/ml we observed a significantly increase in granularity for cells exposed of 70 nm Pt NPs ($P < 0.000$). In comparison, there was not observed any significant change in cell size (FSC-A) for cells exposed and unexposed to Pt NPs *(Figure 2, panel **A**)*.

The CellROX measurement *(Figure 2, panel **B**)*, did not show any sign of oxidative stress in the cells when exposed to different concentrations (0, 0.08, 0.4, 2, 10, 50 µg/ml) of Pt NPs. The values were consistent which the statistical interpretation also indicates, no significant level of $P < 0.05$.

In the cell death assay *(Figure 3)*, there was no observed difference of all the parameters, viable cells, necrotic cells, early apoptotic cells, and late apoptotic cells. For cells after 24 hour exposure to all concentration of Pt30, Pt50, and Pt70, relative to cells not exposed to NPs. This was also observed in the statistical interpretation.

Laser treatment and microscopy image

The laser treatment analysis discloses that SK-OV-3 cells exposed to Pt NPs are demolished (killed) after five minutes of the laser treatment at 45W/cm^2 using an 808 nm laser. The laser power indicates how much energy is transferred to the cells. Observing the laser treatment with Pt NPs, cell death is observed – while the control sample, with cells and laser only, there is no observed cell death. Furthermore, the exposed laser area in the well showed a clear damage of the cells, this implies a high localized photothermal effect.

The controls without Pt NPs showed no cell damage after laser exposure, at different laser power densities from 5 to 45 W/cm^2. *(See Appendix, figure 7)*

The dark spot indicates photothermal destruction induced by Pt NPs. It can be verified that the cells died as a result of the laser radiation as the dark spot is measured to be 5000 µm, and the laser produces a homogenous 5 mm diameter beam, according to the laser manufacturer.

The laser treatment was repeated with all sizes of Pt NPs, but no photothermal effect was observed. This could either be due to a problem with particle exposure or the laser itself. The reason for the failed photothermal effect is still ongoing.

Discussion

The DLS data showed a pattern as all the hydrodynamic sizes increased from what the manufacturer stated. In Milli-Q water they are a lot smaller and so is the standard deviation, in comparison to when the Pt NPs are in 0 hour medium, 24 hours medium or 24 hours cell medium. When NPs are in biological fluid they associate with proteins[40]. The proteins adsorb to the surface of NPs, resulting in forming a protein layer around the NPs, this is termed the protein corona[41]. Other studies have also observed an increase in the hydrodynamic size of Au NPs due to a possible protein corona formation on the NP surface[8,12,42]. The formation of the protein corona is determined by factors as the NP surface chemistry, size, and charge[41]. The protein coronas compositions and molecular properties have shown to be important factors of the cellular uptake of NPs[41]. The fully interactions between NPs and proteins are yet to be further studied[40,41]. The results from flow cytometry, showed a concentration-dependent relationship between the exposure and cellular Pt NP-uptake in the SK-OV-3 cells for high concentrations of Pt NPs. Klingberg *et al.,*[8] had similar observations of a concentration-dependent increase in granularity[8]. The increase in the granularity indicates that there is an uptake of these particles by the cells, due to a greater reflection of increased complexity of the cells. It is easiest to see the uptake of the Pt70, as it is most significant. We cannot conclude from this, that Pt70 has the best uptake in the cells, this can be further examined by ICP-MS, as other studies have for other noble NPs[8,43]. The toxicity of NPs is an important concern, as it is crucial for the use in PTT. The effects of NPs on cellular health depends on the NPs size, shape and surface change[44]. Silver is referred to as the toxic NP[14,37–39], which is why we investigated if Pt NPs showed a toxicological response. The most researched NP are the Au NPs, they have been researched in various different sizes and shapes.

Some experimental works confirms that Au NPs are not toxic[44–46] yet other experiments and investigations revealed a toxicity of the particles[44,47,48]. Gold nanorods have been found to be toxic, however that is due to the synthesis of the rods, as they are usually stabilized in the surfactant cetyltrimethylammonium bromide (CTAB), unlike gold and Pt NPs that are usually stabilized with small molecules such as citrate. An interesting paper by Takahashi *et al.,*[49] investigated the cytotoxicity of gold nanorods to a human epitheloid cervix carcinoma (HeLa) cell line where they substituted the CTAB solution with phosphatidylcholine (PC) and the results showed a low cytotoxicity compared to the gold nanorods stabilized with CTAB[44,49].

We performed a cell death assay[34] to investigate whether the Pt NPs were toxic to SK-OV-3 cells. The assay did not show any difference in cell death due to exposure to particles. Even at high concentrations of Pt NPs, there were no difference in the amount of dead cells. This is an optimistic result as it confirms that the particles were not toxic to the cells. In comparison to our experiment, Villiers *et al.,*[44,50] investigated Au NPs incubated in dendritic cells, they found a non-toxic response of the Au NPs in the cells, even at high concentrations.

Oxidative stress in the cells were also examined and did not show any significant difference within the used concentrations when the particles were added to the cells, indicating no evidence of induced oxidative stress. From these experiments, we assume that the particles are not toxic for SK-OV-3 cells. Since there are no changes in cell death and oxidative stress despite the relatively high concentrations of particles, we would expect that the cells will not be damaged by the exposure of Pt NPs, and we will thus be able to continue with the cell experiments without worrying about inducing a toxicological effect with the particles alone.

In a work from Tedesco *et al.,*[51] they examined oxidative stress and cytotoxicity of Au NPs with a diameter of 5.3 nm, and their results showed that the small sized Au NPs caused oxidative stress and cytotoxicity significantly more, than other studies have for Au NPs of larger sizes[47,51]. This could give rise to think whether our experiment could have shown if the use of smaller Pt NPs sizes would have induced oxidative stress and toxicity, but we did not observe this for Pt30 compared to Pt50 or Pt70.

PTT has been proved to be an effective weapon against different cancer models. Nanoparticles in collaboration with the NIR laser have repeatedly managed to kill cancer cells[16,52,53].

Numerous studies, have experimented with different NPs, wavelengths and power densities. These studies all have in common that they succeed to kill the irradiated cells with NPs. El-Sayed *et al.,*[54] demonstrated the efficiency of gold nanospheres as a photothermal agent in vitro to two oral squamous carcinoma cells (HOC and HSC) and one epithelial cell line (HaCaT) that overexpresses EGFR, a cancer biomarker. The laser used for their experiments operated at 514 nm, and the used power densities were 19, 25, 38, 50, 64, and 76 W/cm^2, respectively, to irradiate cells for 4 minutes. The cells were irradiated at a power density of 76 W/cm^2 in the absence of NPs, it was here observed that no cell death had occurred. They demonstrated that HaCaT cells after incubation with anti-EGPR antibody conjugated Au NPs showed the photothermal effect with the laser density of 57 W/cm^2 or above. The HSC cells showed cell death when exposed to a laser density of 25 W/cm^2, whilst at 19 W/cm^2 and lower laser densities, no cell death was observed. Laser treatment of HOC cells showed cell death at a much lower laser density at 19 W/cm^2, whilst at 13 W/cm^2 and lower laser densities, no cell death was observed. In conclusion, they state that for clinical application of cancer treatment on tissue, a NIR laser light is needed, preferably between 650 and 900 nm that can penetrate in larger depths[54]. Later El-Sayed *et al.,*[16] upgraded their experiments and worked with gold nanorods at higher wavelength due to the earlier mentioned biological window. They now operated at 800 nm. They irradiated the cells at different power densities for 4 minutes each. Their results showed that the HOC and HSC cells were injured at 10 W/cm^2. HaCaT cells were injured at 15 W/cm^2 and died when exposed to 20 W/cm^2 and above at 800 nm[16]. These results and findings indicate that there could be a correlation between the laser wavelength and power. Bernardi *et al.*[52] demonstrated the use of gold-silica nanoshells (immunonanoshells), their reasoning of using nanoshells is due to their extremely efficient absorption of NIR, and their great converting abilities to generate laser light into heat to kill cancer cells. In this study, they demonstrated the use of a laser at 800 nm and 80 W/cm^2 for 2 minutes in medulloblastoma cell line (Daoy.2)[52]. Their results describe that the strategy used can selectively kill cells that express the HER-2 gene without killing cells that do not express the gene. This is due to Bernardi *et al.,* modified the used gold-silica nanoshells to be incorporated into HER-2 positive cells (antibody), but they are not taken up by other cells due to polyethylene glycol (PEG)[52].

In El Sayed *et al.,*[54] study, we found that when using a laser at lower wavelength (514 nm), they used higher power densities for the HaCaT cells (57 W/cm^2), to observe destruction[54], whilst we observed destruction at laser density at 45 W/cm^2 for SK-OV-3 cells. Both in the presence of NPs. The other two cell lines they irradiated already showed cell death at 25 W/cm^2 and 19 W/cm^2. Comparing these results to the later study of El Sayed *et al.,*[16] where they used a higher laser wavelength (800 nm), here they observed cell death at lower power densities than in their previous study[54]. This could indicate that some cell lines are more susceptible to laser treatment and can thus be destroyed by lower laser power densities. In the absence of NPs our experiment did not show cell death at 45 W/cm^2 when using an 808 nm laser. El Sayed *et al.*,[54] made a similar control experiment without NPs in their cells, neither of them were injured even at a high power density (76 W/cm^2). These observations are surprisingly at these laser power densities compared to other studies with example SK-BR-3 cells and Au NSs (820 nm, 35 W/cm^2 for 7 min)[53]. Another interesting work of Van de Broek *et al.,*[29] where they used branched gold nanoparticles biofunctionalized with antibodies as potential photothermal therapy agents in SK-OV-3 cells, they observe cell destruction after laser treatment (690 nm) at 38 W/cm^2 for 5 minutes[29]. This observation by Van de Broek *et al.,* is in accordance with what we also observed for the same type of cells.

All these different studies, implies that the experiments also depend on the cell type, as some cells could be more resilient to treatment. They all have in common that they manage to induce a photothermal effect in different cell lines. PTT has many factors that take part in whether the experiment is successful or not, for

example the use of different laser wavelengths, power densities, cell lines and most importantly, the particles used in the experiment could give changes in the outcome.

In conclusion, our experiment and results showed that cellular uptake of the Pt NP was efficient. Furthermore, we observed that the Pt NP uptake did not lead to a toxicological response, and no level of stress was induced in the SK-OV-3 cells, at the given concentrations. Finally, the laser treatment with a wavelength of 808 nm at 45 W/cm^2 for 5 minutes, demonstrated that we were able to perform a photothermal effect in the SK-OV-3 cells in presence of 70 nm Pt NPs, whilst cells in the absence of Pt NPs were not harmed using the same laser treatment.

Further work

In further work, we could take advantage of SK-OV-3 cells that have a high surface expression of the protein HER-2, which is a protein found in certain forms of cancer. HER-2 is highly expressed in SK-OV-3 cells so it is easy to target them.
We chose a cell type that could be used in further work to make a regressive tumour model in nude mice.
The use of NPs for cancer treatment still has a lot of work ahead, and the investigation of whether cells die from the laser treatment or from the NPs, and in that case, which wavelength and power density are most ideal? The next step could be to further develop Pt NPs so they can work more efficiently and at lower dose.

Acknowledgements

Special thanks, to our supervisor Postdoc Henrik Klingberg, for supporting, helping and guiding us through this bachelor project over this period. We would also like to thank Associate Professor Poul Martin Bendix for introducing us to the Optical Tweezers Group, and Professor, PI of Optical Tweezers Group, Lene B. Oddershede for introducing us to the project.
This project was part of Laser activated nanoparticles for tumor elimination (LANTERN) funded by Novo Nordisk Foundation Interdisciplinary Synergy Programme. We would like to thank Professor Andreas Kjær, cluster for molecular imaging a LANTERN partner for the use the flow cytometer.
Lastly, we would like to thank all the group members of the Optical Tweezers Group for their welcomeness and company over this period.

Address: Nano-Science Center & XXXXXXXXX, University of Copenhagen, Universitetsparken 5, 2100 København Ø, Denmark.; E-mail: svg537@alumni.ku.dk and xnq328@alumni.ku.dk

References

1. Porcel, E. *et al.* Platinum nanoparticles: a promising material for future cancer therapy? *Nanotechnology* **21,** 85103 (2010).
2. Ferrari, M. Nanoncology. *Tumori* **94,** 197–199 (2008).
3. Manikandan, M., Hasan, N. & Wu, H. F. Platinum nanoparticles for the photothermal treatment of Neuro 2A cancer cells. *Biomaterials* **34,** 5833–5842 (2013).
4. Huang, X. & El-Sayed, M. A. Gold nanoparticles: Optical properties and implementations in cancer diagnosis and photothermal therapy. *J. Adv. Res.* **1,** 13–28 (2010).
5. Jørgensen, J. T. *et al.* Single Particle and PET-based Platform for Identifying Optimal Plasmonic Nano-Heaters for Photothermal Cancer Therapy. *Sci. Rep.* **6,** 30076 (2016).
6. Jain, P. K., Lee, K. S., El-Sayed, I. H. & El-Sayed, M. A. Calculated absorption and scattering properties of gold nanoparticles of different size, shape, and composition: Applications in biological imaging and biomedicine. *J. Phys. Chem. B* **110,** 7238–7248 (2006).
7. Loo, C., Lowery, A., Halas, N., West, J. & Drezek, R. Immunotargeted nanoshells for integrated cancer imaging and therapy. *Nano Lett.* **5,** 709–711 (2005).
8. Klingberg, H. *et al.* Uptake of gold nanoparticles in primary human endothelial cells. *Toxicol. Res.* **4,** 655–666 (2015).
9. Agilent | UV-Vis-NIR Spectroscopy Tutorial. Available at: http://www.agilent.com/en-us/products/uv-vis-uv-vis-nir/tutorial. (Accessed: 28th April 2017)
10. Martin, G. & Pretzel, B. UV-VIS-NIR spectroscopy: what is it & what does it do? - Victoria and Albert Museum. (1991). Available at: http://www.vam.ac.uk/content/journals/conservation-journal/issue-01/uv-vis-nir-spectrocopy-what-is-it-and-what-does-it-do/. (Accessed: 29th May 2017)
11. Albanese, A. *et al.* Secreted biomolecules alter the biological identity and cellular interactions of nanoparticles. *ACS Nano* **8,** 5515–5526 (2014).
12. Brun, E. & Sicard – Roselli, C. Could nanoparticle corona characterization help for biological consequence prediction? *Cancer Nanotechnol.* **5,** 7 (2014).
13. Malvern. Dynamic Light Scattering Common Terms Defined. 6 (2011). Available at: https://www.malvern.com/en/support/resource-center/Whitepapers/WP111214DLSTermsDefined.html. (Accessed: 28th April 2017)
14. Konieczny, P. *et al.* Effects triggered by platinum nanoparticles on primary keratinocytes. *Int. J. Nanomedicine* **8,** 3963–3975 (2013).
15. Stepanov AL, Golubev AN, N. S. Synthesis and Applications of Platinum Nanoparticles : A Review. *Nanotechnology* **2,** 173–199 (2013).
16. Huang, X., El-sayed, I. H., Qian, W. & El-sayed, M. A. Cancer Cell Imaging and Photothermal Therapy in the Near-Infrared Region by Using Gold Nanorods Cancer Cell Imaging and Photothermal Therapy in the Near-Infrared Region by Using Gold Nanorods. 2115–2120 (2006). doi:10.1021/ja057254a
17. Kyrsting, A., Bendix, P. M., Stamou, D. G. & Oddershede, L. B. Heat profiling of three-dimensionally optically trapped gold nanoparticles using vesicle cargo release. *Nano Lett.* **11,** 888–892 (2011).
18. Huang, X., Jain, P. K., El-Sayed, I. H. & El-Sayed, M. A. Plasmonic photothermal therapy (PPTT) using gold nanoparticles. *Lasers Med. Sci.* **23,** 217–228 (2008).
19. Wang, C. *et al.* Trifolium-like Platinum Nanoparticle-

Mediated Photothermal Therapy Inhibits Tumor Growth and Osteolysis in a Bone Metastasis Model. *Small* **11,** 2080–2086 (2015).
20. Elmore, S. Apoptosis: A Review of Programmed Cell Death. *Toxicol. Pathol.* **35,** 495–516 (2007).
21. Annexin V Conjugates for Apoptosis Detection. (2011). Available at: https://tools.thermofisher.com/content/sfs/manuals/mp13199.pdf. (Accessed: 13th May 2017)
22. Fink, S. L., Cookson, B. T., Fink, S. L. & Cookson, B. T. Eukaryotic Cells MINIREVIEW Apoptosis , Pyroptosis , and Necrosis : Mechanistic Description of Dead and Dying Eukaryotic Cells. *Infect. Immun.* **73,** 1907–1916 (2005).
23. Engeland, M. van, Nieland, Luc, J., W., Ramaekers, Frans C., S., Schutte, B. & Reutelingsperger, Chris, P., M. Annexin V-Affinity Assay: A Review on an Apoptosis Detection System Based on Phosphatidylserine Exposure. *Wiley-Liss, Inc* **31,** 1–9 (1998).
24. Vermes, I., Haanen, C., Steffens-Nakken, H. & Reutellingsperger, C. A novel assay for apoptosis Flow cytometric detection of phosphatidylserine expression on early apoptotic cells using fluorescein labelled Annexin V. *J. Immunol. Methods* **184,** 39–51 (1995).
25. Edinger, A. L. & Thompson, C. B. Death by design: Apoptosis, necrosis and autophagy. *Curr. Opin. Cell Biol.* **16,** 663–669 (2004).
26. Golstein, P. & Kroemer, G. Cell death by necrosis: towards a molecular definition. *Trends Biochem. Sci.* **32,** 37–43 (2007).
27. Proskuryakov, S. Y., Konoplyannikov, A. G. & Gabai, V. L. Necrosis: A specific form of programmed cell death? *Exp. Cell Res.* **283,** 1–16 (2003).
28. Fisher Scientific, T. LIVE/DEAD Fixable Dead Cell Stain Kits. Available at: https://tools.thermofisher.com/content/sfs/manuals/MAN0010989_LIVE_DEAD_Fixable_Dead_Cell_Stain_Kits_UG.pdf. (Accessed: 3rd May 2017)
29. Broek, B. Van De, Devoogdt, N., Hollander, A. D., Gijs, H. & Jans, K. Specific Cell Targeting with Nanobody Conjugated Branched Gold Nanoparticles for Photothermal Therapy. *ACS Nano* **5,** 4319–4328 (2011).
30. Schieber, M. & Chandel, N. S. ROS function in redox signaling and oxidative stress. *Curr. Biol.* **24,** R453–R462 (2014).
31. CellROX® Oxidative Stress Reagents. (2012). Available at: https://tools.thermofisher.com/content/sfs/manuals/mp10422.pdf. (Accessed: 3rd May 2017)
32. CellROX Deep Red Reagent, for oxidative stress detection - Thermo Fisher Scientific. Available at: https://www.thermofisher.com/order/catalog/product/C10422. (Accessed: 3rd May 2017)
33. Ormerod, M. G. *Flow Cytometry - A Basic Introduction*. (De Novo, 2008). Chapter 1-4, 7, 9.
34. Adan, A., Alizada, G., Kiraz, Y., Baran, Y. & Nalbant, A. Flow cytometry: basic principles and applications. *Crit. Rev. Biotechnol.* **37,** 163–176 (2017).
35. Brown, M. & Wittwer, C. Flow Cytometry: Principles and Clinical Applications in Hematology. *Clin. Chem.* **46,** 1221–1229 (2000).
36. Gutierrez, C. & Schiff, R. HER 2: Biology, Detection, and Clinical Implications. *Arch. Pathol.* **135,** 55–62 (2011).
37. Ravindran, A., Chandran, P. & Khan, S. S. Biofunctionalized silver nanoparticles: Advances and prospects. *Colloids Surfaces B Biointerfaces* **105,** 342–352 (2013).
38. Yamada, M., Foote, M. & Prow, T. W. Therapeutic gold, silver, and platinum nanoparticles. *Wiley Interdiscip. Rev. Nanomedicine Nanobiotechnology* **7,** 428–445 (2015).
39. Braydich-Stolle, L., Hussain, S., Schlager, J. J. & Hofmann, M. C. In vitro cytotoxicity of nanoparticles in mammalian germline stem cells. *Toxicol. Sci.* **88,** 412–419 (2005).
40. Cedervall, T. *et al.* Understanding the nanoparticle-protein corona using methods to quantify exchange rates and affinities of proteins for nanoparticles. *Proc. Natl. Acad. Sci.* **104,** 2050–2055 (2007).
41. Treuel, L., Docter, D., Maskos, M. & Stauber, R. H. Protein corona - from molecular adsorption to physiological complexity. *Beilstein J. Nanotechnol.* **6,** 857–873 (2015).
42. Cheng, X. *et al.* Protein Corona Influences Cellular Uptake of Gold Nanoparticles by Phagocytic and Nonphagocytic Cells in a Size-Dependent Manner. *ACS Appl. Mater. Interfaces* **7,** 20568–20575 (2015).
43. Mitrano, D. M. *et al.* Silver nanoparticle characterization using single particle ICP-MS (SP-ICP-MS) and asymmetrical flow field flow fractionation ICP-MS (AF4-ICP-MS). *J. Anal. At. Spectrom.* **27,** 1131 (2012).
44. Fratoddi, I., Venditti, I., Cametti, C. & Russo, M. V. How toxic are gold nanoparticles? The state-of-the-art. *Nano Res.* **8,** 1771–1799 (2015).
45. Dobrovolskaia, M. A. & McNeil, S. E. Immunological properties of engineered nanomaterials. *Nat. Nanotechnol.* **2,** 469–478 (2007).
46. Patra, H. K., Banerjee, S., Chaudhuri, U., Lahiri, P. & Dasgupta, A. K. Cell selective response to gold nanoparticles. *Nanomedicine Nanotechnology, Biol. Med.* **3,** 111–119 (2007).
47. Pan, Y. *et al.* Size-dependent cytotoxicity of gold nanoparticles. *Small* **3,** 1941–1949 (2007).
48. Zhang, X. D. *et al.* Irradiation stability and cytotoxicity of gold nanoparticles for radiotherapy. *Int. J. Nanomedicine* **4,** 165–173 (2009).
49. Takahashi, H. *et al.* Modification of gold nanorods using phosphatidylcholine to reduce cytotoxicity. *Langmuir* **22,** 2–5 (2006).
50. Villiers, C., Freitas, H., Couderc, R., Villiers, M.-B. &

Marche, P. Analysis of the toxicity of gold nano particles on the immune system: effect on dendritic cell functions. *J. Nanopart. Res.* **12,** 55–60 (2010).
51. Tedesco, S., Doyle, H., Blasco, J., Redmond, G. & Sheehan, D. Oxidative stress and toxicity of gold nanoparticles in Mytilus edulis. *Aquat. Toxicol.* **100,** 178–186 (2010).
52. Bernardi, R. J., Lowery, A. R., Thompson, P. A., Blaney, S. M. & West, J. L. Immunonanoshells for targeted photothermal ablation in medulloblastoma and glioma: An in vitro evaluation using human cell lines. *J. Neurooncol.* **86,** 165–172 (2008).
53. Hirsch, L. R. *et al.* Nanoshell-mediated near-infrared thermal therapy of tumors under magnetic resonance guidance. *Proc. Natl. Acad. Sci.* **100,** 13549–13554 (2003).
54. El-Sayed, I. H., Huang, X. & El-Sayed, M. A. Selective laser photo-thermal therapy of epithelial carcinoma using anti-EGFR antibody conjugated gold nanoparticles. *Cancer Lett.* **239,** 129–135 (2006).

UCPH NanoScience
NanoVidenskab KU

tidsskrift.dk/index.php/NanoVidenskabKU

Report

Synthesis and characterization of $CuCrO_2$ delafossite nanoplatelets through Rietveld refinement and Pair distribution function analysis

Emil Thyge Skaaning Kjær

Received June 2017, Accepted April 2018

Delafossite (ABO_2) nanostructures such as $CuCrO_2$ nanoparticles have shown promising properties in dye-sensitized solar cells (DSSCs). Previous studies have shown that changing the metal on either the A or B site in the structure, influences both the conditions required to synthesize delafossite compounds, their properties, and their tendency of forming nanocrystals or bulk particles. The crystallites can further be doped changing the conductivity further. Here, we present a series of syntheses with varying parameters, illustrating how the conditions must be optimized to obtain the pure delafossite $CuCrO_2$ phase. Structure characterization was done through Powder X-ray Diffraction (PXRD) showing change in crystallite size with increasing synthesis time and temperature. By varying both temperature and time, the amount of secondary phase (CuO) in the final product can be minimized. It was only possible to synthesize pure delafossite when certain criteria regarding pH, temperature and time were met. Rietveld refinement of the PXRD data showed anisotropic nanocrystallites with approximate sizes of 130x130x40Å with the trigonal delafossite unit cell. However, the crystallites are too small and anisotropic to give a satisfying fit using conventional Rietveld refinement, and the sizes were obtained through anisotropic "no rules" model. Pair Distribution Function (PDF) analysis of X-ray total scattering data were used to obtain further understanding of structural disorder in the crystallites.

Introduction

Delafossite crystals have over the last years received a large amount of attention because of their p-type electrical conductivity and low fabrication cost.[1,2] A large diversity of delafossite compositions have been synthesized with different metals on the A and B sites, A = Ag or Cu, B = B, Al, Ga, In, Fe, Cr, Sc, Y, etc. all having high p-type conductivity.[3] Delafossite materials have many different applications, such as in transparent conducting oxides, luminescent materials, catalysts, batteries, ferroelectrics, etc.[4] Especially $CuAlO_2$, $CuGaO_2$, $CuCrO_2$ and $AgCrO_2$ show promising properties as dye-sensitized solar cells (DSSCs) because of their p-type conductivity.[3]

Delafossite is an ABO_2 structure with a transition metal at the A site and a transition or post-transition metal at the B site. This study will only present delafossite structures with Cu at A site, and Cr or Fe on B site. Delafossite is a layered structure, with a Cu and a Cr/Fe layer, where oxygens are octahedrally coordinated around Cr/Fe. Cu is linear coordinated to two oxygens, Cu having an oxygen directly above and below it in the c-axis. It can exist in two different space groups R-3mH, trigonal, or P63/mmc, hexagonal. R-3mH has two additional Cu layer in the unit cell. Both unit cells are shown in Figure 1, A) R-3mH and B) P63/mmc.

To obtain pure delafossite compound phases, hydrothermal reactions at temperatures between 70°C-700°C are needed, depending on the metals on the A and B sites. Hydrothermal synthesis of phase pure $CuCrO_2$ or $CuFeO_2$ have been reported.[1, 5] $CuCrO_2$ form the R-3mH polymorph as nanocrystals at 240°C, and $CuFeO_2$ form both polymorphs but as bulk phase at 70°C.[5, 6]

This study will focus on the synthesis and characterization of $CuCrO_2$ nanoparticles through Rietveld refinement and PDF analysis, and will illustrate the difficulties in modelling highly anisotropic and disordered materials. Several approaches will be carried out trying to describe the structural composition of the delafossite crystallites.

Delafossite polymorphs

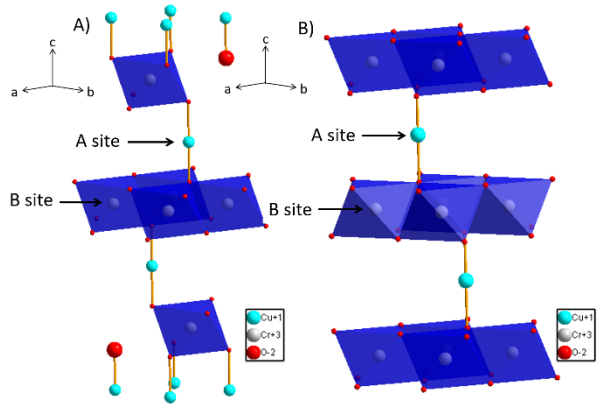

Figure 1. A) The R-3mH polymorph. Sides a = b = 2.974Å and c = 17.1Å. Angles α = β = 90° and γ = 120°. B) The P63/mmc polymorph. Sides a = b = 2.974Å and c = 11.4Å. Angles α = β = 90° and γ = 120°.

Multiple articles state different oxidation states for the same structures. A site stated as either +1 or +2 and B site +3 or +2.[4, 5] A proposal for a reaction mechanism and oxidation states of the metals will be stated, through considerations of the electrochemistry by Pourbaix analysis. See supporting information about Pourbaix diagrams. The synthesis and final product of $CuCrO_2$ will furthermore be compared to the one of $CuFeO_2$.

Theory

XRD and Rietveld Refinement

In a classical powder diffraction sample, a powder of small crystalline particles, all with random orientation, is radiated with a monochromatic X-ray beam. This beam, due to the periodic structural order of the crystal, is diffracted and a characteristic dataset is collected for that specific compound.

A diffraction peak arises when the X-ray beam interferes constructively with itself after diffraction, as described by Bragg.

$$2d \cdot \sin(\theta) = n \cdot \lambda$$

The distance between the planes, d, is measured with a wave having the wavelength λ. The angle between the incoming wave and the plane being θ. Data points are collected as intensities changing as a function of θ. Distances between the planes are related to the angle θ as seen in Bragg law. By relating distances within the unit cell to the angle, unique characteristics of a crystallite can be described with Bragg law, each crystallite having a unique diffraction pattern.

The intensity of a Bragg peak is proportional to the squared norm of the structure factor, $I \propto |F|^2$. The structure factor is given by the eq.

$$F = \sum_{i=1}^{Atom} f_i \cdot \exp\left(-B_i \cdot \frac{sin^2(\theta_h)}{\lambda^2}\right) \cdot \exp\left(2\pi i \vec{h} \vec{x_i}\right)$$

The structure factor sums over all atoms within the unit cell. X-ray scatters on electrons, and electron rich atoms scatter more as expressed by the atomic form factor, f_i. B_i is the Debye-Waller displacement factor. $\vec{h}$ is the Miller-indices for the reflection and $\vec{x_i}$ is the fractional coordinates for an atom within the unit cell.

Two things can cause broadening of Bragg peaks, either the instrument or the sample. Instrumental broadening arises from e.g. beam divergence and a spread in X-ray wavelength. Sample broadening is divided into two categories, strain and size broadening.

A crystal is described through an infinite translation of its unit cell, which gives rise to sharp Bragg peaks. Perfect crystals larger than c. 1μm can be described through an infinite translation of the unit cell. This is no longer the case working with nanocrystals, since the particles are only a few unit cell large. Scherrer eq. can through the width of the peaks estimate a size of the average crystallite.

$$D = \frac{K \cdot \lambda}{FWHM \cdot \cos(\theta)}$$

D being crystallite size, K shape factor, often set to 0.94, λ the wavelength of the incoming beam, full width at half maximum of a Bragg peak(FWHM) and the angle of the incoming beam, θ.

Strain broadening is caused by distortions in the crystal lattice. This results in different distances between two planes and thereby causes broadening. Bragg peak strain broadening varies proportional with tan(θ) and causes the effect to increase at higher angles. Strain and size broadening is weighted differently as a function of the scattering angle. Through the divergence in dependency of the angle the two can be distinguished from one another.

Rietveld refinement is a method where all the above, and much more, is taken into account when refining different parameters to fit a model to a dataset.[7] Different models can be used to describe the crystallites strain and size broadening, modelling the crystal as isotropic, a linear combination of symmetrized spherical harmonics(Popa-rules)[8] or an anisotropic "no rule model" where a combination of six vectors are used to describe the particle shape.

The Popa rule method describes the crystallites dimensions through an average of radius' starting from a sphere or an ellipsoid. A linear combination of symmetric harmonic functions is then refined to adjust the final shape of the particle. Each function depending on the Laue group of the crystal and anisotropy. More information about Popa-rules and anisotropic "no rule model" can be found in the supporting information.

Total Scattering and PDF

To make a PDF analysis, high Q space synchrotron data is needed, this requires a monochromatic high flux X-ray beam. Q space data can be Fourier transformed to gain structural information in real space. A broader spectrum of structural information is obtainable through PDF compared to Rietveld. An advantage of PDF is furthermore that the data allows separate analysis of local and global structural order.[9] By analysing the PDF under e.g. 10Å, it is possible to describe the local structure, and above 10Å the global structure. Deviations in model compared to measured data can be translated to errors in either the local or global structure.

I(Q) is the raw collected data. I(Q) contains both structural information, incoherent Compton scattering, scattering from the capillary etc. I(Q) is then corrected and normalized into the

structure function.

$$S(Q) = \frac{I(Q) - \langle f(Q)^2 \rangle + \langle f(Q) \rangle^2}{\langle f(Q) \rangle^2}$$

f(Q) being the form factor. S(Q) is the structure function. Because of the Debye-Waller factor the intensities die out with increasing Q. To get higher intensities at high Q, S(Q) is converted into F(Q).

$$F(Q) = Q[S(Q) - 1]$$

F(Q) is the reduced structure function which oscillates around zero and approach it with increasing Q. F(Q) is a function in reciprocal space but through Fourier transformation, it can be translated into real space distances, G(r).

$$G(r) = \frac{2}{\pi} \int_0^\infty F(Q) \sin(Qr)\, dQ$$

G(r) is directly comparable to real space due to its R(r) dependence.

$$G(r) = \frac{R(r)}{r} - 4\pi\rho_0$$

R(r) is the radial distribution function and real space distances, r is distances between atom within the sample and ρ_0 is the average number density of atoms.[10] Each peak indicates a distribution of distances within the sample. The formula for R(r) is.

$$R(r) = \sum_v \sum_\mu \frac{b_v b_\mu}{\langle b \rangle^2} \delta(r - r_{v\mu})$$

R(r) is described through a series of delta functions, $\delta(r - r_{v\mu})$. $r_{v\mu}$ is the magnitude of the separation of the atoms. The formula summing over all atoms, u and μ. The scattering factor of v and μ is multiplied and then divided with the squared mean scattering factor. $r_{v\mu}$ is the magnitude of the separation of the atoms.[10,11,12]

Experimental methods

Syntheses of $CuCrO_2$

The synthesis applied is based on the work by Xiong et al.[1] All chemicals were of >98% purity and was used without any further purification. 0.76g $Cu(NO_3)_2 \cdot 3H_2O$, 1.23g $Cr(NO_3)_3 \cdot 9H_2O$ and 0.71g NaOH were mixed into a total volume of 10ml using demineralized water as solvent. NaOH was used as a mineralizer and to increase the pH of the solution. The resulting suspension was stirred for about 20 minutes or until all powder was completely dissolved. The black/dark green solution was put into a 25ml Teflon-lined stainless steel autoclave. The autoclave was afterwards put into a preheated oven at 180-240°C for 24-120h. After heating, the autoclave was cooled for 1-2h at room temperature. The black precipitate was then washed 3 times with demineralized water, by centrifugation at 4500 rpm for 5-8minuttes. After centrifugation a black precipitate was seen in a yellow solution, and was washed until only a clear liquid plus the black precipitate was left. The final product was then dried for about 2 days in a fume hood.

All syntheses for $CuCrO_2$ delafossite and their different parameters can be seen in Table 1.

Table 1. $CrCuO_2$ experiments.

Experiment	Time [h]	Temperature [°C]
1	72	180
2	72	200
3	72	220
4	72	240
5	24	240
6	48	240
7	96	240
8	120	240

Parameter used in the synthesis making $CuCrO_2$. All syntheses are constant in NaOH and metal source concentration.

Syntheses of $CuFeO_2$

The synthesis applied is based on the work by John et al.[6] All chemicals were of >98% purity and was used without any further purification. 0.6g of $CuSO_4 \cdot 5H_2O$ was mixed with 15ml demineralized water in a 50ml Teflon-lined during magnetic stirring and heated to 70°C. After heating 0.66g of $Fe(SO_4) \cdot 7H_2O$ was added to the solution while kept at 70°C. When all powder was dissolved NaOH was slowly added until a pH of 11 was reached. While adding NaOH the temperature was measured to make sure it did not deviate more than a few degrees Celsius from 70°C. To determine the pH of the solution pH-paper was used. Afterwards the Teflon-lined was sealed in a stainless steel autoclave and put into a preheated oven at 70 °C. The solution was heated for 24h and the precipitate was washed and dried just as for CuCrO2.

XRD

XRD data were collected using a Bragg–Brentano setup using a $CuK_{\alpha 1}$(1.54Å) source on a BRUKER D8 Discover and a LYNXEYE detector. The CuK_α wavelength corresponds to the excitation energy for Fe causing it to fluoresce. The fluorescence will add background noise, and when obtaining data from the $CuFeO_2$ the lower and upper energy discriminators of the detector are therefore narrowed from 0.11V-0.25V to 0.19V-0.27V. All data were collected from 5-90θ with a step size of 0.005h and collected for 5h. To absorb the CuK_β radiation a nickel filter was used.

PDF

All PDF data were collected at Deutsches Elektronen-Synchrotron(DESY), beamline P02.1. The x-ray wavelength was determined to be 0.20717Å. CeO_2 was used as standard. All measurements were done at room temperature and all samples were loaded in 1mm kapton capillaries. A 2D Perkin-Elmer amorphous silicon detector were used.

Results and Discussion

$CuCrO_2$ synthesis and characterization

Figure 2 shows the PXRD data obtained for the $CuCrO_2$ samples. The data sets show both sharp and broad peaks. The sharps peaks indicating the presence of highly crystalline particles. These peaks can be assigned to CuO. While the broad peaks can be assigned to the delafossite structure in space group R-3mH. Two sets of syntheses were made, one changing the temperature and

one varying time heated.

At Figure 2 A) only one of the dataset have no sharp peaks, this indicating the absence of the CuO phase. The data from samples synthesized at 24h, 48h, 96h and 120h looks remarkably similar. It would appear that forming $CuCrO_2$ and CuO at these temperatures are equally favourable. The CuO phase simply disappear at 72h. This indicates how dependent $CuCrO_2$ nanocrystals are of the chemical environment. The sample at 72h have been reproduced to verify the absence of CuO. If the heating is continued beyond 72h the CuO phase reappears.

B) shows a clear change in the ratio between the two phases. At 180°C the intensities between the CuO and $CuCrO_2$ phases are large. This is seen by comparing the sharp CuO peaks with the broad $CuCrO_2$ peaks. As the temperature increases the ratio between the $CuCrO_2$ and CuO phase change. This indicates that an increase in temperature makes the delafossite formation more favourable than CuO.

In both A) and B) there are only indications of one of the two polymorphs of $CuCrO_2$, namely the R-3mH polymorph. This does not agree with the results of Xiong et al[1] who obtained both polymorphs at 240°C heated for 60h, while PXRD from this article only indicates the presence of the P63/mmc polymorph.

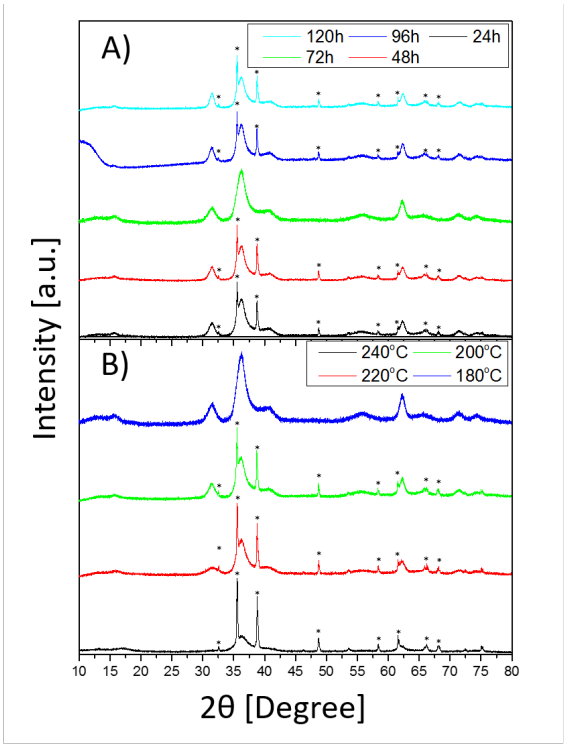

PXRD-data, time and temperature

Figure 2. A) shows PXRD data from the samples varying in time. The one obtained at 96h has a broad peak at low angle caused be bad calibration of the instrument. B) shows PXRD data from syntheses at different temperatures. Indication of CuO as marked with *.

To obtain more structural information about the pure delafossite phase, synthesised for 72h at 240°C, multiple Rietveld refinements were made. First an isotropic model assuming spherical crystallite sizes was fitted to the data from the $CuCrO_2$ nanoparticles. As seen in Figure 3 A) multiple peaks are not well describe through this model, [0 1 4], [0 1 8] and [0 0 12] reflections. The model furthermore does not describe the peak broadening. This indicates that the broadening cannot be described through an isotropic model, therefore the intensities of the peaks are increased trying to fit the broadening. by modelling the particles as a sphere too much intensity is obtained. The [1 1 0] indicates the exact opposite since the intensity is lower than measured. This could indicate presence of anisotropic particles and is therefore not able to fit all peak intensities. All peak having to high intensity is a reflection having a high l value compared to h and k. By modelling a crystallite being shortened at the l direction, the intensities will drop at these reflections. This corresponds to the [1 1 0] being too low in intensity. By prolonging the crystallite in the h and k directions the intensity of the peak will amplify. Broadening of the peaks causes the intensities to be spread over larger angles, and thereby decreasing the height of the peaks.

B) Is modelled using Popa-rules. With Popa-rules a linear combination of symmetrized spherical harmonics is refined trying to describe the particle size and shape. By describing the particle shape with four parameters the fit has improved significantly. Popa rules are described further in supporting information. The [0 1 4], [0 1 8] and [1 1 0] reflection now match the intensities of the measured data. Only the fit of the [0 1 8] reflection seem to have deteriorated. Figure 4 shows the particle shape modelled with Popa-rules. The modelled particle shape is highly unphysical, but it helps indicating a possible average shape for the particles. The most likely shape for $CuCrO_2$ to form would be platelets. The idea that $CuCrO_2$ crystalizes as platelets match the deviation in peak broadening when using an isotropic model. A better fit is possible by adding more parameters in the Popa-rules. This would also change the shape of the average crystallite and quite possible make an even more unphysical shape.

To get a more physical crystallite shape anisotropic “no rule refinement” was used. The refinement is shown in Figure 3 C). To model the platelet, the size along three vectors were refined, 11, 22 and 33 vector. The 11 and 22 vectors are formed by translation of the trigonal unit cell along the a and b axis, see Figure 1. The 11 and 22 vector forms the plane of the platelet and 33 the size along c, i.e. gives information about the number of layers stacked. The sizes along 11 and 22 are set to be equal each other, as a and b are equal in the trigonal unit cell.

Rietveld refinements of pure $CuCrO_2$

Figure 3. A) Is modelled as isotropic spherical particles. B) Is modelled with Popa-rules and C) with anisotropic "no rules model". Above each peak the reflection is written.

The largest difference in using the Popa-rules model and the anisotropy no rules model is the intensity of the [0 1 8]. While using Popa-rules the intensity of the [0 1 8] reflection is not fitted.

$CuCrO_2$ is a layered structure and translation along the a and b direction would form a platelet. Distortion between the layers could cause the thickness of the platelet to differ causing strain broadening.

Table 2. Weighted R-factor

Model	R_{wp} [%]
Isotropic, spherical	5.3284
Popa-rules	4.4448
Anisotropic no rules, platelet	4.3889

The table compares different models R_{wp} values.

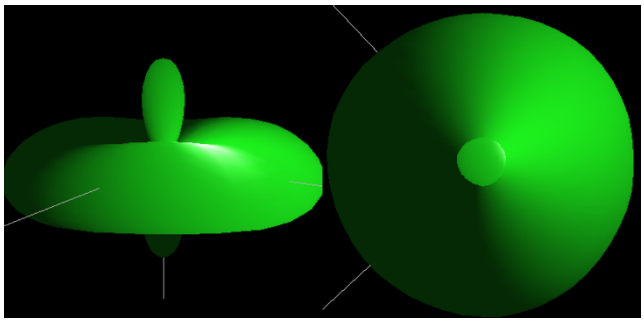

Popa-rules particle model

Figure 4. Shows a model of the particle obtained through Popa-rules. The model is platelet shaped in the x-y plane but have a p-orbital shape along the z-axis.

All models described above are fitting the [0 0 6] reflection width, intensity and position, but all are having problems fitting the [0 0 3] reflection at lower 2θ values. This indicates that the large anisotropy of the particles means that conventional Scherrer analysis cannot be used. Applying Scherrers several assumptions were made, one of them being that a crystal can be described as a sphere. Making Rietveld refinement on nanoparticles makes the infinite translation assumption invalid, and the correlation between the broadening of the peaks and the size of the crystallite unable to be described by Scherrers eq.[13]

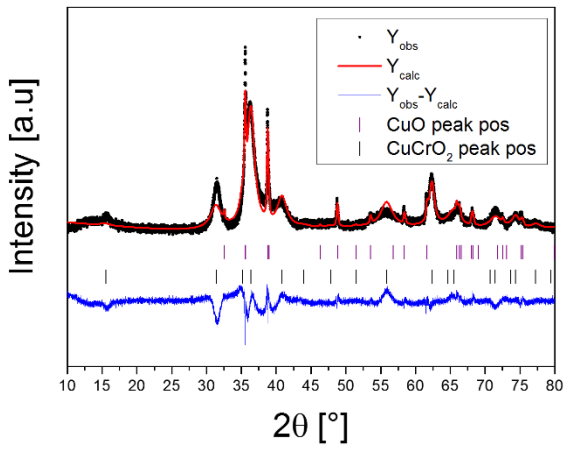

Rietveld refinement on multiple phases

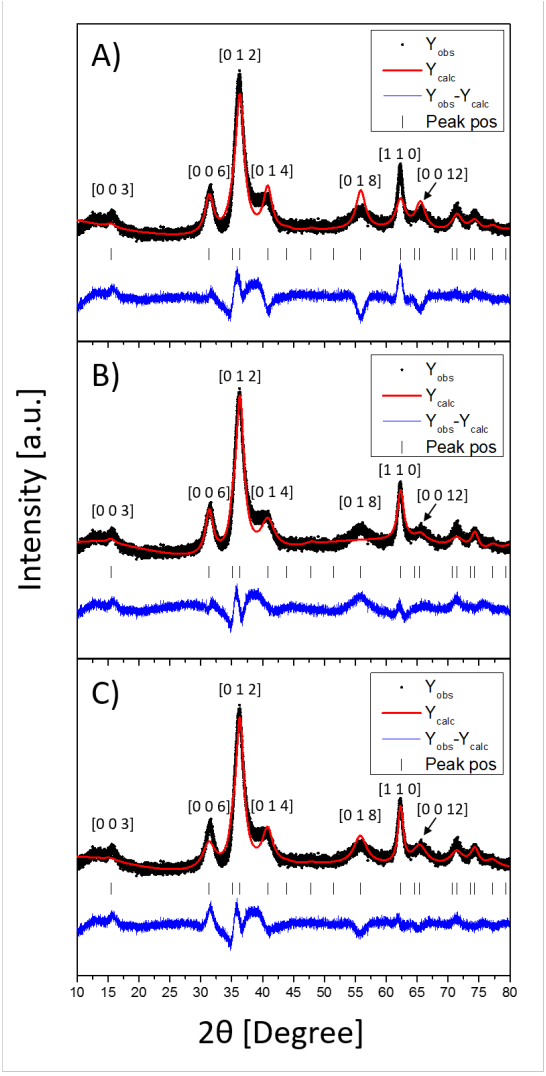

Figure 5. Rietveld refinement of multiple phases on 24h.

To get a better understanding on how the change in parameters affect the final product, Rietveld refinements of the $CuCrO_2$ and CuO phase were made. CuO being modelled as isotropic crystallites. All data, shown in Figure 2, have been refined and through Rietveld refinement sizes and phase ratios were obtained. Refinements for $CuCrO_2$ were done using anisotropic "no rule" model. Figure 6 shows the changes in size and ratio between the phases. The crystallite size along a and c only varies about 2nm no matter the synthesis parameters. The only outlier is 96h, this could be caused by the bad data. The sizes obtained through Rietveld refinement is only an average of the scattering crystallite, and not the definite particle size. It is therefore not possible to conclusive say anything about the whole particle, but only the crystalline part of it. Other methods have to be used to determine the definite size of the particle e.g. transmission electron microscopy(TEM).

Figure 6 C) and D) show the ratio between the two phases. When having time as varying parameter, all samples except 72h have a CuO/$CuCrO_2$ ratio about 1:1. It is interesting to notice that the ratio almost does not change from 24h to 48h, but from 48h to

72h the delafossite structure is so favourable that no CuO is synthesized. Further increase in time shifts this equilibrium back to a 1:1 ratio between the phases. In some extent D) shows the same tendency. Increasing the temperature by 20°C changes the percentage between the phases with approximately 2%. This continuously happens until 240°C. Here the equilibrium gets pushed sufficiently in favour of $CuCrO_2$ and the product is 100% delafossite. The synthesis producing pure $CuCrO_2$ have been reproduced.

Phase ratio and size distribution

Figure 6. A) and B) showing the sizes along A and B in nm. C) and D) shows the percentage of the two phases present. A) and C) being the syntheses with time as changing parameter, B) and D) temperature. Data is received through anisotropic no rules model.

To understand why the gap of synthesizing $CuCrO_2$ delafossite is so narrow a further analysis at the reaction must be done. In older literature, the oxidation states of the metals (Cu and Cr) in the delafossite structure are only vaguely described. Both Cu(II) with Cr(II) or Cu(I) with Cr(III) are being used.[14] Previous studies have shown that $CuCrO_2$ only forms at elevated pH value.[15] In the reaction used here, Cu(II) is added in the form of $Cu(NO_3)_2{\cdot}3H_2O$. The reaction is strongly pH dependent, if the pH is not high enough no delafossite is formed. This could indicate that Cu(II) needs to be reduced to Cu(I) for the reaction to take place, as this will only happen at high pH values. This is supported by the Pourbaix diagram for Cu, which can be found in supporting information. When looking at the diagram it is seen that the region where Cu(I) is stable is very narrow. Comparing the Pourbaix diagram for Cr and Cu, it shows that the zones where Cu(I) and Cr(III) are stable overlap. Pourbaix diagram for Cr can be found in supporting information.

The stability of the Cr^{3+} ion can be understood through metal-ligand interactions. Cr is coordinated octahedrally to oxygen. All of Cr ligands feel the same environment so they bind equally strong to Cr. This is supported both by the crystallography file and others research for $CuCrO_2$.[2, 16] This conformation makes the classic octahedral orbital splitting, having three orbitals being equally low in energy and two equally high in energy. Cr(III) is especially favourable in octahedral conformation since it can put one electron into each of the low energy levelled orbitals. This leaves a big energy gap between HOMO and LUMO. Each orbital is coordinated perpendicular to each other, causing the electrons to not repel each other. Oxygen coordinates to three Cr and one Cu, while Cu coordinates to two oxygens. Oxygen having a coordination number of 4 and -2 charge making oxygen share 0.5 electron density into each orbital it coordinates with.

PDF on $CuCrO_2$

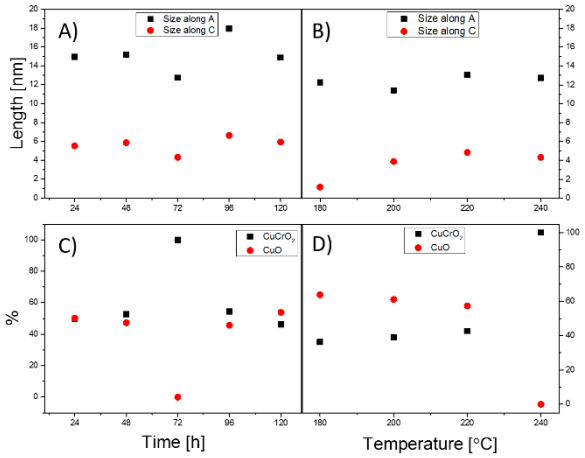

Several Rietveld refinements were carried out trying to describe the crystal structure and morphology of $CuCrO_2$. None of the models were able to make a fit describing all peak positions, widths and intensities. To obtain additionally structural information about the crystallites, PDF analysis was applied. Each peak within the PDF analysis can be directly assigned to interatomic distances within the sample.

PDF data

Figure 7. A) Model of $CuCrO_2$ fitted to local structure, 0.5-10Å value and B) fit from 0.5-19Å. 1) Indicating the metal oxygen distance. 2) Is the Cr-Cr distance. 3) Cu-Cr distance 4) Cr-O distance 5) Cu-O distance 6) Cu-Cu or Cr-Cr distance in another layer of the structure.

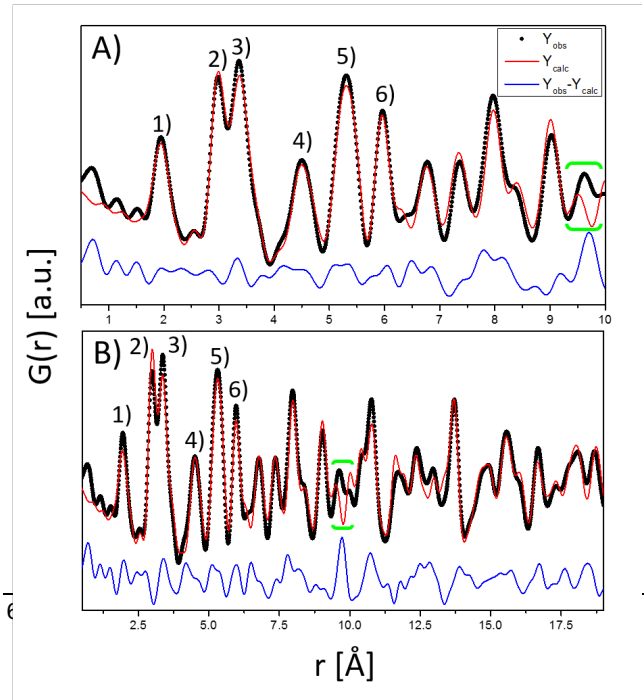

Two refinements of $CuCrO_2$ were made. One only fitting the local structure 0.5-10Å, and one fitting the global structure 0.5-19Å. Figure 7 shows both fit of the local and global structure. Figure 7 A) shows a fit which almost matches at all peak positions and intensities. At 6Å the intensities start deviating a bit but the positions still match. Peak 1) are the metal oxygen distances, Cr-O distance shown in Figure 8 A) and the Cu-O distance can be seen in Figure 1. Peak 2) is the Cr-Cr distance between octahedral sharing an edge, which is shown in Figure 8 B). Peak 3) is the distance between Cu to the nearest Cr. Peak 4) is the Cr-O shown in Figure 8 D). Peak 5) corresponds to the Cu-O distance and is visualized at Figure 8 C) as the 5.34Å distance. Peak 6) is either Cr-Cr or Cu-Cu distance between the layers. All these peaks are well described by the chosen structure.

Figure 7 B) is the same model but fitted to longer range data. As the model is fitted to higher r the R_{wp} rises. This could be due to faults in the structure, since high r value describe distances between unit cells and no longer only within them. Stacking fault then causes periodic distances between unit cells to deviate from the model used. The model is trying to describe the long range

order, which may contain stacking faults. Stacking faults then forces the unit cell to change trying to describe the global structure. By only fitting below e.g. 10Å the local structure can be determined, depending on the unit cell. This consequence is clear when looking at the 2) peaks as it gain an intensity increase. The loss or increase in intensities could also be due to Cu or Cr atoms coordinating at the wrong site, because the scatter differently from each other. Trying to describe the stacking faults

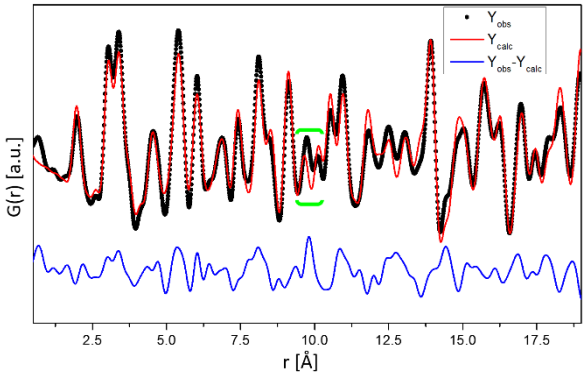

all atoms were refined to have a separate displacement factor along the c axis. This gave a small decrease in the R_{wp}.

Distances within the unit cell

Figure 8. A) Distance from Cr to its oxygen ligands. B) Cr-Cr distance between to octahedra sharing an edge. C) Shows the distance from Cu to the nearest oxygen layer. An oxygen being directly beneath the Cu. D) The distance from Cr to oxygen in the neighbouring octahedra.

A green area is marked on Figure 7 both on A) and B). This distance is not within the model for the R-3mH delafossite structure. This peak could be caused by stacking faults or by both structural polymorph being present in the sample. In fact, the P63/mmc polymorph describes the marked distance, few distances differ between the two polymorphs, making it hard to separate them from each other. The separation of the two polymorphs become even harder when analysing anisotropic nanocrystals, the broadening causing the peaks to have a large

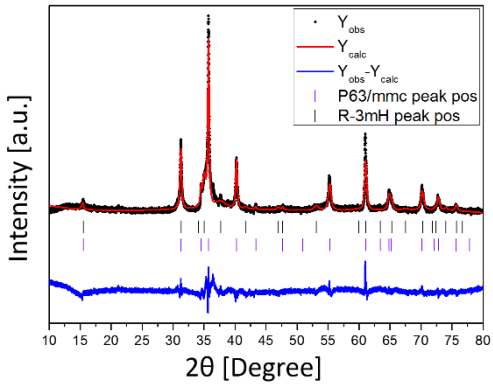

overlap with adjacent peaks. The platelets could be a stacked structure of the two polymorphs, with the R-3mH being the dominating one. The P63/mmc cannot describe the locale structure as well as the R-3mH polymorph. This could indicate that only a small amount of P63/mmc is formed.

Discussion on Rietveld and PDF $CuFeO_2$

The synthesis of $CuFeO_2$ were made three times to show reproducibility of final product. All three PXRD data sets are indicating that the same phases are present, therefore only one were analysed further. The PXRD data can be found in the supporting information.

Rietveld of $CuFeO_2$

Figure 9. The Popa rule model were used to describe the shape of the particles size and ratio between the of the two polymorphs.

To characterize the structure Rietveld refinement were used. Isotropic, Popa rules and anisotropic "no rules" were used to describe the synthesized compounds. Refined parameters for all three models are found in supporting information. PXRD data for $CuFeO_2$ R-3mH polymorph was not obtainable at ICSD. To make a characterization of the structure the model for $CuCrO_2$ was modified. Cr was exchanged with Fe, since they scatter differently, and the dimensions of the unit cell was changed to match the ones for $CuFeO_2$.

PDF analysis of $CuFeO_2$

Figure 10. PDF analysis of $CuFeO_2$. PDF data is only fitted with the R-3mH polymorph. Same undescribed peak for $CuCrO_2$ occur for $CuFeO_2$ and is marked with green.

Figure 9 showing the Rietveld refinement of $CuFeO_2$. The refinement indicating the presence of both polymorphs in a 1:1

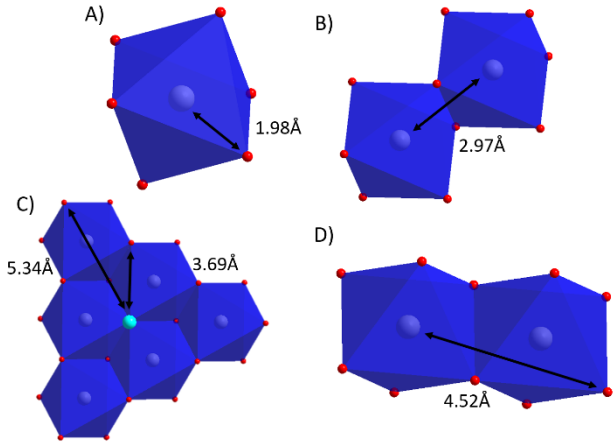

ratio. Popa rules indicating that the crystallite described from the R-3mH polymorph form platelets and the P63/mmc as spheres. Pictures can be found in supporting information. It is possible that two different crystallites are formed, one being described through the R-3mH polymorph as platelets, and the other by the P63/mmc polymorph as isotropic. One could imagine the two polymorphs stacking on top of another along c, but holding the symmetry along a and b while translate. More complicated mixtures of the polymorphs could also be a solution.

To get further structural information PDF is used. PDF analysis supports the Rietveld refinement, showing that $CuFeO_2$ has been synthesized, as seen in Figure 10. All peak positions and most intensities match. The same peak at 9.6Å is poorly described as for $CuCrO_2$. The R-3mH polymorph gave the best fit, despite of the Rietveld refinement indicating the presence of both polymorphs. Despite the $CuFeO_2$ particles being larger than the one of $CuCrO_2$, the PDF indicate the same stacking faults.

Conclusion

The delafossite crystallite size is extremely dependent on which metal occupies the A and B site. Having Cu located at A site then forces the synthesis to be done at high pH values. Cu(II) has to be reduced to Cu(I) before the delafossite structure can form. Changing the B site from Cr to Fe causes the crystallites size to differ.

Through multiple Rietveld refinements of $CuCrO_2$ the particles were determined to form nanoplatelets described by the R-3mH polymorph. Rietveld refinements only indicate one of the two polymorphs being present within the samples. Through PDF the local structure was determined, but the global structure could not be completely understood. PDF showed one distance which the R-3mH polymorph could not describe, but further analysis showed that the P63/mmc polymorph could describe it. This indicates that the P63/mmc polymorph might be present within the samples. Several guesses were made trying to describe the global structure. Whether the crystallites contain both polymorphs or different types of crystallites are present, are yet to be determined. Both PDF and Rietveld indicates that stacking faults or defect are present within the nanoparticles.

Rietveld refinement and PDF analysis reveals the presence of both $CuFeO_2$ polymorphs in the sample. $CuFeO_2$ have been proven possible to synthesize at 70°C. Despite $CuFeO_2$ being larger than $CuCrO_2$ indications of similar stacking faults are visible.

For further studies X-ray absorption near edge structure(XANES) should be tested to identify the metals oxidation states. To check the size of the particles and see if they are concealed by an amorphous layer TEM can be used. By using TEM the shape of the particles could be verified and thereby see if the crystallites are anisotropic.

Acknowledgements

Special thanks to the people who have worked so hard getting me through this project. My supervisor Kirsten M.Ø Jensen adjunct at the Nanoscience Center and Department of Chemistry, University of Copenhagen, for being an outstanding supervisor who always makes time to guide and give constructive feedback. A Supervisor who always have a new idea or adjustment to improve the project. Troels Lindahl Christiansen Ph.D student at the Nanoscience Center and Department of Chemistry, University of Copenhagen, for always being there to answer questions about anything, no matter how stupid it should be. Mikkel Juelsholt master student at the Nanoscience Center and Department of Chemistry, University of Copenhagen, for helping me with different types of Rietveld refinements in Maud and PDF analysis. Emil Rössing Elholm master student at the Nanoscience Center and Department of Chemistry, University of Copenhagen, for always wanting to discuss my data and refinements with me. Patrick Nawrocki bachelor student at the Nanoscience Center and Department of Chemistry, University of Copenhagen, for bringing me coffee in the direst of moments.

Notes and references

1. D. H. Xiong, Z. Xu, X. W. Zeng, W. J. Zhang, W. Chen, X. B. Xu, M. K. Wang and Y. B. Cheng, *J. Mater. Chem.*, 2012, **22**, 24760-24768.
2. I. C. Kaya, M. A. Sevindik and H. Akyildiz, *J. Mater. Sci.-Mater. Electron.*, 2016, **27**, 2404-2411.
3. D. H. Xiong, Q. Q. Zhang, S. K. Verma, H. Li, W. Chen and X. J. Zhao, *J. Alloy. Compd.*, 2016, **662**, 374-380.
4. H. N. Abdelhamid, S. Kumaran and H. F. Wu, *RSC Adv.*, 2016, **6**, 97629-97635.
5. M. John, S. Heuss-Assbichler, S. H. Park, A. Ullrich, G. Benka, N. Petersen, D. Rettenwander and S. R. Horn, *J. Solid State Chem.*, 2016, **233**, 390-396.
6. M. John, S. Heuss-Assbichler and A. Ullrich, *J. Solid State Chem.*, 2016, **234**, 55-62.
7. R. A. Young, *The Rietveld Method*, Oxford University Press, 1995.
8. N. Popa, *Journal of Applied Crystallography*, 1998, **31**, 176-180.
9. G. Paglia, E. S. Bozin and S. J. L. Billinge, *Chem. Mat.*, 2006, **18**, 3242-3248.
10. T. Egami, Billinge, S. J. L., *Underneath The Bragg Peaks*, 2003, **Second volume**.
11. P. Juhas, T. Davis, C. L. Farrow and S. J. L. Billinge, *Journal of Applied Crystallography*, 2013, **46**, 560-566.
12. S. J. L. Billinge, in *Uniting Electron Crystallography and Powder Diffraction*, eds. U. Kolb, K. Shankland, L. Meshi, A. Avilov and W. I. F. David, Springer Netherlands, Dordrecht, 2012, DOI: 10.1007/978-94-007-5580-2_17, pp. 183-193.
13. J. Baruchel, *Neutron and synchrotron radiation for condensed matter studies*, Springer-Verlag, 1993.
14. W. Dannhauser and P. A. Vaughan, *Journal of the American Chemical Society*, 1955, **77**, 896-897.
15. B. J. Ingram, G. B. Gonzalez, T. O. Mason, D. Y. Shahriari, A. Barnabe, D. G. Ko and K. R. Poeppelmeier, *Chem. Mat.*, 2004, **16**, 5616-5622.
16. T. N. M. Ngo, T. T. M. Palstra and G. R. Blake, *RSC Adv.*, 2016, **6**, 91171-91178.

UCPH NanoScience
NanoVidenskab KU

tidsskrift.dk/index.php/NanoVidenskabKU

Thesis Paper

Heterogeneous Nucleation of Calcium Carbonate: Effects of Substrate Chemistry

Lasse V. Nikolajsen

Received June 2017, Accepted April 2018

Investigating heterogeneous calcium carbonate nucleation is essential in the pursuit to the barriers of nucleation. However, heterogeneous calcium carbonate systems are difficult to characterize due to the influence of homogeneous nucleation. Homogeneous nucleation must be removed in order to reliably report the saturation indices used in the experiments. In this paper, homogeneous nucleation and heterogeneous nucleation are experimentally examined with atomic absorption spectroscopy, optical microscopy and ultraviolet-visible spectroscopy. The impact of homogeneous nucleation on concentration and the correlation between concentration and induction time are investigated. We document a significant impact on concentration suggesting data from current literature is compromised. Based on data, we propose a concentration range of 0.7 mM – 0.9 mM for obtaining barriers to nucleation using optical microscopy. Learning how surfaces influence the barriers and kinetics of $CaCO_3$ nucleation can increase our understanding of biomineralization and improve carbon sequestration.

1 Introduction

Calcium carbonates ($CaCO_3$) are found both dissolved in water and as naturally occurring minerals in the subsurface. Following classical nucleation theory $CaCO_3$ is considered to precipitate in two ways[1]: in the presence of a surface, known as heterogeneous nucleation, and free in solution, known as homogeneous nucleation. Homogeneous nucleation occurs when the saturation index (SI) is high enough and either calcite forms directly or more commonly, through the precursor phases amorphous calcium carbonate (ACC) and vaterite. Both are unstable intermediates. ACC has water in the structure and generally transforms to vaterite in seconds. Vaterite can be stable for minutes to several hours before transforming to calcite[2]. Heterogeneous nucleation dominates at lower saturation indices and happens because the presence of a substrate (e.g. mineral surface or polymer) decrease the interfacial free energy and hence lowers the barriers to nucleation. Barriers to nucleation can be obtained using classical nucleation theory and by counting heterogeneously precipitated nuclei pr area over time at different saturation levels[3 4 5].

Previous work investigated the difference in interfacial free energy for $CaCO_3$ and different substrates, resulting in different nucleations per second. Giuffre *et al.*[4] and Hamm *et al.*[5] found that surface charge and structure can control the heterogeneous nucleation rate.

The initial aim of this study was to test how different substrates could alter the interfacial free energy and promote heterogeneous nucleation. Replicating the results by Hu *et al.*[3] and Hamm *et al.*[5] resulted in an unexpected amount of homogeneous nucleation, as seen in figure 1.

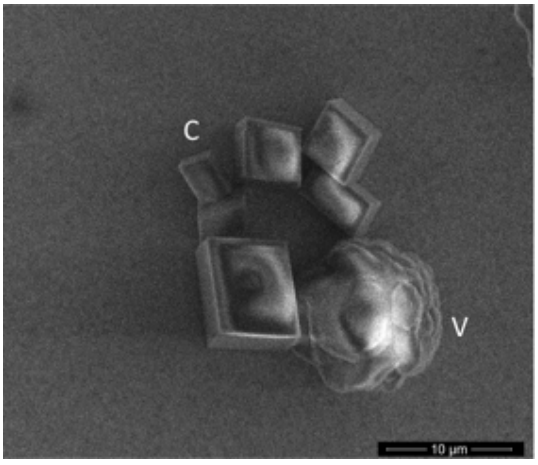

Fig. 1 Scanning electron microscope image, showing both calcite, marked with c, and vaterite, marked with v, on the substrate. The sample were made at a SI of 1.71 on an amin-functionalized substrate.

If we have homogeneous nucleation the SI is expected to change significantly and we have no control over the SI, hence we cannot calculate the true barriers. We therefore

modified our aim to removing homogeneous nucleation from the experiments. We used self-assembled monolayers[6] as substrates: A 11-Mercaptoundecanoic acid monolayer result in a carboxyl-functionalized surface and a 11-Amino-1-undecanethiol monolayer giving an aminfuntionalized surface, at the pH conditions of this study that gives a negative and a positive surface charge respectively. An optical microscope was used to examine a substrate's effect on heterogeneous nucleation. The SI's used are shown in Table 1.

Table 1 Concentrations and saturation indices

Concentration of Ca and CO_3 [mM]	Saturation index
2.5	2.28
1.3	1.88
1.25	1.86
0.8	1.56
0.6	1.35
0.4	1.04
0.2	0.45

The concentration of Ca and CO_3 are assumed to be equal.
Saturation indices used in this study, in log scale calculated with PHREEQC.

The SI's have been calculated by the following equation:

$$SI = log_{10}\left(\frac{IAP}{K_{sp}}\right) \quad (1)$$

where the ionic activity product, IAP, is the product of $a_{Ca^{2+}}$ and $a_{CO_3^{2-}}$. The solubility constant, K_{sp}, is the value of how soluble $CaCO_3$ is in water.

We investigate homogeneous nucleation with Ultraviolet-visible spectroscopy (UV-Vis) and Atomic absorption spectroscopy (AAS) to find a concentration window where homogeneous nucleation is avoided. AAS was used to find the concentration of a specific ion in solution, this is used to track the impact on concentration due to homogeneous nucleation. UV-Vis follows the onset and progress of homogeneous nucleation live, by monitoring an increase in absorption due to particles forming in the solution. The Avrami equation is fitted to the UV-Vis data to obtain three parameters, the rate constant, the order of nucleation, and the induction time. The latter parameter is particularly interesting because it provides a time frame where heterogeneous nucleation can be studied without interference from homogeneous precipitation.

By obtaining a fundamental kinetic and thermodynamic understanding of $CaCO_3$ mineral formation barriers and stability in the presence of a range of biological and mineral substrates, we can predict and engineer the fate of trapped CO_2 to a much greater extent than what is possible with current knowledge.

2 Experimental setup

In this section, the materials used and the experimental setups will be covered. Further information is reported in supporting information.

2.1 Materials

Solutions used for calcite nucleation experiments contain Na_2CO_3 (Merck ACS reagent ≥ 99 %) and $CaCl_2$ (Sigma-Aldrich ACS reagent > 99 %), which provides equal concentrations of Ca^{2+} and CO_3^{2-} when mixed. The pH of the mixed solution was 11.3. The water used for dilution and equipment cleaning was MilliQ water with a resistivity of > 18 Mcm. For AAS the samples were diluted with 2 % HNO_3 and 0.1 % KCl. All materials used were reagent grade.

Substrates were prepared using the self-assembled monolayers (SAMs) technique[6] on template stripped gold surfaces from platypus®.

2.2 Experiments

We collected scanning electron microscopy (SEM) images of selected substrates using a Quanta 3D FEG 200/600 SEM, in high vacuum ($5 \cdot 10^{-}4$ Pa), with an acceleration voltage of 2.00 kV and a beam current of 16.6 pA.

For SI calculations, the software PHREEQC with the phreeqc.dat database, was used. PHREEQC calculates the SI by equation 1 using the ionic activity for each ion.

For nucleation experiments a flow cell within an optical microscopy was used. The microscope was a Zeiss optical microscope set at 10x zoom and bright field. The experiment was conducted under the assumption that all nuclei will grow, since the initial nucleation is the energy barrier, therefore, 10x zoom will be sufficient to see all crystals. The setup consists of two beakers containing Na_2CO_3 in one and $CaCl_2$ in the other. The liquids are pumped into a mixer and from there flow into the flow cell which contains the substrate. The flow rate should be above 1 ml/min to ensure enough flow to have a diffusion controlled environment[5]. The flow cell setup is illustrated in Figure 2 and is inspired by the setup used by Hu *et al.*[3] and Hamm *et al.*[5]. One significant difference between our setup and the one e.g. Hamm *et al.*[5] used is that they placed the substrate on the top of the flow cell, facing down, to avoid fall-down of homogeneous nucleation, where we placed it in the bottom of the cell facing up. Having the substrate facing down in the cell makes homogeneous nucleation difficult to detect and they therefore assumed that all crystals on the substrate were from heterogeneous nucleation. In contrast having

the substrate in the bottom means that the crystals on the substrate are a combination of homogeneous and heterogeneous nucleated crystals, making homogeneous nucleation visible, therefore, experiments for this study were set up to investigate the effect of homogeneous nucleation.

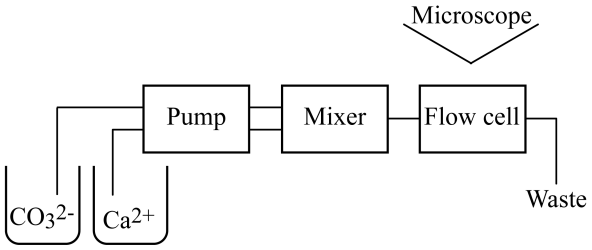

Fig. 2 Experimental setup for the flow cell experiment. The induction time is the time between the mixer and the flow cell. The experiment time is started once the solution covers the entire substrate.

The flow cell setup was rinsed with Milli-Q water and 0.5 mM HCl after every experiment.

AAS was carried out on Perkin Elmer precisely AAnalyst 800 using AS 93plus for sample management and WinLab32 for AA as software. The AAS measure the concentration of Ca^{2+}-ions in a sample at 422.7 nm. One sample (a) was made for each concentration before mixing $CaCl_2$ and Na_2CO_3. The second sample (b) was made by mixing equal amounts of the two solutions and allowed to equilibrate for a few days. The sample was filtered to remove any crystals and acid were added to stop any further nucleation.

UV-Vis experiment was carried out on Avantes AvaLight-DH-S-BAL using OceanView as software at 450 nm wavelength. The experiment measure absorption, if homogeneous nucleation are present, the absorption will increase. In the cuvettes CO_3^{-2} was added first and then Ca^{2+}. To ensure proper mixing a magnetic stirring rod was inside the cuvette during the experiment. To analyze the UV-Vis data, the Avrami equation was fitted. The Avrami equation is given by:

$$\alpha = 1 - e^{-(k\cdot(x-i))^n} \tag{2}$$

The Avrami equation encompasses three parameters: the rate constant (k), the order of reaction (n) and the induction time (i) prior to nucleation. In the top right corner in Figure 4 is a fitting shown for 2.5 mM.

The rate constant is the rate at which nucleation occurs.

The order of reaction is determined by several qualities of the reaction. It follows the given equation:

$$n = N_{dim} \cdot g + B \tag{3}$$

The order of reaction encompasses three different components, two are related to growth, that is N_{dim}, the dimensions of growth, and g, the nature of the growth limiting reaction, being 1 for surface controlled reactions and 0.5 for diffusion controlled reactions. The last component is B, the rate of nucleation, being 0 if all nuclei are present initially and 1 if nuclei are formed at a constant rate. For homogeneous nucleation B should be 1 since the nucleation rate is constant until the concentration drops too low.

The induction time is the time from the beginning of the experiment till nucleation starts.

AAS and UV-Vis were conducted multiple times to improve statistics. Sample (a) were taken before mixing and sample (b) were taken after mixed during UV-Vis and then measured with AAS afterwards, thereby ensuring that the two experiments can be compared. In this paper one experiment is followed, but all experiments are used for calculating averages. Each concentration have been color coded for all experiments.

3 Results and discussion

To observe heterogeneous nucleation on a substrate the flow cell setup is used. Replicating the SI reported in literature[5], showed homogeneous nucleation in the flow cell. The highest SI reported is 2.28 and the lowest is 1.88. Homogeneous nucleation was observed in both. The optical microscopy experiments at SI 1.86 in Figure 3 show homogeneous nucleation.

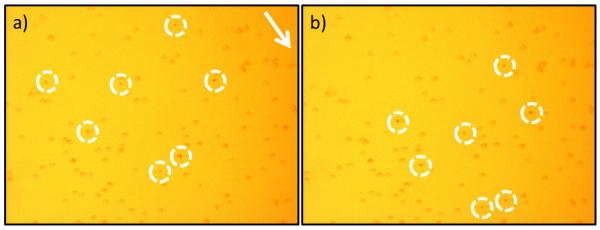

Fig. 3 Optical microscopy at SI 1.86, 1 ml/min flow rate, on a carboxyl-functionalized substrate. a) is after 136 s and b) is after 138 s. Focus in both pictures are above the substrate. All 7 crystals move down right from picture a) to picture b). All the circles show homogeneous nucleated crystals flowing freely in the water.

Each homogeneous nucleation is marked with a white circle. The two pictures are taken in the same location with a 2 second time interval. All the crystals move in the flow direction at almost the same speed indicating that they flow freely in solution as homogeneous nucleated crystals. In the background the substrate can be seen, it is not in focus, because the crystals in focus are above the substrate. The crystals are thus not in contact with the substrate and that indicate that the crystals are indeed homogeneously nucleated.

The homogeneous nucleations fell down on the substrate and in addition to changing the chemistry of the reacting solution the particles made it impossible to differentiate between heterogeneous and homogeneous nucleation using optical microscopy. To avoid homogeneous nucleation we needed lower concentrations. Changes in the concentration due to homogeneous nucleation were investigated using AAS

Atomic absorption spectroscopy

Two samples were measured for each concentration. Sample (a) contained $CaCl_2$ and sample (b) was a mixture of $CaCl_2$ and Na_2CO_3. The measured value of sample (a) should be close to the expected value, since no nucleation could occur. The measured value of sample (b) should, without any nucleation, be half that of sample (a) due to dilution.

Table 2 AAS results

	Exp. [mM]	Meas. [mM]	Meas./Exp.	% loss
	(a) 5.0	4.835	96.7 %	96.2
	(b) 2.5	0.01	0.5 %	
	(a) 2.6	1.419	54.6 %	52.8
	(b) 1.3	0.024	1.8 %	
	(a) 1.6	0.895	55.9 %	53.5
	(b) 0.8	0.020	2.4 %	
	(a) 1.2	0.608	50.7 %	46.6
	(b) 0.6	0.024	4.1 %	
	(a) 0.8	0.556	69.5 %	65.6
	(b) 0.4	0.016	3.9 %	
	(a) 0.4	0.211	52.7 %	-8.5
	(b) 0.2	0.122	61.2 %	

(a) is the sample before mixing and (b) is after mixing.

Table 2 show the intended and measured calcium content before and after UV-Vis experiments (as shown in Figure 4. Any calcium loss between before and after the experiment is indicativve of homogeneous precipitation. The first column shows the color coding for each concentration. The second column show the expected concentration in mili molar of each sample. Here (a) is the sample before mixing and (b) is after mixing. The third column show the measured concentration in mili molar. The fourth column show how close the measured Ca^{2+} concentration is to the expected concentration. The fifth column show how much further the b-sample is from the expected value than the a-sample is. A high number means a large impact on the concentration due to homogeneous nucleation.

As seen in Table 2 the measured concentration of the (b) sample is much lower than half that of sample (a). The closer the measured percentage is between sample (a) and (b), the less homogeneous nucleation has occurred. Most of the samples show large discrepancy between (a) and (b), confirming that homogeneous nucleation does have a large impact on the concentration. Only the lowest concentration has no sign of homogeneous nucleation. The large impact on the concentration means that homogeneous nucleation will disrupt the concentration of available Ca^{2+} and CO_3^{-2} and the reported SI will be wrong. Using a too low concentration can lead to no nucleation at all, therefore UV-Vis were used to determine induction time, to use as high a concentration as possible without homogeneous nucleation.

UV-Vis

The UV-Vis setup will show the induction time and if there is any difference in the pathway for the homogeneous nucleation. The induction time is determined for all the concentrations of $CaCO_3$ used in AAS, to investigate the increase in induction time, due to decrease in concentration, furthermore, the nucleation path at different concentrations were also examined by the Avrami parameters.

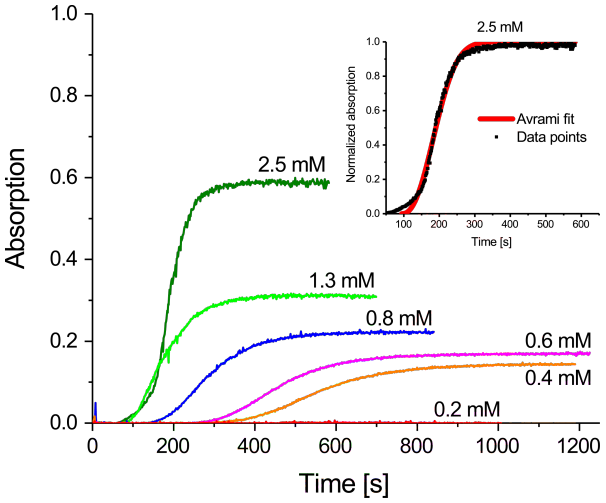

Fig. 4 UV-Vis experiment showing absorption for 2.5 mM (dark green), 1.3 mM (light green), 0.8 mM (blue), 0.6 mM (mangan), 0.4 mM (orange), and 0.2 mM (red) as a function of time in seconds. In the top right corner is a graph showing the fitting profile of an Avrami fitting to the 2.5 mM curve. In the Avrami plot the y-axis is normalized absorption and the x-axis is time in seconds. Data from the fitting for all concentrations is shown in Table 3.

Figure 4 show, that homogeneous nucleation follows a s-formed curve. The 2.5 mM concentration show the shortest induction time, the steepest slope, and the highest absorption maximum. The trend for all the lower concentrations are longer induction time, lower slope, and a lower absorption maximum. The 0.2 mM sample is the only con-

centration which has no homogeneous nucleation in the duration of the experiment. The trend is as expected since these phenomena are diffusion controlled[1] and therefore directly related to the concentration. To make a mathematical foundation for the data analysis, an Avrami fitting is used[7]. The results from the Avrami analysis can be seen in Table 3.

Table 3 Avrami data

	Conc. [mM]	k	n	i [s]
	2.5	0.0089	2.36	94.3
	2.5 *avg.*	0.0092	1.65	95.3
	1.3	0.0091	1.31	90.6
	1.3 *avg.*	0.0093	1.35	92.0
	0.8	0.0065	1.23	168
	0.8 *avg.*	0.0055	1.44	218
	0.6	0.0047	1.31	291
	0.6 *avg.*	0.0040	1.33	387
	0.4	0.0035	1.31	323
	0.4 *avg.*	0.0043	1.54	265

Mathematical analysis of the UV-Vis absorption curves shown in Figure 4 and averages from multiple identical experiments. Conc. is the $CaCO_3$ concentration in mM. k is the rate constant, n, is the order of reaction, and i, is the induction time.

The first column in Table 3 show the color corresponding to the UV-Vis figure. The second column show the concentration of each sample. The third, fourth, and fifth column show the three fitted Avrami parameters, the rate constant, k, the order of reaction, n, and the induction time, i. The average values have been calculated for: 2.5 mM, 3 experiments; 1.3 mM, 4 experiments; 0.8 mM, 5 experiments; 0.6 mM, 3 experiments; and 0.4 mM, 2 experiments.

The Avrami parameters shows that the rate constant decrease with decreasing concentration. That was as expected due to it being diffusion controlled, since there was no surface present and no limiting steps in mixing the solutions. In contrast the average order of reaction, for each concentration, is stable and only varies between 1.33 and 1.65. The similar order of reaction between the different concentrations suggest that nucleation and growth mechanisms are similar in the majority of the experiments. To explain the approximately order of reaction to be 1.5, equation 3 is used with three-dimensional growth, diffusion controlled as the limiting factor and that there is nucleation sites present.

$$1.5 = 3 \cdot 0.5 + 0 \tag{4}$$

The presence of nucleation sites could explain why there is homogeneous nucleation in the flow cell experiment.

The induction time increases with decreasing concentration. The induction time can provide a window in which pure heterogeneous nucleation experiments can be conducted. The discrepancy between the shown experiment and the average, indicates an instability at low concentrations.

The flow time between the mixer and the substrate in the flow cell setup is 60 seconds. The mixing in the flow cell was not identical to the mixing in the UV-Vis experiment, therefore, was the actual induction time not the same, though the trend to increase time with reducing concentration remains. At 0.8 mM the measured induction time is more than double the flow time and is therefore chosen as the best candidate for the flow cell setup.

Flow cell

At 0.8 mM $CaCO_3$ there should be no homogeneous nucleation and pure heterogeneous nucleation was expected.

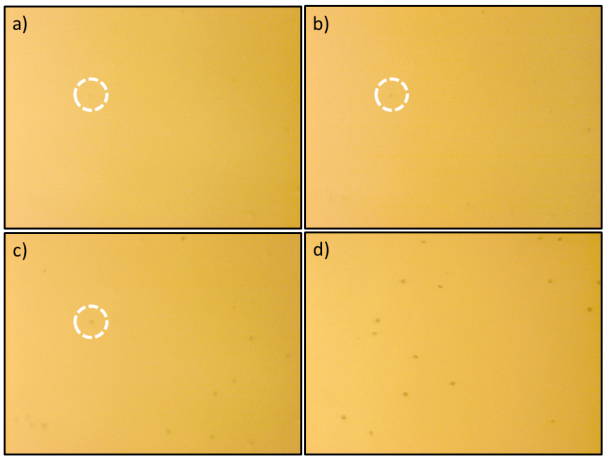

Fig. 5 Optical microscopy at 3 ml/min, 0.8 mM on a carboxyl-functionalized gold substrate. a) is after 210 s, b) is after 352 s, and c) is after 581 s. a), b), and c) are all taken in the same location, showing signs of steady nuclear growth over time. d) is taken after 613 s in a different location showing nucleation forming uniformly across the substrate.

Figure 5 show a pure heterogeneous nucleation, because there are no crystals floating in the solution and there is growth over time. From picture a trough b to c there is a steady growth of the nuclei, highlighted by the one inside the white circle. Picture d is taken in another location showing heterogeneous nucleation forming uniformly across the surface. The result is exactly what was expected.

To study the nucleation behavior at 0.8 mM concentration, an amin-functionalized substrate was used. The interfacial free energy between this substrate and $CaCO_3$ is different. It was expected to see pure heterogeneous nucleation though at a different nucleation rate than the

carboxyl-functionalized substrate. The difference in nucleation rate was expected based on the results by Hamm *et al.*[5]. Here they found that the surface charge effects the nucleation rate.

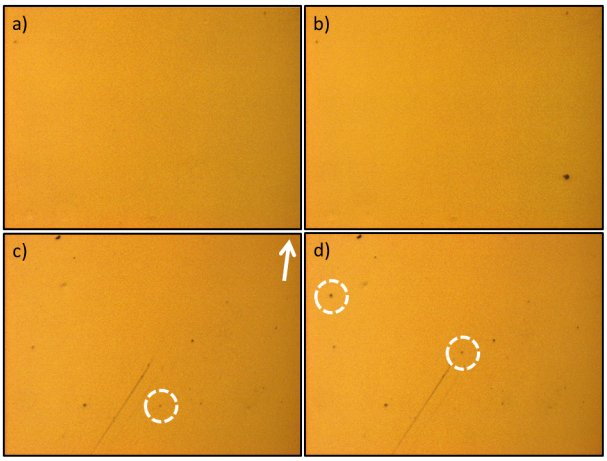

Fig. 6 Optical microscopy at 3 ml/min, 0.8 mM on an amin-functionalized gold substrate. Here a) and b) are from the same experiment, and c) and d) are from a second experiment. a) is after 251 s and b) is after 905 s. The impurity in the bottom right grows but no new nucleations occur. c) is after 324 s and d) is after 326 s. The white circles indicate homogeneous nucleation. The white circle in c) move up to according to the arrow shown ending in the right circle in d).

The top of Figure 6 shows no nucleation at 0.8 mM concentration while the bottom show homogeneous nucleation. All three experiments at 0.8 mM should yield similar results. The inconsistency in whether homogeneous nucleation was produced can be due to external disruption e.g. crystals from previous experiment. The flow cell is a closed system and the setup was washed with water and acid before each experiment to reduce unwanted influence. However, it is found that the change in substrate affects the heterogeneous nucleation. Extreme care should be taken when cleaning the flow cell system between experiments, to prevent any residue to build up. More research is needed to develop a better understanding of the system and obtain consistent results.

4 Conclusion

These studies show that AAS and UV-Vis provides knowledge of induction time and homogeneous nucleation's impact on concentration. If homogeneous nucleation is present during a flow cell experiment the initial specific saturation index should not be reported, since it will not be representative for the SI in the actual reaction. Conducting the experiment at a concentration range of 0.7 mM – 0.9 mM are proposed as a suitable range for pure heterogeneous nucleation. Once heterogeneous nucleation is obtained further research in inhibiting and promoting substrates could be conducted. Discovering how substrates interact with $CaCO_3$ during heterogeneous nucleation could prove significant in the development of carbon sequestration approaches and further our understanding of biomineralization processes.

5 Acknowledgements

I would like to express my great appreciation to my supervisor Karina Krarup Sand Assistant Professor at the Department of Chemistry, University of Copenhagen, for guidance during experiments and feedback on the article.Thanks to the Nano Geo Science group at the Department of Chemistry, University of Copenhagen, for providing a great scientific environment to conduct research in, espceially Anne Rath Nielsen, Ph.D., Mia Rohde Nielsen, Ph.D., Maria Bjørn, Lab Technician, and Knud Dideriksen, Associate Professor, for help with experimental setup and data analyzis.

References

1 *Principles of crystal nucleation and growth*, ed. J. J. De Yoreo and P. G. Vekilov, Mineralogical Soc America, Napa valley, california, 2003.

2 J. D. Rodriguez-Blanco, S. Shaw and L. G. Benning, *Nanoscale*, 2010, **3**, 265–271.

3 Q. Hu, M. H. Nielsen, C. L. Freeman, L. M. Hamm, J. Tao, J. R. I. Lee, T. Y. J. Han, U. Becker, J. H. Harding, P. M. Dove and J. J. De Yoreo, *Faraday Discussions*, 2012, **159**, 509–523.

4 A. J. Giuffre, L. M. Hamm, N. Han, J. J. De Yoreo and P. M. Dove, *Proceedings of the National Academy of Sciences of the United States of America*, 2013, **110**, 9261–9266.

5 L. M. Hamm, A. J. Giuffre, N. Han, J. H. Tao, D. B. Wang, D. Y. J. J. and P. M. Dove, *Proceedings of the National Academy of Sciences of the United States of America*, 2014, **111**, 1304–1309.

6 M. H. Nielsen and J. R. I. Lee, *Methods in Enzymology*, 2013, **532**, 209–224.

7 S. F. Hulbert, *J. Brit. Ceram. Soc.*, 1969, **6**, 11–20.

UCPH NanoScience
NanoVidenskab KU

tidsskrift.dk/index.php/NanoVidenskabKU

Thesis Paper

Local Current Through Helical Orbitals

Louise Oxen Høgh Hyllested

Received June 2017, Accepted April 2018

Traditional chemical research has given great information about the physical properties of molecules. This research provides understanding of how molecules work in the classical ways, but the limit is reached when molecules are used in a non-traditional way. Now molecules can be inserted in molecular junctions, which makes it possible to examine molecules in new ways. Recent theoretical work has shown that some linear molecules can have helical orbitals. Here the question of interest is whether the current density around these particular molecules are affected by the helical orbitals and the coupling of the electrodes. We show that the helical orbitals in combination with the coupling of the electrodes, indeed has an impact on the current and that the orbitals contribute to a circular current around these linear molecules. As the understanding of the currents behavior around the molecules expand, it paves the way for new chemical questions about how we can control the current. For example, how helical current may induce magnetic properties in non-magnetic molecules, and how chemical substituent can be used to impact these effects.

1 Introduction

Molecular electronics have been of great interest in the field of chemistry and physics in the past few years. The possibilities associated with understanding how the molecules behave when introduced to new surroundings, e.g. when put in a junction, paves the way for new possibilities for using molecules in electronics.

Earlier studies have found that molecules can be used for electron transport, where the molecule is used as gate switches or other transport elements[1]. Though several things have an impact on how well the molecule conducts, a study found that electron transport across a molecule can go through-space and not only through-bond[2]. This indicates that there is still much to learn about how current travels across molecules. Apart from being used for electron transport, molecules can be used for spintronics, where the electron's spins is used to transfer information. Though this is a newer discovery and by now it is primarily associated with inorganic metals[3]. The interest lies in how the spin transport can be controlled by use of magnetic polarized electrodes or single-radical molecular junctions[4,5]. Another study found that molecules could be used as a field effect transistor made by using molecular orbitals, which suggests that the possibilities for using molecules for electronic devices only is limited to the current understanding of molecules[6] . Recent studies found that some linear molecules have helical orbitals[7,8], these molecules have recently been synthesized successfully[9]. Their ability to have helical orbitals paves the way for new chemical questions, of how these orbitals can contribute to the current around these molecules, and whether these currents can be controlled.

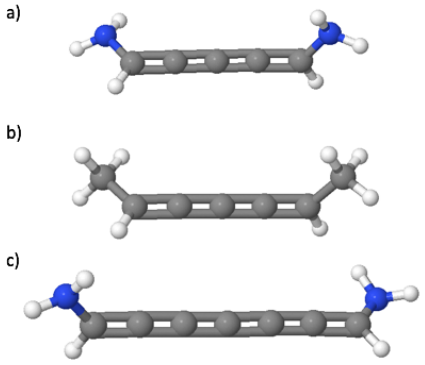

Fig. 1 The investigated molecules, a) (5)allene with amine as substituent, b) (5)allene with methyl as substituent, c) (7)allene with amine as substituent.

In this article, the focus is on how the helical orbitals affect the current around these linear molecules and how the coupling of electrodes to the molecule, changes the currents path across the molecule. The molecules were chosen based on examination of linear molecules with helical orbitals by Hendon *et al.*[8]. They use cumulene for linear molecules with an even number of double bound carbons,

and allene for linear molecules with an uneven number of double bound carbons. This nomenclature is adopted, as (n)allene, where n is the number of carbons. Hendon *et al.* found that the orbitals only twist in allene and not in cumulene. Therefore the focus in this article is on allene. The molecules chosen for this investigation are (5)allene and (7)allene with substituent groups replacing one of the hydrogens in each end of the carbon chain. The substituent groups for (5)allene is methyl and amine. For (7)allene the substituent group is amine, as seen in Figure 1.

The interest in these specific molecules lies in their ability to have helical orbitals. The twisting of the orbitals in (5)allene at the highest occupied molecular orbital (HOMO) and lowest unoccupied molecular orbital (LUMO) are illustrated in Figure 2.

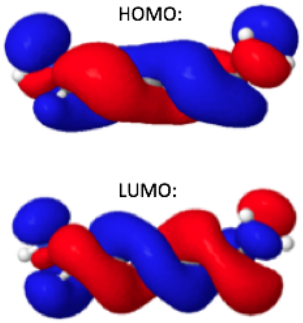

Fig. 2 Orbitals of (5)allene with amine as substituent. Here with HOMO top and LUMO bottom.

Aside from the orbitals' contribution, the placement of the electrodes is interesting in relation to which orbital the electrodes couple into. Figure 3 illustrates the coupling to the molecule. The black dot marks the position of the electrode. Here Figure 3a show the position of the electrode for the positive dihedral for amine (top) and methyl (bottom) and 3b shows the position of the electrode for the negative dihedral for amine (top) and methyl (bottom). The electrodes in each end can be either on the positive or negative dihedral. The electrodes placed at the positive dihedral will from now on be mentioned as p and the electrodes placed at the negative dihedral mentioned as m. If the electrodes are at the positive dihedral in each end, they will be mentioned as pp. If they are placed at the negative dihedral in each end, they will be mentioned as mm and if they are placed at the positive and negative dihedral, respectively, they will be mentioned as pm. The electrodes consist of dioxygen. These were chosen in order to overcome the limitations of using the Gaussian program, and the local current code. Additionally these electrodes make it easier to control the coupling to the molecule. Compared to a gold electrode, dioxygen provides the possibility of choosing specific Fermi energies, and can be thought of as the tip of a gold electrode.

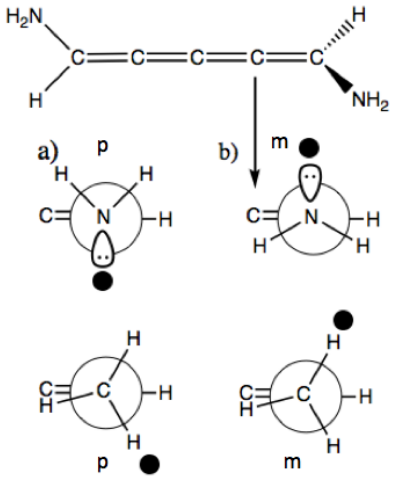

Fig. 3 A Newman projection illustrating the coupling of the electrode to the molecule. The black dot marks where the electrode is coupled. a) Illustrates the coupling to the positive dihedral for amine (top) and methyl (bottom). b) Illustrates the coupling to the negative dihedral for amine (top) and methyl (bottom).

To understand how the current is affected by the coupling of the electrodes into the molecule, the current density must be calculated. The current density is given by the following as they derive in Xue et al [10], with atomic units:

$$j(r) = \frac{1}{2} \cdot \sum_{ij} \left(\int dE \cdot G^{<}_{ij}(E) \right) \cdot dS_{ij}(r) \qquad (1)$$

where $dS_{ij}(r) = \phi_i(r) \cdot \nabla\phi_j(r) - \phi_j(r) \cdot \nabla\phi_i(r)$. Here ϕ_i and ϕ_j is the wave function and ∇ is the gradient to the wave function. The lesser Green's function ($G^{<}(E)$) is given by $G^{<}(E) = G^R \cdot \Sigma^{<} \cdot G^A$, where $G^R = [E \cdot S - H + \Sigma^R]^{-1}$. Here E is the energy, S is the overlap integral, H is the Hamiltonian and Σ^R is the self energy of the retarded Green's function(G^R) and $\Sigma^{<}$ is the self energy of the lesser Green's function [11 12 13]. In order to get $G^{<}$ and calculate the current density, a density functional theory (DFT) calculation of the molecule is necessary. From the output file of the DFT calculations, information for $G^{<}$ is given and thereby it is possible to calculate the current density. The DFT output file also gives information to the calculations of the orbitals as mentioned in SI.

2 Results and discussion

In order to explain how the current is affected by the orbitals and the position of the electrodes compared to the

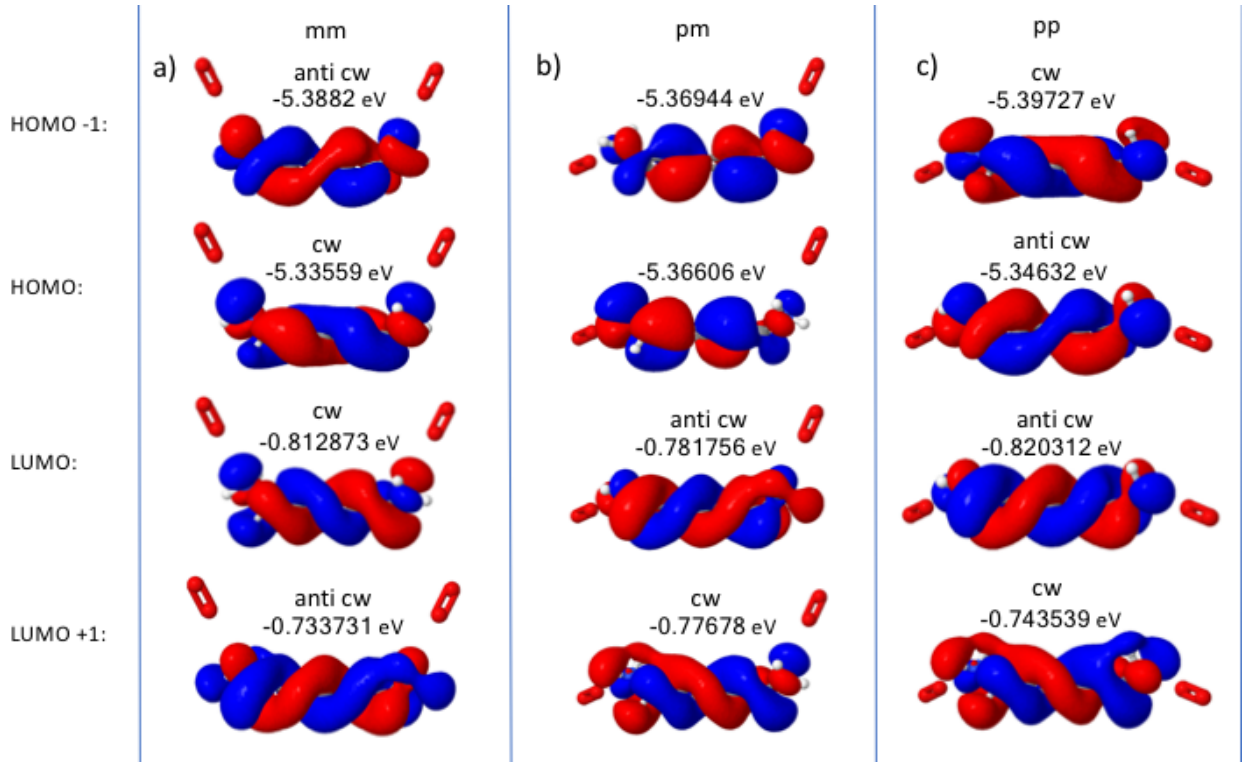

Fig. 4 Orbitals of (5)allene with amine as substituent. The HOMO-1, HOMO, LUMO and LUMO+1 orbitals are illustrated with their energies shown above. a) Electrodes placed at mm, b) Electrodes placed at pm, c) Electrodes placed at pp.

molecule, it is essential to see how the current density and the orbitals behave. Figure 4 illustrates the orbitals of (5)allene with amine as substituent. Here with the electrodes at mm (Figure 4a), pm (Figure 4b) and pp (Figure 4c). The orbitals are either clockwise (cw) or anti clockwise (anti cw) around the molecule. It is seen that with the electrodes at mm, for the HOMO-1 and the HOMO orbital, the twisting is anti cw and cw respectively. For the LUMO and the LUMO+1, the orbitals twist cw and anti cw. In contrast, when the electrodes are placed at pp the twisting is cw and anti cw for the HOMO-1 and the HOMO orbital and vice versa for LUMO and LUMO+1. Thus for the mm position of the electrodes the HOMO and the LUMO orbitals twist cw, where for pp position of the electrodes, the HOMO and the LUMO orbitals twists anti cw. The same effect is seen for (7)allene with amine as substituent (Figure S2). For (5)allene with methyl as substituent, the helical orbitals are mostly seen for the mm coupling (Figure S1). In general it is seen that the orbitals at the LUMO energy has one more node than the orbitals at the HOMO energy.

In Figure 5 the transmission and current density of (5)allene with amine as substituent is shown. Here the electrodes are at mm (5a), pm (5b) and pp (5c). From each of these electrode positions the current density is calculated at the HOMO energy (green), LUMO energy (blue) and a Fermi energy in between (red). Based on this, the current does not have helical behavior. Consequently no helical current is seen, though circular currents around the molecules are seen. The white and yellow arrows illustrates which way the current runs around the molecule. The white arrows indicate the current that circulates the molecule and the yellow, the current that runs along the molecule.

The pictures are difficult to interpret. The main current moves in the same direction as the voltage, still some currents seem to move in the opposite direction. Furthermore the pictures can not be compared to each other, only the direction of the circular currents around the molecules can be compared due to normalization. The question of quantifying what percentage of the current that flows linear and what flows circular is still unresolved. Moreover, it is relevant to have in mind whether this circular current contributes to the net current.

For (5)allene with amine as substituent a tendency is seen for the HOMO and the LUMO energies. Here the circular current runs the opposite direction of the orbitals at the HOMO energy, but in the same direction as the orbitals at the LUMO energy. The circular current seen around these molecules does not only differ in the the way

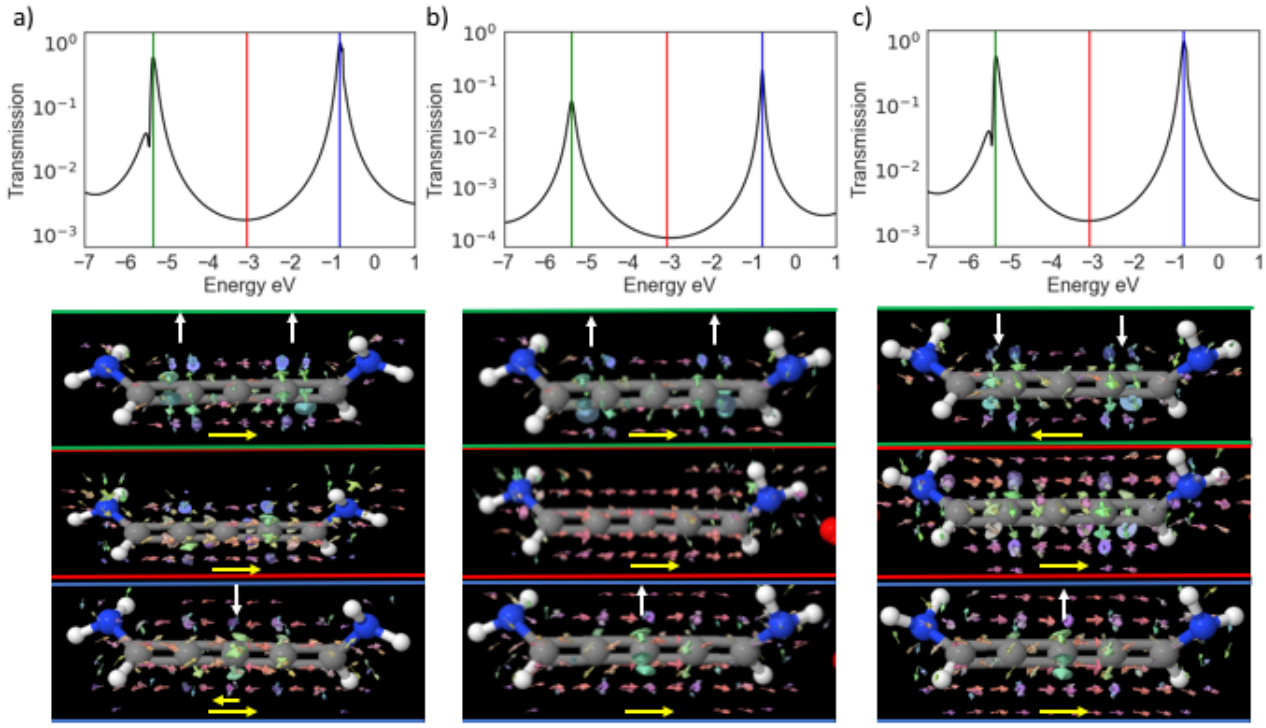

Fig. 5 Transmission and current density of (5)allene with amine as substituent. Here for three different energies, HOMO (green), LUMO (blue) and a Fermi energy in between (red). The green line on the graph correlates to the green box, and so forth. The yellow arrows illustrate the way the current runs along the molecule and the white arrows illustrate the way the circular current runs around the molecule. a) For (5)allene with the electrodes placed mm, with the HOMO energy at -5.33559 eV, the LUMO energy at -0.812873 eV and a Fermi energy at -3.0742315 eV. b) For (5)allene with the electrodes placed mp, with the HOMO energy at -5.36606 eV, the LUMO energy at -0.781756 eV and a Fermi energy at -3.073908 eV. c) For (5)allene with the electrodes placed pp, with the HOMO energy at -5.34632 eV, the LUMO energy at -0.820312 eV and a Fermi energy at -3.083316 eV. The arrows illustrating the current can only be compared at one energy and not at different energies due to the normalization, although the direction of the current can be compared.

they run around the molecule, they also differ in quantity and the distance between the circular currents. At the HOMO energy For (5)allene with amine as substituent (Figure 5), two circular currents are seen, where for the longer molecule (7)allene with amine as substituent three circular currents are seen (Figure 7). Both seem to have the same distance between the circular currents. For (5)allene with methyl as substituent (Figure 6), the circular currents for the HOMO energy and the LUMO energy have three circular currents, though for the LUMO energy the circular currents occur closer to each other. Apart from this the circular currents change direction, where the first circular current goes anti cw around the molecule, the second goes cw and the last anti cw. Furthermore, for (5)allene and (7)allene with amine as substituent it seems that the circular current prefers to go around an atom, where for (5)allene with methyl substituent the circular current is both around an atom and a bond.

At the Fermi energy in between the HOMO energy and the LUMO energy the current exhibits a mix of the HOMO and the LUMO current for all three molecules. They show no clear sign of a circular current at this energy, though (5)allene and (7)allene with amine as substituent (Figure 5 and 7) exhibit more affinity for circular current than (5)allene with methyl substituent (Figure 6) at this energy. Comparing the transmission of all three molecules, it is seen that the transmissions are lower when the electrodes are placed pm than when the electrodes are placed mm and pp. For all three molecules with the electrodes placed pm a cancellation of the current is seen, to varying degree, for the LUMO energy and the energy between the HOMO and LUMO energy. This cancellation causes the main current to be linear. The clearest cancellation is seen for (7)allene with amine (Figure 7), where both the current calculated at the LUMO energy and the Fermi energy in between the HOMO energy and LUMO energy is linear. This cancellation is due to coupling into both the negative and positive dihedral (coupling pm)[14].

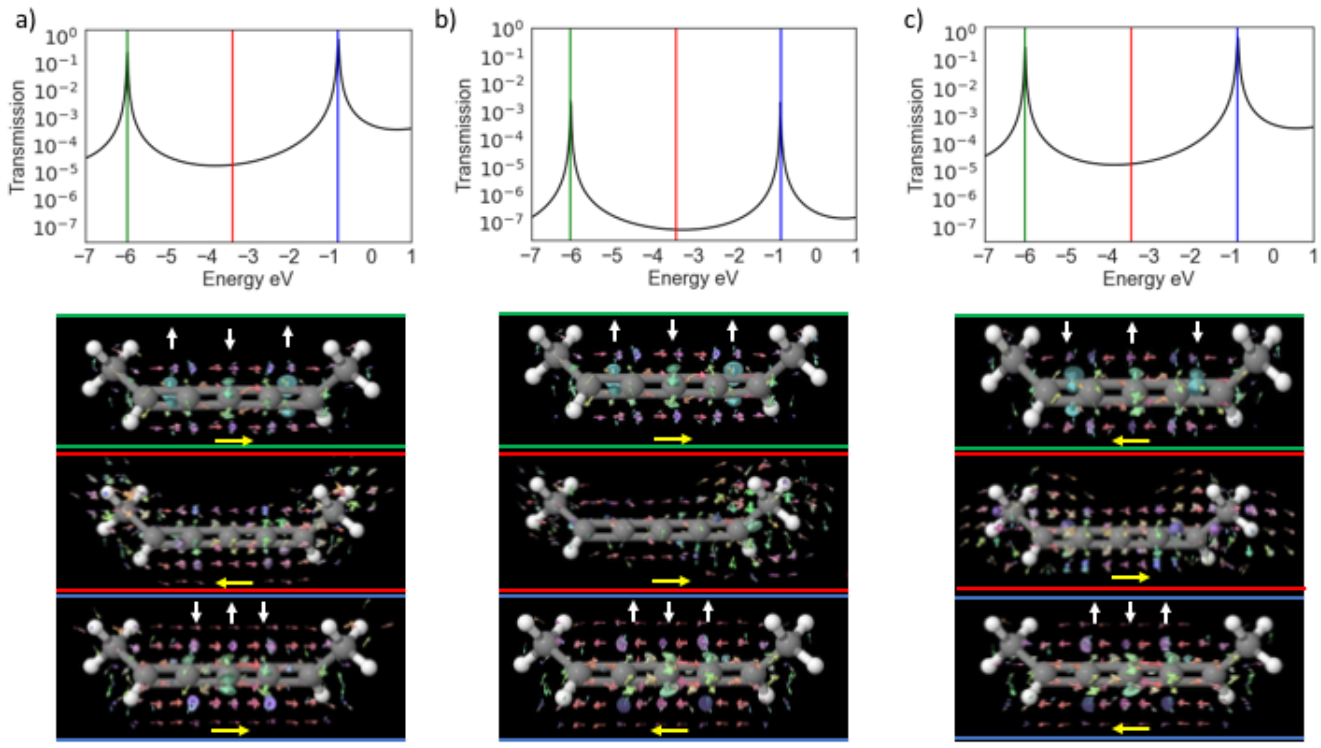

Fig. 6 Transmission and current density of (5)allene with methyl as substituent. Here for three different energies, HOMO (green), LUMO (blue) and a Fermi energy in between (red). The green line on the graph correlates to the green box, and so forth. The yellow arrows illustrates the way the current runs along the molecule and the white arrow illustrate the way the circular current runs around the molecule. a) For (5)allene with the electrodes placed mm, with the HOMO energy at -5.96372 eV, the LUMO energy at -0.795731 eV and a Fermi energy at -3.3797255 eV. b) For (5)allene with the electrodes placed mp, with the HOMO energy at -6.0237 eV, the LUMO energy at -0.859986 eV and a Fermi energy at -3.441843 eV. c) For (5)allene with the electrodes placed pp, with the HOMO energy at -6.00667 eV, the LUMO energy at -0.844707 eV and a Fermi energy at -3.4256885 eV. The arrows illustrating the current can only be compared at one energy and not at different energies due to the normalization, although the direction of the current can be compared.

At this point, no obvious correlation between the current and the orbitals is seen. It is not clear which orbital that contributes to the current at the HOMO energy and LUMO energy. For (5)allene with amine as substituent (Figure 5) the circular current at the LUMO energy runs in the same direction as the LUMO orbital, though this is only seen for this molecule. For (7)allene with amine as substituent (Figure 7) the opposite effect is seen.

A tendency for (5)allene and (7)allene with amine as substituent is observed for the circular current at the HOMO energy. The distance, direction and quantity of circular currents around these correlates with the length of the molecule. For (5)allene two circular currents for the HOMO energy were seen, where for (7)allene three circular currents were seen. The distance between the circular currents does not seem to be affected by the length of the molecule, only the quantity of circular currents seems to change. For both (7)allene and (5)allene all of the circular current turns in the same directions at each energy. At the LUMO energy the same effect is seen. (5)allene has one clear circular current where (7)allene has two clear circular currents. (5)allene with methyl as substituent has, as mentioned, three circular currents at the HOMO energy, running different directions around the molecule. At the LUMO energy three circular currents are still seen, though each current has changed direction around the molecule and the circular currents has a decreased distance between each other.

Another way to find out if the helical orbitals gives helical current, is to look at the scattering states/eigenchannels [15]. If these have helical character, the helical orbitals do not give helical current but only the circular current, as seen. If the scattering state does not have helical character the question is still unresolved.

In summary circular current is seen for all three molecules. (5)allene and (7)allene with amine as substituent shows best examples of circular current. This could be explained by amine being more electron-

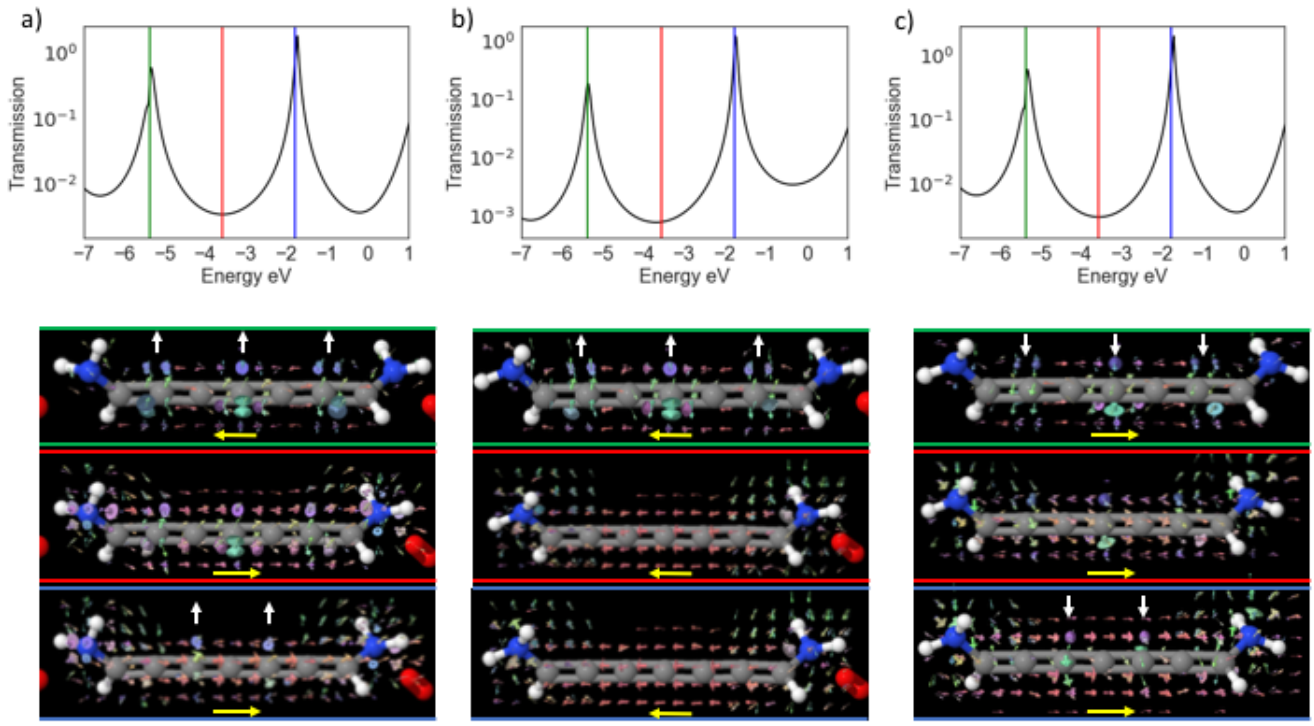

Fig. 7 Transmission and current density of (7)allene with amine as substituent. Here for three different energies, HOMO (green), LUMO (blue) and a Fermi energy in between (red). The green line on the graph correlates to the green box, and so forth. The yellow arrows illustrates the way the current runs along the molecule and the white arrow illustrate the way the circular current runs around the molecule. a) For (5)allene with the electrodes placed mm, with the HOMO energy at -5.37633 eV, the LUMO energy at -1.79429 eV and a Fermi energy at -3.58531 eV. b) For (5)allene with the electrodes placed mp, with the HOMO energy at -5.38005 eV, the LUMO energy at -1.76854 eV and a Fermi energy at -3.574295 eV. c) For (5)allene with the electrodes placed pp, with the HOMO energy at -5.37228 eV, the LUMO energy at -1.79072 eV and a Fermi energy at -3.5815 eV. The arrows illustrating the current can only be compared at one energy and not at different energies due to the normalization, although the direction of the current can be compared.

withdrawing compared to methyl, thereby contributing more to the splitting of the orbitals [16]. When the number of carbons in the chain increases, the number of circular currents increases. Furthermore, when going from the HOMO energy to the LUMO energy, the number of circular currents decreases by one for both (5)allene and (7)allene with amine as substituent. This could be due to the number of nodes increasing from the HOMO to the LUMO energy, indicating that the helical orbitals contributes to the current across the molecule, through the circular currents.

3 Methods

(5)allene and (7)allene were investigated using DFT and current density calculations. The substituent groups chosen were amine and methyl. Here only methyl for (5)allene and amine for both (5)allene and (7)allene. The molecules alone were optimized once, and a DFT calculation of the molecules with electrodes attached was done. The electrodes consist of dioxygen, and were placed 3 Å from the molecules at each end at three different positions (mm, pm and pp). The optimization of (5)allene without electrodes was done using Gaussian with the following keywords: opt=verytight b3lyp/6-31g(d) int=ultrafine. The DFT calculation of (5)allene with the electrodes attached were done using, b3lyp/6-31g, int=ultrafine, nosymm, SCF (maxcyc=200, XQC) as keywords. For (7)allene the basis set was changed to 6-311g(d) and 6-311g for the optimization of the molecule and the DFT calculation with electrodes attached respectively, as described in SI. From the output obtained from Gaussian, the lesser Green's function ($G^<$) was calculated as mentioned earlier. From $G^<$ the current density and, by diagonalizing H_{ao}, the molecular orbitals, were calculated. The current was calculated at three chosen Fermi energies, the HOMO energy, the LUMO energy, and a Fermi energy in between the two. The placement of the HOMO energy and LUMO energy were obtained by getting the eigenenergies from

the output of Gaussian and finding the biggest gap.

4 Conclusion

(5)allene and (7)allene with methyl and amine as substituent groups, were investigated through DFT using the output to calculate the orbitals and current density around the molecules. From these calculations it is seen that the orbitals are helical both at the HOMO and the LUMO energy. The current around the molecules does not exhibit helical behavior, though circular current around the molecules is seen. Both linear and helical current are present. Furthermore depending on the energy at which the current is calculated, the current along the molecule changes direction. Circular current is seen at all three molecules, however, predominantly with amine as substituent, when the electrodes were placed mm and pp. Looking at the orbitals in relation to the current, when going from the HOMO energy to the LUMO energy, the number of nodes in the orbitals increase, whereas the number of circular currents seems to decrease. From this it can be concluded that even though there are circular currents around the molecules there are no clear signs that the orbitals match the current at the given energy. This investigation leads on to a deeper understanding of how the orbitals contribute to the circular current around the molecules and how this can be controlled.

5 Acknowledgements

I would like to express my gratitude to my supervisor Gemma C. Solomon Associate Professor at the Department of Chemistry, University of Copenhagen, for guidance and feedback on the project. A special thanks to Anders Jensen Ph.D student, Department of Chemistry, University of Copenhagen for providing the computational background and for the big help on the technical understanding. Also thanks to Marc Hamilton Garner Ph.D student, Department of Chemistry, University of Copenhagen for helping with the chemical aspect of the project. At last a thanks to the whole group for making me feel welcome and always being available.

References

1 A. Nitzan and M. A. Ratner, *Science Review*, 2003, **300**, 1384–1389.
2 G. C. Solomon, C. Herrmann, T. Hansen, V. Mujica and M. A. Ratner, *Nature Chemistry*, 2010.
3 R. Naaman and D. H. Waldeck, *Annual Review of Physical Chemistry*, 2015, **66**, 263–281.
4 A. C. Aragones, D. Aravena, J. I. Cerda, Z. Acs-Castillo, H. Li, J. A. Real, F. Sanz, J. Hihath, E. Ruiz and I. Dez-Peez, *Nano Letters*, 2016, **16**, 218–226.
5 R. Hayakawa, M. A. Karimi, J. Wolf, T. Huhn, M. S. Zllner, C. Herrmann and E. Scheer, *Nano Letters*, 2016, **76**, 4960–4967.
6 H. Song, Y. Kim, Y. H. Jang, H. Jeong, M. A. Reed and T. Lee, *Nature Letters*, 2009, **462**, 1039–1043.
7 A. Imamura and Y. Aoki, *Chem. Phys Letters*, 2013, **590**, 136–140.
8 C. H. Hendon, D. Tiana, A. T. Murray, D. R. Carbery and A. Walsh, *Chem. Sci.*, 2013, **4**, 4278–4284.
9 D. Wendinger and R. R. Tykwinski, *American Chemical Society*, 2017.
10 Y. Xue and M. A. Ratner, *Physical Review*, 2004, **70**, 1–4.
11 *Many-Body Quantum Theory in Condensed Matter Physics*, ed. H. Bruus and K. Flensberg, Oxford University Press, Oxford, 12th edn, 2011.
12 *Molecular Electronics*, ed. J. C. Cuevas and E. Scheer, World Scientific Publishing, Singapore, 1st edn, 2010.
13 *Electronic Transport in Mesoscopic Systems*, ed. S. Datta, Cambridge University Press, Cambridge, 1st edn, 1995.
14 K. Yoshizawa, T. Tada and A. Staykov, *J. Am. Chem. Soc.*, 2008, **130**, 9406–9413.
15 M. Paulsson and M. Brandbyge, *Physical Review*, 207, **16**, 115127–1–115117–7.
16 C. Hansch, A.Leo and R. W. Taft, *American Chemical Society*, 1991, **91**, 165–195.

UCPH NanoScience
NanoVidenskab KU

tidsskrift.dk/index.php/NanoVidenskabKU

Thesis Paper

Predicting insertion: external force application onto cells allow nanowire arrays to insert into cytosol

Nicolai Vanggaard Bærentsen*, Nina Buch-Månson, and Karen L. Martinez

Received June 2017, Accepted April 2018

The use of vertical nanowires in biosensing application is limited by the extend of how efficient nanowires can reach the intracellular domains. Studies have found nanowire insertion to be successful through single nanowire experiments with high force pr. nanowire, using AFM. This is inadequate for producing high throughput analysis of several cells with multiple nanowires inserting in each cell. Here, we present a model for prediction of the nanowire insertion rates, when centrifugating cell samples down onto arrays of vertical indium arsenide nanowires, with a diameter of 100 nm, height of 3 μm and spacing of 3-5 μm. The model utilizes sedimentation rate of cells in conjunction with the centrifugal force field applied to objects subjected to centrifugation. Various conditions tested with the model, including lowering the temperature of the experiment from room temperature to 4 °C, show that cell viability is not negatively affected by any of the conditions. The insertion rate has been shown to be largely affected by the density of the nanowire array substrate, with a lower density resulting in a higher NW insertion rate, as the model predicts. The percentage of cells with at least one successful nanowire insertion is, however, oppositely affected by density, as a higher density results in larger percentage of cells with successful insertions.

1 Introduction

Many scientific applications require entry into the inside of a living cell, with regards to detections of biochemical composition or delivery of larger molecules[1,2]. Vertical nanowires (NWs) are emerging as promising candidates for this task, with the addition of allowing high throughput methods by arranging NWs in highly ordered arrays. NWs have small enough dimensions to penetrate the plasma membrane without causing significant damage to the membrane or the cell[3,4]. Different NWs are currently being used in the field, in many different ways to access the intracellular parts, with varying lengths, diameters, geometric patterns, surface coatings etc. to try to approach the problem in as many ways as possible[2,5–7]. Examples utilizing NWs to study live cells include using a NW on an AFM tip to punch, into the surface of the membrane, gentle seeding of cells on NWs, a NW-based cell endoscope, and electroporation[1,8–14]. In addition to single NW experiments, highly ordered arrays of NWs have been developed, which allows for deeper understanding of cell/NW interaction. Calculations on cell/NW array interaction have shown that indentation can be predicted, since the difference between cell suspension and NWs indentation depends on whether the energetically gain of cell-surface contact with NWs and substrate can outweigh the cost of a NW invagination[15]. Arrays of NWs have also been used to co-deliver multiple different molecules and proteins into cells simultaneously by co-positioning them on the same NW array[2]. When arrays of NWs are utilized for insertion, as opposed to a single NW, the cell sometimes experience suspension on the NW arrays like tiny fakirs, while the viability of the cells remain unchanged in either condition[15]. Cells cultured on NW arrays of various diameter have shown to survive and proliferate for several days after seeding, though the highest viability rates result from the smallest NW diameter[12]. Furthermore, studies observing cellular health as affected by interaction of different types of NW arrays, show that membrane integrity, enzymatic activity, and other cellular functions have been maintained during NW array exposure, including on Indium Arsenide (InAs) NW arrays, that are used in these experiments[5]. Some publications on experiments of NW arrays as intracellular delivery methods have suggested that there are other factors, than the lipid bilayer, that plays a role in NW insertion, which has lead to the exploration of the cytoskeleton as a factor for penetration[6,12,14,16]. Studies have shown that the elasticity of the membrane, more specifically the actin filaments and mi-

*Bionanotechnology and Nanomedicine Laboratory, Department of Chemistry and Nano-science Center, University of Copenhagen, Universitetsparken 5, DK-2100, Copenhagen, Denmark. *Corresponding author, e-mail: gcf945@alumni.ku.dk*

crotubules, has a great influence on how successful insertion of a NW is [8]. The cytoskeleton protein mesh creates a structure which hardens the membrane and, depending on the cell type, requires a stronger force to indent it; preventing insertion from easily happening [11]. The presence of the cytoskeleton is, however, crucial for successful penetration of the plasma membrane, as studies on liposomes as well as many different cell types with cytoskeletons show that membranes consisting of pure lipid bilayer can not be ruptured by a nanoneedle(NW with a larger diameter) [8].

The fraction of cells having at least one NW inserted have shown to reach almost 100%, when using a high enough density of NWs, but the fraction of NWs that are inserted remain very low in publications where gravitational force alone acts to insert the NWs [13]. A mechanical model has established that insertion exclusively from gravitational pull only happens in very rare cases, and primarily in setups where the NW diameter is less than 10 nm [17]. Rare cases like this is not adequate for the development of a model for insertion rates, and thus the centrifuge is utilized to increase the force application during interfacing on NW arrays, with the hope that the additional force can lead to better insertion rates.

The theoretical force calculations are based on a model from a previously developed interfacing setup, in the research group, where cells were centrifuged directly down onto a NW array through a swing bucket centrifuge. This allow readily calculating force application on the cells, and adjusting the model in accord with the discoveries. The purpose of this study is to theoretically simulate the centrifugation of cells onto a substrate, and improve the experimental centrifugation based interfacing method. The method uses the consistent force of a centrifuge to force the array of InAs NWs through the cell membrane, as they sediment, and then allow determining viability and insertion in the cells afterwards through fluorescent confocal microscopy and widefield microscopy.

2 Materials and methods

Force calculations. Cell sedimentation speed (V_s) was calculated based on distance from cell to centrifuge (r), density of the cell (D), viscosity of the medium(η), centrifugal acceleration (ω)(Eppendorf 5810R), medium density (ρ), cell radius (R), and build up speed of rotor (Eppendorf A-4-81). The velocity was evaluated for each 0.01 second to be recalculated based on the new distance to the centrifuge center and new rotor speed. The calculations were made through scripting in Python 2.7, as were the graphics depicting the results.

Cell culture and preparation. Mammalian Flp-in™ T-REx™ Human embryonic kidney 293 (HEK293) cells were used as the staple cell line for the experiments, with a SNAP-TAC domain inserted at the Flp-in site in the plasmid. The SNAP-TAC was expressed upon addition of tetracycline to the media, as the tetracycline acted as a regulator of the active *tet* repressor homo-dimer, by unblocking the transcription of the Flp-in site. For all centrifugation experiments, a special Hyper-DMEM (420 mOsm/L) buffer was used (500 mL Dulbecco's Modified Eagle Medium (DMEM, Gibco), 7.2 g glucose (Sigma) and 10 mM $MgCl_2$ (Fluka), pH 7.4) to increase the osmolarity of the surrounding medium, in order to reduce the cytoplasmic volume of the cells, leaving the cells with surplus membrane. Prior experiments in the research group (unpublished data) have shown that using Hyper-DMEM promotes NW insertion further, compared to using regular buffer. Hyper-DMEM was only used during the experiments and not as growth medium. The mammalian cells were grown in a T25 culture flasks (Cellstar) in 4 mL 10% Fetal Bovine Serum (FBS, Gibco) in DMEM (growth medium) and split in order to monitor the confluency level. Prior to each centrifugation experiment, and always every 3-4th day, 4 mL of mammalian cell culture was split, by addition of first 2 mL 5 mM EGTA (Invitrogen)(for experiment) or Trypsin-EDTA (Gibco)(for normal splitting) in Phosphate-Buffered Saline (PBS, Gibco) at 37°C for 2 minutes, followed by addition of 2 mL growth medium and subsequent harvesting at 1200 rpm (Eppendorf 5702, Eppendorf A-4-38) for 2 minutes. The cell pellet was resuspended in either 1 mL (for experiments) or 2 mL (for normal splitting) DMEM. For experiments, the cells were counted to ensure a concentration of approx. 350,000 cells pr 50-100 μL. For normal cell splitting, 500 μL of resuspended cell pellet was transferred to a new culture flask with 3.5 mL 10% FBS in DMEM, 1.5 μM Blasticidin(Gibco), 2 μM Hygromycin B(Gibco), and left in incubator at 37°C, 5% CO_2 and >95% humidity. The mammalian cells were split in order to prevent too high confluency. Cells were split no later than two days before an experiment, in order to ensure a better separation of living and dead cells, by allowing the live cells time to adhere to the surface of the culture flask.

Interfacing by centrifugation. Initial experiments were carried out on glass slides to find suitable conditions for later testing on NWs. A 15 mL falcon tube was filled with 13 mL Hyper-DMEM buffer and adjusted to the correct temperature for the experiment. A glass slide and a fitting polystyrene adapter(custom made at on-site workshop) were washed in 70% EtOH and MQ H_2O. The glass slide was then inserted into the adapter, to create a flat surface for the cell to hit during experiments, and slowly lowered into the test tube, while keeping the slide in place. The addition of the adapter to the tube brought the combined volum of the contents to the 15 mL mark, and ensured that the cells would travel exactly 8 cm in the test tube, before

reaching the bottom. Approximately 350,000 cells were extracted from the cell culture, equivalent to 50-100 μL depending on the cell growth, and gently pipetted onto the meniscus, followed by immediate centrifugation of the test tube, in order to limit possible premature sedimentation. After centrifugation the adapter, including the glass slide, was gently lifted out of the tube, and the glass slide was placed in a 25 mm petri dish (VWR) with 2 mL Hyper-DMEM and left to rest in at 37 °C for 4 hours. The part of the experiments regarding interfacing was exactly identical for glass slides and NW arrays, with the exception of which substrate was placed in the polystyrene adapter.

Viability assay. After 4 hours, three fluorophores were added to the petri dish to allow differentiation between living, dead and total cell count. For mammalian cells centrifuged onto glass slides, the SNAP-TAC was not expressed, instead the cells were dyed with 3 μM Calcein AM (Invitrogen, peak excitation: 495 nm and emission: 515 nm[18]), 6 μM Ethidium homodimer-1 (EthD-1, Invotrogen, peak excitation: 528 nm and emission: 617 nm[19]), and 5 μM DRAQ5 (Biostatus, peak excitation: 600 nm and emission: 697 nm[20]). After staining, the cells were visualized using a wide field microscope (Leica DM 5500, upright fluorescent wide field) with the following filter cubes: GFP (excitation: 470 nm $\pm$40, nm emission: 525 nm $\pm$25 nm) to identify signals from Calcein, Cy3 (excitation: 531 nm $\pm$40 nm, emission: 593 nm $\pm$40 nm) for signals from EthD-1, and Cy5 (excitation: 620 nm $\pm$60 nm, emission: 700 nm $\pm$75 nm) for signals from DRAQ5. Image analysis was conducted using ImageJ freeware.

Nanowire penetration assay. For experiments with NW arrays, 20 μL tetracycline (0.5% volume)(Sigma) was added to the 4 mL cell culture, to initiate the expression of the SNAP-TAC, approximately 24 hours before use. During the resting period after centrifugation, an additional 10 μL tetracycline was added to the 2 mL Hyper-DMEM to keep the expression of the SNAP-TAC at a high level. After 5 hours of resting time, the NW chip was moved from the petri dish to an 8-well μ-slide chamber (Ibidi) containing 300 μL Hyper-DMEM and 5 μM SNAP-Surface 649 dye (New England Biolabs, excitation: 655 nm, emission: 676 nm[21]), in order to attach the dye to the SNAP-tag, and left at 37 °C. After 30 minutes, the NW array chip was washed twice with Hyper-DMEM, and transferred to a microscope chamber pre washed with 70% EtOH and MQ H_2O, containing 300 μL Hyper-DMEM, 3 μM calcein AM and 6 μM EthD-1. The microscope chamber was rested for 5 minutes in darkness, to shield the fluorophores and to let the dyes bind, before visualization on the wide field microscope, for viability images, and inverted confocal microscope (Leica TCS SP5), for NW insertion detection. The settings for the confocal microscope were: 8 bit, 400 Hz, bidirectional scan, zoom 5, z-step 0.17 μm, between stacks. The specific laser settings for the different inspections were as follows: For surface and NW: HeNe 633 nm at 3%, reflection 623-643 nm, variable gain. For Calcein: Argon (0%) 488 nm at 3%, emission 508-540 nm, variable gain. For SNAP-Surface 649: HeNe 633 nm at 20%, emission 653-750 nm, gain 1000 V, line average 4. Image analysis was conducted using ImageJ freeware.

3 Results

The experimental results were obtained by centrifugation cells onto a flat glass slide through 8 cm of buffer in a test tube (Figure 1). After centrifugation the glass slide was incubated at 37 °C for 4-5 hours followed by staining and counted to test viability. Following the data analysis the experiment conditions were optimized and conducted using nanowire (NW) arrays, instead of glass slides, to test for insertion efficiency.

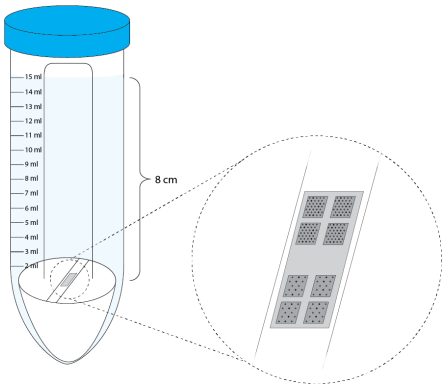

Fig. 1 The physical setup of the test tube with a chip of NW arrays resting in a narrow slit in a polystyrene adapter. The tube was filled with ~13 ml Hyper-DMEM buffer and upon addition of the adapter, the meniscus reached 15 ml - equivalent to 8 cm from chip to top. The adapter could be inserted/removed from the test tube by holding the long metal hoop extending beyond the buffer solution. Immediately before centrifugation the cells were added to the top of the buffer.)

Calculations of force application

In order to achieve the best possible insertion rate of NWs into the cells, the force applied onto the cells have to be maximized as (Berthing *et al*, 2012)[22] showed that gravitational force application alone is insufficient when it comes to penetration of the cell surface. As such, increasing the force between NW and cell surface was suspected to reduce the majority of failed membrane and cytoskeleton penetrations. The insertion rate was tested theoretically in two phases: first by calculating the velocity of cells during

centrifugation in the setup available and second by calculating how the parameters of the centrifuge available affects the total centrifugation time.

Velocity of cells during centrifugation

In order to produce a sensible model for NW insertion into cells, calculations on the cell sedimentation rate, and its dependencies, was performed by following (Katkov *et al*, 1999)[23], using the function for calculating sedimentation velocity of a cell:

$$v_s = \frac{2R^2 \cdot (D-\rho) \cdot \omega^2 \cdot r}{9\eta} \quad (1)$$

where v_s is the velocity of the cell, R is the radius of the cell, D is the density of the cell, ρ is the density of the medium, ω is the angular velocity of the rotor, r is the distance from the cell to the center of the rotor, and η is the viscosity of the medium (DMEM)(Bacabac *et al*, 2005)[24]. The angular velocity is a function of time and can be calculated as $\omega(t) = \frac{t}{34} \cdot \omega_{\max}$, as the centrifuge takes 34 seconds to reach max speed of ~440 radians/second(3000 G). The distance travelled by the cells is calculated after each 0.01 second, based on the velocity of the cells and the velocity of the rotor as it builds up its speed. A graph depicting the velocity of the cell sample during centrifugation as a function of time was made by simulations in Python shown in Figure 2. From the data points of the graph, the time of impact at $t_{R=0.15m}$, can be calculated as the sum of the velocity v_s times 0.01 second per iteration n until the sum = 0.08 m. This will show at which iteration the cells have travelled the 8 cm in the test tube, and be at the 15 cm mark, as they start 7 cm from the center of the rotor. The procedure is similar to integrating the function of the curve, but in this case more precise since a regression function would be needed. The calculations show impact time to be 23.43 seconds or about $2/3$ of the time the centrifuge takes to reach max velocity (ω), meaning that the cells reach the bottom even before the centrifuge is at full speed.

The model shown in Figure 2 assumes no sedimentation prior to centrifugation initiation, a practically impossible scenario, and the sedimentation time is therefore likely to be affected and thereby slightly lower.

The centrifuge parameters tested for effects on the final centrifugation time were the maximum angular velocity of the centrifuge, the maximum distance from the center of the rotor that the cells can reach, and the build up speed of the centrifuge.

Plotting time needed to reach the bottom as a function of two of the three parameters with the remaining being at the default setup, shows how each parameter influences the time in the setup (Figure 3). Faster centrifugation time results in most cases, in higher velocity and greater force

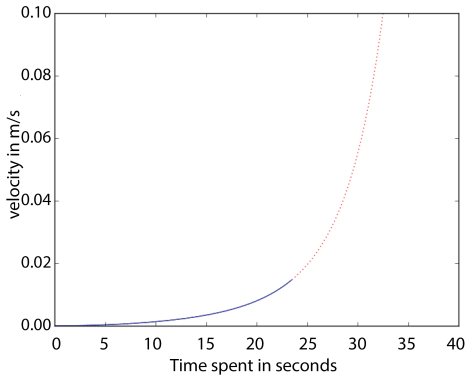

Fig. 2 The graph depicts the velocity of cells vs time. The blue line represents the segment of the speed reached by the cells in the possible setup with the centrifuge, which means a max final distance of 15 cm. The red line represents the theoretical propagation assuming an infinitely deep tube. The graph is made using Python 2.7. y-axis: velocity (m/s); x-axis: time (s))

exerted on the cells, with the exception of near-zero results where the short centrifugation time is more likely attributed to the miniscule travel distance. As seen in Figure 3A the change in either final distance travelled or angular velocity does not appear to significantly affect the time required in the regime of the default setup. Figure 3B does however indicate that build up time of the centrifuge lowers the time spend from ~20 seconds to $<$10 seconds at 0 seconds build up. For both Figure 3A+B the time scale is significantly larger than the time scale for Figure 3C due to the major impact from the angular velocity of the rotor in the low regime $<$150 radians/second. The build up time parameter is seen as having the greatest impact on centrifugation time and thus cell velocity at impact, as can be seen in Figure 3C. Going from 34 seconds in the default setup to optimally 0 seconds decreases the time spend by more than a factor 5, and with an almost linear effect on the time, a relative change to the default setup would bring the greatest impact to time spent.

From the above calculations, it appears that the cells can reach the bottom of the test tube significantly faster than previous experiments conducted in the research group assumes(unpublished data), where a 120 second centrifugation time was employed. To test if centrifugation time has any influence, and how great it possibly is, a setup with a glass slide was tested to see the effect on viability. In case this showed a constant amount of cells, the calculations on sedimentation time would be confirmed. A set of values was determined to be used in the following experiments, where one or two were varied at a time. They will subsequently be referred to as the default parameters (end distance from rotor = 15 cm, angular velocity of the rotor = 2*π*70 or approximately 440 radians/second (3000 G),

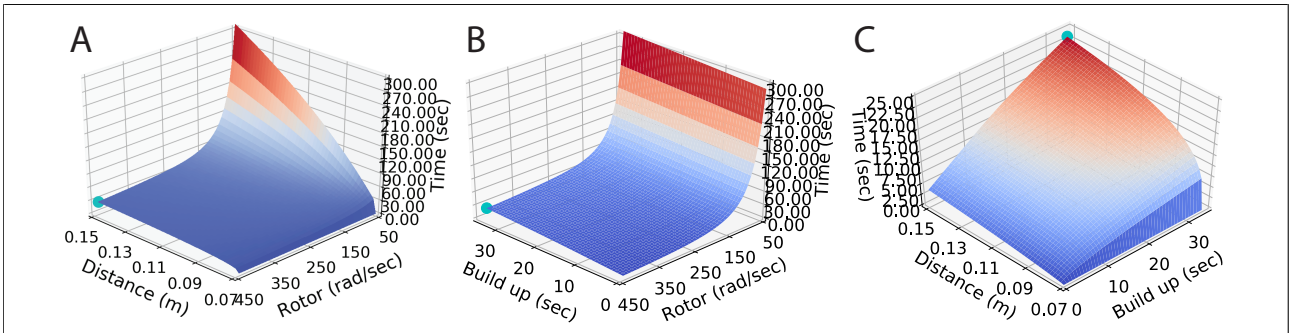

Fig. 3 3D plots of the time required to centrifuge a cell to the bottom, by changing two conditions at a time and leaving the third by default. The teal point marked on each graph indicate the default settings. A: Changes of the travel distance inside the tube (r) and the angular velocity of the rotor (ω). B: changing the build up speed of the centrifuge and the angular velocity of the rotor (ω). C: changing the travel distance inside the tube (r) and the build up speed of the centrifuge. The default parameters are r=0.15 m, ω=2*π*70 radians/second, build up speed of the centrifuge = 34 second. The graphs are made with Python 2.7.

build up speed = 34 seconds and centrifugation time = 60 seconds). After analyzing the effects, if any, centrifugation time has on cell viability and availability at the bottom, the best parameters were chosen for NW array insertion experiments, where the parameters were evaluated to optimize insertion efficiency.

Viability tests on glass slides

The viability tests were made by centrifugation of a droplet of cells onto a glass slide resting as a flat surface on the adapter inside the test tube (Figure 1). The cell line employed was a Flp-in T-REx HEK293 stable cell line, which was dyed using calcein AM and ethidium homodimer 1 (EthD-1) and DRAQ5. The images were produced with a wide field microscope, using GFP, Cy3 and Cy5 (data not shown) filter cubes. All assays using the glass slide substrate were tested using the default parameters, but with varying centrifugation time. The experiments on glass slides were carried out at two different centrifugation times, one at 120 seconds as a reference point and upper margin, as this was the centrifugation time at which all previous experiments in the research group had been conducted at, and one 60 seconds to see whether it could lead to any significant differences (Figure 4A+B). An increase in cell viability at 60 seconds compared to 120 seconds (77.77% survival for 60 seconds vs 69.32% survival for 120 seconds) was observed (Table 1). Because of this another experiment with 30 seconds of centrifugation time was conducted to investigate whether this tendency would continue even at shorter centrifugation times. The cells were also centrifuged for 60 seconds as a control in this experiment, to be able to directly compare the state of the cells relative to the previous experiment. Even though cell viability after 60 seconds of centrifugation time decreased in the second experiment, compared to the first experiment, the relative cell viability after 30 seconds of centrifugation was still higher (Figure 4C+D, 75.12% survival for 30 seconds vs 71.81% survival for 60 seconds). Assuming the average cell viability for 60 second centrifugation time lying somewhere in between the two measurements, and the cell viability at 30 and 120 seconds are adjusted accordingly, there is clearly a change between 30, 60 and 120 seconds of centrifugation time. The viability tests

Table 1 The viability of the cells from two individual experiments, the first conducted at 60 and 120 seconds, and the second conducted at 30 and 60 seconds. The cells were centrifuged onto glass slides, using the default parameters with varying centrifugation time, to test the effect of centrifugation time as well as impact force on the viability of the cells.

Experiment/ centrifugation time (sec)	30	60	120
1		77.77%	69.32%
2	75.12%	71.82%	

of glass slides show that centrifugation time has some influence on the viability of the cells, but is most likely not the difference between the results as seen and a 100% survival rate, since changing from 120 seconds to 30 seconds only resulted in ~10% more surviving cells. This suggests that, of the two conditions tested, initial impact is probably the greater contributor towards cell death rather than prolonged exposure to centrifugation. From the images of the viability experiments it appears that the shorter centrifugation times (Figure 4C+D) effects to total amount of cells reaching the bottom. For each experiment eight wide field microscope images were taken at various locations on the glass slide, to provide an average result of the cell density and viability. For the first experiment, the average amount of cells that reached the bottom, that is the total cell count on each image, for the 60 second and 120 second tests had less than 1% variation between them (data not shown). For the second experiment, with centrifugation times of 30

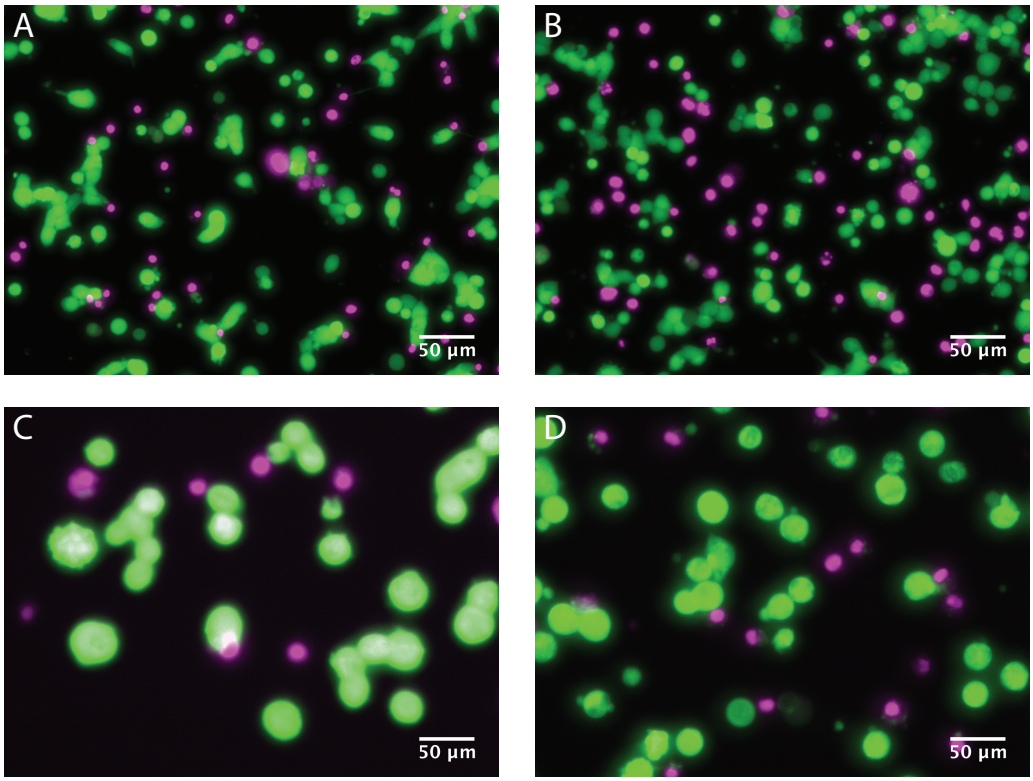

Fig. 4 Viability tests of cells centrifuged onto glass slides using the default conditions and varying centrifugation time. The green channel show the living cells dyed with 3 μM Calcein AM, and the magenta channel show dead cells dyed with 6 μM EthD-1. The nuclei of the cells were also colored using DRAQ5 (data not shown), to ensure that the total cell count was within a reasonable margin of the living and dead combined. (A) experiment 1 at 60 seconds; (B) experiment 1 at 120 seconds; (C) experiment 2 at 30 seconds; (D) experiment 2 at 60 seconds. Images were obtained with wide field microscopy, using GFP and Cy3 filter cubes. In all four images it is clear that the amount of living cells outnumber the dead by a large ratio.

seconds and 60 seconds, the variation was 18% (data not shown). The difference in average cell count between the two sets of experiments is however a factor 5-7. This suggests, that even though there is a significant change in the total amount of cells at 30 seconds and 120 seconds, and the two 60 second experiments, the difference originates not from centrifugation time but rather from the amount of cells used in the two experiments. Therefore cell death is most likely caused by multiple factors, including some that are not directly related to these experiments. Dead cells were only removed from the cell culture before splitting when all living cells adhered to the surface, and thus any treatment thereafter producing dead cells was unavoidable, such as the slower centrifugation at 1200 rmp (~20 radians/second) during harvest of the cells for the experiment. Based on the initial calculations and the viability tests on the glass slides, the centrifugation time for the NW arrays was set to 60 seconds, as 120 seconds would increase the risk of cell death and 30 seconds might be too short if the effect of continuous exposure had any influence on the insertion rate.

Nanowire insertion assay using arrays of equally spaced nanowires

For the NW insertion assay, the HEK 293 cell line had their SNAP-TAC expressed, to allow binding of the SNAP-Surface 649 dye used. The dye tag, is attached to the TAC part, which has a transmembrane helix anchoring the complex in the membrane. The expression of SNAP-TAC is initiated upon addition of tetracycline, which binds a *tet* repressor homodimer upstream of the flp-in site causing the repressor to disengage and allow for transcription of the gene, ~24 hours before use. The SNAP-tag binds SNAP-Surface 649 dye which labels the membrane and the cytosol is stained with calcein AM. The calcein AM enters viable cells due to the hydrophobicity of the AM derivative, then once inside the cytosol, intracellular esterases cleave the AM groups off of the non-fluorescent calcein AM, leaving fluorescent calcein inside. Only viable cells have active esterases and thus dead cell will not produce the fluorescence. The resulting images were produced on an inverted confocal microscope as a series of Z-stack images made on various locations of the chip. Along lines of

NWs under the cells, the Z-stacks were inspected orthogonally to see the effect of NWs in the cell. The arrays used consisted of NWs arranged in an isometric pattern with either 3 μm or 5 μm between each NW. These will hereafter be referred to as 3 μm and 5 μm density. All array chips originated from the same batch and all of its NWs were 3 μm high with a diameter of 100 nm. Figure 5 show the anticipated effect of NW insertion in a cell through detection of calcein (Figure 5A) and SNAP-Surface 649 dye (Figure 5B). The calcein dye only functions in live cells, and is not visible when a NW is taking up space as it eliminates the fluorescent signal. As such all NWs should, however indirectly, be visible as a shadow against the signal, and this is used a reference to verify whether a NW is present or not. The SNAP-Surface 649 dye binds to the surface of the SNAP-TAC on the membrane and should show the perimeter of the cell as well as any NWs that deform the surface to wrap around it, however the signal is not visible if the NWs penetrate the plasma membrane. Figure 5C show the expected composite image, where the shadows in the calcein signal verify the presence of a NW inside the cytosol, and the SNAP-Surface 649 signal show NWs that have indented but not penetrated the surface. According to

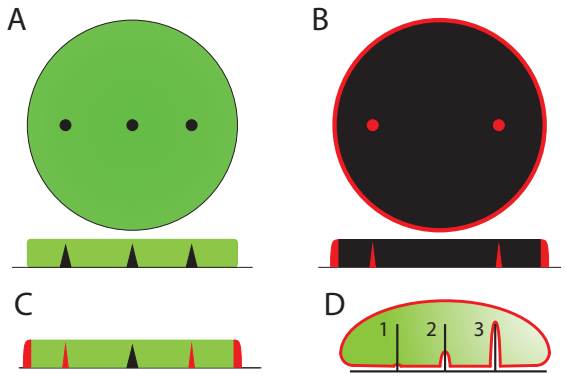

Fig. 5 Simplified illustration of a cell covering three NWs, where two are indenting the cell plasma membrane and one is penetrating it. (A+B) The circular shape is a slice of a cell as seen from above, and the dots are NWs underneath. The bars below are expected orthogonal view of Z-stacks along a line of NWs, where black is a shadow cast by the NWs, red is the cell plasma membrane at the perimeter of the cell and where indentation is observed, and green is cytosol. (C) expected composite image of two orthogonal views of A and B. (D) side view of a cell with a fully inserted NW (1), partially inserted (2) and completely indenting NW (3).

(Xie *et al*, 2013)[17] the force required for successful insertion is ~1.78 nN for a single nanostructure (with a diameter of 50 nm) on an AFM-tip, indicating that a denser array of NWs would lead to less successful insertion rate, as the force is distributed onto several NWs. The force exerted onto the cells was calculated with conditions at the time of impact with the default setup, and under the assumption that the cell has a spherical volume. The centrifugal net force on the cell is given by:

$$F = m * \omega(t)^2 * r \tag{2}$$

where F is force, m is mass of the cell, ω(t) is the angular velocity of the rotor at impact time t, and r is the distance from impact point to the center of the rotor. Here F is calculated to be 16.9 nN or approximately a factor 10 larger than the documented requirement for a single penetration, meaning that cells covering just 10 NWs or more are likely to have high rates of penetration failure.

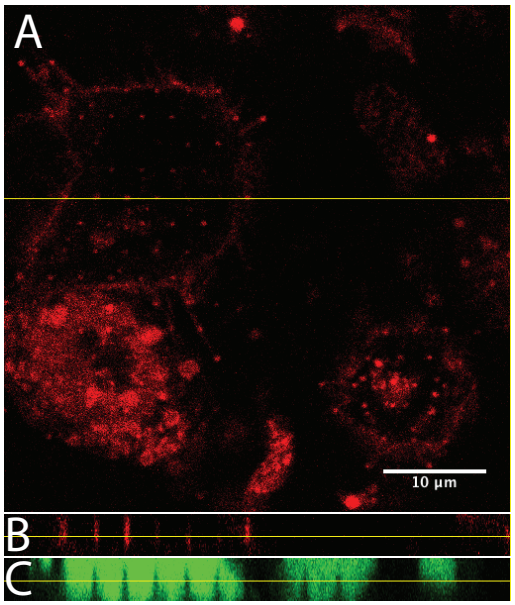

Fig. 6 (A) confocal slice through several cells as they appear after centrifugation on a NW array with 3 μm between each NW, at 60 seconds with default setup. Red is the SNAP-Surface 649 dye binding to the SNAP-tag on the outside of the membrane. The yellow line indicates the location of the orthogonal view. (B-C) orthogonal view of Z-stack showing the cytosol (green) dyed with calcein and the membrane (red) dyed with SNAP-Surface 649. Black shadows in the cytosol represent vertical NWs eliminating the signal. Red vertical lines represent membrane bending around the NWs as they indent the membrane. A shadow in the green channel without a corresponding red vertical line shows a NW that has successfully penetrated the membrane. The perimeters of the focal plane were set to the apical side of the cell and at the surface of the substrate.

Figure 6A shows a visual cut-through of a cell that covers more than 30 NWs but still has some NWs that are successfully inserted into the cell. Figure 6B-C shows the orthogonal view through the z-axis at the position indicated with the yellow line, and the green calcein signal

Table 2 Counted data from two experiments (RT, 60 seconds and 4 °C, 60 seconds) as well as data from a previous unpublished experiment from the research group (RT, 120 seconds). The counts represent a sum of 6-10 images of cells and account for the amount of NWs covered by each viable cell in the images as well as the amount of NWs that have successfully or partially inserted into the cell. Each row show a different condition with the corresponding insertion efficiency, how many cells had at least one NW inserted and how many NWs were covered by a cell on average.

Density (μm), temperature and time (seconds)	NW covered	NW inserted	% NW insertion	% cells inserted	wires/cell (avg.)
3, RT, 60	223	25	10.00%	56.25%	15.5
5, RT, 60	82	11	11.83%	31.25%	2.90
3, 4°C, 60	107	5	4.46%	30.77%	8.86
5, 4°C, 60	7	1	12.50%	16.67%	1.14
3, RT, 120			8.15% (S_E= 1.35)	62.28% (S_E= 8.45)	
5, RT, 120			13.81% (S_E= 5.00)	57.98% (S_E= 6.84)	

with shadows cast by the NWs as expected. The red membrane signal however shows that insertion has failed for the majority of the NWs, in accordance with the expectations. Cells on the 3 μm spacing arrays cover anywhere from 10 to +30 NWs with an average of 13.75 NWs, whereas the 5 μm spacing arrays only has cells covering less than 10 NWs with an averaging of 3.36 NWs. Both 3 μm (Figure 6A) and 5 μm (data not shown) density show cells with NWs inserted, with a larger fraction inserted with the 5 μm spacing (Table 2), as expected from the calculations. However, the difference in total amount of NWs inserted could also originate from a difference in the amount of NWs present under the cells. An increase in sheer numbers would potentially increase the number of insertions, until a certain density is reached at which point the NWs act as a flat surface to the membrane, or the force is diluted too much by the distribution on a denser NW array. The percentage of cells with at least one NW inserted is significantly higher for 3 μm density compared to 5 μm density arrays and the total amount of successful insertions follow the same trend. This suggests that the density of successful insertions are equally spread on the available cells in both 5 μm density and 3 μm density NW arrays. This means that the rate of cells with successful insertion is governed by the amount of NWs and not the density of the NW arrays.

Nanowire assay at 4 °C

According to (Kawamura *et al*, 2016)[10], lowering the temperature to 4 °C should increase the insertion rate, by rigidifying the membrane. Therefore, an experiment was set up, with the temperature of the cells and the medium reduced to 4 °C prior to centrifugation, to see if this would create a more stiff membrane, allowing for higher rates of insertion. Figure 7 shows three cells where the orthogonal view is taken from the yellow line, and shows that the NWs are all deforming the membrane and failing to insert into the cells. At 4 °C, the 3 μm density has an insertion rate that is approximately half of that of the RT (room temperature ~25°C) experiment, which could be influenced by the reduced number of NWs, as the amount of NWs covered by each cell is also approximately half of that for the RT experiment. Subsequent investigations of the chips showed that, especially on the 5 μm density arrays, several NWs were missing so that no cells were found to cover more than one NW, thus de facto mimicking an infinitely low density. The same issue was also partially observed for the 3 μm density arrays, where the fraction of missing NWs only affected the density in certain areas below the cells as the cells spanned a much higher number of NWs. For the two 5 μm arrays, the average number of NWs covered by each cell is less than half at 4 °C but unlike the 3 μm arrays, the % NW insertion rate is slightly higher (Table 2), probably due to the low availability of NWs in the 5 μm array, leading to statistical anomalies. Ideally, the insertion rate would be higher when the array density get smaller, as the force is distributed on only one wire instead of many. The NW arrays were also observed in the fluorosence widefield microscope to see if the presence of the NWs would change the death rate of the cells. Both experiments (Table 3) show a survival rate of ~75-80%, at RT and 4 °C, indicating that neither the NW nor the colder environment had any significant influence on the viability of the cells during centrifugation as compared to the glass slides experiments at 60 seconds(Table 1). From table 4 it can be seen that across all results from the 60 second experiments, a tendency towards single NW penetration is evident. The lack of statistical variation in the number of NWs inserted in each cell is clearly expressed, as the

Table 3 The viability rates of cells from the experiments on the 3 μm density NW arrays. Both experiments were centrifuged for 60 seconds.

NW array, RT	79.10%
NW array, 4°C	77.73%

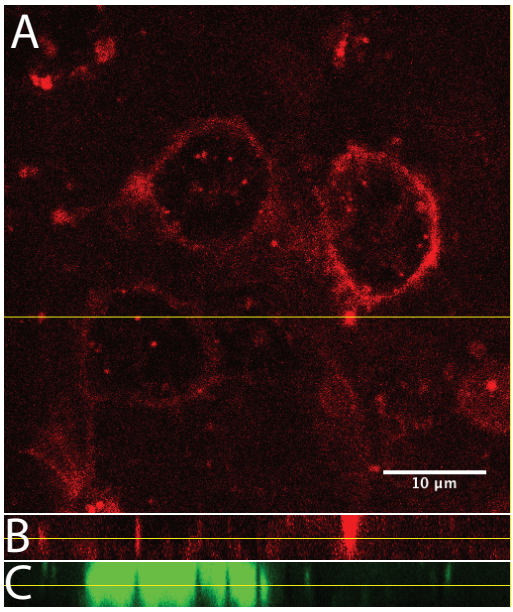

Fig. 7 (A) confocal slice through several cells as they appear after centrifugation on a NW array with 3 μm between each NW, at 60 seconds, 4 °C, with default setup. Red is the SNAP-Surface 649 dye binding to the SNAP-tag on the outside of the membrane. The yellow line indicates the location of the orthogonal view. (B-C) orthogonal view of Z-stack showing the cytosol (green) dyed with calcein and the membrane (red) dyed with SNAP-Surface 649. Black shadows in the cytosol represent vertical NWs eliminating the signal. Red vertical lines represent membrane bending around the NWs as they indent the membrane. A shadow in the green channel without a corresponding red vertical line shows a NW that has successfully penetrated the membrane. The perimeters of the focal plane were set to the apical side of the cell and at the surface of the substrate.

number of cells with NWs inserted for each condition only includes 5-11 cells. For the 4 °C experiment, just one additional cell with two or three NWs inserted would change the percentage of both cells that have NWs inserted, and the rate of NWs inserted, by quite a bit. As such the distribution of inserted NWs on different cells are quite different from the 120 second setup because of the relatively few data points.

4 Discussion

From the results it is observed that the centrifugation time is determining the viability of the cells when centrifuged on both glass slides and NW arrays. However, the time merely changes the fraction of dead cells by a few percent rather than produce an all or nothing scenario. The tests on NW arrays show that at both RT and 4 °C are the NWs

Table 4 Calculated data from two produced experiments (RT, 60 seconds and 4 °C, 60 seconds) as well as data from a previous unpublished experiments in the group (RT, 120 seconds). The calculations show the distribution of inserted NWs inside cells with at least one NW.

Density (μm), temperature and time(seconds)	1 NW	2 NWs	+3 NWs
3, RT, 60	73%	0%	27%
5, RT, 60	82%	18%	0%
3, 4°C, 60	40%	0%	60%
5, 4°C, 60	100%	0%	0%
3, RT, 120	32%	22%	46%
5, RT, 120	75%	14%	11%

inserted into the cells, though the primary data would suggest that insertion at 4 °C is somewhat lower compared to RT. The difference in insertion rate between 3 μm and 5 μm follows the hypothesis that a lower density leads to larger force application per NW and thus a higher insertion rate.

Comparison of insertion rate and cell penetration with previous experiments from the research group, using the same setup but with different centrifugation time shows how this parameter affects the results(Table 2). NW insertion rate for both 3 μm and 5 μm at 120 second centrifugation time appear in the same range as the tested values, except for the 4 °C 3 μm result which is off by about a factor 2, suggesting that prolonged centrifugation has a mild or no effect on insertion when it comes to RT experiments.

Since the centrifugation time is observed to only slightly affect the insertion rate, but to have a clear relation to cell death, centrifugation time is thus a less important factor in determining the optimal conditions. This means the data supports the original hypothesis that the initial impact of the cells is the primary cause for NW insertion. The variation however, in number of cells with at least one NW inserted is significantly greater across all experiments with the highest percentage for both 3 μm and 5 μm at the 120 second experiments. It can be deducted that even though the same fractions of NWs are inserted into cells, the fact that the actual successful insertions are spread out on many cells, can hardly be attributed to the increased centrifugation time.

From the experiment conducted at 4 °C it is seen that fewer cells have NWs inserted, and at least for 3 μm density, there is also a lower fraction of all NWs that are inserted. The low temperature has likely had the desired effect of making the cytoskeleton more rigid, but also the undesired effect of hardening the cell membrane as a whole, which explains the low rate of cells with NWs inserted. This could probably be countered by an increase in applied force through speed up of the centrifuge. (Kawamura *et al*, 2016)[10] found that cooling the cells would increase inser-

tion rate when tested with AFM, but in their experiments, they used a single tip along with a force of 40 nN to rupture the plasma membrane at a single location, which is quite far from anything that have been tested here; indeed the closest setup is the 5 μm array that had an insertion rate of 12.5%, similar to the results from the RT tests. To provide a definite conclusion on whether 4 °C has a positive effect on insertion, using our conditions, more independent experiments would have to be conducted.

The results used from the 120 second setup are collected based on a much larger data sets and therefore represent a greater statistical confidence. This also becomes clear from the arrangement of the NW insertion across the different cells.

(VanDersarl *et al*, 2012)[5] found that the success rate for nanostraw insertion through cell suspension was effectively seen to be 1-10% per nanostraw, and even as their setup had ~10-100 nanostraws of diameter >100 nm under each cell, they recorded a success rate of cell penetrated to be 40-70%. This could suggest that that a very high density array can still allow a high rate of cells with successful insertions.

5 Conclusion

In summary, this paper uses theoretical force calculations from a centrifuge acting on a cell sample, in conjunction with methods from recent publications to predict the effect of externally applied forces on cells as they sediment on arrays of NWs. The calculations predict that lower array densities will have greater chance of successfully penetrating the cell plasma membrane, as is indeed observed for experiments conducted at both 4 °C and RT. The effect of lowering the temperature of cells and medium to 4 °C does however not appear to positively affect the rate of NW insertion in general. Viability tests conducted at different centrifugation times, and with both NW arrays and glass slides as substrates show that cell viability is not affected by the presence of a NW array compared to a glass slide. It does however show that between prolonged centrifugation and initial impact the latter is the greater contributor to cell death, since centrifugation only had a minor impact of the viability. Based on the results showing that centrifugation time only has minor influence on NW insertion, and that initial impact seems to follow the theoretical model for force application, it is safe to say that initial impact very well could be the major cause for successful NW insertion, as originally suggested.

6 Acknowledgements

I would like to thank Bogdan Cristinoi and Nikolaj K. Brinkenfeldt for any help provided making the experiments for this paper.

References

1 C. Xie, Z. Lin, L. Hanson, Y. Cui1 and B. Cui, *Nature nanotechnology*, 2012, **7**, 185–190.
2 A. K. Shalek, J. T. Robinson, E. S. Karp, J. S. Lee, D.-R. Ahn, M.-H. Yoon, A. Sutton, M. Jorgolli, R. S. Gertner, T. S. Gujral, G. MacBeath, E. G. Yang and H. Park, *PNAS*, 2010, **107**, 1870–1875.
3 L. Lacerda, S. Raffa, M. Prato, A. Bianco and K. Kostarelos, *Nano today*, 2007, **2**, 38–43.
4 S. Bonde, T. Berthing, M. H. Madsen, T. K. Andersen, N. Buch-MåŁnso, L. Gu, X. L, F. Badique, K. Anselme, J. Nygård and K. L. Martinez, *A S C Appl. Mater. Interfaces*, 2013, **5**, 10510–10519.
5 J. J. VanDersarl, A. M. Xu, and N. A. Melosh, *Nano letters*, 2012, **12**, 3881–3886.
6 T. Berthing, S. Bonde, C. B. Sørensen, P. Utko, J. Nygård and K. L. Martinez, *Small*, 2011, **7**, 640–647.
7 T. E. McKnight, A. V. Melechko, G. D. Griffin, M. A. Guillorn, V. I. Merkulov, F. Serna, D. K. Hensley, M. J. Doktycz, D. H. Lowndes and M. L. Simpson, *Nanotechnology*, 2003, **14**, 551–556.
8 H. Kagiwada, C. Nakamura, T. Kihara, H. Kamiishi, K. Kawano, N. Nakamura and J. Miyake, *Wiley-Liss*, 2010, **67**, 496–503.
9 I. Obataya, C. Nakamura, S. Han, N. Nakamura and J. Miyake, *Nano Letters*, 2005, **5**, 27–30.
10 R. Kawamura, K. Shimizu, Y. Matsumoto, A. Yamagishi, Y. R. Silberg, M. Iijima, S. Kuroda and K. Fukazawa, *Journal of Nanobiotechnology*, 2016, **14**, 1–9.
11 A. Aalipour, A. M. Xu, S. Leal-Ortiz, C. C. Garner and N. A. Melosh, *Langmuir*, 2014, **30**, 12362–12367.
12 W. Kim, J. K. Ng, M. E. Kunitake, B. R. Conklin and P. Yang, *J. Am. Chem. Soc. communication*, 2007, **129**, 7228–7229.
13 A. M. Xu, A. Aalipour, S. Leal-Ortiz, A. H. Mekhdjian, X. Xie, A. R. Dunn, C. C. Garner and N. A. Melosh, *Nature communications*, 2014, **5**, 1–8.
14 R. Yan, J.-H. Park1, Y. Choi, C.-J. Heo, S.-M. Yang, L. P. Lee and P. Yang, *Nature nanotechnology*, 2011, **7**, 191–193.
15 N. Buch-Månson, S. Bonde, J. Bolinsson, T. Berthing, J. Nygård and K. L. Martinez, *Advanced functional materials*, 2015, **25**, 3246–3255.
16 J. T. Robinson, M. Jorgolli, A. K. Shalek, M.-H. Yoon, R. S. Gertner and H. Park, *Nature nanotechnology*, 2012, **7**, 180–182.
17 X. Xie, A. M. Xu, M. R. Angle, N. Tayebi, P. Verma, and N. A. Melosh, *Nano letters*, 2013, **13**, 6002–6008.
18 `\url{https://www.bdbiosciences.com/ds/pm/tds/564061}`, last visited, 30.05.17, 21.00.
19 `\url{https://www.thermofisher.com/order/catalog/product/E1169}`, last visited, 23.05.17, 11.00.
20 `\url{www.biostatus.com/site/biostatus/documents/DR5.TDS003040714.pdf}`, last visited, 01.06.17, 22.00.
21 `\url{https://www.neb.com/products/s9159-snap-surface-649}`, last visited, 23.05.17, 11.00.
22 T. Berthing, S. Bonde, K. R. Rostgaard, M. H. Madsen, C. B. Sørensen, J. Nygård, and K. L. Martinez, *Nanotechnology*, 2012, **23**, 0–0.
23 I. L. Katkov, and P. Mazur, *Cell Biochemistry and Biophysics*, 1999, **31**, 231–245.
24 R. G. Bacabaca, T. H. Smitb, S. C. Cowinc, J. J. V. Loona, F. T. Nieuwstadtd, R. Heethaarb and J. Klein-Nulend, *Journal of Biomechanics*, 2005, **38**, 159–167.

UCPH NanoScience
NanoVidenskab KU

tidsskrift.dk/index.php/NanoVidenskabKU

Thesis Paper

Speciation and structure of dipicolinate complexes and Eu(III) ions in solution

Patrick R. Nawrocki*

Received June 2017, Accepted April 2018

Complexation between Eu(III) ions and dipicolinate tridentate ligands (DPA) have been studied to expand on our current understanding of structural and photophysical properties of lanthanides in solution. The dynamic ligand-exchange of labile lanthanide ions, has made it difficult to properly identify the bis ligated Eu(III) complex, as optical spectroscopy only reveals a weighted average of the present species. In this article, evidence for the bis ligated Eu(III) complex will be presented, which is a necessary component in accurately determining the binding constants and to gain further insight in the structure-property relationship of the systems. Additionally, NMR, luminescence spectroscopy and X-ray scattering were used as structural corroboration to further establish the relationship between the solution structure and the intensities of Laporte parity forbidden *f-f* transitions, characteristic of the lanthanides.

Introduction

f-block elements are essential to our modern society. They have unique optical properties in the form of sharp transitions bands, and their electron configuration makes them exceptional components in magnetic applications.[1] They are also used in the medical field as contrast agents in MRI scans.[2, 3] Furthermore, understanding the solution chemistry of lanthanides are of great interest in dealing with the nuclear waste problem.[4] The chemistry of lanthanides, consist almost exclusively of complexation by coordination. This is a result of the 4f orbitals being contracted within the circumference of the 5s orbitals, effectively shielding the valence orbitals from outside interactions.[5] This phenomenon is the basis for many of the unique properties of lanthanides. Conversely, it also complicates elemental separation, as all lanthanides effectively behave as spheres of varying sizes. The current most effective method of separation is highly polluting, and is currently only done industrially in China.[6] A greater understanding of lanthanide solution chemistry, will lead to improvements of the separation method, eventually making lanthanides more readily available on a global scale.

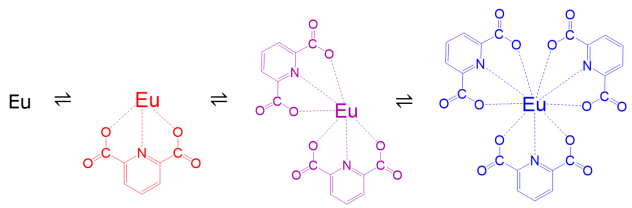

Figure 1 – Scheme of complexation equilibria for EuDPA in the aqueous, mono-, bis- and tris ligated species, with their related symmetries.

For this purpose, constructing and understanding lanthanide model systems as a foundation for lanthanide structure-property relationships in solution, is an essential step in lanthanide solution chemistry studies. For such a model system, Eu(III) is an excellent example because of its non-degenerate $^5D_0$ emissive state. Lanthanides possess strong spin-orbit coupling[7] This induces a large separation of absorption and emission bands, preventing spectral overlap in the spectra. Each transition will emit to $^7F_{J\ (J=0\text{-}6)}$ sub-levels of different degeneracies, and can be utilized to deduce structural information of the complex.

Of eligible ligands for this model system, classes such as acetylacetonate,[8, 9] cyclen-based polydentates[10, 11] and the tridentate dipicolinates,[12, 13] are among the most studied. Model systems of cyclen compounds is an active field, but DPA ability to form highly symmetric complexes with 9-coordinate lanthanides, merits its own field of research. Both the fully hydrated and the fully complexed europium ion has so far been reported to have tricapped trigonal prismatic structure in solution,

with D_3 point group symmetry. The mono ligated complex will have a lower C_2 symmetry and the bis ligated is presumed to have C_2 or C_S symmetry, depending on its immediate conformation. A representation of the dynamic equilibria of complexation can be seen in Figure 1.

Here, the foundation for a EuDPA based model system is laid, with the ambition for the model system to be applicable to other LnDPA complexes. So far, three objectives have been accomplished. Initially, a standard for sample preparation is formulated, with the purpose of successfully reproducing previously reported results with spectroscopic techniques. Then an investigation of DPA complex speciation is done. Despite the extensive studies of DPA based lanthanide complexes, the photophysical behaviour of these systems has been described without appropriate identification of the **2** species. Speciation is followed by optical spectroscopy and the trends modelled. Finally, the structure has been determined to confirm the presence of complex species in specific solutions, as predicted by NMR and optical spectroscopy.

Results and Discussion

Several samples were made with varying metal-to-ligand ratios. The 1:0, 1:1, 1:2 and 1:3 samples have been included in all investigations, as reference points to discern the specific properties of the mono, bis and tris DPA complexes. Additional samples have been produced for specific measurements, to probe complex speciation as the solutions shift into a different equilibrium domain. Especially the **2** complex has shown to be difficult to observe.[12, 13] Preparing the solution samples initially posed a challenge, as complexes of europium hydroxides would form at high pH. Below pH 2, the hydroxide complex was successfully dissolved, and a transparent solution observed, although DPA would start to crash out as dipicolinic acid if left at pH < 2. For 1:0 and 1:3 solution samples, precipitation will not occur. It appeared that the point of solvation for DPA and Eu(OH), respectively, were overlapping for solutions with lower DPA concentrations that 3 eq. of Eu.

Fortunately, precipitation was not observed until approximately 3 hours after reducing pH below 2 in samples with 20 µM Eu(III), so that measurements could still be made on the samples. Pictures of both precipitate types are shown in SI Figure 1 & 2.

To probe the speciation, a 14 point titration series was made for luminescence and diffraction measurements, with DPA concentrations ranging from 0 to 4 equivalents of metal ion. For the NMR studies, 8 samples were prepared with DPA eq. of 0 to 3. Due to the dynamic equilibria of the complexes and long lifetimes of the lanthanides, the excited states will frequently emit from a different species than the absorbing species. Lifetime data therefore illustrate a weighted average of these species. Therefore, only samples with DPA concentrations with stoichiometric multiples of the metal ions were prepared.

Establishing speciation

The titration series of Eu with DPA has been measured using time-gated emission spectroscopy, and are shown in Figure 2. The emission peaks match the characteristic $^5D_0 \rightarrow {}^7F_{0\text{-}6}$ transitions known for Eu(III) ions.[14, 15] The literature describe the development of the peak intensities as complexation proceeds.[1,2] Drastic changes in both intensity and crystal-field fine structure arise when the restrictions of the Laporte forbidden *f-f* transitions are relaxed as DPA coordinates.[5] The degree to which the Laporte selection rules are relaxed is specific for each distinct transition, and depends on the metal ions local symmetry. Emission spectroscopy can measure the changes in the spectral lines and intensities that are unique to each complex type. The symmetries can then be deduced using Tanner's method of descending symmetry by the crystal-field splitting,[7] as has been previously established.[12]

By understanding the changes in intensity and crystal-field splitting of the spectral lines, it should be possible to designate specific spectral signatures to each stage of EuDPA complexation. An example of this is the appearance of the $^7F_0$ transition peak in the presence of low symmetry **1** and **2**

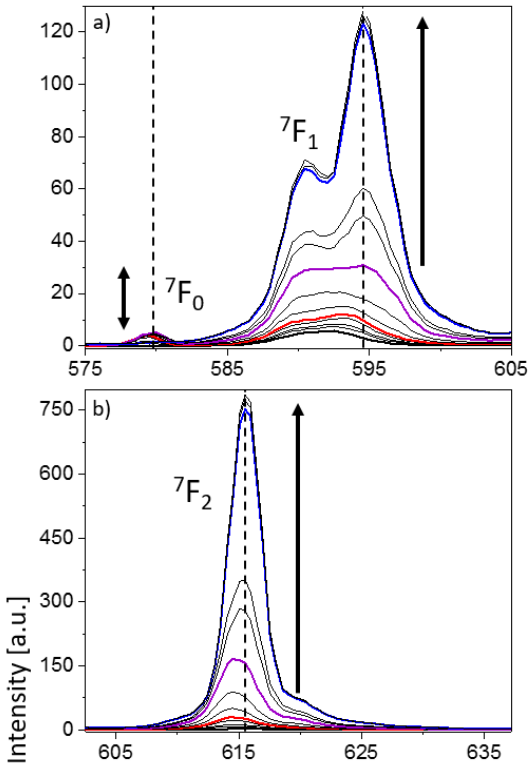

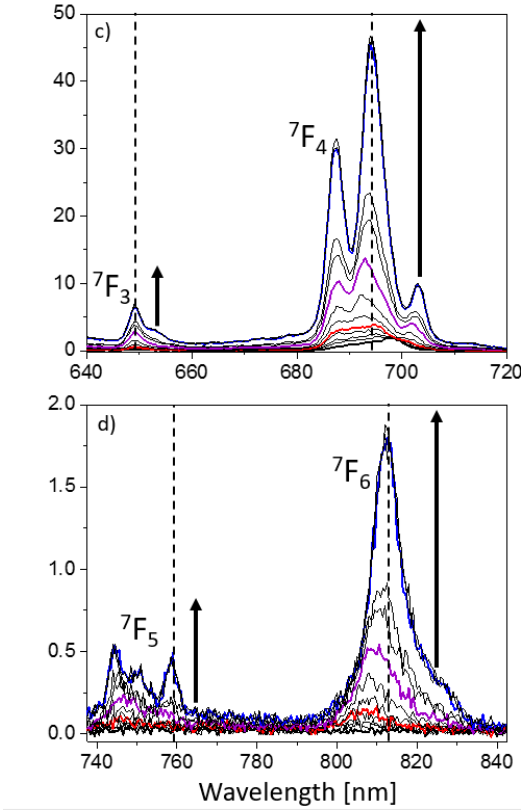

Figure 2 – Time-gated emission spectra of a 14 point titration of 0.02 M Eu(III) ions with increasing DPA concentrations from 0 to 4 equivalents of ligand molecules per metal ion in water. Complexation can be monitored by changes in transition peak intensities and splitting of spectral lines from crystal-field perturbations.

Table 1 – Calculated lifetimes and q for stoichiometric EuDPA solutions.

Eu:DPA	τ H2O [ms]	τ D2O [ms]	q (exp.)	q (lit.)[16]
1:0	0.1	3.9	10.1	-
1:1	0.2	3.2	6.0	-
1:2	0.4	3.0	2.8	2.9
1:3	1.0	3.1	0.5	0.3

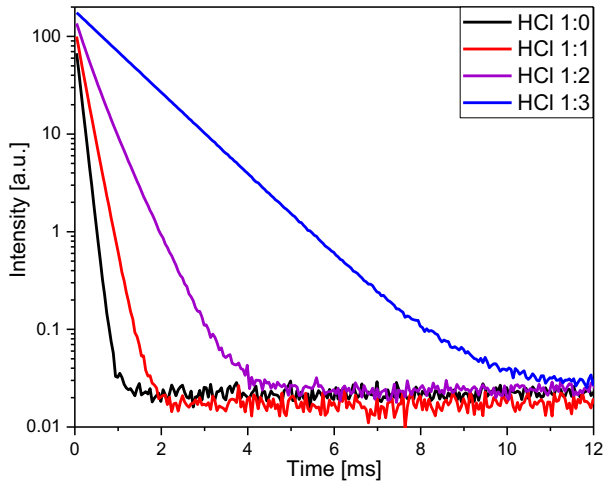

Figure 3 – Lifetimes of EuDPA complexes in H_2O. Inherent uncertainty increases as the lifetime decrease, as is the case of the 1:0 and 1:1 solutions.

complexes, and their consequent disappearance as the complexes shift towards **3**. The luminescence spectra show a definite development for complexation, but emission is unable to probe the distribution of species in solution. This is a consequence of fast ligand exchange rates characteristic of lanthanide metal ions as well as their long lifetimes in the millisecond timescale.

The spectra will therefore show a weighted average of the emissive species present in solution. An insight into the dynamic equilibrium of the solutions has been achieved by measuring the lifetimes of samples with integer multiple concentrations of DPA to europium. By measuring the lifetimes of these samples as well as their deuterated analogues, an approximation of the average number of solvent molecules in the inner coordination sphere can be determined. This can be calculated using the modified Horrocks equation, with the number of inner sphere solvent molecules denoted by q (Eq. 1).[17] The calculation accounts for the greater quenching effect that O-H oscillators have on excited states of europium(III) and terbium(III), as compared to the deuterated analogue of O-D oscillators. The modified Horrocks equation calculates the number of coordinated solvent molecules by considering this difference in quenching efficiency:

$$q = A(k(H_2O) - k(D_2O) - B) \qquad \text{Eq. 1}$$

With A = 1.2 ms^{-1} being the proportionality constant, and B = 0.25 ms^{-1} a correction for outer sphere effects, both specifically for Eu.[17] The calculated q's are listed in Table 1 along with previously reported values for the 1:2 and 1:3 solutions. In the absence of DPA, the hydration number of the 9-coordinate Eu(III) ion should be 9. For each added ligand, q should decrease by 3, with q = 0 when no water is present in the inner sphere, when the tris complex is achieved. Calculated q for the 1:3 solution is 0.5 and shows that the equilibrium is shifted towards **3** to a high degree, yet the solution does not consist entirely of this specie alone. This is in agreement with europium(III) ions forming labile complexes rapid ligand exchange. During ligand exchange, it is possible for water molecules to coordinate briefly, increasing the average value of q. It should be noted that while q is efficient at approximating the hydration number, the method has some inherent uncertainty when measuring solutions with short lifetimes. As is the case for fully hydrated Eu in H_2O as seen in Figure 3, and from the calculated q of 10.1 from Table 1.

The complexation can be monitored via q and by the intensities and splitting of J-sublevels of transition bands. Tanner's diagram of descending symmetry correlates the J-sublevel splitting with the symmetry of each complex species[7]. The same development was observed by NMR spectroscopy. Samples of varying Eu:DPA ratios were measured with ^{1}H-NMR spectroscopy as shown in Figure 4.

An advantage of NMR measurements of most lanthanide based complexes, are the large chemical shifts arising from paramagnetic Eu(III). The ^{1}H-NMR spectra of the titration series help to further facilitate the presence of each complex species. In the spectra of the EuDPA complexes, two peaks appear to be from the complex: one shifting from about 2.5 to 3.7 ppm, and another from 4.4 to 4.8 ppm. The large peak coming from water at 4.7 ppm overlap with the most shifted DPA peak, and should be supressed in further studies. The peak of DPA is presumed to

reflect the hydrogen atoms of the para- and meta-positions compared to the nitrogen atom of pyridine. Another possibility could be that both hydrogen atoms are represented simultaneously within the peaks, and that the peaks instead represent the averages of coordinated versus uncoordinated DPA. This could be established by using a DPA derivative with a substituent group with no hydrogens, in the para position of the nitrogen atoms.

NMR spectroscopy operate on the microsecond timescale. As ligand exchange rates of the complexes occur closer to the nanosecond timescale, the NMR spectra will portray a weighted average of the present species. On this basis, shifting of the peak

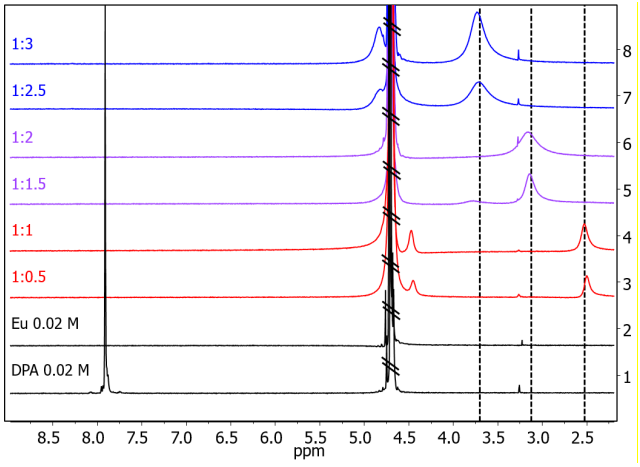

Figure 4 – Paramagnetic ^{1}H-NMR spectroscopy of EuDPA titration of 0.02 M Eu with equivalent DPA concentrations as shown on the figure. Both complex peaks show periodic shifts instead of a gradual migration, indicative of a single equilibrium being dominant in a given solution. The sharp water peak at 4.7 overlaps with the most shifted complex peak, why the peak shift between the 1:1.5 to 1:2.5 solutions is difficult to observe.

would be expected to be gradual if every equilibrium between the **0**, **1**, **2** and **3** complexes were expressed simultaneously. Instead, the peak shift are observed to be systematic, as spectra of the 0.5, 1.5 and 2.5 eq. Eu:DPA solutions are near identical to those of the 1, 2 and 3 eq. solutions, respectively. It can be assumed that each of these intermediate stoichiometric solutions, will assume the same dominant equilibrium, as the subsequent stoichiometric solution operates within. This agrees with the prediction, that the equilibrium of the 0.5 eq. solution as well as the 1 eq., is dominated by $Eu^{3+} + DPA^{2-} \rightleftharpoons Eu(DPA)^{+}$. When the ligand concentration surpasses that of the metal ion, the $Eu(DPA)^{+} + DPA^{2-} \rightleftharpoons Eu(DPA)_2^{-}$ start to become the prevalent equilibrium, of which the trends continues for $Eu(DPA)_2^{-} + DPA^{2-} \rightleftharpoons Eu(DPA)_3^{3-}$. A few points of interest could be explored further, such as probing the threshold at which a new dominant equilibrium is established, by expanding the titration series. Additionally, interchanging the paramagnetic europium complex core with a diamagnetic yttrium ion will help us understand the paramagnetic influence.

Electronic transitions in Eu(III)

Before proceeding to the discussion of europium(III)-based complexation, a short outline of the electronic properties of the metal ion is required, to justify the connection made between spectral results and the structure in solution.

Within the field of lanthanide photophysics, transition intensities of optical spectroscopy are commonly described by Judd-Ofelt theory.[18, 19] The theory attempts to express intensities in terms of dipole strengths and are calculated based on experimentally determined parameters. While the theory is capable of approximating the transition intensities, calculated intensities often differ from the experimental values by up to 15 %.[13]

This intrinsic uncertainty of the theory has prompted the use of the more fundamental Laporte selection rules as a framework. Rather than determining the exact intensities, the selection rules are used for predicting certain trends in transition bands.

For Eu(III), the $^{5}D_0 \rightarrow {}^{7}F_{0\text{-}6}$ transitions are induced electric dipoles, save for the magnetic dipole transition of $^{5}D_0 \rightarrow {}^{7}F_1$. They are induced transitions compared to standard electric dipole transitions, with much weaker intensities, as dictated by the parity rule. When a crystal-field perturbation is introduced, parity mixing is possible and the number of available Stark sublevels increase.

A correlation between the symmetry system and the quantum number J to determine the number of available Stark levels has been reported.[20] Selection rules for *f-f* transitions are listed according to symmetry by Tanner. The correlations between different transitions of $^{5}D_0 \rightarrow {}^{7}F_{0\text{-}6}$ and the solution symmetry can be extrapolated, and has been constructed by mathematical treatment of these phenomena.

The selection rules predict stronger intensities for induced electric dipole transition $^{5}D_0 \rightarrow {}^{7}F_J$ of J = 2, 4 and 6, and weak intensities for J = 0, 3 and 5. Noticeably, the $^{5}D_0 \rightarrow {}^{7}F_2$ induced electric dipole transition follows the selection rule of an electric quadrupole transition. These so-called pseudo-quadrupole transitions are known for their hypersensitivity to the local environment, by which immense intensity increases in the transition band can be observed.

By use of crystal-field splitting, changes in intensities and the aforementioned diagram of descending symmetry by Tanner, the correlations between different transitions of $^{5}D_0 \rightarrow {}^{7}F_{0\text{-}6}$ and the solution symmetry can be extrapolated. The transitions for Eu(III) has been described by Binnemans.[15] Some of the clearer trends include the high-symmetry dependant ΔJ = 0, and the ΔJ = 1 magnetic dipole transitions that is assumed to be insensitive to the environment[15]. Conversely, the ΔJ = 2 hypersensitive transition is very susceptible to its local environment. It has been shown experimentally that the intensity of ΔJ = 2 is related to the degree of covalency between metal and ligand, according to Judd-Ofelt theory.[21]

Table 2 – Selection rules generated on the basis of Laporte's parity rule

Operator	Parity	ΔS	ΔL	ΔJ
ED	Opposite	0	≤6	≤6 (2,4,6 if J or J'=0)
MD	Same	0	0	0, ± 1
EQ	Same	0	0, ± 1, ± 2	0, ± 1, ± 2

The $^{5}D_0 \rightarrow {}^{7}F_{3\text{-}6}$ transitions show less clear trends and will not be attempted to be generalised in the same manner at this point.

Speciation modelling

The empirical data presented from the emission spectra, hydration numbers and NMR spectra, show evidence for

signatures specific to each complex type, including the bis complex. The trends observed from the emission spectra can be used as a foundation for speciation modelling. Luminescence spectroscopy can probe a system on a time-scale reflecting the lifetimes of the complexes that are measured. For these complexes, the timescale is in the microsecond timescale, similar to NMR. The emission data is therefore also a result of a weighted average of present species. In particular, **2** becomes difficult to distinguish from the emission spectra. If the complex signatures are expressed in terms of transition band intensities, the trends become more pronounced. The intensities have been plotted as isotherms in Figure 5a. The isotherms of the intensities show a significant increase upon complexation. This is primarily an effect of relaxed selection rules. To a lesser degree it is due to fewer interacting O-H oscillators available to quench the europium excited states. Noticeably for the $^7F_0$ isotherms, the magnitude of the intensities decreases as the DPA concentration surpass 2 equivalents of the metal ion, as symmetry starts to reform.

Figure 5b show the relative intensities of the transitions opposed to the environmentally stable magnetic dipole transitions. The changes in the $^7F_1$ transition are small, and can be neglected for the current purpose. Division by the stable $^7F_1$ intensity eliminates the variance created by the increase in the total intensity. The plots showing the intensity ratios describe the symmetry-dependant behaviour of the transitions in a clear way. The model describes the data well, but the fit can be improved by increasing the number of titration points in the series. With the currently presented data, the finer details are lost.

The intensive isotherms describing the mono complex are the $\Delta J = 0$ and 4 transitions. The bis complex is indicated by the $\Delta J = 3$ and 6 transitions, and the tris complex by the $\Delta J = 2$, 3, 4 and 5 transitions. Using the DynaFit software to fit these trends, the association constants for each complex has been modelled and tabulated in Table 3, with association constants from literature for reference.[22, 23] The $^7F_2$ / $^7F_1$ intensive isotherm has been excluded to improve the current model fit.

Table 3 – Binding constants obtained by model fitting of isotherms using DynaFit software.

Binding constants	Experimental	Literature[22]
β1 = [**1**]/[**0**][DPA]	4.4e8	5.01e8
β2 = [**2**]/[**1**][DPA]	2e8	1.26e8
β3 = [**3**]/[**2**][DPA]	1.3e8	3.99e5

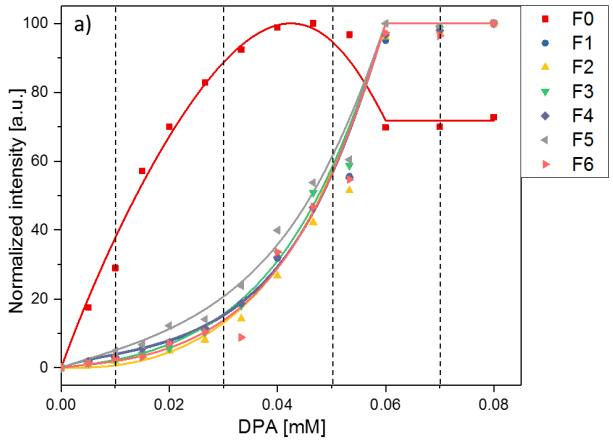

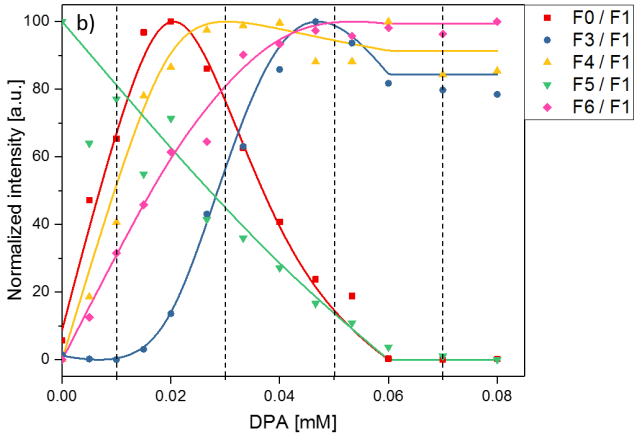

Figure 5 – Normalized intensity isotherm plots as a function of added DPA ligand. Isotherms of a) show the development of the intensities themselves, of which only the $^5D_0 \rightarrow {}^7F_0$ transition changes irregularly. The intensive isotherms of b) show much more pronounced changes upon complexation. The $^5D_0 \rightarrow {}^7F_2$ transition of the intensive isotherms is left out, as the inclusion in the data fit result in a poor model.

The isotherm should be included when a titration series with many additional EuDPA ratio increments has been made.

Structure determination

With the techniques presented, speciation of EuDPA complexes has been provided, and binding constants for each equilibrium determined.

As has been discussed, results from ^{1}H-NMR and optical spectroscopy mainly reveal the speciation of complexation, due to weighted average data from millisecond timescales. Structural information available from the emission data could potentially be elaborated upon more carefully by use of the symmetry-based trends presented for Eu's electronic transitions. Analysing the spectral intensities and crystal-field splitting could reveal much about the local symmetry of the complex, especially if done in conjunction with absorption spectra. In contrast to the millisecond timescale emission and NMR spectroscopy methods, absorption spectroscopy measures data on the femtosecond timescale,[24] probing the instantaneous environment.

In this project, probing of the instantaneous environments has been attempted using X-ray diffraction data, a method also operating on the femtosecond time-scale.[25] Additionally, X-ray scattering can directly reveal the complex structure from treated diffraction data, even for solution structure.

X-ray scattering

Discerning structural information using X-ray scattering has the advantage of probing the instantaneous environment of the sample,[26] instead of giving a weighted average representation. Diffraction patterns arise when X-rays interact with electrons of a sample, effectively scattering the photons. Scattered photons interact with each other as they propagate through space. The interference pattern (scattering intensity as function of scattering angle) thus contain information about the position of atoms in a sample. The diffractions patterns will emerge when the

interference of waves satisfy Bragg's Law, and show up as intensities on the detector.

$$n\lambda = 2d\sin(\theta) \qquad \text{Eq. 2}$$

These intensities are proportional to the distribution of electron density of atoms within the unit cell of a structure, called the structure factor.

$$I \propto |F|^2 \qquad \text{Eq. 3}$$

The structure factor sums over the electron densities of each atom in the unit cell, described by the form factor, f, which itself is proportional to the number of electrons in an atom. Another significant part of the structure factor is the Debye-Waller factor that accounts for thermal motion of atoms.

The Pair Distribution Function (PDF) is achieved when total scattering data collected in Q-space is corrected and converted to a real space function[27]. The PDF has the advantage of illustrating the data as a function of r, essentially creating a histogram of interatomic distances that are intuitively easier to interpret.

Total scattering includes both standard Bragg scattering as well as Thomson scattering. After subtracting background scattering and correcting for incoherent scattering from the raw data, the coherent scattering function I(Q) is formed. This function is normalized according to the mean squared form factor, creating the total scattering structure function.

$$S(Q) = \frac{I(Q) - \langle f(Q)^2 \rangle + \langle f(Q) \rangle^2}{\langle f(Q) \rangle^2} \qquad \text{Eq. 4}$$

The structure function is the normalized scattering function that oscillates around 1. By subtracting S(Q) by 1 and multiplying the term with Q, the weight of intensities at high Q-values will be amplified, and the function will oscillate around 0. Finally, a Fourier transformation will convert the Q-space function into real space in the shape of the PDF, G(r).

$$G(r) = \frac{2}{\pi}\int_0^\infty F(Q)\sin(Qr)dQ \qquad \text{Eq. 5}$$

Table 4 – Characteristic interatomic distances assigned the PDF peaks in Figure 6.

r [Å]	Atomic pairs
1.25	C – O (Carboxylic)
1.3	C = C (Pyridine neighbours)
2.4	Eu – O C – C (Pyridine meta)
2.5	Eu – N
2.7	C – C (Pyridine Para) C – N (Pyridine Para)
3.4	Eu – C (Carboxylic)
4.6	Eu – O (Oxo)
5.2	Eu – C (Para to nitrogen)

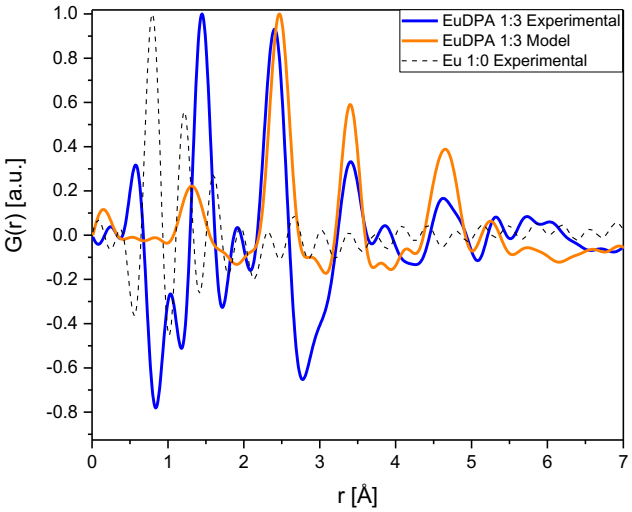

Figure 6 – Normalized PDF of experimental data versus calculated interatomic distances. Model and experimental data of the 1:3 complex is in moderate agreement and confirm the presence of the complex.

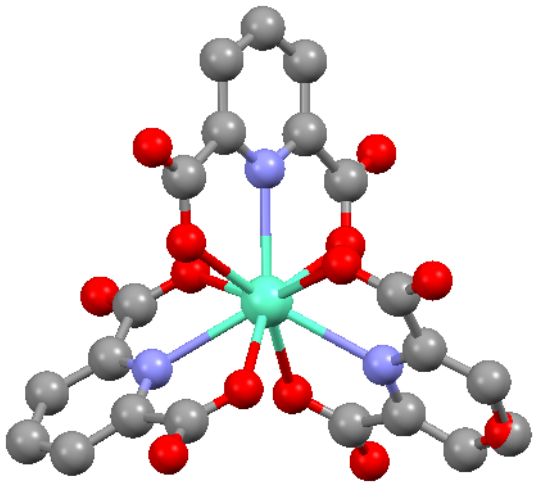

Figure 7 – Crystal structure of $Eu(DPA)_3^{-3}$.

The function essentially serves as a histogram of interatomic distances in the sample. Studying interatomic distances using PDF has gained much traction over the last couple of decades.[28, 29] Standard crystallographic methods have been limited to study only materials with long range structure, but high flux synchrotrons with large X-ray energies can achieve high Q-space data. This allows local atomic structure to be studied. Here, we use total scattering and PDF to study structure in solution. The PDF illustrated in Figure 6 show the structural information of a 1:3 ratio solution, along a model of the expected PDF, as well as a 0.2 M Eu sample with poor data as reference. A structural illustration of the tris complex can be seen on Figure 7. To stay in accordance with reported literature, the samples were initially prepared with 20 mM Eu(III), to minimize changed parameters. Based on the diffraction data, the sample concentrations were too low to distinguish complex related distances from solvent background in the X-ray scattering data. A selection of samples were remade at the synchrotron with higher concentrations.

Clear features are observed for the 100 mM 1:3 sample. A cursory inspection of Table 4 shows the assignments for specific

atomic pair distances in the complex. Many of the distances found, are in agreement with crystallographic data reported of a $Eu(DPA)_3^{-3}$ crystal structure of the complex.[30] The experimental data of **3** have similar pronounced features as the calculated PDF, yet a general discrepancy between model and experimental data can be observed throughout the PDF's. Most noticeable is the peak at about 1.4 Å that is shifted slightly to longer distances in the experimental PDF.

The PDF study suggests the presence of **3**, but is currently inconclusive in several aspects of the study. Nevertheless, a greater understanding of the complex' chemistry has been achieved, and of the concentration limitations that must be dealt with when using X-ray scattering.

Conclusion

The aim of this project was to reproduce data previously presented in the literature, and subsequently identify the **2** complex species in solution and thereby incorporate in speciation modelling.

The EuDPA complexes has successfully been made, along with a method useable for reproducing every point in a titration series with no precipitation observed 3 hours after mixing.

Luminescence and NMR spectroscopy has enabled us to observe and monitor the complexation of europium with dipicolinate as $Eu(DPA)_3^{-3}$. This serves to establish a foundation for researching lanthanide complexes using dipicolinate ligands within our research team. With optical spectroscopy, the development of the crystal-field perturbations could be followed. By fitting the isotherms, the spectral changes could be modelled and the binding constants of the three equilibria determined. $\beta 1$ and $\beta 2$ in particular are comparable to those reported in the literature, while $\beta 3$ were about 3 orders of magnitude larger. The intensive isotherms clearly show that **2** is influencing the spectral intensities, effectively confirming its participation in the complex' equilibria.

The presence of **2** is corroborated by the ^{1}H-NMR titration series, from which each equilibrium domain was clearly probed, while the hydration numbers calculated from complex excited state lifetimes, further indicate the shifted equilibrium of the complex species.

Finally, the presented PDF is indicative of the solution structure expected of **3**, but the total scattering experiments are currently inconclusive, and will continue in further studies.

In summary, the project has been successful in pinpointing the bis complex species and determining the binding constants of the equilibria. Additionally, proof-of-concept of the lanthanide complex structure-property relationship has been outlined. The identification of the **2** species should emphasize, that revisiting the already established photophysical behaviour of lanthanides in this model complex systems, will add valuable knowledge to our understanding of lanthanide properties.

Experimental

The synthesis of all complex solutions with varying metal to ligand ratios, follow the procedure described in the original work of Binnemans and Görler-Walrand.[12] However, samples with Eu:DPA ratios around 1:2 tend to precipitate. This prompted the devising of a more synthesis route that could be dependably reproduced. This is especially necessary for samples with DPA contents close to 2 equivalents per Eu ion, as precipitation readily took place.

The complications experienced when making the samples, included dipicolinic acid precipitating approximately 3 hours after mixing, creating a flaky precipitate. At higher pH, europium hydroxides form, which appears as a foggy white precipitate. To reproduce results made in the original literature, the metal ion concentrations were standardized at 0.02 M Eu, and DPA contents ranging from 0 to 4 equivalents. For each sample, a 0.1 M Eu stock solution was made by dissolving Eu_2O_3 in 10 % $HClO_4$ or 2.38 M HCl/DCl. For each sample, appropriate amounts of DPA were weighed and dissolved in 2.38 M NaOH equal to one fifth of the final volume. When both solutions had properly dissolved, the Eu solution was added to the DPA solution in a 1:1 ratio, after which precipitate of the hydroxide complex should form. This leaves 3/5 of the intended final volume, to dissolve precipitate by pH adjustments. If any flaky DPA precipitate hasn't dissolved after mixing, pH is increased. This is done using 4 M NaOH in 20 µl addition. When only the foggy precipitate of the hydroxide complex is present, pH can be cycled back down below pH 2. A clear solution should be observed. The specific limits of solubility were not determined, but the dipicolinic acid was dissolved at pH = 8, while the europium hydroxides were dissolved at pH = 2. A dilution series of the DPA solution would make the procedure much more efficient, but precipitate was difficult to control, after which this method was terminated.

The samples could be made in the exact same manner using HCl or DCl in place of $HClO_4$.

Acknowledgement

I would like to thank the entire TJS lanthanide research team of the Nano Chemistry group, whose experience has helped me immensely to understand the field for this thesis. Dr. Riikka Arppe in particular has invested a lot of time in helping me understand the spectroscopic methods I have used. My supervisor Associate Professor Thomas Just Sørensen's enthusiastic encouraging and unwavering faith in me, has made it easy to stay motivated during the project. Lea and Nicolaj, my fellow undergraduate students, has provided endless moral support during late nights at the office.

Special thanks to Assistant Professor Kirsten M. Ø. Jensen and her structure determination group for assisting me in all respects in the field of scattering. Her undergraduate student Emil Kjær's understanding of scattering phenomena has succeeded when my own fell short. I would also like to thank MSc Nina Salinas from the BWL group for repeatedly noticing the times I was lost in the lab.

Finally, special thanks go to my Nanoscience study group. They have helped me stay focused during the project, and have when necessary, offered constructive criticism among other types of criticism.

Notes and references

Address: Nano-Science Center & Department of Chemistry, University of Copenhagen, Universitetsparken 5, 2100 København Ø, Denmark.; E-mail: skf209@alumni.ku.dk
† Electronic Supplementary Information (ESI) available: [details of any supplementary information available should be included here]. See DOI: 10.1039/b000000x/

1. S. Liu, D. Lee, M.-q. Huang, A. Higgins, Y.-h. Shen, Y. He and C. Chen, *Journal of Iron and Steel Research, International*, 2006, **13**, 123-135.
2. S. Faulkner and O. A. Blackburn, *The Chemsitry of Molecular Imaging*, 2014, **179-197**.
3. P. Caravan, *Chemical Reviews*, 1999, **99**, 2293-2352.
4. B. J. Mincher, G. Modolo and S. P. Mezyk, *Solvent Extraction and Ion Exchange*, 2009, **27**, 579-606.
5. M. Weller, T. Overton, J. Rourke and F. Armstrong, *Inorganic Chemistry*, OUP Oxford, 2014.
6. Y. Guoan, H. Hui, L. Rushan and Z. Wenbin, *Procedia Chemistry*, 2012, **7**, 215-221.
7. P. A. Tanner, *Springer Ser. Fluoresc.* , 2011, **7**, 183-234.
8. N. P. Kuzmina, L. I. Martynenko, N. V. Chugarov, I. G. Zaitseva, A. N. Grigoriev and A. N. Yakushevich, *Journal of Alloys and Compounds*, 2000, **308**, 158-162.
9. J. Rydberg and Y. Albinsson, *Solvent Extraction and Ion Exchange*, 1989, **7**, 577-612.
10. M. Tropiano, O. A. Blackburn, J. A. Tilney, L. R. Hill, M. P. Placidi, R. J. Aarons, D. Sykes, M. W. Jones, A. M. Kenwright, J. S. Snaith, T. J. Sørensen and S. Faulkner, *Chemistry – A European Journal*, 2013, **19**, 16566-16571.
11. M. Tropiano, O. A. Blackburn, J. A. Tilney, L. R. Hill, T. J. Sorensen and S. Faulkner, *J. Lumines.*, 2015, **167**, 296-304.
12. K. Binnemans, K. VanHerck and C. GorllerWalrand, *Chem. Phys. Lett.*, 1997, **266**, 297-302.
13. M. H. V. Werts, R. T. F. Jukes and J. W. Verhoeven, *Phys. Chem. Chem. Phys.*, 2002, **4**, 1542-1548.
14. W. T. Carnall, G. L. Goodman, K. Rajnak and R. S. Rana, *The Journal of Chemical Physics*, 1989, **90**, 3443-3457.
15. K. Binnemans, *Coord. Chem. Rev.*, 2015, **295**, 1-45.
16. E. G. Moore, *Dalton Trans.*, 2012, **41**, 5272-5279.
17. A. Beeby, I. M. Clarkson, R. S. Dickins, S. Faulkner, D. Parker, L. Royle, A. S. de Sousa, J. A. Gareth Williams and M. Woods, *Journal of the Chemical Society, Perkin Transactions 2*, 1999, DOI: 10.1039/A808692C, 493-504.
18. B. R. Judd, *Physical Review*, 1962, **127**, 750-&.
19. G. S. Ofelt, *J. Chem. Phys.*, 1962, **37**, 511-&.
20. G. K. J. B. Liu, *Tsinghua University Press & Springer*, 2005.
21. C. K. Jørgensen and R. Reisfeld, *Journal of the Less Common Metals*, 1983, **93**, 107-112.
22. J. C. G. Bünzli and A. S. Chauvin, *Spectroscopy Letters*, 2004, **37**, 517-532.
23. I. Grenthe, *J. Am. Chem. Soc.*, 1961, **83**, 360.
24. T. Kowall, F. Foglia, L. Helm and A. E. Merbach, *Journal of the American Chemical Society*, 1995, **117**, 3790-3799.
25. A. Barty, C. Caleman, A. Aquila, N. Timneanu, L. Lomb, T. A. White, J. Andreasson, D. Arnlund, S. Bajt, T. R. M. Barends, M. Barthelmess, M. J. Bogan, C. Bostedt, J. D. Bozek, R. Coffee, N. Coppola, J. Davidsson, D. P. DePonte, R. B. Doak, T. Ekeberg, V. Elser, S. W. Epp, B. Erk, H. Fleckenstein, L. Foucar, P. Fromme, H. Graafsma, L. Gumprecht, J. Hajdu, C. Y. Hampton, R. Hartmann, A. Hartmann, G. Hauser, H. Hirsemann, P. Holl, M. S. Hunter, L. Johansson, S. Kassemeyer, N. Kimmel, R. A. Kirian, M. Liang, F. R. N. C. Maia, E. Malmerberg, S. Marchesini, A. V. Martin, K. Nass, R. Neutze, C. Reich, D. Rolles, B. Rudek, A. Rudenko, H. Scott, I. Schlichting, J. Schulz, M. M. Seibert, R. L. Shoeman, R. G. Sierra, H. Soltau, J. C. H. Spence, F. Stellato, S. Stern, L. Struder, J. Ullrich, WangX, G. Weidenspointner, U. Weierstall, C. B. Wunderer and H. N. Chapman, *Nat Photon*, 2012, **6**, 35-40.
26. T. Egami and S. J. L. Billinge, *Elsevier*, 2012, **Pergamon Materials Series**.
27. S. J. L. Billinge, *Department of Applied Physics and Applied Mathematics, Columbia*.
28. K. M. Ø. Jensen, M. Christensen, P. Juhas, C. Tyrsted, E. D. Bøjesen, N. Lock, S. J. L. Billinge and B. B. Iversen, *Journal of the American Chemical Society*, 2012, **134**, 6785-6792.
29. N. Lock, M. Christensen, K. M. Ø. Jensen and B. B. Iversen, *Angew. Chem., Int. Ed.*, 2011, **50**, 7045.
30. P. A. Brayshaw, J. C. G. Bünzli, P. Froidevaux, J. M. Harrowfield, Y. Kim and A. N. Sobolev, *Inorg. Chem.*, 1995, **34**, 2068.

UCPH NanoScience
NanoVidenskab KU

tidsskrift.dk/index.php/NanoVidenskabKU

Thesis Paper

Population size matters: The cause & effect of heterogeneous β_1AR expression and its influence on receptor internalization.

Sylvester Houstrup Langvad,*‡ Randi Westh Hansen, Johannes Holm, and Karen Laurence Martinez

Received June 2017, Accepted April 2018

In cellular physiology, the impact of heterogeneous receptor expression is a topic that has recently started to receive much attention from the scientific community. However, much is still not understood about the specifics on the origin of this heterogeneity nor how it affects bulk measurements of heterogeneous population. While the literature often acknowledges this heterogeneity, it falls short of offering an explanation of what practical implications this variability may have. In this paper, we examine two methods for evoking protein expression of G Protein-Coupled Receptors, transient transfection and inducible cell lines, and show that these methods have markedly different expression variabilities. While the inducible cell lines have relatively homogeneous expression profiles, the transient transfected cells showed large variability to an extent that bulk measurements of transfected cells may yield misleading data. We hope that the results presented in this paper may inspire future research in the field to fully consider the effects of heterogeneous expression profiles.

Undoubtedly, it is a fair label to term the superfamily of the G-Protein-Coupled-Receptors (GPCRs) as the doorbells of the cell. These membrane receptors are involved in a wide range of varying signaling events initiated by extra-cellular ligands such as hormones, neurotransmitters, photons and growth factors, and are responsible for the continuation of these signals through the plasma membrane, a process they accomplish by activating G-proteins located on the inner leaflet of the membrane.[1,2] The presence of GPCRs is indeed so pervasive that they contribute to all known physiological processes in mammals.[3] As a direct consequence of this, the GPCRs as a group is by far the largest target for drugs and pharmaceutical-related research, with these drugs accounting for the largest amount of medicine being sold worldwide.[4] Of the GPCRs, a common target of study is the GPCR-subfamily of the β-adrenergic receptors, amongst which the subtype β_1AR is the most abundant in the mammalian brain.[5] This receptor is known to mediate interactions with the neurotransmitter norepinephrine and plays a crucial role in synaptic plasticity and memory regulation, including the formation of emotionally charged memories.[6,7]

An emerging field of study in cellular biology is protein heterogeneity. It has been long known that there exists a large variability in protein expression (the proteome), even for cells of completely identical genomes, but recent advancement in single-cell studies have allowed for even better characterization.[8,9] This natural variability is largely a consequence of stochasticity in genetic translation and transcription, and has the advantage that variable gene expression can broaden the range of stress resistance across a population of cells.[10] This advantage however, can quickly turn into a problem when it confers a resistance to diseased cells against various treatments such as antibiotics and cancer-therapy, and has even been speculated to be responsible for the process of aging.[11] Perhaps most importantly, there are cases in the literature where the functional characterization of the pharmaceutical properties of ligand-type drugs have yielded completely different results due to variance in protein expression levels.[12]

Despite this knowledge, a lot of research is still done without much consideration to the variability of protein expression in assays. A common method to evoke protein expression in cell lines is through transient transfection that introduce genes of interest into cells transiently.[13,14] Another less common method to evoke expression of protein is to develop or acquire an inducible monoclonal cell line, where the expression of a protein of interest is initially inhibited by a repressor, though expression of the protein can be activated and tuned by the addition of a correspond-

Bio-Nanotechnology and Nanomedicine Laboratory, Department of Chemistry & Nano-Science Center, University of Copenhagen, Universitetsparken 5, DK-2100 Copenhagen, Denmark.
‡ *Copenhagen, Denmark. E-mail: smh645@alumni.ku.dk*

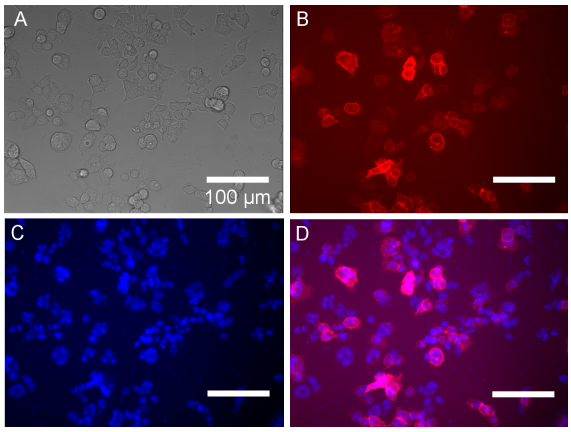

Fig. 1 Inverted light microscopy of transient transfected β_1AR T-REX^{TM} cells. One set of images of inverted light microscopy of transient transfected β_1AR T-REX^{TM} cells with **(A)** bright-field image, **(B)** β_1AR labelled with SNAP-surface BG549 and **(C)** cell nuclei labelled with NucBlue. **(D)** Overlaid image show co-localization and help determine the number of transfected cells. Scale bar: 100 μm.

ing effector. One such system is the tetracycline-controlled transcriptional activation system where tetracycline (TET) is used as effector to de-repress a promoter by binding to a corresponding inhibitor. [15,16]. Both of these methods has their own merits, but may result in different protein expression heterogeneities. If we take together the facts that GPCR expression may impact regulation and function as stated above, while a lot of current GPCR studies only has little or no consideration for variability of protein expression, a worrying trend begin to appear.

In this study, we investigated the variability of β_1AR expression across the transient transfection and the inducible cell line methods, as well as what impact varying receptor expression levels has on its own regulation, information that might prove crucial in order to make proper investigations of GPCRs in the future. As a model system, we employed the mammalian Flp-In^{TM} T-REX^{TM} 293 cell line with SNAP-tag derived from embryonic human kidney cells. We found that receptor expression variability is largely influenced by the chosen protein expression method and that it is possible for important parameters such as receptor internalization properties to be hidden in bulk measurements for very heterogeneous protein profiles. Essentially, protein expression methods evoking little heterogeneity, e.g. inducible cell lines, may be more desirable than a more heterogeneous counterpart.

Transient transfection yields heterogeneous expression

We imaged cells transient transfected with SNAP-β_1AR DNA (henceforth only referred to as β_1AR) with inverted light microscopy images (**Figure 1**. n=1, image shown is one representative image out of four). To determine if and how many cells were successfully expressing β_1AR receptor, the receptor and the cell nuclei were labelled with SNAP-Surface-BG549 and NucBlue respectively (see Materials and Methods). Manual data treatment revealed a transfection efficiency of 53.8 $\pm$ 5.1%. This is an estimate based on a manual count of the number of nuclei with overlapping receptor expression. Note then, that also dead, non-transfected cells contribute to the total number of nuclei counted, as these can be indiscernible from healthy cells. The imaging also revealed large cell-to-cell variability of expression levels of β_1AR for the cells with successful uptake (up to a factor 2.45 increase between low- and high-expression, found by comparing the average intensities of six cells of similar size showing low and high expression). Altogether, these results suggest that transient transfection yield heterogeneous expression of transfected protein, with a high amount of cells having low to no expression.

Monoclonal cell lines have more homogeneous expression than transient transfected cell lines

Next, we investigated the heterogeneity of transfected cell lines in a more quantitative manner. For this purpose, we used Flow Cytometry (FC) [17] to measure receptor expression of individual transfected cells (**Figure 2A-B**, n=1). For transfection, the total DNA concentration was always kept constant at 0.002 g/l (see materials and methods), with varying ratios of β_1AR DNA and pcDNA3 (Nonsense DNA with no coding properties). The point of keeping the total DNA concentration total (while increasing the [receptor:empty] DNA ratio), as opposed to simply increase the amount of transfected receptor DNA, is to make sure that approximately the same number of cells gets transfected for all the experiments. For all β_1AR DNA transfection quantities, there was a huge variance in receptor expression levels of individual cells, confirming the suggestion of the previous microscopy recordings. The transfection efficiency remained around a level close to approx. 55% for all receptor transfection quantities, which is close to the efficiency estimated with the microscope images. Note that the flow cytometry revealed much larger variance between low- and high-expressing cells than the inverted light microscopy did. While microscopy only revealed an intensity difference of almost a factor 2.5 between low- and high-expression, FC revealed expression differences of more than a factor 1000. This is likely a question of resolution: FC has a much higher signal-to-noise ratio, and thus much lower individual expression levels can be gathered. It is also important to note that the FC experiments each counted 10000 cells, while there only were a few hundreds cells in the microscope images from where we found our

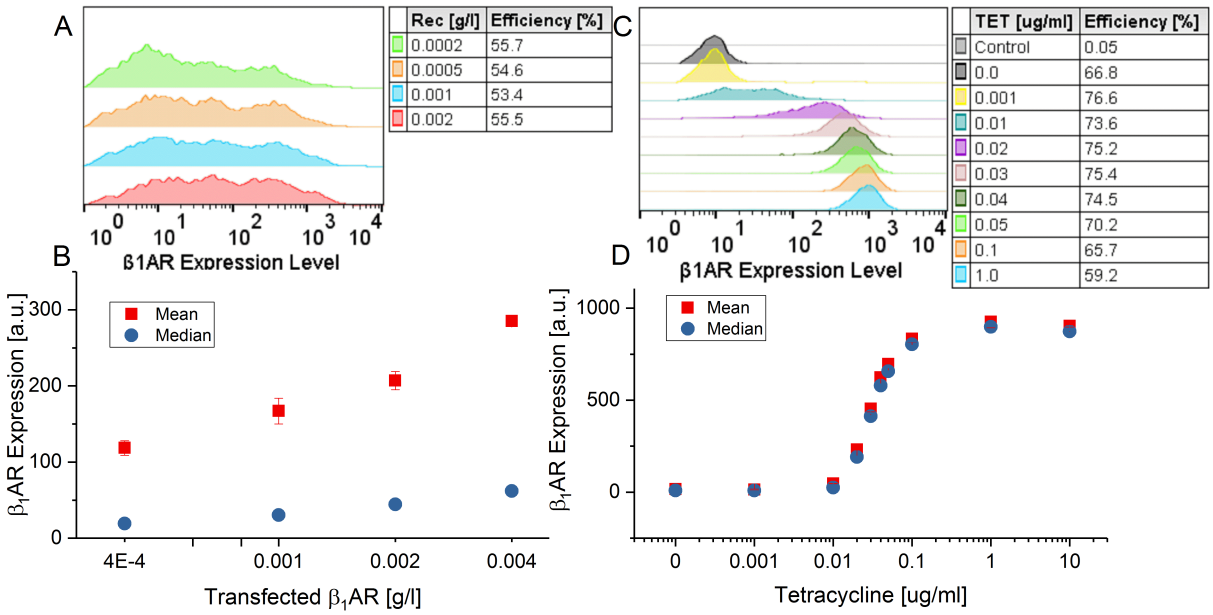

Fig. 2 Flow cytometry of cell lines reveal distinct heterogeneities (A) (n=1) Histograms of β_1AR expression for transfected cell lines for varying amounts of β_1AR DNA used for transfection. Experiment was carried out with duplicates. β_1AR expression is derived from fluorescence intensity of SNAP-BG649. Total DNA concentration was kept constant at 0.002 g/l per well for each condition, and the legend denotes how much of this total was made up of receptor DNA (while the rest was nonsense DNA). Efficiency refers to the transfection efficiency, and is the amount of cells of reasonable size and shape that express the receptor. Note that the size of the right 'tail' of expression increases as the quantity of transfected receptor DNA increases, but not the length. **(B)** Mean and median values ± S.D. of β_1AR expression for transfected cell lines. Note that for absolute values, the mean increases faster than the median for transfection, suggesting a skewing of the expression profile. **(C)** (n=1) Histograms of β_1AR expression for inducible cell lines for varying amounts of added tetracycline (TET). Except for a critical area between concentrations of 0.001-0.02 [ug/ml] tetracycline, the receptor expressions are much more confined for inducible cell lines than for the transfected cell lines. **(D)** Mean and median values of β_1AR expression from inducible cell lines. Though slightly lower, the median follows the mean throughout the increasing receptor expressions.

six extreme cell samples. While the overall receptor expression level rises as the β_1AR DNA ratios increases, the mean value of the expression levels rises more in absolute terms than the median does (with an increase of 166.5 as opposed to 42.9 [a.u.]). While the arithmetic mean is simply the average expression level of a cell, the median is the middle value of a population, and is therefore less affected by extreme outliers. The mean increase and the approximately constant median can be attributed to a skewing of the expression profile; more cells are expressing a large amount of protein and fewer cells are expressing a low amount of protein, while the extreme (both low and high) expression levels remain the same. This description fits the tendency shown by the expression profiles. To summarize, the data show the following: First, that transfection yield large $\beta_1$1AR expression heterogeneity, and secondly, that there is a skewing of the expression profile instead of just a shift to higher expressions for increased transfection quantities (for constant total DNA quantities).

In the search for a method to minimize $\beta_1$1AR heterogeneity, we tested further the intrinsic diversity of protein expression of inducible cell lines by performing a similar FC-recording on a β_1AR monoclonal inducible cell lines (**Figure 2C-D**, n=1), using tetracycline concentrations ranging from 0.0 to 10.0 ug/ml. Here tetracycline acts as an effector and activates expression of $\beta_1$1AR when used on our $\beta_1$1AR inducible cell line. Comparing the expression profile of the inducible cell lines with the transfected cell lines, there is a marked difference. First, the efficiency of receptor expression is higher than for transient transfection, with the amount of cells of appropriate size and shape expressing sufficient quantities of receptor being at around approx. 70%. In addition, most of the tetracycline concentrations resulted in, compared to the transfected cells, very homogeneous expression profiles. As all cells in a monoclonal cell line have identical genomes,[18] a relative homogeneous receptor expression is not unexpected. A possible contributor to variability is likely the binding of the effector to the inhibitor. If this is true, we predict that a constitutive monoclonal cell line (that is, one

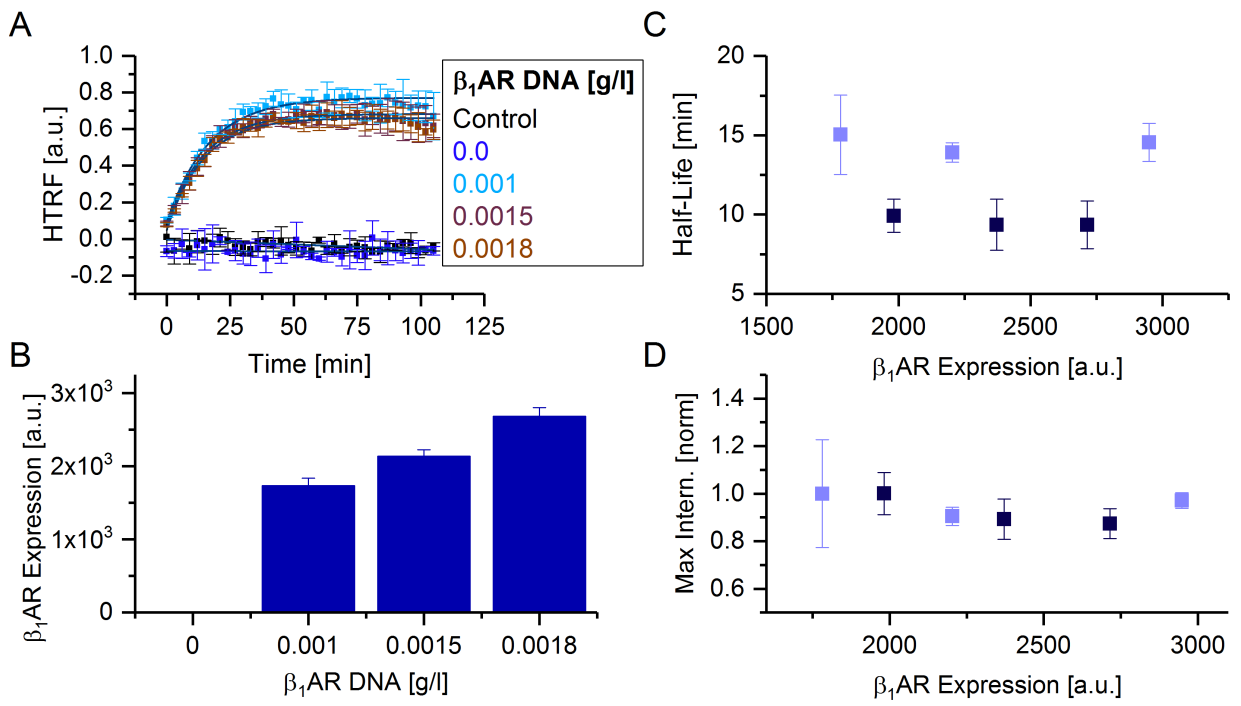

Fig. 3 Internalization of transient transfected cell lines (n=2) For C-D, each gradient denotes an independent experiment. **(A)** HTRF-value ± S.D. ($I_{Donor}/I_{Acceptor}$) evaluated over two hours. Experiment carried out in triplicates. Data shown is of one representative experiment out of two. Legend denotes how much of the total 0.002 [g/l] transfection DNA was made up of β_1AR DNA. The control group was non-transfected T-REX^{TM} 293 cells. **(B)** Mean ± S.E. receptor expression as a function of transfected receptor DNA quantity measured before internalization. Note that instead of transfection conditions, the internalization kinetics are described in regards to the receptor expression measured, as this gives a clearer view of the factual receptor concentration. **(C)** Half-life ± S.D. as a function of receptor level derived from the HTRF fits. **(D)** The maximal internalization (Max Intern.) ± S.D. of receptor as a function of receptor level derived from the HTRF fits. This data is normalized with regards the the maximum value of each dataset.

that does not have an inhibitor associated with the stably transfected gene) could be more homogeneous than an inducible one, though using a constitutive cell line means we loose control over the level of expression. We did not investigate this proposition any further. Supported by the shapes and position of the expression profiles, as well as the similar values of the median and mean, our results suggest that inducible cell lines are much more homogeneous than transfected cell lines in regards to protein expression, and that increased concentrations of effector lead primarily to a shift towards higher expression as opposed to a skewing of the expression profile. What comes next is an attempt to elucidate what effect a homogeneous protein expression has on experimental bulk measurements compared to the effects of a heterogeneous expression.

Internalization kinetic properties of transiently transfected cells could be hidden in bulk measurements

GPCRs are subject to a high degree of internal regulation, a process that is believed to finetune cellular receptor sensitivity and involves receptor desensitization by the GRK-β-arrestin system as well as internalization and recycling.[19,20] Due to the importance of this regulation, both constitutive and agonist-induced receptor internalization are typical subjects of study in cell physiology.[21,22] In order to study the practical implications of heterogeneous versus homogeneous receptor expression profiles, we investigate β_1AR internalization for different systems utilizing a novel Homogeneous Time Resolved Fluorescence (HTRF) assay.[23] This assay combines Fluorescence Resonance Energy Transfer (FRET)[24] with a Time Resolved measurement (TR). This HTRF assay works by labeling the receptor and solution with respectively a donor and an acceptor fluorophore capable of energy transfer, a so called FRET pair. Receptor internalization results in a quantifiable reduction of energy transfer that, if measured over time, gives an estimate of the amplitude of internalization. We will coin this estimate the HTRF-value.

First we tested the β_1AR internalization of cells transient transfected with increasing amount of receptor DNA using the transfection reagent Turbofect (**Figure 3**, n=2)

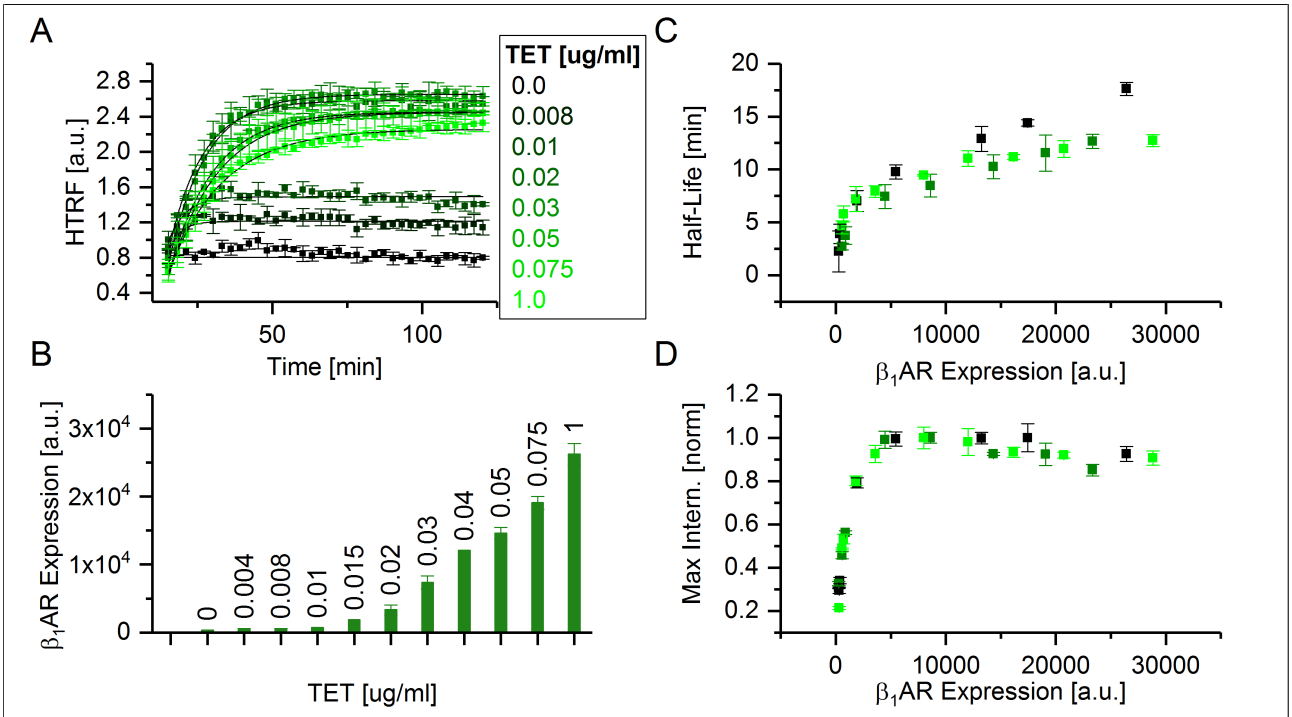

Fig. 4 Internalization kinetics of tetracycline-inducible cell lines (n=3) For C-D, each gradient denotes an independent experiment. **(A)** HTRF-value ± S.D. ($I_{Donor}/I_{Acceptor}$) evaluated over two hours. Experiment carried out in triplicates. Data shown is of one representative experiment out of three. Legend denotes how much tetracycline (TET) was used to induce receptor expression. The control group was non-transfected T-REX^{TM} 293 cells. **(B)** Average ± S.E. receptor expression as a function of tetracycline used for induction measured before internalization. Note that instead of induction conditions, the internalization kinetics are described in regards to the receptor expression measured, as this gives a clearer view of the factual receptor concentration. **(C)** Half-life ± S.D. as a function of receptor level derived from the HTRF fits. **(D)** The maximal internalization ± S.D. (Max Intern.) of receptor as a function of receptor level derived from the HTRF fits. This data is normalized with regards to the maximum value of each dataset.

with the total DNA concentration kept total. (See materials and methods). Note that the HTRF measurements are bulk measurement, and therefore the β_1AR expressions measured corresponds to the mean values of receptor expression. While the β_1AR expression rises steadily for larger quantities of receptor DNA, neither the half-life nor the maximal amount of internalization seems to be influenced by receptor expression for our transfected cells. It has been suggested by the literature that there exist a correlation between receptor regulation and receptor homo-oligomerization,[3,25] which would suggest that large receptor concentrations impacts receptor internalization. Another newer study also claim that self-regulation of receptor systems and inhibition of internalization are not necessarily due to oligomerization, but to depletion of the endocytic machinery.[26] The investigation of these mechanisms are far beyond the scope of this study, but no matter the cause, the scientific community suggests that high receptor density might inhibit the rate of internalization. As we do not observe this tendency of inhibited internalization in our transient transfection measurement, we speculate that it is caused by the extremely broad and heterogeneous protein expression profiles. Though increasing the receptor-DNA transfection quantity increases the average amount of protein the cells express, we maintain a large amount of cells expressing low quantities of the receptor (**Figure 2A**). The large quantity of low-expressing cells may well have a faster rate of internalization while making up for a large portion of the energy transfer. The large population of rapidly internalizing cells thus contributes to a large part of the bulk HTRF measurement in a way that limits the measurable HTRF-value difference between the different experimental conditions used. We describe this phenomena as *bulk-shielding*. Bulk-shielding could similarly explain why the maximal amount of internalization remains virtually unchanged even for larger averages of expressed receptor. Assuming this is true, we can further hypothesize that the marked difference in the measured half-life between the two transfection-experiments (**Figure 3C**) is due to variance in cell survivability at time of transfection. The increased half-life of the one experiment could be contributed to a transfection where less cells were transfected

with more receptor, possibly caused by a lower fraction of healthy cells at time of transfection. This condition would explain why for one experiment the receptor expression remains close to the other experiment while the internalization rate is slower. To repeat our findings, we suggest that the large heterogeneity of the receptor expression profile for transfected cell lines could influence HTRF measurements due to bulk-shielding. If this is true, then bulk measurements on cell lines with more homogeneous expression profiles should better show the hidden kinetic properties discussed.

Inducible cell line reveals distinct internalization kinetic properties compared to transfected cells

We now move on to investigate the more homogeneous expression profiles of inducible β_1AR cell lines with the HTRF-assay (**Figure 4**, n=3). The expression profiles for most of the induction condition were very homogeneous (**Figure 2C**), and as such we anticipate that far the majority of the cells to express a protein density comparable to the average that we measure with our HTRF machinery. Because of this, we expect that there would be little-to-no bulk-shielding taking place, and that the internalization kinetics are not independent of the receptor densities. We found that by increasing the receptor expression level by inducing with increasing concentrations of tetracycline (from 0.0 through 1.0 [ug/ml]), the half-lives and the maximal internalization amounts both increased in accordance with our expectations (**Figure 4C,D**). Note that the value of maximal internalization does not converge to a specific value, but slowly starts declining at large receptor densities. We contribute the peak level of the maximal internalization to saturation of the endocytosis.[27] This means that even though the amount of receptors on the cell surface increases, the amount of receptors that are internalized do not, which results in the slow decrease in the HTRF-value for high amounts of receptor expression. Our findings here point to the fact that homogeneous protein profiles allows bulk measurements to better seize the true properties of reviewed cells. Based on a comparison of our data between the transient transfection and induction β_1AR expression methods, we propose that properties of internalization kinetics are easier hidden in bulk measurements for very heterogeneous cell profiles, than it is for homogeneous populations. Note that there are some considerations towards the credibility of our proposition, and these are discussed in the Functional Relevance section further below.

The effect of post-synaptic density protein 95 on transfected cell lines kinetics

We have proposed so far how relatively simple kinetic assays might be influenced by the expression profile of the

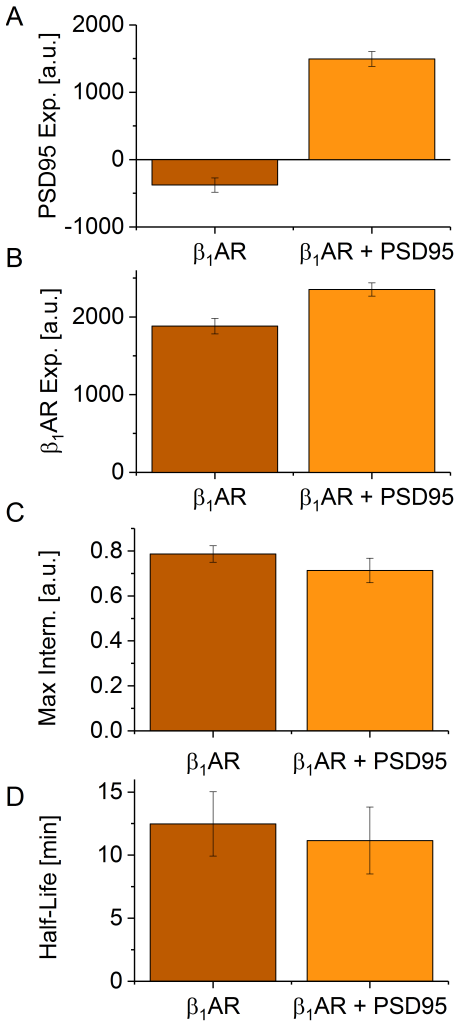

Fig. 5 Scaffold protein PSD95 stabilizes β_1AR on cell surface (n=2). Conditions carried out with the same total quantity of transfection DNA of 0.002 [g/l], the first being a 1:1 mix between β_1AR DNA and pcDNA3 DNA and the second an equal mix of β_1AR DNA and PSD95 DNA. The control was non-transfected T-Rex cells. **(A)** Mean PSD95-GFP expression $\pm$ S.E. **(B)** Mean receptor expression $\pm$ S.E., **(C)** mean max internalization $\pm$ S.E. and **(D)** mean half-life $\pm$ S.E. for β_1AR transfected cells transfected with and without PSD95.

receptors of interest. We suggest that a future step in the investigation of protein expression profiles could be to look into if and how receptor-interacting proteins influences the behavior of the receptor of interest dependent on receptor heterogeneity. Determining the practical implications of heterogeneity on important cellular functions could provide useful information on cell physiology. One such example is the post-synaptic density protein PSD95, a protein that specifically interacts with β_1AR[28] and is responsible for antagonizing receptor endocytosis in re-

sponse to agonist activation, stabilizing the receptor at cell surface.[29,30]

To illustrate how such a study might be undertaken, we investigated the effect of co-transfection of PSD95 with β_1AR for transiently transfected cell lines alongside the HTRF measurements (**Figure 5**, n=2). As before, the total quantity of transfected DNA remains constant, with cells being transfected either with a mix of β_1AR DNA and nonsense DNA, or β_1AR DNA and PSD95 DNA. This experiment supports what is already known in the literature; that PSD95 stabilizes β_1AR on the cell surface, as both indicated by increased receptor expression (more receptors on cell surface means more labeled receptors), and the decreased maximal internalization. No statistically significant enough change to the Half-life is observed to conclude anything, though the literature have demonstrated that PSD95 slows rate of agonist-induced β_1AR internalization.[7] This discrepancy can likely be blamed on the small number of experiments. Following a more in-depth study of PSD95's influence on transfected cell lines, a study of constitutive PSD95-expressing β_1AR inducible cell lines should follow, as to allow comparison between heterogeneous and homogeneous conditions.

Functional Relevance

A valid argument against our proposition of bulk-shielding is that the two cell lines investigated are not exactly identical due to the natural constraints of the experiment. This is a common problem for cross-cell line studies, but as both transfection and induction are methods used for modern research, it is nonetheless important to be able to pit them against each other. The practical implications of evoking receptor expression through the use of transient transfection compared to inducible cell lines has been presented in this article. We propose that it is primarily protein heterogeneity that is the cause of the disparity between the two methods, though we acknowledge the fact that this result cannot be completely unambiguous as per the use of differently treated cell lines.

Another troubling matter is the low number of independent replications of our experiments and the slightly varying β_1AR DNA and tetracycline concentrations between the FC- and the HTRF-measurements. The ramifications of this matter is ultimately that our conclusions and propositions should not be weighted too heavily, and instead of proposing a final truth, this paper should rather act as an inspiration for further protein studies to remember to consider protein heterogeneity as an important factor in experimental measurements. This heterogeneity-consideration is not only limited to the protein of interest, but should also cover natural variations of the proteome of interacting cells for in vivo experimentation. Even though some papers do acknowledge the heterogeneous nature of their samples, heterogeneity is also a matter of degree, and is something that could and should be characterized by future research.

Conclusional Remarks

Our study investigated what effect transient transfection and inducible cell lines might have on types of variability for receptor expression and how this influences receptor internalization. For this study, we have primarily utilized the novel homogeneous time resolved fluorescence measurement method as well as flow cytometry. Evoking β_1AR expression through tetracycline induction yielded markedly more homogeneous protein expression profiles than what transient transfection with β_1AR-DNA did (**Figure 2A,C**). Likewise, HTRF measurements on cells with the two forms of evoked β_1AR expression also revealed distinct tendencies in internalization kinetics (**Figure 3 & 4**). In accordance with the literature, the receptor expression was shown to drastically regulate both the half-life and maximal value of β_1AR internalization for the tetracycline-inducible cell line (**Figure 4C-D**), while these tendencies were completely omitted from the measurements on the transient transfected cell lines (**Figure 3C-D**. This, we propose, could be attributed to bulk-shielding, an indispensable phenomena of bulk measurements on heterogeneous cell profiles in which the change in a minority of cells is hidden by the large contribution of the unchanged majority. Altogether, our study concludes that it is imperative to take into account the heterogeneity of protein expression profiles when conducting bulk experiments. It should be noted however, that we admit the fact that our experiments are not altogether statistically valid, with many of the experiments only having been performed independently once or twice. Our conclusions should therefore only be considered a suggestion of the cause and effect of heterogeneous β_1AR expression and its influence on receptor internalization.

Acknowledgements

We would like to extend our sincerest and most heartfelt gratitude to Nina Buch-Månson, Liridon Aliti, Bjarke Salling, Adam Coln Hundahl and Nikolaj Korre Brinkenfeldt that all in some way aided to the completion of this project.

Materials and Methods

Cell Culture and preparation Mammalian Flp-In^{TM} T-REX^{TM} 293 cells (Invitrogen), were grown in Dulbecco's Modified Eagle Medium: Nutrient Mixture F-12 (DMEM/F-12) 1:1 with GlutaMAX^{TM} and phenol red, supplemented with 10% FBS (henceforth referred to only

as DMEM, bought from Invitrogen). Antibiotics Zeocin (0.1 mg/ml, Gibco) and Blasticidin (0.015 mg/ml, Gibco) were mixed in the medium when used for cell growth but not for transfection. The tetracycline inducible stable cell line with inhibited expression of SNAP-β_1AR were obtained previous to the study by FLP-FRT recombination with pc3.1DNA/FRT/TO vectors (Genscript), and the antibiotics Blasticidin (0.015 mg/ml) and Hygromycin (0.1 mg/ml, Gibco) were used for cell growth but not for induction. When referring to β_1AR or the receptor(Rec) in regards to the practical experiments, we are actually referring to a SNAP tagged β_1AR variant. To prepare cells for experimentation, cells were seeded onto Perkin Elmer 384- or 24-well culture plates and incubated overnight in medium. The 384-well culture plates were incubated with 25 μg/well 0.001 % Poly-L-Lysine (Sigma-Aldrich) for 30 minutes before seeding. The next day, the medium was replaced by μl fresh DMEM with either transfection or induction reagent (see below). After 24 hour incubation, the cells were ready for HTRF, Microscopy and/or FC preparation and measurement.

Transfection and Induction Reagents Transient transfections were carried out using Turbofect Transfection Reagent (Life Technologies) using the transfection medium Opti-MEM (Life Technologies) and plasmids containing genes for β_1AR and/or PSD95-GFP-expression (Both from Cisbio). The total DNA concentration was always kept constant at 0.002 g/l DNA. When varying the quantity of β_1AR for transfection, pcDNA3 (Nonsense DNA plasmid that didn't, code for anything relevant, from Invitrogen) were added to the transfection mix in order to maintain a constant total DNA level. To prepare each transfection reagent, 2 μg DNA was suspended in 50 μl Opti-mem while 4 μl Turbofect was mixed also with 50 μl Opti-Mem. After 20 minutes of incubation, the two solutions were mixed and diluted 1:10 with DMEM. See Turbofect's online guide for additional information on successful transfection.[31] Induction reagent was fresh DMEM containing appropriate ligand (tetracycline) concentrations. Tetracycline was protected from light at all times.

Inverted Light Microscopy. Live cells were imaged using a Leica DMI6000B inverted light microscope (Leica Microsystems) with a HG-lamp. 2 mL of T-REX^{TM} cells transiently transfected with β_1AR (DNA concentration: 0.002 g/l DNA to 400.000 cells/ml. DNA was 1:1 mix between β_1AR and pcDNA3) were plated onto a glass-coverslip, and incubated with SNAP-Surface-BG549 (Bionordika) for 10 minutes. Subsequently, the plates were washed thrice with DMEM and twice with imaging medium (DMEM/F-12 (1:1) (1x) + L-glutamine + 15 mM HEPES (No Gluta-MAX and phenol red)). Finally, imaging medium and NucBlue^{TM} (Life Technologies) were added to the plates before measuring. The filter cubes EC3(SNAP-549), BGR(NucBlue) and TL-BF(Bright-Field)s were used for measurement. Image analysis was subsequently carried out using the software ImageJ.

Flow Cytometry. Flow Cytometry was carried out using a BD FACS Calibur Flow Cytometer, courtesy of the Biotech Research and Innovation Center (BRIC) of Copenhagen University. The heterogeneity of β_1AR expression was probed in T-REX^{TM} cells where expression was initiated by transient transfection, as well as with tetracycline activation on the inducible stable cell lines expressing β_1AR. Each experiment was done in duplicates and cells were grown on 24-well culture plates (300.000 cells/well). For labeling of cells for FC, the SNAP-Surface BG649 photostable fluoresent substrate (Bionordika) was added to the cells with appropriate medium containing 4 nM of the dye solution, and left to incubate for 10 minutes. The cells were then washed two times with labeling medium (DMEM/F-12 with L-glutamine and HEPES without phenol red (Gibco) and one time with FACS medium (phosphate buffered saline (PBS) with 1% FBS), carefully, as not to disturb the cells. After washing, the cells were suspended in FACS medium before commencing flow cytometry. A gating based on a side and forward scatter was used, as to only allow the cytometer to count cells of an appropriate size, that is, the living cells. The FC data was subsequently treated with FlowJo software.

HTRF Measurements. Homogeneous Time Resolved Fluorescence measurements were carried out using a Synergy H4 Hybrid Reader (BioTek Instruments) microplate reader. Measurements were carried out on either T-REX^{TM} cells transiently transfected with β_1AR, PSD95-GFP and/or pcDNA3, or on the β_1AR inducible cell line. Cells were transfected/induced and measured in a Perkin Elmer white CulturPlate-384 (0.07 cm^2/well growth area, 20.000 cells/well). Each experiment was done in triplicates. The ready cells were initially washed first with commercially available Tag-Lite buffer, pH = 7.4 (Cisbio), and then dyed with the donor, the long-lived fluorophore SNAP-Lumi4 Terbium Cryptate in DMSO solvent (Cisbio Bioassays, 100 μM stock solution diluted 1000 times in Tag-Lite buffer) that labels SNAP-β_1AR. The cells were from now on cooled on ice, inhibiting constitutive internalization. After a 3 hour long incubation the wells were washed four times with Tag-Lite buffer followed by addition of 50 μl Tag-Lite buffer to every well. The receptor expression was measured; donor intensities were collected using 340/30 nm excitation and 620/10 nm emission filters, sensitivity: 100. PSD95-GFP expression was measured with sensitivity 60. The Tag-lite medium was replaced by 25 μl of acceptor fluorophore biotin-4-Fluorescein (Cisbio) and 25 μl 2 μM of the ligand isoprotenerol to ini-

tiate internalization of the receptor. Immediately after, a new time-resolved measurement was started and carried out for two hours, with the intensity being gathered every third minute at 37^{o}C. Acceptor intensities were collected using 340/30 nm excitation and 520/10 emission filters, sensitivity: 120 for acceptor and 140 for donor. Measurements were taken with a 1500 μs time delay to account for short-lived background fluorescence. HTRF-values were obtained using the simple relationship between the measured donor- and acceptor-intensity: I_{HTRF} = I_{DONOR} / $I_{ACCEPTOR}$, and the data fitted with the equation $Y = A_1 - A_2 * e^{-kx}$. Half-Lives were found by taking $ln(2)/k$ while the maximal internalizations (Max Intern.) were the convergent values of the HTRF fits.

References

1 A. Serge and B. Snaar-Jagalska et al, *Integr. Biol.*, 2011, **3**, 675–683.

2 A. G. Gilman, *Annu.Rev. Biochem.*, 1987, **56**, 615–649.

3 B. Farran, *Pharmacol. Res.*, 2017, **117**, 303–327.

4 M. Rask-Andersen, S. Masuram and H. B. Schioth, *Annu. Rev. Pharmacol. Toxicol.*, 2014, **54**, 9–26.

5 T. Warne and M. J. Serrano-Vega et al, *Nature*, 2008, **454**, 486–491.

6 J. L. McGauch, *Science.*, 2000, **287**, 248–251.

7 L. A. Hu et al, *The Journ. of Biol. Chem.*, 2000, **275**, 38659–38666.

8 M. Niepel, S. L. Spencer and P. K. Sorger, *Chem. Biol.*, 2009, **13**, 556–561.

9 A. Raj and A. van Oudernaarden, *Cell.*, 2008, **125**, 216–226.

10 M. Kærn et al, *Cell.*, 2005, **6**, 451–465.

11 E. McCullagh et al, *Nature Chem. Biol.*, 2009, **5**, 699–704.

12 L. B. Knudsen et al, *Regulatory Peptids*, 2013, **182**, 59–61.

13 M. Oba and M. Tanaka, *Biol. Pharm. Bull.*, 2012, **35**, 1064–1068.

14 K. Ding et al, *Applied Microbiology and Biotechnology*, 2017, **101**, 1889–1898.

15 M. Gossen et al, *Science*, 1995, **268**, 1766–1769.

16 C. Lacroix et al, *Nature Protocols*, 2011, **6**, 1412–1428.

17 R. Robinson and P. Stefan, *Antibodies-Online [accessed 2017 Feb 20]*.

18 L. Bojarskaite, *Ph.D. Thesis. Faculti of Science, University of Copenhagen*, 2015.

19 J. A. Pitcher, N. J. Freedman and R. J. Lefkowitz, *Annu. Rev. Biochem.*, 1998, **67**, 653–692.

20 A. Claing, S. A. Laporte and M. G. Caron, *Prog. Neurobiol.*, 2002, **66**, 61–79.

21 S. S. G. Ferguson, *Pharmacol.*, 2001, **53**, 1–24.

22 C. Castaldo and V. Porcari et al, *Journal of Biomolecular Screening*, 2014, **19**, 859–869.

23 A. Levoye, J. M. Zwier and A. Jaracz-Ros et al, *Frontiers in Endocrinology*, 2015, **6**,.

24 B. N. G. Giepmans, S. R. Adams, M. H. Ellisman and R. Y. Tsien, *Science*, 2006, **312**, 217–224.

25 L. Stanisila and S. Cotecchia et al, *The Journal of Biol. Chem.*, 2003, **278**, 40239–40251.

26 O. Faklaris and T. Durroux, *The Faseb Jounal*, 2015, **29**, 2235–2245.

27 R. A. Warren, F. A. Green and C. A. Enns, *Journal of Biol. Chem.*, 1997, **272**, 2116–2121.

28 T. C. Møller and K. L. Martinez, *Plos One*, 2013.

29 W. Feng and M. Zhan, *Nature Reviews*, 2009, **10**, 97–99.

30 H. A. Dunn and S. S. G. Ferguson, *Molecular Pharmacologyy*, 2015, **88**, 624–639.

31 Thermofischer, *User Guide: TurboFect Transfection Reagent [Accessed 2017 Nov 28]*.